Universität Bonn

Physikalisches Institut

Search for Flavour Changing Neutral Currents through Single Top-Quark Production at $\sqrt{s}$= 8 TeV with the ATLAS Detector

Ozan Arslan

Flavour changing neutral current processes are highly suppressed in the Standard Model due to the Glashow-Iliopoulos-Maiani mechanism. However, many extensions of the Standard Model predict the existence of these processes with higher branching fractions, where some are within the reach of the current particle accelerators. In this thesis, an experimental search for flavour changing neutral currents during single top-quark production in proton–proton collisions at the LHC is presented. The main search process involves the interaction of an up- or charm–quark with a gluon, producing a single top quark, which then decays into a W boson and a b quark. The W boson then decays leptonically. The data collected by the ATLAS detector during 2012 from the 8 TeV centre-of-mass energy collisions, corresponding to an integrated luminosity of 20.3 fb^{-1} are used. The signal- and background-like events are classifed using neural networks. As no sign of signal is observed, an upper limit on the production cross-section multiplied by the $t \to Wb$ branching fraction is set. The observed 95 % CL limit is $\sigma_{qg\to t} \times \mathcal{B}(t \to Wb) < 2.9\,\text{pb}$. The observed limit can be interpreted as upper limits on the coupling constants of the flavour-changing neutral current interactions divided by the scale of new physics $\kappa_{ugt}/\Lambda < 5.8 \times 10^{-3}\,\text{TeV}^{-1}$ and $\kappa_{cgt}/\Lambda < 13 \times 10^{-3}\,\text{TeV}^{-1}$ and on the branching fractions $\mathcal{B}(t \to ug) < 4.0 \times 10^{-5}$ and $\mathcal{B}(t \to cg) < 20 \times 10^{-5}$.

Physikalisches Institut der
Universität Bonn
Nussallee 12
D-53115 Bonn

BONN-IR-2017-07
November 2017
ISSN-0172-8741

Search for Flavour Changing Neutral Currents through Single Top-Quark Production at $\sqrt{s}$= 8 TeV with the ATLAS Detector

Dissertation
zur
Erlangung des Doktorgrades (Dr. rer. nat.)
der
Mathematisch-Naturwissenschaftlichen Fakultät
der
Rheinischen Friedrich-Wilhelms-Universität Bonn

von
Ozan Arslan
aus
Samsun, Türkei

Bonn, 11.05.2017

Dieser Forschungsbericht wurde als Dissertation von der Mathematisch-Naturwissenschaftlichen Fakultät der Universität Bonn angenommen und ist auf dem Hochschulschriftenserver der ULB Bonn http://hss.ulb.uni-bonn.de/diss_online elektronisch publiziert.

1. Gutachter:	Prof. Dr. Ian C. Brock
2. Gutachter:	Prof. Dr. Jochen Dingfelder
Tag der Promotion:	20.07.2017
Erscheinungsjahr:	2017

Contents

CHAPTER 1

Introduction

There is no shortcut to truth, no way to gain knowledge of the universe except through the gateway of the scientific method.

-Karl Pearson

The achievements of the Ancient Egyptians and the Ancient Greeks are usually referred as the milestones of the human advancement in the context of the history of science in early cultures. Their knowledge in mathematics, architecture and astronomy allowed them to build monumental structures with almost perfect astronomical precision, which stand still to this date. However, humans could have employed sophisticated knowledge in their lives much earlier than the era of Ancient Egyptians. In 1994, German archaeologist Klaus Schmidt, of the German Archaeological Institute, discovered the ruins of an ancient monolithic temple, Göbekli Tepe [1], located in Southeastern Anatolia. The temple dates back to 9130 BCE, some 6000 years before the construction of the Great Pyramid of Giza, making it the oldest temple discovered. The stones used in the construction of the temple weigh as much as 20 tonnes and were quarried several kilometres away from the construction site. The walls were decorated with carvings of abstract forms of art. The stones were cut and positioned with great precision. Similar to the other ancient monolithic structures, Göbekli Tepe could also have an astronomical significance as the positioning of the temple might signal the rise of Sirius [2]. The construction of such a temple requires advanced organisational skills, which were previously thought to occur only after the development of the agriculture, which is generally considered to mark the beginning of the civilisation. However, Göbekli Tepe was constructed much earlier, during the Stone Age, when humans were hunter-gatherers. The discovery of the temple initially caused a controversy in the scientific community then changed the way historians looked at the past. Göbekli Tepe is an early example of human achievement; it represents the

humankind's ability to put the knowledge into use, organisation power and dedication.

Around 3100 BCE, the first writing system was invented by the Ancient Sumer in Mesapotamia and quickly after that humans began to develop early forms of geometry, astronomy, philosophy, medicine and mathematics.

However, after Göbekli Tepe, it would be only many millennia later that humans would start taking the first steps towards establishing modern scientific methods. The scientific revolution, which took place at the end of the Renaissance in Europe, fuelled the development and establishment of the scientific method. The principles of it, such as observation of a phenomenon, formulation of a hypothesis, testing the hypotheses by conducting experiments and analysing the results, quickly became common practices of science. The scientific methods were then enriched with the invention of the concepts of the repeatability of the results and peer review, and the formation of scholarly journals.

The scientific revolution led to a significant advancement on the understanding of the nature. The theory of evolution and natural selection, Newton's laws of motion, special and general relativity, the formation of the periodic table of elements, quantum mechanics, the development of thermodynamics, the discovery of DNA are merely a few examples of the achievements of science.

In the 20th century, the scientific methods were further refined and enriched by the introduction of the concepts of falsifiability, double-blind experiments, randomised design and controlled placebo trial.

Physics is probably one of the branches of the natural sciences that benefited the most from the era of the scientific revolution but the history of physics goes as far back as the Ancient Greeks. For instance, the concept of fundamental, indivisible particles of which the universe is made existed back then. However, it was a philosophical idea that lacked experimental verification and it remained as it was for more than two millennia. It took until the nineteenth century to theorise the concept of the atom by John Dalton, an English physicist, chemist and meteorologist.

Physics is also probably the first branch of natural sciences where the harmony between the nature and the mathematics was manifested. The calculations written on a paper using symbols, numbers and letters would agree with the motion of the stars and planets. How come one could precisely predict where and when a star rises above the horizon by requiring only a pen and a paper? However, this was not sorcery but science.

The equations scribbled on a paper that agree with the observations of nature are in fact merely the reflections of the thoughts of the brain that commands the hand to write those equations down. However, brain is nature itself; it is a complex network of neurons that interact and communicate with each other, sending electrical signals, completely obeying the laws of physics. Therefore, the human brain is the concious form of nature, observing and trying to understand itself. It looks at the stars, as well as at the atoms. It collides the atoms, *breaks* them down to their most fundamental constituents and studies them. This is the branch of physics that investigates the properties and the interactions of the subatomic particles, called particle physics.

The study that is described in this thesis is a subject of experimental particle physics. It searches for a hypothetical interaction between the fundamental constituents of matter, which has not been observed yet, but is predicted by many theories. For this purpose, the study employs the heaviest fundamental particle known. The details of the study presented here will be revealed in the following order:

Chapter 2 gives an overview of the Standard Model (SM) of particle physics. It describes the types fundamental particles of nature and their interactions. Furthermore, it introduces the Flavour Changing Neutral Currents (FCNC) which are the search subjects of the thesis. The chapter is concluded with the description of the shortcomings of the SM.

Chapter 3 provides short descriptions of various extensions of the Standard Model. It describes the FCNC interactions in the context of Beyond Standard Model (BSM) theories and emphasises why FCNC are important in search for new physics phenomena.

Chapter 4 details the main experimental setup employed in this analysis which are the Large Hadron Collider (LHC) and the ATLAS detector. It provides a detailed description of each component of the detector and their operation purposes.

Chapter 5 lists the properties of the dataset used in the analysis presented here, as well as the signal and background Monte Carlo (SM) simulations.

Chapter 6 gives a detailed description of the particle reconstruction and identification methods employed in this analysis.

Chapter 7 describes the event selection that is applied on the data and the MC in order to enrich the dataset with a possible FCNC signal.

Chapter 8 details the procedure of the production of the multi-jet events sample, which is a major background in the analysis presented here. This is the only background process that an entire chapter is dedicated to, as it is the most studied background in this thesis.

Chapter 9 explains the signal separation technique that is adopted in the study presented in this thesis. It gives a detailed description of Artificial Neural Networks (ANN), which are used as a multivariate analysis technique.

Chapter 10 summarises all the systematic uncertainties that are considered in this analysis. It describes the source of of each uncertainty, as well as it reveals the methods used to evaluate them.

Chapter 11 describes the statistical analysis performed on the data in order to extract a possible sign of a FCNC signal. Further, the results of the analysis described in this thesis is presented.

Chapter 12 explains the impact of the results of this thesis on the predictions of BSM theories. It further introduces a study that is aimed at addressing what could be expected from possible future experiments. The chapter is concluded by summarising the analysis presented in this thesis.

CHAPTER 2

The Standard Model of Particle Physics

2.1 Introduction to the fundamental forces of nature and the Standard Model

There are four known fundamental forces in nature. All the observable matter in the universe interacts through these forces. The gravitational force, or gravity, is the first discovered force of nature. Galileo Galilei proved that the gravitational acceleration is the same for every object regardless of its mass. Later, Sir Isaac Newton postulated the inverse square law which states that the attraction force between two massive objects is inversely proportional to the square of the distance between them. This was a great success at the time since it could precisely explain the distance of the planets to the Sun, their orbits around the Sun and their masses. It could also predict the existence of Neptune from the anomalies of Uranus' orbit. However, Newton's theory could not explain the perturbations in Mercury's orbit. A search for a nearby massive body around Mercury gave no results.

Later, Einstein proposed that gravity is an aspect of space-time by introducing the concept of the space-time fabric which changes form and becomes curved in the presence of matter. In a curved space-time, if there are no other forces involved, the motion of a free falling object is always a straight line, called a geodesic. Einstein gathered his ideas in the theory of General Relativity that could explain the anomalies in Mercury's orbit which is called anomalous perihelion precession of Mercury. It could also predict/explain several other phenomena such as black holes, gravitational time dilation and gravitational lensing.

The electromagnetic force, or electromagnetism, is the second force of nature to be discovered and formulated. Although electricity and magnetism were known since Ancient Greece, they were first thought to be two distinct and unrelated forces of nature until Michael Faraday experimentally demonstrated electromagnetic induction in 1831. Later, James Clerk Maxwell published his electromagnetic theory of

light in 1864 where he mathematically introduced the idea of electric and magnetic fields and showed that light is an electromagnetic wave and it is the propagator of this force. He summarized them in his famous Maxwell's equations. Paul Adrien Maurice Dirac was the first person to create a toy model using harmonic oscillators where he could quantize the electromagnetic field in 1920. Shortly after that, Enrico Fermi, Wolfgang Pauli, Eugine Wigner, Werner Heisenberg and Pascual Jordan contributed to the development of quantum mechanics and later Sin-Itiro Tomonaga, Julian Schwinger and Richard Feynman established quantum electrodynamics.

Weak interaction, or the weak force, is the force that is responsible for the beta decay. Radioactivity was experimentally demonstrated to exist in the late 19th century by Henri Becquerel, Marie Skłodowska-Curie and Pierre Curie. However, no concrete theoretical explanation existed until Enrico Fermi published his explanation of beta decay in 1933 called Fermi's theory which is the precursor to the theory of weak interaction where the force is mediated by massive particles unlike photon.

The strong interaction, or the strong nuclear force, is the force that holds the atomic nucleus together. Although the protons carry a positive electric charge, they are packed tightly inside the nucleus of the atom. Physicists thought that there had to be another force which would overcome the electromagnetic repulsion of the protons and hold them together. In the mid 1960s, it was realised that nucleons are not fundamental particles but they are made up of constituent particles called quarks. The force that was thought to propagate between the nucleons was actually an indirect effect of a more fundamental force, the strong force, which acted on the quarks.

These four forces were known to exist before the postulation of the SM which is a combination of quantum field theories that successfully adds up these forces (except for the gravity). The SM explains the interaction of these forces with matter and each other, as well as it predicts the existence of fundamental particles and their properties.

The details of the SM and the fundamental forces of nature are discussed in the following sections.

2.2 The elementary particles in the SM

According to the SM, matter is composed of elementary particles with a spin[1] of $\frac{1}{2}$, called fermions. The forces are mediated between the matter particles by the exchange of spin-1 particles called gauge bosons. The electromagnetic force is mediated by the massless photon and the weak force is mediated by three massive gauge boson called W^+, W^- and the Z boson, where the superscript indicates their electric charge. The electromagnetic and the weak forces merge into a single force called the electroweak (EW) force at higher energies, before spontaneous symmetry breaking through the Higgs Mechanism (see Section 2.3.3), therefore the SM treats them as two different aspects of the same force. The strong force is mediated by eight massless bosons called gluons. Table 2.1 shows the list of gauge bosons in the SM and some of their properties.

There are two types of fermions, called leptons and quarks. Leptons are either electrically charged, which are called charged leptons ($e^{\pm}$, $\mu^{\pm}$ $\tau^{\pm}$) or neutral which are called neutrinos (ν_e, ν_μ and ν_τ). All quarks carry fractional electric charges of either $-\frac{1}{3}e$ or $\frac{2}{3}e$. Every fermion has an antiparticle of itself, which has the same mass but opposite charge.

[1] Spin is the quantized intrinsic angular momentum of a particle that can only have values which are multiples of either integers of half integers. A spin-$\frac{1}{2}$ particle can have spin states of $+\frac{1}{2}$ and $-\frac{1}{2}$ which are often called spin-up and spin-down states.

[2] ev (electronvolt) is the amount of energy required to move an electron through a electric potential difference of one volt. 1 ev = 1.6×10^{-19} joules.

[3] e stands for the electric charge. 1 e = 1.6×10^{-19} coulombs (C).

[4] Photon and gluon are theoretically postulated to be massless. Experimentally, there are very small upper limits on their masses [3, 4].

Gauge Boson	Mass m [GeV][2]	Force	Electric Charge Q [e][3]
Photon[4] (γ)	0	Electromagnetic	0
Gluon (g)	0	Strong	0
W boson $W^{\pm}$	80.385 ± 0.015	Weak	± 1
Z boson Z^0	91.1876 ± 0.0021	Weak	0

Table 2.1: The list of gauge boson in the SM. The force they mediate, their masses and their electric charges are indicated [5].

Fermions are categorized into generations or families of doublets, where each generation is identical to each other except for the mass and flavour which is a quantum number to describe the type of the fermion.

There are six quarks which form three generations of doublets. The first doublet consists of the up quark (u) and the down quark (d), the second generation consists of the charm quark (c) and the strange quark (s) and the third generation consists of the top quark (t) and the bottom quark (b). Quarks are the only fermions that carry colour charge (C) which has three types (called red, green, blue). Quarks are confined in baryons or mesons. A baryon is a particle made up of three quarks and a meson is a particle made up of a quark and an antiquark. Baryons and mesons are in general called hadrons. There are no hadrons that carry a colour charge although they are made up of quarks and there are no observed free quarks[5]. This indicates that quarks are confined in colourless composite particles whose components' colour charges add up to zero. This is due to the nature of the strong force, explained by the theory of quantum chromodynamics (QCD) which will be detailed in Section 2.3.2. Table 2.2 lists the fermions of the SM and some of their properties. Figure 2.1 gives an illustration of the interactions between the bosons and the fermions in the SM.

Fermion type	Generation	Fermion	Charge Q [e]	Mass m [GeV]
Quarks	1st	up (u)	+ 2/3	$2.3\ ^{-0.5}_{+0.7} \times 10^{-3}$
		down (d)	- 1/3	$4.8\ ^{-0.3}_{+0.5} \times 10^{-3}$
	2nd	charm (c)	+ 2/3	1.275 ± 0.02 ($\overline{\text{MS}}$[6])
		strange (s)	- 1/3	$95 \pm 5 \times 10^{-3}$
	3rd	top (t)	+ 2/3	173.07 ± 0.89 (pole)
		bottom (b)	- 1/3	4.18 ± 0.03($\overline{\text{MS}}$)
Leptons	1st	electron (e^-)	- 1	0.5110×10^{-3}
		el. neutrino (ν_e)	0	$<0.002 \times 10^{-3}$
	2nd	muon (μ^-)	- 1	0.1057
		mu. neutrino (ν_μ)	0	0.19×10^{-3}
	3rd	tau (τ^-)	- 1	1.7768
		tau. neutrino (ν_τ)	0	18.2×10^{-3}

Table 2.2: The list of fermions in the SM and some of their properties [5].

[5] The only exception to this is the top quark, which decays before it hadronises due to its short lifetime (see Section 2.3.4.)

[6] In Quantum Field Theory, modified minimal subtraction scheme or $\overline{\text{MS}}$ scheme, is a type of renormalisation scheme used to absorb infinites in higher order perturbative calculations. The Ref. [6] provides further detailed description.

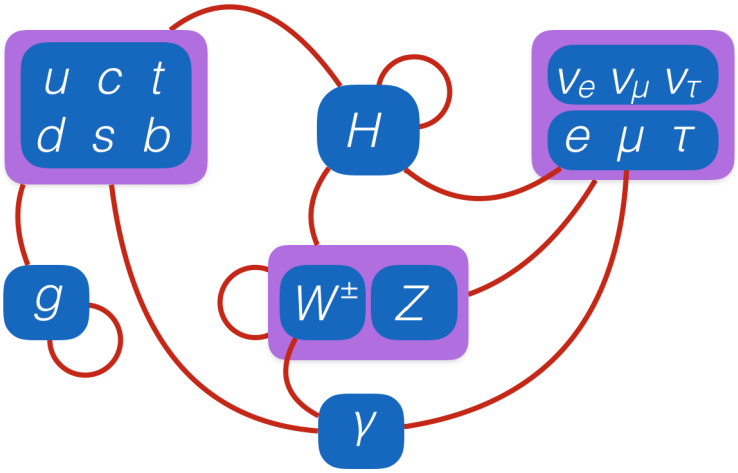

Figure 2.1: Overview of the fermions and bosons in the SM and their interactions.

2.3 Properties of the SM

The SM is a field theory where the particles are represented by fields, and their interactions and behaviour are described by mathematical constructions called Lagrange densities or shortly Lagrangians. It is specifically a gauge theory where the global Poincaré symmetry is maintained. This indicates that the Lagrangian is invariant under rotational, translational and boost transformations. The invariance under a transformation is due to a symmetry in the Lagrangian. According to the Noether theorem [7], every symmetry in a physical system has a corresponding conserved physical quantity. Lorentz symmetry, or more generally the Poincaré symmetry of the SM Lagrangian, implies the conservation of energy, momentum and angular momentum. Furthermore, it indicates that the speed of interactions between particles described by the SM does not exceed the speed of light. The conservation of different charges of the particles is due to the invariance of the Lagrangian under non-abelian[7] special gauge unitary group[8] gauge transformations of the form:

$$\mathrm{SU}(3)_C \times \mathrm{SU}(2)_{T_3} \times \mathrm{U}(1)_Y.$$

The $\mathrm{SU}(3)_C$ symmetry group indicates the QCD gauge group where C is the colour charge, which is the conserved quantity of the symmetry. It implies the existence of eight gauge bosons, in this case the gluons. This means that the gluons also carry colour (as well as anticolour) charge, this is implied by the SU(3) group being non-abelian. Therefore, gluons interact with each other strongly and just as quarks, no free gluons are observed.

The $\mathrm{SU}(2)_{T_3}\times\mathrm{U}(1)_Y$ represents the non-abelian gauge group of the electroweak sector. The conserved quantities of the symmetry group are the T_3 and Y, where T_3 refers to the weak isospin and Y is called the hypercharge which is a linear combination of the weak isospin and electric charge:

[7] In group theory, a non-abelian group is a group that has at least two members which do not commute.

[8] A special unitary group is a special form of a unitary group, which is a Lie group of unitary matrices whose determinants are equal to 1. A Lie group is a finite dimensional smooth manifold and the group operations of inversion and multiplication are smooth maps.

$$Y = 2(Q - T_3).$$

After the symmetry breaking, the $SU(2)_{T_3}\times U(1)_Y$ symmetry is reduced to $U(1)_{EM}$, where the conserved quantity is now the electric charge.

The details of the strong and electroweak sectors of the SM will be described in Sections 2.3.2 and 2.3.1.

The SM Lagrangian, in its most compact form has four terms [8]:

$$\begin{aligned}\mathcal{L}_{\text{SM}} &= \mathcal{L}_{\text{fermions}} + \mathcal{L}_{\text{bosons}} + \mathcal{L}_{\text{Yukawa}} + \mathcal{L}_{\text{Higgs}} \\ &= (i\bar{\psi}^i\gamma^\mu D_\mu\psi^i) - \frac{1}{4}F^a_{\mu\nu}F^{a\mu\nu} + (\bar{\psi}^i_L V_{ij}\Phi\psi^j_R + h.c.) + (|D_\mu\Phi|^2 - V(\Phi))\end{aligned} \tag{2.1}$$

The first term describes the interaction of fermions with the gauge bosons. The ψ^i are the fields representing the fermions, γ^μ are the Dirac gamma matrices and the D_μ is the gauge covariant derivative:

$$D_\mu = \partial_\mu - i\frac{e}{\hbar}A_\mu$$

where e is the electric charge, $\hbar$ is the reduced Planck constant and A_μ is the gauge field. The second term in Equation 2.1 is the term that describes self-interactions of the gauge bosons and their kinetic energies. $F^a_{\mu\nu}$ is the so called stress-energy tensor. The third term is called the Yukawa term and is responsible for giving masses to the fermions and to the $W^\pm$ and Z^0 bosons. V is the Higgs potential and Φ is the Higgs field. The last term is the Higgs term which is responsible for the spontaneous symmetry breaking.

2.3.1 Electroweak interaction

The weak and the electromagnetic interactions, which are valid only at low energies, are in fact special cases of the more fundamental electroweak interaction. The unification of the electromagnetic and weak interactions, which gave rise to the Glashow-Salam-Weinberg theory of electroweak interactions, was proposed by Steven Weinberg and Abdus Salam independently in 1967 [9, 10]. Sheldon Lee Glashow was the first scientist to propose a SU(2)×U(1) symmetry group [11]. In 1973 the existence of the weak neutral current (Z boson exchange) was confirmed experimentally and in 1979 these three scientists were awarded the Physics Nobel Prize *"for their contributions to the theory of the unified weak and electromagnetic interaction between elementary particles, including, inter alia, the prediction of the weak neutral current"* [12]. Later in 1983 the W and Z boson were discovered at Super Proton Synchrotron by the UA1 and UA2 experiments [13, 14]. One month after that, the Z boson was discovered by the same collaborations [15, 16]

In electroweak theory, the isospin T_3 and the chirality[9] are strongly related. The left-handed fermions carry an isospin of $T_3 = \pm 1/2$ and the right-handed fermions have $T_3 = 0$. Therefore left-handed fermions form isospin doublets of $SU(2)_{T_3}$ and right-handed fermions form singlets which are $SU(2)_{T_3}$ symmetric. The fermions can then be grouped according to their isospin states as:

[9] In mathematics, the chirality of an object determines whether its mirror image is identical to itself. The object is called chiral if it is different than its mirror image. In particle physics, another term called helicity or handedness is defined for massless particles (such as photon and gluon) which is the direction of its spin relative to its momentum. The particle is called left-handed if the spin and the momentum have opposite directions and it is called right-handed if the spin and the momentum are in the same direction. Helicity is a frame independent aspect. Helicity and chirality become identical if the particle is massless. Nevertheless, a handedness can still be defined for a massive particle which is valid only for the frame of reference it is defined in. Therefore it is possible to define left- and right-handed fermions for a given frame.

$$\Psi_L^{\text{lepton}} = \begin{pmatrix} \nu_e \\ e \end{pmatrix}_L, \begin{pmatrix} \nu_\mu \\ \mu \end{pmatrix}_L, \begin{pmatrix} \nu_\tau \\ \tau \end{pmatrix}_L$$
$$\Psi_R^{\text{lepton}} = e_R, \mu_R, \tau_R$$
$$\Psi_L^{\text{quark}} = \begin{pmatrix} \nu_u \\ d \end{pmatrix}_L, \begin{pmatrix} \nu_c \\ s \end{pmatrix}_L, \begin{pmatrix} \nu_t \\ b \end{pmatrix}_L,$$
$$\Psi_R^{\text{quark}} = \begin{pmatrix} \nu_u \\ d \end{pmatrix}_R, \begin{pmatrix} \nu_c \\ s \end{pmatrix}_R, \begin{pmatrix} \nu_t \\ b \end{pmatrix}_R,$$

where up-type fermions (u, c, t, ν_e, ν_μ, ν_τ) have $T_3 = 1/2$ and the down-type fermions (d, s, b, e, μ, τ) have $T_3 = -1/2$.

There are four vector gauge boson fields corresponding to the $SU(2)_{T_3} \times U(1)_Y$ symmetry group of electroweak interactions. Three of them (W_μ^1, W_μ^2, W_μ^3) arise from the $SU(2)_{T_3}$ symmetry and one (B_μ) from the $U(1)_Y$ symmetry and they are all massless. These gauge fields appear in the first two terms of the SM Lagrangian given in Equation 2.1. The $W^\pm$, Z bosons and the photon are linear combinations of these massless gauge bosons:

$$\begin{pmatrix} A_\mu \\ Z_\mu \end{pmatrix} = \begin{pmatrix} \cos\theta_W & \sin\theta_W \\ -\sin\theta_W & \cos\theta_W \end{pmatrix} \begin{pmatrix} B_\mu \\ W_\mu^3 \end{pmatrix}$$

$$W_\mu^\pm = \sqrt{\frac{1}{2}}(W_\mu^1 + W_\mu^2),$$

$$\tan\theta_W = \frac{g'}{g}.$$

The coupling strengths g and g' of the boson W_μ^3 and the B_μ are related by the weak mixing angle, or Weinberg angle, θ_W. The bosons A_μ and the Z_μ represent the photon and the Z boson.

The formulation of the electroweak interaction in the SM assures the experimentally observed aspects of it, such as:

- Only left-handed fermions (and right-handed anti-fermions) interact with $W^\pm$ bosons through weak interaction.
- There are no right-handed neutrinos.
- Since quarks have both left- and right-handed isospin doublets, the W boson is capable of changing the flavour of quarks, which is called Flavour Changing Charged Current (FCCC) by coupling to an up and a down type quark. However since right-handed neutrinos do not exist, flavour changing of a lepton is not allowed by the SM.
- Direct Z boson exchange between different flavours of either quarks or leptons is not allowed.
- The SM neutrinos are postulated to be massless since the SM has no right-handed neutrinos. However, neutrino oscillations indicate that neutrinos have a small mass [17]. One possibility that can explain this is that neutrinos could be their own anti-particles.

It is experimentally observed that the $W^\pm$ bosons couple and change the flavour of quarks not only within the same generation but are also capable of changing the flavour of a quark into a flavour of

a different generation. However, the coupling between flavours of different generation is suppressed compared to the flavour change within the same generation. This observation is interpreted as the mass eigenstates of quarks which are the physical quark states being different than the weak isospin states that the $W^{\pm}$ boson couples to. Instead, the weak eigenstates of quarks are combinations of up- and down type mass eigenstates. Conventionally, the down-type quarks are chosen to be mixed and the weak isospin and mass eigenstates of the up-type quarks are kept identical. For the weak eigenstates (d', s', b') and the mass eigenstates (d, s, b) of the down-type quarks, one can then write the Cabibbo-Kobayashi-Maskawa matrix $\mathrm{V_{CKM}}$:

$$\begin{pmatrix} d' \\ s' \\ b' \end{pmatrix} = \begin{pmatrix} V_{ud} & V_{us} & V_{ub} \\ V_{cd} & V_{cs} & V_{cb} \\ V_{td} & V_{ts} & V_{tb} \end{pmatrix} \begin{pmatrix} d \\ s \\ b \end{pmatrix}$$

$$\mathrm{V_{CKM}} = \begin{pmatrix} |V_{ud}| & |V_{us}| & |V_{ub}| \\ |V_{cd}| & |V_{cs}| & |V_{cb}| \\ |V_{td}| & |V_{ts}| & |V_{tb}| \end{pmatrix} \approx \begin{pmatrix} 0.974 & 0.225 & 0.003 \\ 0.225 & 0.973 & 0.041 \\ 0.009 & 0.040 & 0.999 \end{pmatrix}$$

The numbers given in the matrix are obtained through a global fit from the combination of many experiments [5]. Mathematically, the choice of mixing the down-type quarks is purely arbitrary. This is due to the fact that the $\mathrm{V_{CKM}}$ is unitary. One would obtain the same matrix if the up-type quarks were chosen to be mixed. Each term in $\mathrm{V_{CKM}}$ represents the probability of one quark to change it's flavour into another flavour through FCCC. The numbers given in the matrix are obtained through a global fit from the combination of many experiments [5].

One can directly observe that the diagonal elements of the $\mathrm{V_{CKM}}$ are close to one, whereas the off-diagonal elements are small. This means that mixing between quarks of different generations is suppressed. One can also note that the mixing of the first two generations is significantly larger than the mixing of the second and third generations.The mixing of the first and the third generations is the smallest.

2.3.2 Strong interactions and quantum chromodynamics

The eight generators of the non-abelian $\mathrm{SU}(3)_C$ symmetry group of QCD correspond to the eight massless colour charged gluons. The three colour charges of the strong interaction are manifested by the degree of the symmetry group. Gluons themselves carry colour charge and therefore they interact with each other. Quarks and gluons are the only particles with colour, making them the only set of particles that interact through strong force.

Confinement

As was mentioned earlier, there are no free quarks (or gluons) observed and they are always found confined in hadrons. This is related to the nature of the strong interactions. Unlike all the other forces of nature, the force between two colour carrying particles does not diminish with the distance between them but rather increases. There is no analytic proof that can describe this phenomenon. However, numerical approximations of QCD carry a term which is linear in distance between the two particles. The force grows as the distance increases but the amount of force to hold the colour carrying particles bound to each other has an upper limit. After a certain distance, it becomes more favourable for the particles to pair with their anti-partners, which spontaneously appear to form new hadrons. Therefore in particle accelerators, when hadrons collide, *jets* (see Section 6.2.3) of new hadrons are observed rather than individual quarks.

Asymptotic freedom

In contrast to confinement, at very short distances, another phenomenon, somewhat opposite to confinement occurs, which is called asymptotic freedom. At very short distances, the strong force between particles decreases logarithmically and inside the hadrons quarks can be treated as quasi-free particles. The asymptotic freedom was first described in 1973 by David J. Gross, Frank Wilczek and H. David Politzer. They were awarded the physics Nobel prize in 2004 *"for the discovery of asymptotic freedom in the theory of the strong interaction"* [18].

The field created by a particle carrying a certain charge polarises its surroundings due to short lived particle and anti-particle pairs it creates. The number of these *virtual* particle and anti-particle pairs is related to the strength of the field that the charge produces. In the presence of an external field, these virtual particles orient themselves according to the field, reducing the strength of the field on the real particle. This phenomenon is called vacuum polarization.

When the distance between two charged particles gets smaller, the particles that are moving into each others' vacuum fields are exposed to each others' vacuum polarization effects less. This is called screening.

Since quarks carry colour charge, they are also subject to the screening effect when they move relative to each other. However, the force carrier of the strong interaction, the gluon itself carries colour charge. There are eight linearly independent colour states of gluons made of colour and anti-colour pairs equivalent to the Gell-Mann matrices [19]. This arrangement of colour charges in gluons causes the inverse effect of screening near another coloured particle. This is called anti-screening. The screening from the quarks and anti-screening due to gluons reduce the effect of each other. The net effect is related to the number of different colours and quark flavours. Given that there are three colours, as long as there are no more than 16 quark flavours, the anti-screening effect overcomes, causing the theory of QCD to be asymptotically free (there are only six known quark flavours). This can be observed in the beta function[10] of QCD:

$$\beta(\alpha_s) = \frac{\alpha_s}{\pi}(\frac{n_f}{3} - \frac{11N_c}{6})$$

α_s is the strong coupling constant and the n_f is the number of flavours. The number of colours, N_c, is 3. The requirement for the asymptotic freedom is $\beta(\alpha_s) < 0$. From there, n_f is required to be:

$$n_f < \frac{33}{2}.$$

In order to probe the shorter distances, the particles have to be collided with higher energies. At an energy scale of Λ, the strong coupling constant at lowest order is

$$\alpha_s = \frac{1}{\beta_0 \frac{Q}{\Lambda}}$$

where β_0 is constant. This logarithmic decrease of the strong coupling constant by Λ allows the use of perturbation theory. Only at higher energies and short distances, is perturbation theory capable of making approximate predictions on the physical observables.

[10] In quantum field theory, the beta function describes the dependence of the coupling strength on the energy scale.

2.3.3 Higgs mechanism

It has been proven that the $W^{\pm}$ and Z bosons, quarks and up-type fermions are massive. However, without the Higgs term (the last term in Equation 2.1) these particles are massless in the SM. Addition of simple mass terms to the SM Lagrangian breaks the gauge invariance. However, these particles can gain mass through the Higgs mechanism [20, 21] via spontaneous symmetry breaking. The last term in Equation 2.1 contains a complex scalar field Φ:

$$\Phi = \begin{pmatrix} \phi^{+} \\ \phi^{0} \end{pmatrix},$$

which is a weak isospin doublet. The Higgs potential $V(\Phi)$ in the Equation 2.1 can be written in the form:

$$V(\Phi) = -\mu^2 \Phi^{\dagger}\Phi + \lambda(\Phi^{\dagger}\Phi)^2.$$

It can be seen that this potential preserves the renormalisability of the $SU(2)_{T_3} \times U(1)_Y$ invariance. The self interaction between the scalar fields is described by the term λ. For the case $\mu > 0$, the scalar fields gain a non-zero Vacuum Expectation Value (VEV) therefore breaking the symmetry. The minimum energy states which satisfy $\Phi^{\dagger}\Phi = v^2/2$, where $v = \sqrt{\mu^2/\lambda}$, are infinitely degenerate.

One can choose a VEV for the scalar field of the form:

$$\langle \Phi \rangle = \frac{1}{\sqrt{2}} \begin{pmatrix} 0 \\ v \end{pmatrix}$$

This choice allows one to expand the Higgs term of the SM Lagrangian in a perturbative series of the scalar field Φ around the VEV given above. Via this expansion, the gauge bosons except for photon and gluon gain a mass term. The masses of the gauge bosons are:

$$m_{\Phi} = v \cdot \sqrt{s\lambda}$$
$$m_W = g \cdot \frac{v}{2}$$
$$m_Z = \sqrt{g^2 + g'^2} \cdot \frac{v}{2}.$$

The VEV, v, can be determined from the measurements of the $W^{\pm}$ and Z boson masses and the coupling strength ($v \approx$246 GeV[5]).

In 2012, a scalar boson with a mass of ≈126 GeV was discovered at the LHC by the ATLAS and the CMS experiments [22, 23]. At that time, the Higgs boson was the only missing piece of the SM and this newly discovered particle was suspected to be that missing piece. Later studies confirmed that this new boson is a spin-0 particle and has even parity. This is compatible with the Higgs boson predicted by the SM. In 2013 Peter Higgs (whose name is given to the Higgs boson) and François Englert were awarded the Nobel Prize in Physics *"for the theoretical discovery of a mechanism that contributes to our understanding of the origin of mass of subatomic particles, and which recently was confirmed through the discovery of the predicted fundamental particle, by the ATLAS and CMS experiments at CERN's Large Hadron Collider."* [24].

2.3.4 The top quark

The top quark is the heaviest known particle with a mass of ≈173 GeV [5]. It is also the last discovered quark. Together with the b quark, its existence was predicted in 1973 by Makoto Kobayashi and Toshihide

Maskawa in order to explain the charge parity (CP) violations in kaon decay [25]. However, it took 22 years until it is finally discovered at Fermilab in 1995 by the DØ and the CDF collaborations [26] [27]. The top quark is one of the main ingredients of the analysis presented in this thesis.

General properties

Being the heaviest particle in the SM, the top quark has an extremely small lifetime, of the order 5×10^{-25}s. This is much shorter than a typical hadronisation process time, therefore it is impossible for the top quark to form hadrons. In that sense the top quark is unique because it is the only quark that does not form bound states. Therefore its decay products, which can be observed directly in particle detectors are coming from the top quark itself without an intermediate hadron. This in return leads to very precise measurement of its properties such as its mass. Another important aspect of the top quark is that it is the only fermion which has a mass comparable to the Higgs VEV, which makes it a very good candidate to test the SM.

Production mechanism

There are two main mechanisms to produce top quarks in the SM. The most common way the top quarks are produced are in pairs of top and anti-top quarks ($t\bar{t}$) through the strong interaction. In Tevatron, where protons were collided with anti-protons, the $t\bar{t}$ production occurred mostly ($\sim$ 85%) via quark and anti-quark annihilation. However, at the LHC where protons are collided with protons, this channel is suppressed and $t\bar{t}$ production occurs mostly through gluon fusion ($\sim$ 90%). At the LHC, with a centre-of-mass energy of 8 TeV, the predicted cross-section of $t\bar{t}$ production, calculated at the next-to-next-to-leading order (NNLO), is $\sigma = 253^{+13}_{-15}$ pb assuming a top-quark mass of 172.5 GeV [28–30]. The leading order (LO) Feynman diagrams[11] for $t\bar{t}$ production through quark-antiquark annihilation and through gluon fusion are shown in Figure 2.2.

The second mechanism to produce top quarks in the SM is the production of the single top quarks via the weak interaction. There are three processes, called channels, that can produce single top quarks, namely the t-channel production, s-channel production and the Wt channel production. The naming of s- and t-channels comes from the Mandelstam variables [32]. Figure 2.3 shows the LO Feynman diagrams for the single top processes.

The single top-quark production cross-section is much smaller than the $t\bar{t}$ production cross-section and therefore it is more difficult to measure. Among the three single top-quark production channels, the t-channel has the highest cross-section. In the t-channel, a b quark interacts with another quark via a virtual W boson producing a top quark together with another quark. The predicted NNLO cross-section for this channel at the LHC with a centre-of-mass energy of $\sqrt{s} = 8$ TeV is $87.8^{+3.4}_{-1.9}$ pb assuming a top quark mass of 172.5 GeV [33].

The s-channel has the smallest cross-section among the single top processes. In this channel two quarks interact and produce an off-shell W boson which then decays into a b and a top quark. The predicted cross-section for this channel (under the same conditions as t-channel and calculated in a similar method) is 5.6±0.2 pb [34].

[11] Feynman diagrams [31] are the visual representations of the interaction of the particles with each other. However, they are not only simple visualizations to describe the interactions but are used in perturbation theory to calculate the matrix element M of the corresponding interaction. The points where the lines cross are the vertices where the interaction occurs. The direction of the time flow is conventionally chosen from left to right. The lines represent the particles that are involved in the interaction and the arrow on the lines decides whether it is a particle or an antiparticle (if the arrow is against the flow of time it is an antiparticle). Every object in the diagram corresponds to a mathematical structure. By looking at the diagram, one can apply a set of Feynman rules to easily calculate the matrix element of the interaction.

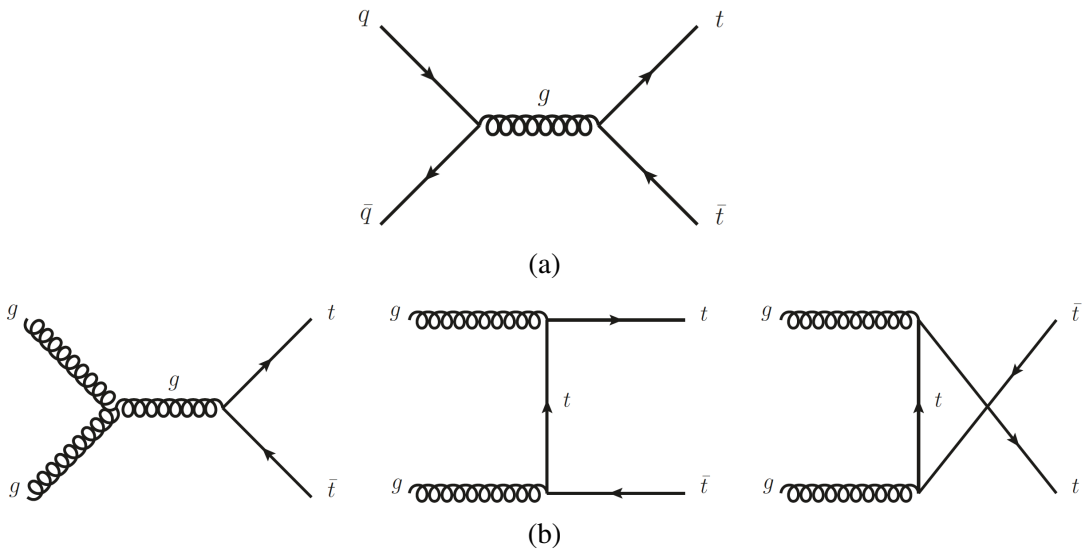

Figure 2.2: $t\bar{t}$ production through quark-antiquark annihilation (a) and through gluon fusion (b).

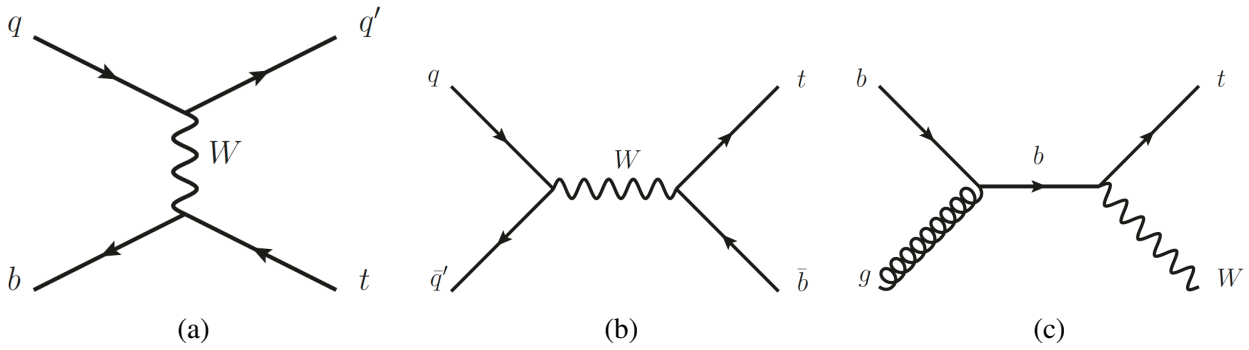

Figure 2.3: LO Feynman diagrams for the single top processes: t-channel (a), s-channel (b) and Wt channel (c) production.

The Wt-channel has the second highest cross-section after the t-channel however it is the most difficult to measure due to other SM processes having similar final state topologies. Typically, a b quark interacts with a gluon and decays into a top quark and an on-shell W boson. The predicted cross-section (under the same conditions as the other two) is 22.4±1.5 pb [35].

Single top-quark production was first discovered in 2009 by the CDF and DØ collaborations separately in a combined search for the t-and s-channels [36, 37]. In 2011, the first observation of the t-channel alone was made by the DØ collaboration [38]. In 2014, the first observation of the s-channel single top-quark production was published by the DØ and CDF collaborations at Tevatron [39] and in 2015 ATLAS published the first evidence observed at the LHC [40]. The first discovery of the Wt channel was made by the CMS collaboration in 2013 [41].

All three single top-quark channels contain a Wtb vertex which is directly related to the V_{tb} element of the V_{CKM}. Therefore these channels can be very useful for determining the value of V_{tb}.

Decay modes

Due to the value of V_{tb} being very close to one ($V_{tb} = 0.999$), top quarks decay almost exclusively to a W boson and a b quark. When it decays, the top quark is the only quark that can produce an on-shell W boson due to its huge mass.

The resulting W boson itself further decays into either a quark–antiquark pair where then the quarks hadronise and form jets inside the particle detectors, or it decays into a lepton and a neutrino. Since the top quark decays almost always into a W boson and a b quark, the decay mode of the W is the determining factor of the final states of the top-quark decay. Depending on the type of decay products of the W boson, the final states of the top quark are usually called the hadronic channel or leptonic channel. The physics analyses that use data from particle collision experiments generally prefer a certain decay mode of the W boson to depending on the background processes that minic the final state topology of the top quark decay channel that is considered.

The second decay product of the top quark, the b quark quickly hadronises into a B meson (as well as into other mesons) which then generally decays into a D meson. The D meson itself decays into *kaons* or *pions* which form jets inside the particle detectors.

Figure 2.4 shows the LO Feynman diagrams of all possible decay modes of the top quark and the two decay modes of the W boson.

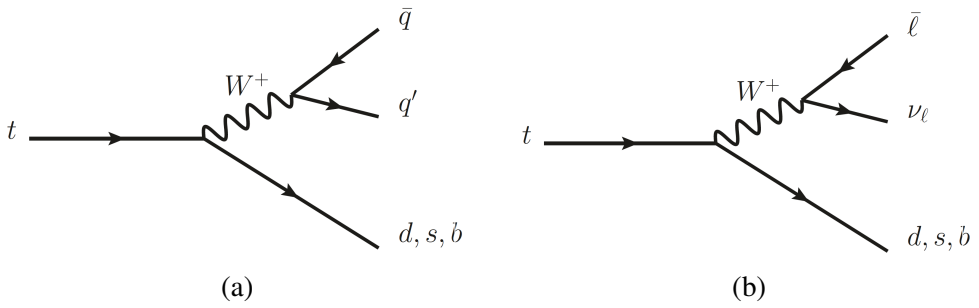

Figure 2.4: LO Feynman diagrams for the hadronic (a) and the leptonic (b) decay modes of the top quark.

2.3.5 Flavour changing neutral currents involving top quarks in the SM

In the SM, only the charged bosons can change the flavour of the quarks through FCCC at tree level[12]. The neutral bosons Z, γ, g and Higgs are sometimes called neutral currents. They cannot change the flavour of fermions at tree level since there is no allowed vertex in the SM that couples a neutral current with two fermions of different flavours. However, the FCNC do exist in the SM in higher order corrections of perturbation theory (loop level).

Figure 2.5 shows an example of an FCNC process allowed in the SM. The top quark changes its flavour into a u or c quark while emitting a Z boson. This is only possible through loop diagrams where a W boson is exchanged. To be able to calculate the branching fraction of the top quark decay through FCNC in the SM, one has to take into account all other possible loop level diagrams involving other quarks (d and s).

In 1973, Sheldon Lee Glashow, John Iliopoulos and Luciano Maiani proved that the addition of the diagrams with all internal quarks (b, s, d), the total amplitude is significantly reduced due to destructive interference. This is due to the fact that the internal quarks have much smaller masses compared to the top

[12] In particle physics, the term tree level stands for the lowest order of perturbation theory.

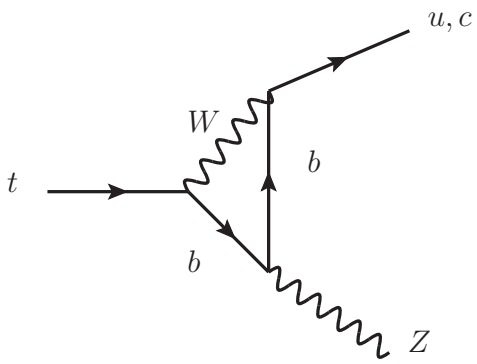

Figure 2.5: A decay of the top quark through FCNC in the SM.

quark mass which is at the order of the Higgs VEV. This suppression mechanism of the FCNC processes in the SM is called Glashow–Iliopoulos–Maiani (GIM) mechanism [42]. The predicted branching fraction of the FCNC processes involving top quarks in the SM is of the order of 10^{-13} [43], which is beyond the reach of today's particle accelerators. However, the FCNCs are still searched for in particle physics experiments since many extensions of the SM predict much higher branching fractions for FCNC processes, which if they exist, can be produced by the current colliders (e.g LHC) and detected by the particle detectors. The FCNC in BSM theories will be discussed in the following chapter.

2.4 Drawbacks of the SM

The SM is a very successful theory capable of explaining many physics phenomena. Over the last few decades, several predictions made by the SM has been confirmed experimentally such as the neutral currents, top quark and the Higgs boson. However there are a number of unexplained theoretical and experimental phenomena which are not covered by the SM. Below is a list of some of the drawbacks of the SM.

- **Gravity** Although the strong and the electroweak interactions are well explained in the SM, gravity is not incorporated into the SM in terms of quantum field theory. Attempts to create a reliable quantum field theory of gravity fail because gravity breaks down before the Planck scale therefore gravity is not understood in the early universe. A propagator particle of gravity (graviton) has not been observed.

- **Contradictions to the SM of cosmology** The SM cannot accommodate the amount of cold dark matter described by cosmology. There is no candidate particle in the SM that could make up the observed cold dark matter. Similarly, the SM cannot explain dark energy. The theories that explain the dark energy by means of vacuum energy disagree with the measured energy density of the universe by at least 60 orders of magnitude. This is sometimes know as the cosmological constant problem.

  The amount of antimatter is extremely small compared to the amount of matter in the universe. The universe is almost entirely made up of matter. This is known as the matter/antimatter asymmetry in the universe. The SM does not predict this observation, neither provides a mechanism that could generate it.

- **Neutrino masses** The neutrinos are postulated to be massless by the classical SM. However, the neutrino oscillation experiments show a small but non-zero mass for the neutrinos. In order to provide masses for the neutrinos, a mass term has to be added to the SM Lagrangian.
- **Hierarchy problem** The masses of the particles in the SM are provided through the spontaneous symmetry breaking due to Higgs mechanism. The Higgs mass receives very large quadratic corrections in higher orders of perturbation theory, which are much larger than the actual mass of the Higgs. This requires an extreme fine tuning for the Higgs mass and the cancellation of the contributions from quadratic corrections. This is known as the hierarchy problem.
- **Number of free parameters** The SM has 19 free parameters which cannot be determined theoretically but only obtained from the measurements. If one also considers the neutrino masses, this number increases to 22. The values of these parameters seem to be unrelated. Incorporation of the measured values of the parameters into the theory can be considered *ad hoc*.

Many extensions to the SM have been developed in order to address these problems as well as others. These extensions to the SM will be covered in the following chapter.

CHAPTER 3

Flavour Changing Neutral Currents in Beyond Standard Model Theories

Due to the several shortcomings of the SM mentioned in Chapter 2, many BSM theories have been developed since the time the SM was first established. These BSM theories aim to either extend or modify the classical SM or they are sometimes stand-alone theories that have been developed independently of the SM. The main purpose of these theories is to establish a more general understanding of particle physics especially in the conditions that the SM fails, such as at very high energies. Some theories attempt to address individual shortcomings of the SM and some have broader aims. This chapter aims to provide basic knowledge on some of the best known BSM theories and tries to motivate why the FCNC have an important role in the search for experimental evidence for these BSM theories.

3.1 Introduction to BSM theories

BSM theories can be categorised depending on the drawbacks of the SM that they try to address. They can also be grouped into models that are mathematically closely related to each other. Sometimes they are very specific mechanisms aiming at solving individual problem of the SM and they are independent from other BSM models. The list of these BSM models with short descriptions is given below.

- Grand unified theories (GUTs) are a famous branch of BSM theories. They are models where the three gauge interactions of the SM merge into a single force at higher energies by merging the coupling constants of the strong and electroweak interactions. Therefore GUTs are described by one single coupling constant and several force carriers described by a larger gauge symmetry. These theories assume that at early stages of the universe, the fundamental forces of nature were not distinct.

- There are also theories that attempt to combine all forces of nature including gravity. In theoretical physics, such a theory is called a theory of everything (ToE). A ToE reconciles general relativity with quantum field theory. One very popular candidate of ToE is string theory. In string theory, the fundamental particles are replaced by one dimensional constructs called strings with lengths of the order of the Planck length. The oscillations of closed strings give rise to a massless spin-2 boson compatible with the graviton of the general relativity. Another candidate ToE is loop quantum gravity (LQG). LQG is a theory which quantises the space-time fabric at the Planck scale. Since gravity is a direct result of the change in the geometry of the space-time, LQG can be perceived as an attempt to describe a ToE.

- One extension of the SM is Supersymmetry (SUSY). In this model, the SM Lagrangian is extended by adding more symmetries. These symmetries introduce a set of new fundamental particles called *sparticles*. Every fermion and boson in the SM is associated to a supersymmetric partner (superpartner) whose spin differs by 1/2 from the SM particle. Hence the superpartner of a fermion is bosonic (with integer spin) and the superpartner of a boson is fermionic. The superpartners are named *sleptons*, *squarks*, *charginos* (superpartners of charged bosons) and *neutralinos* (superpartners of neutral bosons). Since none of the superpartners has been observed, in SUSY it is assumed that the superpartners are significantly heavier than their SM counterparts due to a symmetry breaking at higher energies. However, they can still be within the reach of current particle colliders. SUSY can address the hierarchy and the fine tuning problem of the SM. It is also a GUT since it allows the unification of the gauge interaction at around 10^{16} GeV (GUT scale). SUSY can also address the dark matter problem since some of the sparticles can be good candidates for dark matter. For instance, neutralinos are assumed to be weakly interacting massive particles (WIMPs). WIMPs are considered to be candidate particles for cold dark matter.

- Two Higgs doublet models (2HDMs) are extensions of the SM where a second Higgs doublet is included. There are a few models predicting this, such as axion models, which postulate a hypothetical spin-0 and low mass boson. Axion models can solve the strong charge parity (CP) problem of QCD, the baryon asymmetry of the universe and the dark matter problem. Another 2HDM is the minimal supersymmetric standard model (MSSM) which is the simplest version of SUSY. As in the case of general SUSY models, MSSM can also address dark matter and the hierarchy problems, as well as gauge coupling unification.

- Technicolour theories were developed to describe how the gauge bosons gain mass by introducing additional gauge interactions. These theories do not require a Higgs boson and therefore avoid the hierarchy problem. However, after the discovery of the Higgs boson in 2012, many technicolour theories are excluded, although a Higgs-like boson can still be incorporated into some of the technicolour theories.

- Theories involving exotic quark singlets can also solve the hierarchy problem by introducing a top quark singlet which leads to cancellation of the loop corrections. They are known to predict very high branching fractions for FCNC processes by breaking the unitarity of the CKM matrix and therefore relieve the suppression due to GIM mechanism up to a certain extent.

- The chiral colour model extends the QCD section of the SM, assuming a new gauge group that is $SU(3)_L \times SU(3)_R$ which introduces an additional set of massive colour octet spin-1 bosons called axigluons. These models can address the forward-backward asymmetry of the $t\bar{t}$ processes observed at Tevatron and LHC [44].

- The SM neither predicts nor restricts the observed number of fermion generations. The theories called preon models are developed to address the fermion generation as well as other phenomena which are not explained by the SM.

- There are also theories that involve additional quark generations as the number is not restricted by the SM. These theories also predict significantly higher branching fractions for FCNC interactions than that of the SM.

- The see-saw mechanisms are extensions of the SM which exclusively aim at explaining the unusually small masses of the neutrinos relative to leptons and quarks. In addition to the left-handed neutrinos, these mechanisms introduce right-handed neutrinos which are super-massive ($\simeq 10^{15}$ GeV). The see-saw mechanism introduces a mass matrix for the neutrinos where the greater the mass of the right handed neutrino, the smaller the mass of the left-handed neutrino; this is the reason for the name see-saw mechanism.

The details of the BSM models that predict high branching fractions for FCNC processes are discussed in the following sections.

3.2 FCNC in BSM theories

Although FCNC are highly suppressed in the SM, many extensions of the SM predict significantly higher cross-sections and branching fractions for FCNC processes involving top quarks. Hence, searches for FCNC processes in high energy colliders are one of the best techniques to test BSM phenomena. Any sign of an FCNC process with higher branching fractions than the one that is predicted by the SM can directly indicate new physics.

There are several FCNC vertices involving top quarks with the SM neutral currents, namely either a Z boson, a photon, a Higgs boson or a gluon. The direct[1] FCNC vertices involving top quarks are shown in Figure 3.1. These vertices can be studied both during top-quark production and decay. The experiments at the Large Electron–Positron Collider (LEP), Hadron-Electron Ring Accelerator (HERA), Tevatron and LHC have searched for FCNC both during top production and decay and have set upper limits on the branching fraction and the coupling constants of the considered vertices.

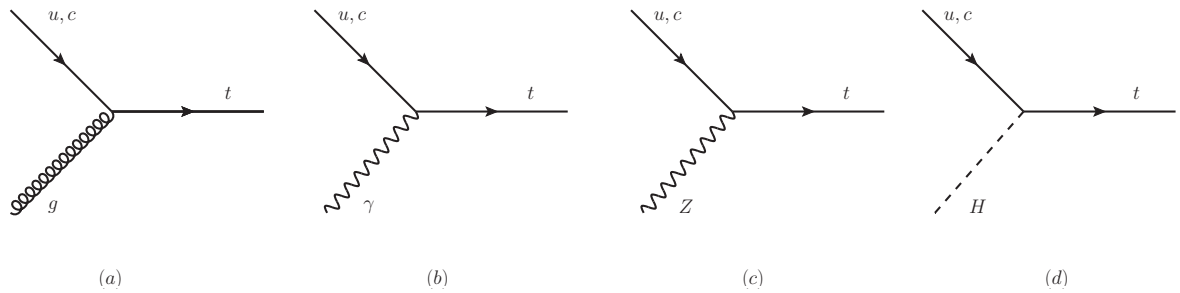

Figure 3.1: FCNC vertices involving top quarks through a gluon (a), a photon (b), a Z boson (c) and a Higgs boson (d).

One important FCNC search channel is the so called qgt process where q is either a u or a c quark (see Figure 3.1(a)). This interaction indicates a vertex where an up-type quark interacts with a gluon producing

[1] In this context, "direct" indicates leading order or tree level.

a top quark. This process can also be called strong FCNC top coupling because of the involvement of the gluon. This kind of vertex is strictly forbidden in the SM. However, such vertices are predicted by a number of BSM theories. The predicted cross-sections by some of the BSM theories lie within the reach of LHC. In certain parameter spaces of some of the BSM models, the predicted branching fractions for the *qgt* processes during top production are as high as 10^{-5} to 10^{-3}. These are significantly higher than some of the other FCNC processes involving top quarks. The list of predictions for the branching fractions by the BSM models is given in Section 3.3.

The ATLAS experiment published results which are already probing these high branching fractions. However, generally the BSM models predict a very large range of branching fractions for a given FCNC process, typically going down to 10^{-8} to 10^{-10}. Due to this fact, although the experimental results became sensitive to these predictions, no entire branching fraction region for a given BSM theory has been excluded experimentally. A list of upper limits set by several collaborations on the branching fractions of the FCNC processes involving top quarks is presented in Section 3.4.

The analysis presented here focuses on the strong FCNC top coupling during the top-quark production. Although it is technically possible to search for the same coupling during top decay, that process is extremely challenging due to the overwhelming background of multi-jet production from QCD processes, which is almost indistinguishable from the final topology of a top-quark decay through strong FCNC. In this analysis, the top quark produced through strong FCNC via *qgt* channel is assumed to decay via a SM process. This implies a *b* quark and a *W* boson in the final state, where the *W* boson can decay either leptonically or hadronically (see Section 2.3.4). Here the leptonic decay of the *W* is considered.

The main search channel in this analysis, where a top quark is produced through strong FCNC which then decays leptonically through SM is shown in Figure 3.2. Not only the specific process that is presented in the figure but also the charge conjugate of the production and the decay as well as next-to-leading-order production processes (see Figure 3.4) are considered in this thesis.

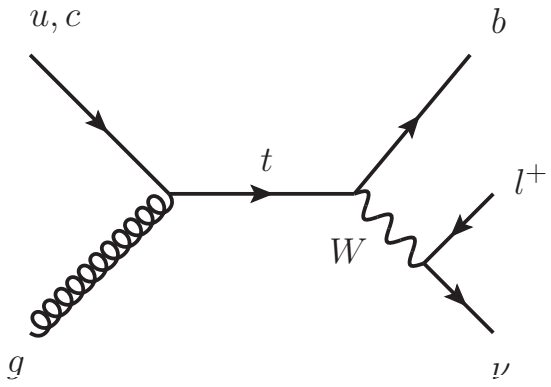

Figure 3.2: Direct top-quark production through FCNC. Top-quark decays leptonically through SM.

3.2.1 Model independent anomalous FCNC couplings

The search for top-quark production through strong FCNC, which is described in this thesis, can be achieved in a model-independent manner, meaning that no specific BSM model is considered. This can be accomplished by the use of an effective operator formalism [45]. It assumes that a more general theory which is valid at higher energies exists and the SM is the low energy limit of it.

The energies at which this general theory is valid can be inaccessible to the current particle colliders. For instance, the particles that this theory predicts can be significantly heavier. However, the formalism

assumes a lower energy scale Λ in which the indirect effects of this theory, such as the effects on the couplings of the particles can be discerned.

The formalism is constructed based on an effective Lagrangian which starts with the SM Lagrangian, $\mathcal{L}_{\text{SM}}$, where then operators with dimension five $\mathcal{L}^5$ and dimention six $\mathcal{L}^6$ in energy[2] are added. The additional operators are invariant under the gauge symmetry group of the SM and they are built by the fields of the SM:

$$\mathcal{L}_{\text{eff}} = \mathcal{L}_{\text{SM}} + \frac{1}{\Lambda}\mathcal{L}^{(5)} + \frac{1}{\Lambda^2}\mathcal{L}^{(6)} + O(\frac{1}{\Lambda^3}). \tag{3.1}$$

The operators $\mathcal{L}^5$ and $\mathcal{L}^6$ are suppressed by powers of Λ which also makes sure that each term in the $\mathcal{L}_{\text{eff}}$ has a dimension of four. The operator $\mathcal{L}^5$ is considered unphysical and dropped since it breaks lepton and baryon number conservation.

The content of $\mathcal{L}^6$ is further simplified by excluding the terms that have no impact on the physics within the reach of the current colliders, as their impacts have been strictly constrained by the experiments at Tevatron and LEP. The terms in $\mathcal{L}^6$ which are kept are the ones that contribute to strong FCNC interactions as they are the ones of interest here and the operators with electroweak gauge bosons are excluded. These simplifications are based on the argumentation given in Reference [46]. In the end, the remaining term describing the qgt processes via strong FCNC can be written as following:

$$O^{ij}_{uG\Phi} = \bar{q}^i_{\text{L}}\,\lambda^a\,\sigma^{\mu\nu}\,u^j_{\text{R}}\,\tilde{\Phi}\,G^{a\mu\nu}\,,$$

where $\bar{q}^i_L$ stands for the left-handed quark doublet, λ^a are the Gell-Mann matrices, $\sigma^{\mu\nu}$ is the anti-symmetric tensor, u^j_R is a right-handed quark singlet, $\tilde{\Phi}$ is the charge conjugate of the Higgs doublet and $G^{a\mu\nu}$ is the gluon field strength tensor. The spinor indices i, j are the flavour indices running over the quark generations. One index is set to 3 due to the requirement of a single top quark and the other index is either 1 or 2. This is because of the fact that the process of interest, qgt, can have either a u or c quark as explained in Section 3.2.

The operators include not only the $qg \to t$ process (direct single top-quark production) but also the $gg \to qt$ and $qg \to tg$ processes. In addition, they also include single top-quark production with gluonic quark-(anti)quark scattering. All these processes are taken into account in this analysis.

These processes are grouped into two, namely the $2 \to 2$ process where a gluon, u or c quark interact via u-,s- or t-channel diagrams, producing a single top quark with associated light quarks or gluons, or the $2 \to 1$ process, without the associated additional light quarks or gluons.

Replacing Φ by its vacuum expectation value $v/\sqrt{2}$, the strong FCNC Lagrangian is written as [47]:

$$\mathcal{L}_{\text{S}} = -g_{\text{s}} \sum_{q=u,c} \frac{\kappa_{qgt}}{\Lambda}\,\bar{q}\,\lambda^a\,\sigma^{\mu\nu}\,(f_q + h_q\gamma_5)\,t\,G^a_{\mu\nu} + \text{h.c.}\,,$$

where g_{s} is the strong coupling strength, κ_{qgt} $(q = u, c)$ are real and positive parameters which relate the strength of new couplings to the strong coupling strength. The parameters f_q and h_q are real, vector and axial chiral parameters, respectively and they satisfy the relation $|f_q|^2 + |h_q|^2 = 1$. The Lagrangian includes both the decay and the production of the single top quarks through FCNC.

The branching fractions of the anomalous FCNC couplings to the top quark have to be calculated, as the new FCNC interaction introduces additional decay modes to the top quark, thus changing its decay width. The calculation of the branching fraction is done by simply dividing the decay width of the new FCNC interaction by the total decay width of the top quark (assuming that the FCNC exist):

[2] In this thesis natural units $c = \hbar = 1$ are assumed.

$$\mathcal{B}(t \to qg) = \frac{\Gamma_{t\to qg}}{\Gamma_{t\to bW} + \Gamma_{t\to qg}}. \tag{3.2}$$

The values for the LO and NLO SM top-quark decay width $\Gamma_{t\to bW}$ is calculated in Reference [48] and the LO and NLO FCNC top-quark decay widths $\Gamma_{t\to qg}$ are derived in Reference [49]. The full form of $\Gamma_{t\to qg}$ at LO is given as:

$$\Gamma^{\mathrm{LO}}_{t\to qg} = \frac{8\alpha_s m_t^3}{3}\left(\frac{\kappa_{qgt}}{\Lambda}\right)^2 \tag{3.3}$$

and at NLO:

$$\Gamma^{\mathrm{NLO}}_{t\to qg} = \Gamma^{\mathrm{LO}}_{t\to qg}\left\{1 + \frac{\alpha_s}{72\pi}\left[174\ln\left(\frac{\mu^2}{m_t^2}\right) - 12N_f\ln\left(\frac{\mu^2}{m_t^2}\right) - 36N_f - 38\pi^2 + 179\right]\right\}. \tag{3.4}$$

where μ is the renormalisation scale, N_f is the number of quark flavours that are involved and m_t is the top-quark mass.

Using a top-quark mass of 172.5 GeV, setting the renormalisation scale to the top-quark mass, choosing $N_f = 5$ and using the SM top decay width provided in the Reference [48], one can combine the Eqs. 3.2, 3.3 and 3.4 in order to calculate the decay rates and branching fractions of the qgt channel FCNC as a function of the coupling constant:

$$\begin{aligned}\Gamma_{t\to qg} &= 1.613 \times \left(\frac{\kappa_{qgt}}{\Lambda}\right)^2, \\ \mathcal{B}(t \to qg) &= 1.2205 \times \left(\frac{\kappa_{qgt}}{\Lambda}\right)^2\end{aligned} \tag{3.5}$$

It can be seen in Figure 3.3 that for small values of the coupling constant κ_{qgt}, e.g. $\kappa_{qgt} < 0.1$ TeV^{-1}, the contribution of the FCNC decay width, $\Gamma_{t\to qg}$, in the denominator of Eq. 3.2 is small. Therefore Eq. 3.2 can be simplified to:

$$\mathcal{B}(t \to qg) = \frac{\Gamma_{t\to qg}}{\Gamma_{t\to bW}}. \tag{3.6}$$

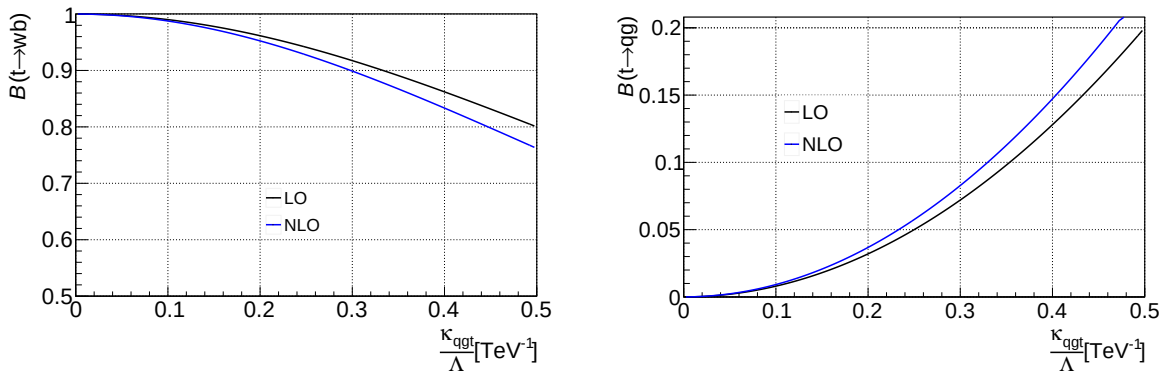

(a) (b)

Figure 3.3: The branching ratios of the SM top decay (a) and the top decay through anomalous FCNC coupling (b).

This simplification is backed by the current experimental result (see Section 3.4).

In order to calculate the cross-section as a function of the coupling constant at NLO, Feynman diagram contributions from real gluon bremsstrahlung and one loop virtual gluon corrections have to be taken into account. A set of NLO contributions in addition to the direct LO top-quark production (Figure 3.2) is presented in Figure 3.4. The details of the exact cross-section derivation as a function of the coupling

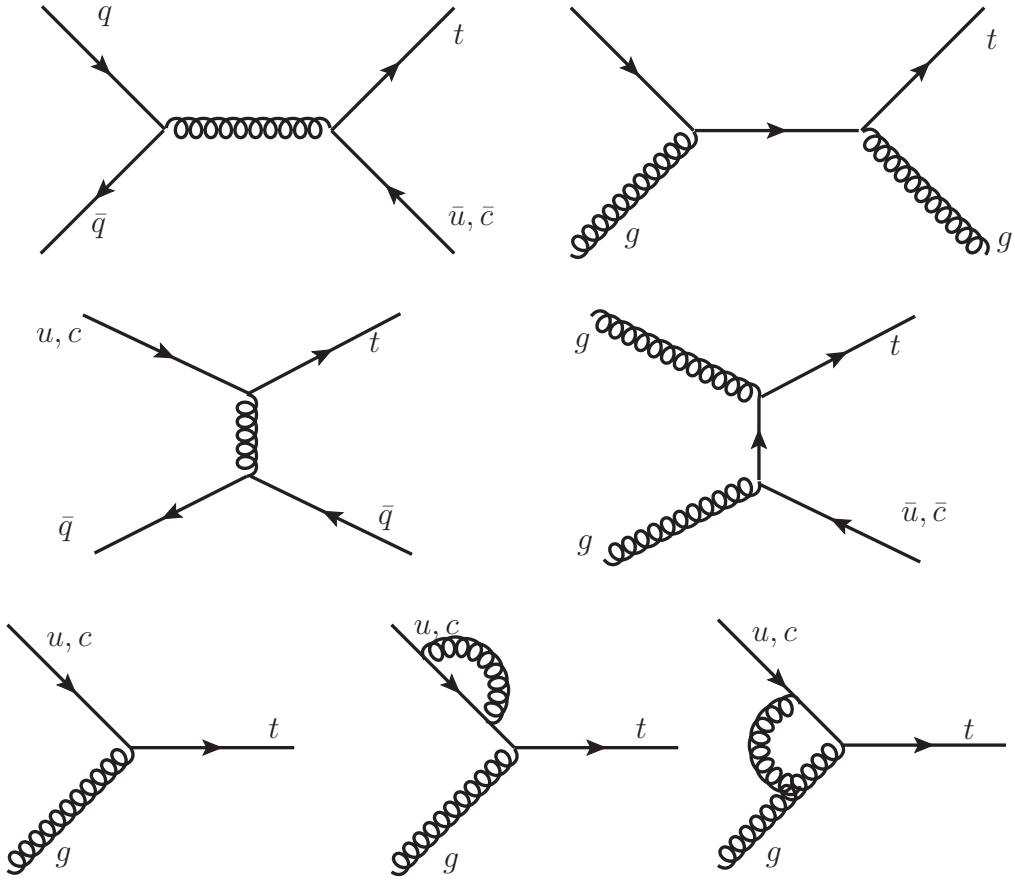

Figure 3.4: Feynman diagrams of anomalous single top-quark production via strong FCNCs at NLO.

constant are given in Reference [50]. The calculation provided in the reference was based on the $\sqrt{s}$ = 7 TeV centre-of-mass energy collisions which used the CTEQ6.6 parton distribution functions (See Section 5.2.1). The top-quark mass was assumed to be m_t =173.1 GeV and the renormalisation scale was set to this value. Omitting the scale uncertainties, e.g. from varying the renormalisation and factorisation scales, the cross-section for single top-quark production can be written as:

$$\sigma_{qg\to t} = \sum_{q=u,c} \left(\frac{\kappa_{gqt}}{\Lambda}\right)^2 (b_{qL}|f_q^L|^2 + b_{qR}|f_q^R|^2)\,, \tag{3.7}$$

where b_{qL}, b_{qR} are simple constants. In order to calculate b_{qL} and b_{qR} for 8 TeV, the values given in [50] are rescaled with the ratio $k_q = \sigma_{qg\to t}(8\,\text{TeV})/\sigma_{qg\to t}(7\,\text{TeV})$ given by METOP [47], resulting in k_u = 1.22 and k_c = 1.32. Assuming only a pure left-handed coupling, $f_q^L = 1$ and $f_q^R = 0$, and adding the negative

and positive interference lepton channels together, Eq. 3.7 can be written as:

$$\sigma^{LO}_{qg\to t} = 75813.12\left(\frac{\kappa_{ugt}}{\Lambda}\right)^2 + 12897.24\left(\frac{\kappa_{cgt}}{\Lambda}\right)^2 \text{pb}\,, \tag{3.8}$$

$$\sigma^{NLO}_{qg\to t} = 100351.97\left(\frac{\kappa_{ugt}}{\Lambda}\right)^2 + 19496.79\left(\frac{\kappa_{cgt}}{\Lambda}\right)^2 \text{pb}\,. \tag{3.9}$$

The equations above allow one to study the anomalous single top-quark production via strong FCNC cross-section for each individual quark channel, namely *ugt* and *cgt*. The LO and NLO results for the cross-section as a function of κ_{ugt} and κ_{cgt} are graphically presented in Figure 3.5. The cross-section for the *ugt* channel is significantly higher than for the *cgt* in proton–proton collisions as the *u* quark is a valence quark.

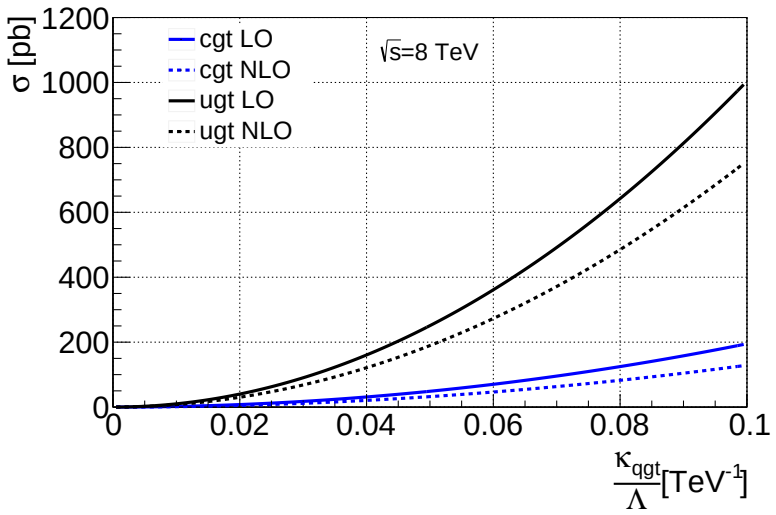

Figure 3.5: Anomalous single top-quark production via FCNC cross-section as a function of the coupling constants κ_{ugt} and κ_{cgt}. The dotted lines represent the NLO calculation.

3.3 Predictions by BSM theories

In this section, a list of predictions on the branching fractions of FCNC couplings by a selection BSM theories is presented. The details of a these models will be explained and the methods they use for their cross-section and branching fraction predictions will be discussed.

3.3.1 2HDM

In this model, the addition of a second Higgs doublet introduces a light neutral Higgs boson *H* (assumed to be the Higgs boson found at LHC), a heavier Higgs boson H_{heavy}, two charged Higgs boson ($H^{\pm}$) and one pseudoscalar particle *A*. One of the most remarkable aspects of the 2HDM models is that they introduce FCNC interactions at tree level. In general, there are 3 classifications for 2HDM, namely type I, type II and type III. In the type I 2HDM, fermions couple only to the second (newly introduced) Higgs doublet. Due to that, this model is sometimes called as fermiophobic. In the type II 2HDM, up- and down-type quarks couple to different pairs of Higgs doublets. This type is called MSSM-like since in

both cases the additional Higgs doublet has opposite isospin assignment. The type III 2HDM is the most interesting model here as in this case FCNC occurs at tree level.

In type III 2HDM, one can define a Yukawa coupling ξ_{ij} between the quarks and one of the neutral Higgs bosons, where i, j are the flavour indices [51]:

$$\xi_{ij} = \lambda_{ij}\frac{\sqrt{2m_i m_j}}{v}, \tag{3.10}$$

where $m_{i,j}$ are the quark masses, v is the SM vacuum expectation value and λ_{ij} is of the order of 1. Under this assumption, the FCNC couplings of the down-type quarks are significantly suppressed due to the small masses of u, d, and s quarks. This agrees with the experimental results. However, due to the large mass of the top quark, this Yukawa coupling can give rise to high branching fractions of the top quark FCNC processes.

In this model, the *ugt* sub-process is also significantly suppressed due to Cheng-Sher ansatz [52] therefore the main focus is on the *cgt* sub-process. The branching fraction of the *cgt* process during top-quark production is predicted as a function of the mass of the charged Higgs bosons as shown in Figure 3.6. For certain parameter spaces, the predicted branching fractions is higher than 10^{-6}, although

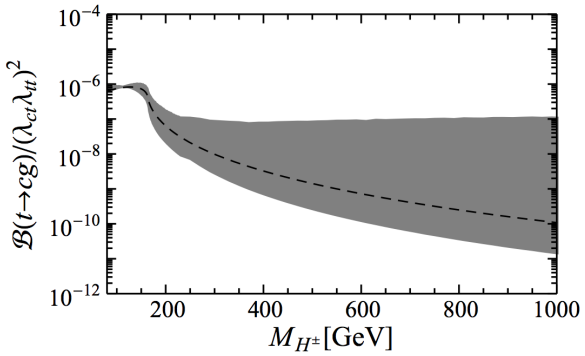

Figure 3.6: Branching fraction of the top quark production through FCNC in *cgt* process. The dashed line is the prediction for $M_{H_{heavy}} = M_H^{\pm} = M_A$. The shaded area is obtained by varying the masses of H_{heavy} and A [51].

this is still beyond the reach of LHC (See Section 3.4 for the latest experimental results). However, the extrapolation studies performed in the analysis presented in this thesis (see Chapter 12) show that a future high luminosity LHC run can become sensitive to these predictions.

3.3.2 Light Axigluons

One specific version of the colour octet theories is the light axigluon model which predicts a relatively lighter massive axigluon A with a mass of around 100–400 GeV [53]. This model was developed mostly to explain the forward-backward asymmetries of $t\bar{t}$ processes observed in collision experiments. However, it also gives rise to very high branching fractions for several FCNC processes [54] discussed in this thesis.

The axigluons can couple to top quarks and other quarks at tree level which can significantly enhance the cross-section of the single top-quark production at the LHC. An example set of Feynman diagram contributions from the light axigluon model to the SM single top-quark production is given in Figure 3.7.

The branching fraction prediction is performed for the *cgt* sub-process as a function of the mass of the light axigluon. Three variations of the axigluon coupling constant are tested. The calculation is performed for the centre-of-mass energy of $\sqrt{s} = 14$ TeV at LHC. The result is shown in Figure 3.8.

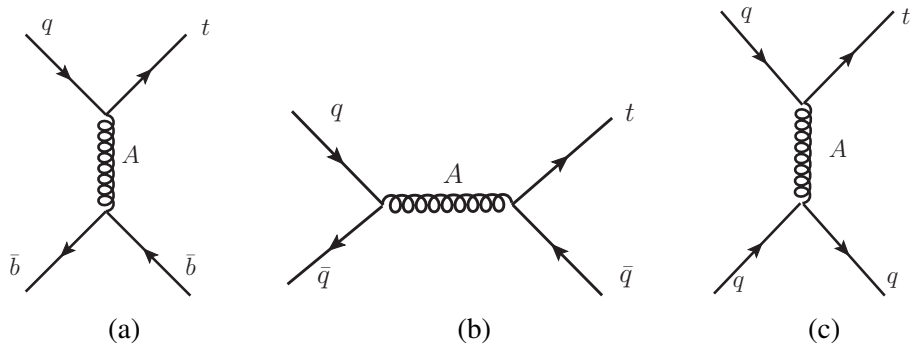

Figure 3.7: Three exemplary contributions of axigluon model to the SM single top-quark production.

The highest predicted branching fraction exceeds 10^{-6}. However, an axigluon-like particle has not been

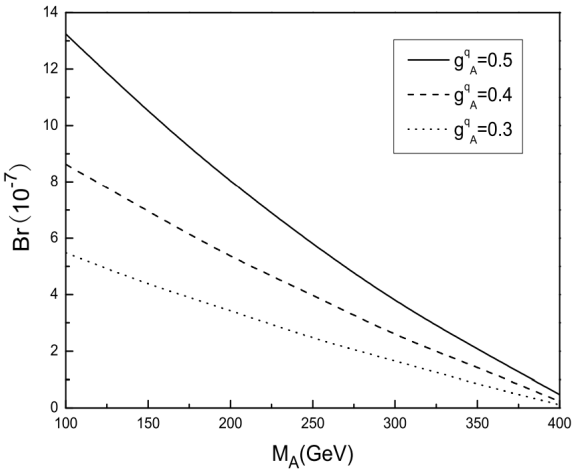

Figure 3.8: Branching fraction of the single top-quark production through FCNC in *cgt* channel as a function of axigluon mass for three variations of the axigluon coupling constant.

observed around 100 GeV and an experimental lower limit on the axigluon mass around 1 TeV has been set [55].

3.3.3 MSSM

The MSSM provides one of the highest predictions on cross-sections and branching fractions for FCNC processes. In the MSSM, FCNC interactions are allowed at tree level. Here, results of the study detailed in Reference [56] are presented.

The cross-section for FCNC interactions of the form $pp \to \kappa\lambda \to t\bar{u}(\bar{c})$ (where κ and λ run over quarks and gluons) can be written as:

$$\sigma(s) = \sum_{\kappa,\lambda} \int_{(m_{u(c)}+m_t)/\sqrt{s}}^{1} dz \frac{dL}{dz} \hat{\sigma}^{\kappa\lambda}(\kappa\lambda \to t\bar{u}(\bar{c})) \tag{3.11}$$

where $\hat{\sigma}^{\kappa\lambda}$ is the partonic cross-section for $\kappa\lambda \to t\bar{u}(\bar{c})$ and the $\frac{dL}{dz}$ is the parton luminosity whose exact forms are given in Reference [56]. $\sqrt{s}$ is the centre of mass energy of the proton-proton collisions which

is chosen to be 14 TeV in the presented study.

For a numerical evaluation, the SM parameters are chosen as follows: $m_t = 174.3$ GeV, $m_W = 80.423$ GeV, $m_Z = 91.1876$ GeV, $m_c = 1.2$ GeV, $\sin^2(\theta_W) = 0.23113$ and $\alpha_s(m_Z) = 0.1172$, and the SUSY parameters are chosen as follows: $M_{\text{SUSY}} = 400, 1000$ GeV, $\tan\beta = 3, 30$, $m_{\tilde{g}} = 200, 300$ GeV and $\mu = 200$ GeV. The cross-section results for $pp \to t\bar{u}$ as a function of the gluino mass are presented in Figure 3.9. The highest predicted cross-section is in the order of 800 pb which is at the same order as the

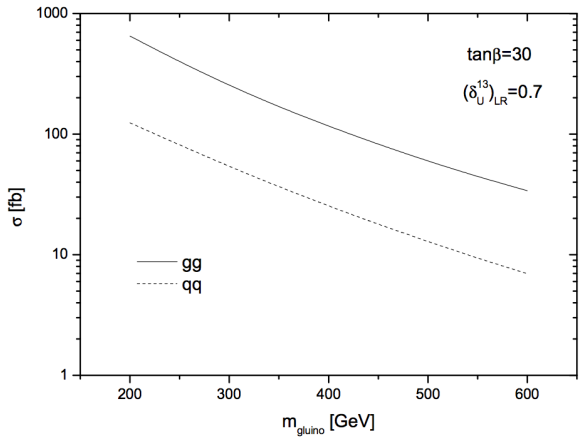

Figure 3.9: Cross-section of the $pp \to t\bar{u}$ process as a function of the gluino mass. The solid line represents the gluon–gluon (gg) initial state and the dashed line represents the quark–quark (qq) initial state.

upper limits set by the ATLAS collaboration. However, experimental results in SUSY searches suggest a significantly higher gluino mass [57].

In addition to the theoretical BSM studies on FCNC in top-quark production which were presented here, many other predictions of several other theories exist. Further theoretical studies that enhance the production rate and hence the branching fractions of the FCNC processes are given in the following: predictions made by 2HDM theories can be found in Reference [58–63], by the MSSM in Reference [64–70], by SUSY with R-parity violation in Reference [71, 72], by the topcolour-assisted technicolour model in Reference [73], by models with extra quarks in Reference [74–76] and by quark-singlet model in Reference [77–79]. Reviews can be found in References [80] and [81].

The list of highest branching fractions predicted by BSM theories for different types of FCNC processes is given in table 3.1.

3.4 Experimental results on FCNC couplings

Since no sign of FCNCs involving top quarks has been observed, experimental limits on the cross-sections and the branching fractions have been set. The experiments at LEP, HERA, Tevatron and LHC have been involved in the searches for direct FCNC processes. Currently, the lowest upper limits at 95 % confidence level (CL) for the coupling constants $\kappa_{\gamma qt}$ and κ_{qgt} are $\kappa_{\gamma qt}/m_t < 0.12\,\text{GeV}^{-1}$ [82] (ZEUS, HERA) and $\mathcal{B}(t \to qg) < 5.7 \times 10^{-5}$ (ugt) and $\mathcal{B}(t \to qg) < 2.7 \times 10^{-4}$ (cgt) [83] (ATLAS, LHC). In the case of $t \to qZ$, upper limits on the branching fractions of the top-quark decay have been determined to be $\mathcal{B}(t \to qZ) < 0.05$ % [84] (CMS, LHC). The discovery of the Higgs Boson opened up the possibility of FCNC searches involving Higgs and top quarks. For the qHt channel, the most stringent limit is set by the ATLAS collaboration with an upper limit of $\mathcal{B}(t \to qH) < 0.79$ % [85]. Table 3.2 summarises the upper

Process	SM	QS	2HDM II	2HDM III	MSSM	$\not{R}$ SUSY	Extra q	TC2
$t \to u\gamma$	3.7×10^{-16}	$\sim 10^{-8}$	—	—	2×10^{-6}	1×10^{-6}	—	—
$t \to uZ$	8×10^{-17}	$\sim 10^{-4}$	—	—	2×10^{-6}	3×10^{-5}	—	—
$t \to ug$	3.7×10^{-14}	$\sim 10^{-7}$	—	—	8×10^{-5}	2×10^{-4}	—	—
$t \to uH$	2.4×10^{-17}	—	—	5.5×10^{-6}	$\sim 10^{-5}$	$\sim 10^{-6}$	—	—
$t \to c\gamma$	4.6×10^{-14}	$\sim 10^{-8}$	$\sim 10^{-7}$	$\sim 10^{-7}$	2×10^{-6}	1×10^{-6}	$\sim 10^{-8}$	$\sim 10^{-7}$
$t \to cZ$	$\sim 1 \times 10^{-14}$	$\sim 10^{-4}$	$\sim 10^{-8}$	$\sim 10^{-6}$	2×10^{-6}	3×10^{-5}	$\sim 10^{-4}$	$\sim 10^{-5}$
$t \to cg$	4.6×10^{-12}	$\sim 10^{-7}$	$\sim 10^{-5}$	$\sim 10^{-4}$	8×10^{-5}	2×10^{-4}	$\sim 10^{-7}$	$\sim 10^{-5}$
$t \to cH$	3.0×10^{-15}	—	$\sim 10^{-5}$	$\sim 1.5 \times 10^{-3}$	$\sim 10^{-5}$	$\sim 10^{-6}$	—	—

Table 3.1: Theoretical values for the branching fractions of FCNC top quark decays as predicted by the SM, the quark-singlet model (QS), two-Higgs doublet models with (2HDM II) or without flavour-conservation (2HDM III), minimal supersymmetric model (MSSM), SUSY with R-parity violation ($\not{R}$ SUSY), models with extra quarks (Extra q) and Topcolour-assisted Technicolour model (TC2) [80, 81].

limits on the branching fractions by several collaborations for the qgt channel and Table 3.3 summarizes the upper limits on $q\gamma t$, qZt and qHt channels. Table 3.2 contains the upper limits up until the analysis presented in this thesis. The results obtained in this thesis are presented in detail in Chapter 11. They are based on the latest publication by the ATLAS collaboration [86].

Coupling	LEP	HERA
$\mathcal{B}(t \to qg)$	17% [87]	13% [88–90]
	Tevatron	LHC
	2.0×10^{-4} (tug), ($2 \to 2$) [91]	—-
	3.9×10^{-3} (tcg), ($2 \to 2$) [91]	—-
	3.9×10^{-4} (tug), ($2 \to 1$) [92]	5.7×10^{-5} (tug), ($2 \to 1$) [83]
	5.7×10^{-3} (tcg), ($2 \to 1$) [92]	2.7×10^{-4} (tcg), ($2 \to 1$) [83]

Table 3.2: Experimental limits at 95 % CL on the branching fractions of the FCNC processes in the qgt channel set by experiments of the LEP, HERA, Tevatron and LHC accelerators.

Although FCNCs involving top quarks have not been observed, the first evidence of FCNC with a b quark was discovered in B_s^0 meson decays by the CDF collaboration [102] in 2005.

Coupling	LEP	HERA
$\mathcal{B}(t \to q\gamma)$	2.4% [93–97]	0.64% ($tu\gamma$) [98]
$\mathcal{B}(t \to qZ)$	7.8% [93–97]	49% (tuZ) [90]
Coupling	Tevatron	LHC
$\mathcal{B}(t \to q\gamma)$	3.2 % [99]	—-
$\mathcal{B}(t \to qZ)$	3.2 % [100]	0.07 % [101]
$\mathcal{B}(t \to qH)$	—	0.07 % [85]

Table 3.3: Experimental limits at 95 % CL on the branching fractions of the FCNC processes in the $q\gamma t$, qZt and qHt channels set by experiments of the LEP, HERA, Tevatron and LHC accelerators.

CHAPTER 4

The Large Hadron Collider and the ATLAS Detector

4.1 Large Hadron Collider

The LHC [103] is a circular proton–proton collider with a circumference of 27 km, buried around 50 to 175 m underground. It is located in European Organization for Nuclear Research (CERN) Geneva, near the French–Swiss border. It is the world's largest particle collider and collides protons at a centre-of-mass energy of $\sqrt{s}$ = 14 TeV at the design operation.

There are two proton beams accelerated in opposite directions in separate beam pipes around the 27 km long LHC tunnel. Before entering the LHC tunnel, the protons are accelerated by a series of pre-accelerators. At first, hydrogen gas is pushed through an electric field to strip off its electrons, therefore leaving only protons. The extracted protons are then directed into the Linear Accelerator (LINAC2) where they are accelerated to an energy of 50 MeV. They are then forwarded in to the Proton Synchrotron Booster (PBS) where their energies reach 1.4 GeV. Later they are transferred into the Proton Synchrotron (PS), increasing their energies to 26 GeV and then into the Super Proton Synchrotron (SPS) which increases the proton energy to 450 GeV. After the SPS, finally they are injected into the LHC. The LHC accelerates the protons to 4 TeV or more. A schematic view of LHC and its pre-accelerators is shown in Figure 4.1.

Inside the beam pipe, the protons are kept within their circular path by means of 1232 superconducting dipole magnets. The superconductivity is sustained by 96 tonnes of helium-4 in superfluid form. The focusing of the beam is achieved by 392 additional quadrupole magnets.

LHC started operating in September 2008 and shortly after that the operations stopped due to a magnet quench incident which damaged more than 50 magnets and the vacuum pipes. Operations began again in November 2009 and the first collisions at the interaction points occurred at $\sqrt{s}$ =450 GeV. A few

days after that, the collision energy was increased to $\sqrt{s} = 2.4$ TeV. During 2010 and 2011, the LHC operated at $\sqrt{s} = 7$ TeV and from 2012 to early 2013 at $\sqrt{s} = 8$ TeV. In February 2013, the LHC was shut down to receive a series of upgrades to increase its energy and luminosity. In April 2015, it started operating again at a centre-of-mass energy of $\sqrt{s} = 13$ TeV. Currently it is still running with this energy. The analysis presented in this thesis is based on the data from 8 TeV centre-of-mass energy collisions collected by the ATLAS experiment corresponding to an integrated luminosity of 20.3 fb^{-1}.

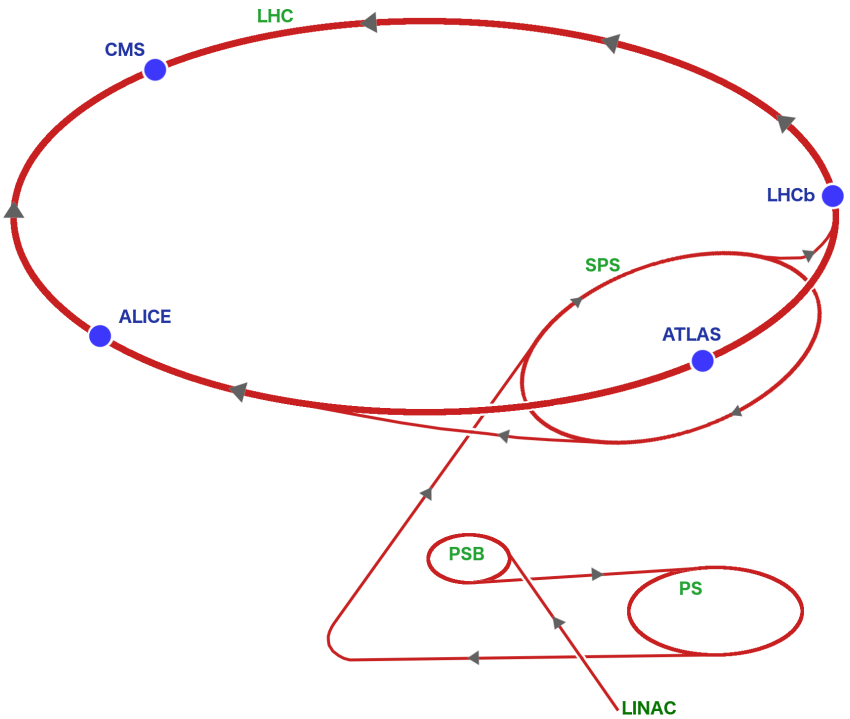

Figure 4.1: A schematic drawing of the LHC and the pre-accelerators (not to scale). The accelerators are labelled in green colour and the interaction points of the proton beams where the four main particle collision experiments take place are labelled in blue colour.The pre-accelerators (in order) are the linear particle accelerator (LINAC), the Proton Synchrotron Booster (PSB), the Proton Synchrotron (PS) and the Super Proton Synchrotron (SPS). The four experiments are ALICE, LHCb, CMS and ATLAS.

At the LHC, the operational period between 2009 and 2013 is called the first run or run 1 and the period from 2015 and onwards is called the run 2. Apart from the proton–proton collision runs, there were also periods of so called heavy-ion runs, where lead ions were injected into LHC, accelerated and collided. There were also runs with proton–lead ion collisions. In addition to these, when the accelerator was not operating, the detectors were kept online, registering particles originating only from cosmic rays. These are called cosmic runs.

The LHC accelerates proton beams in bunches (discrete packets of particles) instead of a continuous stream. The length, spacing and the intensity of the bunches can be adjusted. The bunch properties of the collision data used in this analysis [104] are different than the LHC design values [105] and are given in table 4.1.

There are four main experiments at the LHC, located at each of the four interaction points where particle detectors are positioned. The two general-purpose detectors are ATLAS [106] (A Toroidal LHC ApparatuS) and CMS [107] (Compact Muon Solenoid). These detectors cover almost the full solid angle, meaning that they are sensitive to particles travelling in almost all directions. In addition to the names of

Property	Value
Bunch length [ns]	1.06
Bunch spacing [ns]	50
Protons per bunch	1.1-1.7 $\times 10^{11}$
Max. number of bunches in the ring	1374
Bunch size at the interaction point [μm]	16

Table 4.1: The bunch properties of the data run used in this analysis.

these detectors, ATLAS and CMS stand for the experiments taking place using the data collected by the detectors and the physics collaborations involved in the experiments.

The other two experiments are ALICE [108] (A Large Ion Collider Experiment) and LHCb [109] (Large Hadron Collider beauty). ALICE is designed to study heavy-ion collisions (lead–lead and proton–lead collisions) in order to investigate quark-gluon plasma which is thought to occur during the early universe, within a tiny fraction of the first second of the Big Bang, before colour carrying particles formed hadrons. LHCb focuses on b-physics. It studies Charge Parity (CP) violation[1] involving b-hadrons. CP violation is needed to explain the baryon asymmetry of the universe.

4.2 The ATLAS detector

The ATLAS detector is 25 m high, 44 m long and weights 7000 tonnes, making it the largest particle detector ever built. It has a forward-backward symmetric cylindrical shape and it almost entirely encloses the beam pipe. The detector has several layers, sometimes compared to the layers of an onion and each layer consists of a sub-detector with a specific measurement purpose. Starting from the beam pipe and going outwards, the first sub-detector is the Inner Detector which itself has 3 sub-components: the Pixel Detector (Sec. 4.2.3), the Silicon Strip Tracker (Sec. 4.2.3) and the Transition Radiation Tracker (Sec. 4.2.3). These are the tracking detectors that measure the tracks of the charged particles. The next sub-detector is the ATLAS Calorimeter with the following sub-components: the electromagnetic calorimeter (Sec. 4.2.4) and the hadron calorimeter (Sec. 4.2.4). As the name suggests, the main purpose of the calorimeters is to measure the amount of deposited energies by the neutral or charged particles. The outermost layer consists of the muon spectrometer (Sec. 4.2.5) sub-detector. Apart from the sub-detectors, ATLAS is mounted with a magnet system (Sec. 4.2.2). Figure 4.2 shows a schematic view of the ATLAS detector and its sub-components.

4.2.1 ATLAS coordinate system

ATLAS uses a coordinate system that takes the proton beam direction as reference. The physical parameters that will be introduced in the following sections and chapters are defined in this coordinate system.

In the ATLAS coordinate system, the z-axis points along the beam pipe. The y-axis points directly upwards and the positive x-direction points inwards, towards the centre of the LHC ring. Therefore the

[1] In particle physics, the charge parity violation is the violation of the charge conjugation and parity symmetry. Charge conjugation symmetry is the symmetry of physics laws under charge conjugation. The weak interaction is the only interaction that violates charge conjugation symmetry. The parity symmetry is the symmetry of physics laws after flipping the sign of the space coordinates. The weak interaction violates parity symmetry as well. CP violation occurs during some types of weak decay

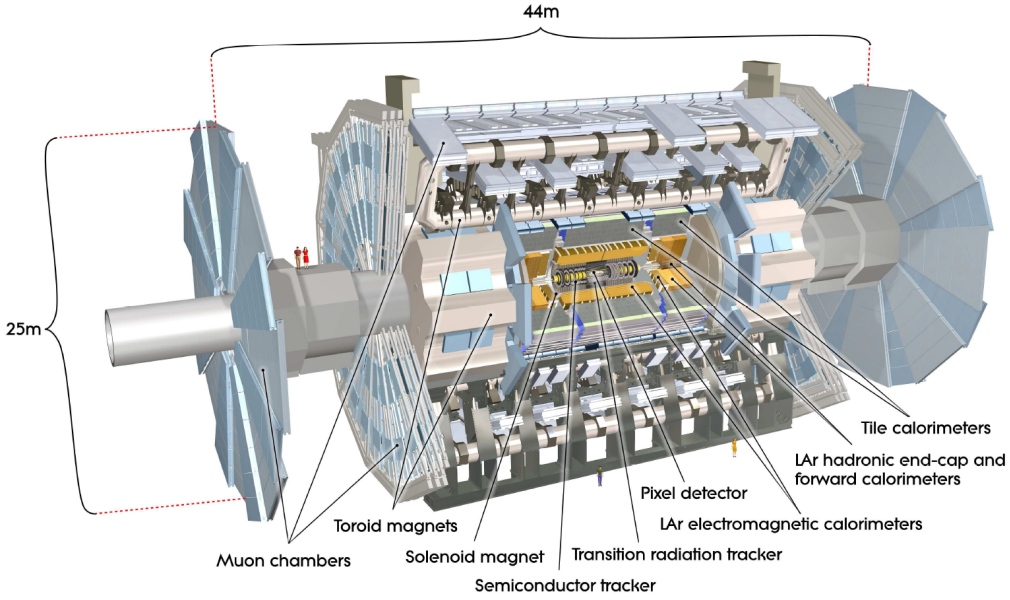

Figure 4.2: A schematic view of the ATLAS detector [110]

x-y-plane is perpendicular to the beam direction, sometimes called the transverse plane. The origin in this coordinate system is positioned at the nominal interaction point. The azimuthal angle $\phi \in [-\pi, \pi]$ is the angle between the x- and the y-axis and the polar angle $\theta \in [0, \pi]$ is the angle with respect to the z-axis.

One important variable that is commonly used in the ATLAS experiment is the pseudo-rapidity, η, which is defined as:

$$\eta = \frac{1}{2} \ln \left(\frac{|\vec{p}| + p_z}{|\vec{p}| - p_z} \right) \tag{4.1}$$

where $\vec{p}$ is a three-dimensional momentum vector and p_z is its z-component. η is equal to the rapidity when the mass of the particle goes to zero. This variable is useful since the difference of two pseudo-rapidities is invariant under Lorentz transformations. η can be written also in terms of θ as:

$$\eta = -\ln \left[\tan \left(\frac{\theta}{2} \right) \right]. \tag{4.2}$$

Another variable, ΔR between two particles, which is also a Lorentz invariant can be constructed as:

$$\Delta R = \sqrt{\Delta\eta^2 + \Delta\phi^2} \tag{4.3}$$

where $\Delta\eta$ is the pseudo-rapidity difference and the $\Delta\phi$ is the azimuthal angle difference between the two particles.

The transverse momentum P_T is also a very commonly used variable and is defined as:

$$P_T = \sqrt{P_x^2 + P_y^2} \tag{4.4}$$

where the P_x and the P_y are the x- and y-components of 3-momentum, respectively.

4.2.2 Magnet system

ATLAS employs a magnet system in order to deflect the direction of the charged particles. This is crucial for two important measurements: the transverse momentum measurement which heavily relies on the curvature of the tracks of the charged particles and the charge measurement which can be deduced from the direction of the deflection.

A schematic view of the ATLAS magnet system is shown in Figure 4.3. It consists of two separate magnets, a solenoid magnet and a toroid magnet. Both are superconducting magnets cooled down by liquid helium with 1.9 K working temperature.

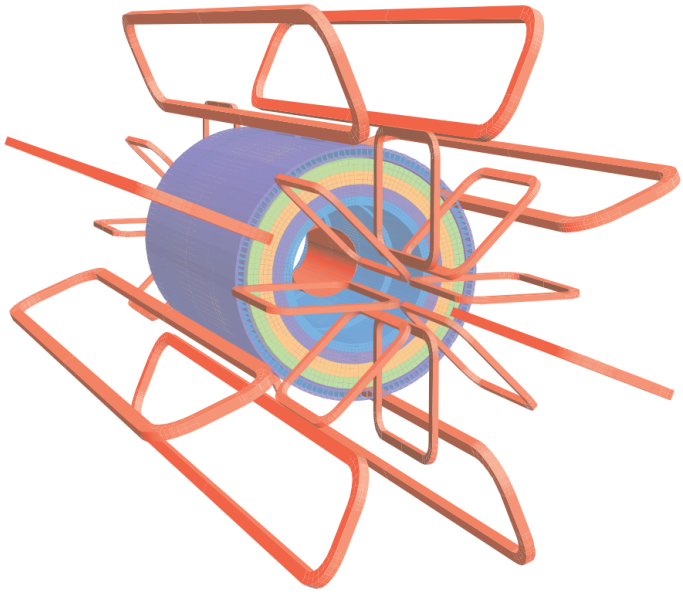

Figure 4.3: ATLAS magnet system. The cylindrical section in the middle is the calorimeter which surrounds the solenoid magnet. The rest of the of the magnets (in red) are the toroid magnets [111].

Solenoid magnet

The solenoid magnet is positioned between the Inner Detector and the calorimeter. It has a cylindrical structure with a diameter of 2.56 m and it is 5.8 m long. It generates a homogeneous magnetic field of 2 T inside the cylindrical structure, bending the charged particles in the Inner Detector. A great effort was necessary while designing and constructing the solenoid magnet to minimise its radial thickness and radiation length[2] it takes as it is positioned just before the calorimeter. This means that some of the particle energy is going to be absorbed by the magnet before it is measured by the calorimeter. The thickness of the magnet is 0.66 radiation lengths.

Toroid magnet

There are three components of the toroid magnet: two at the endcaps and one around the barrel region of the ATLAS detector (red sections in Figure 4.3). They are located outside the calorimeter and encircle

[2] A radiation length is the distance required for an electromagnetically interacting particle to lose all but $1/e$ of its initial energy. When the particle type is kept constant, it becomes an aspect solely of the type of the material.

the muon spectrometer. The toroid magnets' purpose is to bend the charged particles in the muon spectrometer. It is the largest superconducting magnet in the world, weighing over a thousand tonnes. It is 25.3 m long and has a diameter of 20.1 m in the barrel section. It provides a non-uniform magnetic field of 2-8 T.

4.2.3 Inner Detector

The ATLAS Inner Detector (ID) is responsible for detection and tracking of charged particles. It surrounds the beam pipe and starts only 5 cm away from the interaction point. With all its sub-components, it is a 1.1 m high and 3.5 m long cylindrical detector. It covers a polar angle up to $|\eta| < 2.5$. The ID has three geometric sections, namely the barrel which is the cylindrical part that encloses the beam pipe and the two endcaps which are positioned at both ends of the barrel. A schematic view of the full ID and the barrel section with its sub-components are given in Figure 4.4.

Pixel Detector

The Pixel Detector [113] is the innermost component of the ID. Being the closest detector to the interaction point, the Pixel Detector has to be capable of resolving the tracks of the charged particles in very crowded environments. It has three[3] layers of concentric cylinders enclosing the beam pipe in the barrel section and three layers of disks in each endcap. Each layer is made up of segmented silicon pixels with dimensions $50 \times 450\ \mu\text{m}^2$. Overall, this corresponds to 80 million readout channels. When a charged particle passes through a pixel, it excites the valence electrons in the silicon semiconductor and the resulting free electrons are then detected by the electronics, causing a signal from that particular pixel.

The Pixel Detector is exposed to very high radiation, therefore it is designed to operate in harsh environments for a reasonable lifetime. It is also the most precise component of the three components of the ID in position measurements with a resolution of 115 μm in the z-direction and 10 μm in the $R-\phi$ direction. The precision of the measurement is then improved further with the additional information from the other two sub-components of the ID.

Semiconductor Tracker

The next sub-component of the ID is the Semiconductor Tracker [114] (SCT). It starts 30 cm away from the beam pipe and has a thickness of 26 cm. It operates by the same principle as the Pixel Detector. In the barrel, it consists of four layers. Each layer carries 120 mm long silicon strips on both sides. The strips on each side of the layer are tilted by 2.29° with respect to each other. These tilted pairs of strips form a single sensor. In each endcap, there are nine layers. Here the strips are arranged radially.

The resolution of the SCT is 17 μm in the $R-\phi$ direction and 580 μm in the z-direction in the barrel section. In the endcaps, it is 17 μm in the ϕ direction and 580 μm in the R direction.

Transition Radiation Tracker

The Transition Radiation Tracker [115] (TRT) is the outermost component of the ID and it is the largest one among the three. It is 56.3 cm away from the beam pipe and has a radius of 106 cm in the barrel section. It is different in structure and measurement principle with respect to the other two. It is a gaseous

[3] During the break between the run 1 and run 2 periods, a fourth layer is added to Pixel Detector in the barrel section. The analysis presented here uses the data recorded before this upgrade of the Pixel Detector.

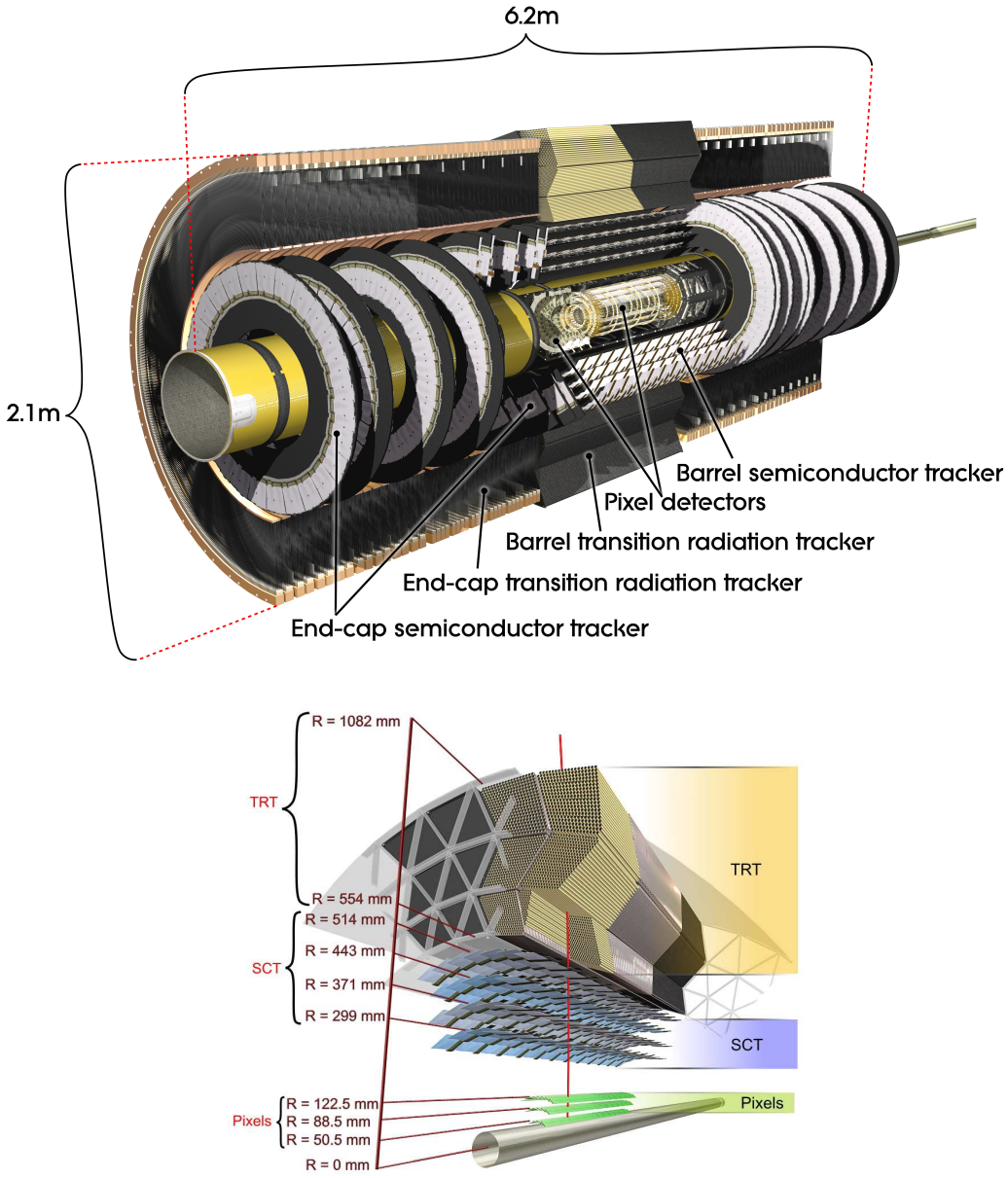

Figure 4.4: A schematic of the full ID (top) and the barrel section (bottom). Sub-components and dimensions are displayed. Red line at the bottom schematic represents a high energy particle crossing the detector[112].

detector composed of straw tubes with a diameter 4 mm. The straw tubes are 144 cm long in in the barrel section and 37 cm long in the endcaps. The straw tubes are filled with a gas mixture of Xe (70%), CO_2 (27%), and O_2 (3%).[4] Each straw contains a gold-plated tungsten wire passing through the centre. The wire acts as anode and the tube itself is the cathode. An electric potential is applied on the wire, producing an electric field between the anode and cathode, which gets weaker towards the cathode. When a charged particle passes through a straw, the gas is ionised and the free electrons starts drifting towards the anode. Approximately, the nearest electron to the centre reaches the wire first. When the electron is very close the wire, the electric field gets very high and the electron itself ionises the gas creating many free electrons and ions forming an avalanche. The electrons are then quickly absorbed by the wire but the ions drift slowly towards the cathode. The movement of the ions around the wire just after the avalanche changes the potential difference between the anode and cathode which then can be read as a signal. The drift time of the electrons can be measured precisely; it is the time between the charged particle passing through the straw until the avalanche occurs. The beginning of the drift time T_0 is set to the bunch crossing time. The drift time can then be converted to distance r as the average speed of the electrons can be estimated. However, it is not possible to identify the exact position of the charged particle with a single straw because there are infinitely many rs around a circle. Therefore a single straw can only provide information of a circle to which the charged particle passed tangentially. This is called a drift circle. By using many straws positioned around each other, the exact track of the charged particle can be reconstructed with a high precision using drift circles provided by the straws in which the charged particle passed.

In the barrel, TRT has 3 large sections called rings where each ring has 32 modules. Each module has 73 layers of straws parallel to the beam pipe (see Figure 4.4). In each endcap, the straws are positioned radially on 160 parallel panels, perpendicular to the beam pipe. Overall there are 351 000 readout channels in the TRT. A charged particle will register a measurement in at least 36 straws when it traverses the TRT. Other than providing tracking information of the charged particle, the TRT is designed to contribute to particle identification. When particles at relativistic speeds travel between the materials of different refractive indices, they emit photons. This is called the transition radiation effect. The amount of photons emitted via this process is a distinctive feature of particles since it is proportional to the gamma factor $\gamma = E/m$. Lighter particles will radiate significantly more photons. The reason for using the Xe gas for the straws is that the photons emitted via transition radiation effect with wavelengths in the X-ray region can be absorbed by the Xe gas. Electrons are easily identifiable via this method due to their very small mass (and therefore very high γ) compared to pions, muons and taus. The electrons with energy E>2 GeV, on average cause ten high threshold hits due to transition radiation.

4.2.4 Calorimeter

The ATLAS calorimeter is designed to absorb the energies of the particles passing through it and stop them. When a particle enters the calorimeter, it interacts with the material, starting a particle shower. The energy measurement can be performed when the entire energy of the original particle is deposited to the calorimeter. Apart from the energy measurement, the calorimeter also helps for track reconstruction and particle identification.

The first component of the ATLAS calorimeter, the electromagnetic calorimeter (ECAL), is positioned close to the inner section. It is designed to absorb showers created by photons, positrons and electrons.

[4] During run-I, a gas leakage occurred in a small fraction of the TRT in an inaccessible section. Due to this, Xe, an highly expensive gas, had to be pumped constantly inside the TRT in order to come up with the sufficient gas pressure. Later, Ar which is relatively much cheaper was used instead of Xe in the sections where the leakage occurred. Currently, Ar is still used in the problematic regions.

The hadronic calorimeter (HCAL) encircles the ECAL and it absorbs hadronic showers of particles that interact with the nuclei through strong interaction. Both ECAL and HCAL consist of successive layers of active and passive materials where the passive layers trigger the particles to create showers and the active layers are used for the energy measurement.

The thickness of the ECAL is around 24 radiation lengths in the forward region ($|\eta| > 1.375$) and 22 radiation lengths in the central region which is compatible to that of the Earth's atmosphere. The thickness of the HCAL is around 10 interaction lengths[5] in the forward region and around 9.7 interaction lengths in the central region. While almost all electromagnetic interactions of electrons and photons are absorbed in the ECAL, some of the energy of the hadronic particles can leak outside the calorimeters. Therefore the calorimeter is covered by a support material with 1.3 radiation lengths. A schematic illustration of the ATLAS calorimeters is shown in Figure 4.5.

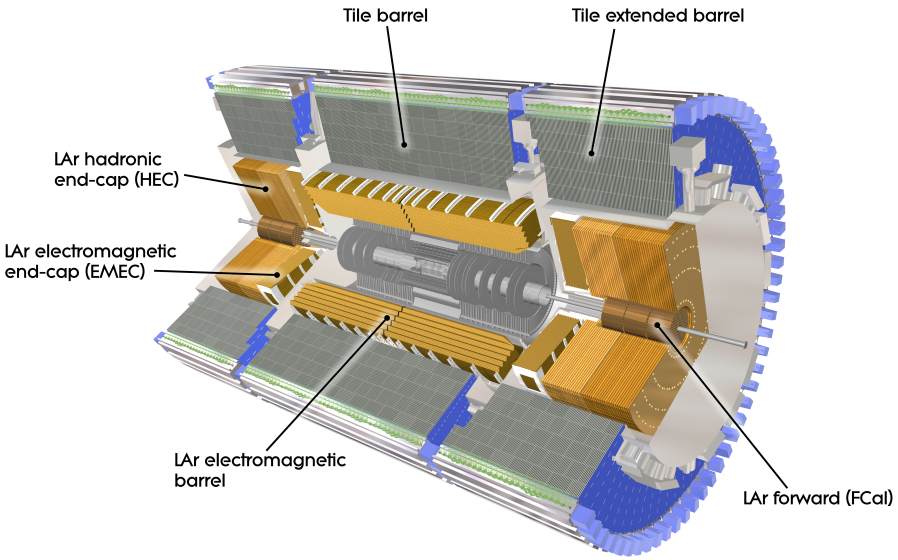

Figure 4.5: A schematic view of the ATLAS calorimeters[116].

Electromagnetic Calorimeter

The ECAL has a barrel section that covers a pseudo-rapidity range of up to $|\eta|<1.475$ and two coaxial endcap sections with a coverage of $1.375<|\eta|<3.2$. The barrel is divided into two cylindrical sections at $z=0$, which are separated by a distance of 4 mm.

The passive material is made of lead. Liquid argon (LAr) is used in the entire ECAL as active material, therefore it is usually called the LAr calorimeter. Between each layer of active and passive material pairs, three layers of copper electrodes are positioned for readout. The charged particles ionise the LAr and the produced free electrons are read as a signal by the copper electrodes.

For $|\eta| < 1.9$, a single, very finely grained LAr layer is placed as a presampler to help estimate the energy loss in front of the calorimeters.

There are three layers in the barrel (see Figure 4.6). The layers in the barrel (as well as in the endcap) are made out of cells forming a grid. The innermost layer is segmented with a granularity of $0.025/8\times0.1$

[5] Similar to the radiation length, but for strongly interacting particles.

in the $\eta - \phi$ plane. Since this is the first layer where the particles enter to the calorimeter, it is sometimes called the pre-shower detector which provides high photon separation. The middle layer forms the largest section of the ECAL barrel and it has the densest granularity (0.025×0.025 in $\eta - \phi$ plane). The largest fraction of the energy of the particles is deposited here. The third layer has a granularity of 0.05×0.025 and is designed to collect the remaining energy from the shower tails.

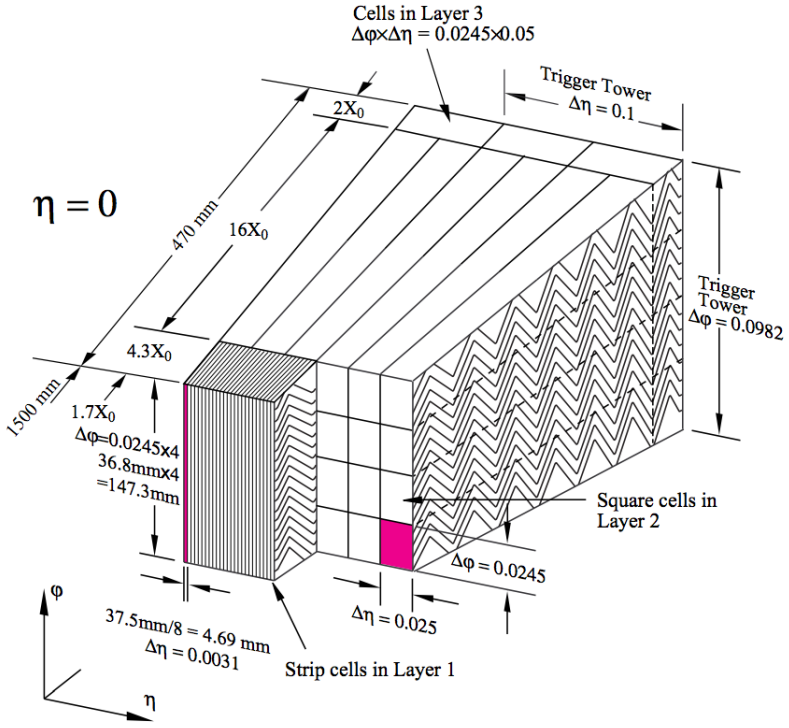

Figure 4.6: A schematic view of the ATLAS calorimeters[116].

Hadron Calorimeter

The HCAL is composed of three sub-components: the tile calorimeter in the barrel, extending in both directions and encircling the endcaps (see Figure 4.5), the LAr hadronic endcap calorimeter in the endcaps and the forward hadronic calorimeter.

The barrel section of the tile calorimeter covers a range of $|\eta| < 1.0$ and the endcap extensions cover $0.8 < |\eta| < 1.7$. Both in the barrel and in the extensions, this is composed of three layers made of cells. In the first two layers, the granularity of a cell is 0.1×0.1 in the $\eta - \phi$ plane and in the outermost layer it is 0.2 in η. It has a different working principle than the LAr calorimeter. The active material is made of plastic scintillator tiles. When a shower of particles traverse the active material, a scintillation light in the ultraviolet region is produced. The active material is doped with a material made of fibre that shifts this ultraviolet light to visible light. The visible light is collected by the fibre cables at each end of the tiles and then directed to photomultipliers which produce the readout signal. The tile calorimeter uses steel as the passive material.

The LAr calorimeter in the endcaps is similar to ECAL and they share the same LAr cryostat. It covers a range of $1.5<|\eta|<3.2$, therefore overlapping with the tile calorimeter. The granularity of the LAr

hadronic endcap calorimeter is the same as the tile calorimeter for $|\eta| < 2.5$.

The forward hadronic calorimeter is also a LAr calorimeter. It covers a range of $3.1<|\eta|<4.9$. It is composed of three layers where the first layer uses copper as passive material and the two other layers use tungsten therefore the forward hadronic calorimeter is also sensitive to electromagnetic showers.

4.2.5 Muon Spectrometer

The ATLAS calorimeter is capable of stopping all the particles except for muons and neutrinos (in rare occasions, a small fraction of the energy of the jets can escape the calorimeter). Since neutrinos carry no electric charge and interact only weakly, they escape the detector. As muons are not stopped by the calorimeter, their transverse momenta can be measured by building a large tracker and a magnet system around the calorimeter.

The muon spectrometer is the outermost section of the ATLAS detector, therefore it is the last sub-component which particles interact with. It serves two purposes: it is a tracker for charged particles (mainly for muons) and it is used as a part of the ATLAS trigger system (more will be discussed on triggering in ATLAS in Section 4.2.6).

A schematic view of the ATLAS Muon Spectrometer is given in Figure 4.7. The tracking for the pseudo-rapidity region of $|\eta|<2.7$ is performed by the Monitored Drift Tube chambers (MDTs). At the innermost layer of the endcaps, for $|\eta| < 2.0$, the MDTs are replaced by a different type of tracker (see below). MDTs are precision tracking chambers which provide high-accuracy measurements. There are:

- three cylindrical layers of drift chambers in the barrel region and four wheels in the endcap region,
- each chamber has three to eight layers of drift tubes,
- each layer in a chamber has 16-72 drift tubes.

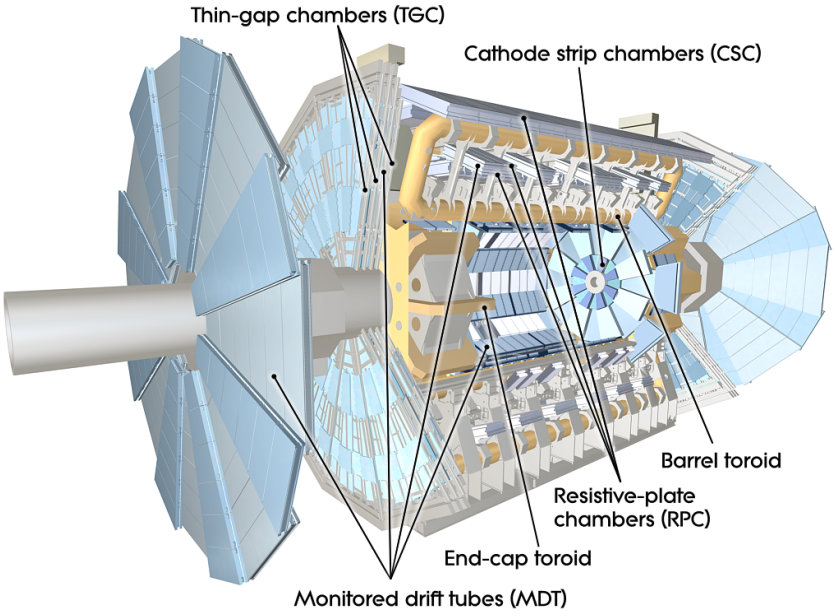

Figure 4.7: A schematic view of the ATLAS muon spectrometer.

The drift tubes have a diameter of 29.97 mm and are filled with a mixture of Ar/CO_2 gases. The anode wire at the centre of the tube is made of gold plated tungsten, similar to that of TRT. The resolution of the MDTs is 35 μm.

The rate of muons at large pseudo-rapidity regions is significantly higher. For regions $2 < \eta < 2.7$, high-rate, high-granularity trackers, called Cathode Strip Chambers (CSCs) are placed at the innermost layer of the endcaps. There are two wheels of CSCs in each endcap, positioned perpendicular to the beam axis. Each wheel consists of eight chambers. The chambers are divided into four multi-wire proportional chambers filled with a Ar/CO_2 gas mixture.

The muon trigger system is composed of Resistive Plate Chambers (RPCs) in the barrel and Thin Gap Chambers (TGCs) in the endcap sections. Overall the trigger system covers the range $|\eta|$ <2.4.

In RPCs, two electrode plates are placed in a volume of gas, parallel to each other. They are separated by a distance of 2 mm and the gap between the two is filled with an insulating material. An electric field is applied between the plates. An avalanche occurs when a muon traverses the plates and the signal is picked up by the anode plate. RPCs cover the pseudo-rapidity range of $|\eta|$ <1.05.

The working principle of TGCs is similar to the multi-wire proportional chambers. The distance between the cathode and the wire is smaller than the distance between each wire. This causes a short drift time and therefore good time resolution. The TGCs provide a time resolution of 1 ns and a spatial resolution of 5-10 mm. They cover a pseudo-rapidity range of 1.05<η<2.4.

4.2.6 ATLAS trigger system

The search for extremely rare physics interactions require the collection of very high statistics. In order to achieve this, LHC provides bunches with a spacing of 25 ns which translates to an event[6] rate of 40 MHz. This requires dozens of terabytes of disk space per second, considering that each event takes up around 1.6 Mb of disk space. This is not feasible, therefore ATLAS employs a trigger system which is designed to select interesting events. Most of the interactions that occur during proton–proton collisions are soft QCD interactions which are out of the scope of the ATLAS physics analyses goals. These events should be filtered out in order to remain with rare and interesting phenomena and reduce the required computing power and disk space.

In ATLAS, triggering on interesting events is done at three stages, namely Level 1 (L1), Level 2 (L2) and Event Filter (EF):

- At L1, the triggering is done entirely electronically by the hardware built in the detector. It uses the muon trigger system and the calorimeter information with reduced resolution in order to make a rough selection of events that contain electrons, muons, jets, taus and missing transverse energy[7] ($E_{\mathrm{T}}^{\mathrm{miss}}$). As soon as an event is selected by the L1 trigger, the readout channels from the entire detector components are read and saved into readout drives (RODs) then passed to the readout buffers (ROBs). L1 also saves the coordinates of the objects it identifies, this is sometimes called the Regions-of-Interest (RoI). This information is then passed on to the L2 trigger. L1 reduces the rate of events drastically, from 40 MHz to a mere 75 kHz.

- The provided information from L1 is then read by the L2. L2 is a software-based trigger system built outside the detector. It first reads the RoI provided by L1 and employs the tracking system as well, in addition to the calorimeter and the muon system. It accesses the full granularity of

[6] Each proton–proton collision is called an event.

[7] The $E_{\mathrm{T}}^{\mathrm{miss}}$ is the missing energy in the transverse plane. The transverse momentum of the particles has to add up to zero as the protons collide along the z-direction. The $E_{\mathrm{T}}^{\mathrm{miss}}$ occurs because of the energy carried away by neutrinos which escape the detector without interacting. Therefore, the presence of a high $E_{\mathrm{T}}^{\mathrm{miss}}$ in an event is a very strong indicator of a neutrino.

the detector around the RoI, refining the objects identified at L1. At this stage, the event rate is reduced to 3.5 kHz. If an event is accepted by L2, the information stored on ROBs for that event is passed to the EF and the occupied memory in ROBs is freed.

- The EF accesses the entire data gathered by the detector at full granularity. It uses reconstruction algorithms to fully select and reconstruct interesting events. The algorithms used by the EF are very similar to the offline[8] reconstruction algorithms used in physics analyses. At EF, the event rate is reduced to 200 Hz. The processing of an event takes up to 4 s with a latency of 1 s. This requires a strong computing power. For this purpose, 1000 processing nodes are employed for EF.

The selected events are then classified depending on the type of the triggering and the objects the event contains. These classes are called physics data streams. There are four data streams, namely, *MinBias*, *JetTauEtmiss*, *Muons* and *Egamma*.

In the *MiniBias* stream, the events are selected randomly. The *JetTauEtmiss* stream contains events with jets, $E_{\mathrm{T}}^{\mathrm{miss}}$, and leptons. These are events with a possibility of containing a tau lepton. The *Muons* stream contains events with muon signature and the *Egamma* stream contains events with electron and/or photon signatures. This analysis uses the data collected in the *Egamma* and *Muons* streams.

[8] In this context, offline means "after the data has been recorded."

CHAPTER 5

Data and the simulated events

As described in Chapters 2 and 3, the analysis presented in this thesis focuses on the search for FCNC interactions during single top-quark production. The top quark decays to a b quark and a W boson, where then the W boson decays leptonically. This indicates that in the final state event topology, there is a lepton (electrons and muons[1]), a neutrino and a b quark. The neutrino manifests itself as $E_{\mathrm{T}}^{\mathrm{miss}}$ in the detector and the b quark forms a b jet.

An event selection is applied on the data to choose events that have the event topology described above. However, the data contains several other physics processes that have exactly the same or very similar event topologies. These processes are called background processes or simply background. All the background processes as well as the FCNC (signal) processes are simulated and compared to the observed data.

This chapter summarises the properties of the data collected by the ATLAS detector and details the simulated signal and background processes involved in this analysis.

5.1 Observed data

The data collected by the ATLAS detector has to be inspected and decided whether it is suitable for physics analysis or not. This is a task where many physicists are involved and is called the data quality check. The data quality check is done in two steps: online and offline monitoring. Online monitoring is performed in the control room directly above the ATLAS detector, on the surface, during data taking. LHC injects proton beams into the beam pipe, sometimes several times a day. Each injection cycle starts with a test beam. Then the energy of the beam is increased and the transverse dimentions of the bunches are squeezed to the target value. After the all properties of the beam reach the working value, ATLAS

[1] As they are not specifically excluded, tau lepton decays are also considered.

starts data taking. This is called a run and during each run, typically a few millions of events are recorded. During the data taking, each detector component is checked, by looking at several distributions and indicators on the monitoring screens in the control room. Sometimes a detector component may not be working as expected. Each problem associated with a run is carefully checked and reported. Sometimes a run has to be stopped even when the collisions are ongoing. The period when the ATLAS detector is not operational for various reasons is called the dead time. Because of the reasons mentioned above, the recorded luminosity by the ATLAS detector is typically lower than then delivered luminosity by the LHC. The offline monitoring is done after the data taking where each recorded run is again inspected per detector component. This is the last step where it is decided if the run is suitable for physics analyses. Sometimes the problems that could occur in the data can be recoverable, such as a drop in efficiency in certain angular region of the ID. If the problem is not recoverable, that particular run is marked as bad and omitted. All the remaining data-taking periods with stable beams and operational detector components are added to the so-called Good Runs List (GRL). The GRL is then used by the analysers to select the data that are suitable for physics analyses.

Because of this, not every run recorded by ATLAS is used; hence the total integrated luminosity used in physics analyses is typically lower than the recorded luminosity by ATLAS and that as well lower than the one delivered by the LHC. Figure 5.1 shows the integrated luminosity delivered by the LHC and gathered by the ATLAS. The actual amount of data in terms of integrated luminosity used in this analysis is 20.3 pb^{-1}, as mentioned in Section 4.1.

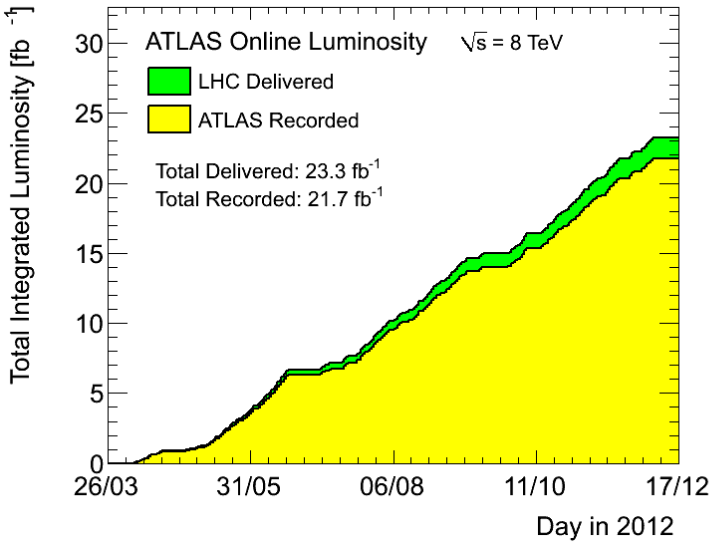

Figure 5.1: Cumulative luminosity delivered by the LHC (green) and recorded by ATLAS (yellow) versus the days. The distribution shows the data taken at centre-of-mass energy of $\sqrt{s}$ = 8 TeV during 2012.

5.2 Monte Carlo simulation

New physics phenomena that are searched for in particle collider experiments, such as the search for FCNC single top-quark production presented in this thesis, are thought to occur very rarely. Out of billions of events collected by the ATLAS detector, only a tiny fraction of them are assumed to originate from such interactions. In order to understand the data and search for possible beyond SM phenomena,

the Monte Carlo (MC) simulation techniques are employed in almost every experimental particle physics analyses. They are generated and stored on an event-by-event basis, similar to that of the observed data. Each MC event contains the information of the physics interaction that is simulated, as well as how the produced particles interact with the detector. This approach has various benefits. For example, in a region where no new physics is expected to occur, such as at low energies, which have been studied and tested by several other experiments in the past, the MC simulations are expected to agree with the observed data. The observed data contains the information of how the produced particles interact with the ATLAS detector in a particular event. However, MC events contain the full information of the physics process that took place (truth information) in addition to the detector information. Therefore, an agreement between the data and the MC can immediately verify our understanding of the behaviour of the detector, as well as the physics processes that occur in that particular energy regime.

In a region of the phase-space, where a possible deviation from the SM can occur, and if the MC simulations are generated based only on the physics processes that can occur in the SM, a difference between the data and the MC is expected. The difference can manifest itself in several forms, for instance the number of data events can be higher or lower than the expected events that are simulated in the MC in a certain phase-space, or the kinematic distributions of physical variables, such as the angular distribution of a particle can be different. If the new physics events are thought to occur extremely rarely and the SM background processes have very similar topologies, these differences can be too subtle to detect "by eye". Therefore, in order to be able to recognise any deviations from the SM in the observed data, sophisticated statistical analysis techniques are employed, such as multivariate analyses, which will be explained in Chapter 9.

In addition to the SM background MC, a signal MC, which simulates the new physics events that are searched for is also generated. One reason for this is to understand if the observed deviation between the observed data and the background MC can be explained by the new physics that is thought to occur. Another reason is to train the multivariate analysis software to be able to distinguish between the topology of the signal events and that of the background MC.

The following sections will detail the techniques that are used to generate the MC simulations used in the analysis presented here.

5.2.1 MC event generation

The MC event generation is the process of simulating the possible physics processes that can occur during proton–proton collisions. It relies on the factorisation technique, where the physics processes are divided into energy regimes that they occur in. Many of the physics processes are not exactly calculable and requires several sophisticated approximations and assumptions in order to be able to provide a sufficiently accurate description of the physics involved in the collision events. Figure 5.2 shows an illustration of a typical simulated proton–proton collision. The next three subsections summarise the steps of the event generation process.

Simulation of the hard scattering process

When the two protons collide at high energies, the actual collisions occur between the constituent particles that the protons are made of, which are called partons. This is called the hard scattering process and this is the main physics process where the phenomena of interest are expected to occur. In Figure 5.2, this is shown by the large green circle. Due to the asymptotic freedom explained in Section 2.3.2, at higher energies the partons are considered as quasi-free particles. The interactions that occur between partons are simulated by matrix element (ME) generators. However, this part of the simulation merely

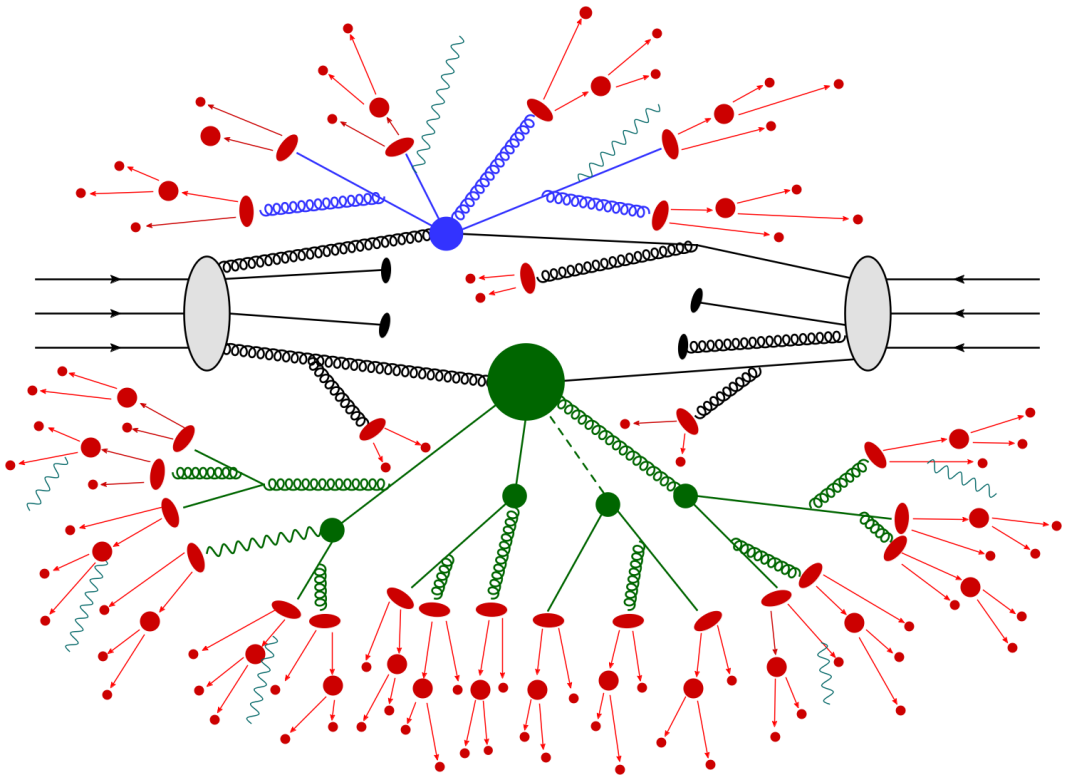

Figure 5.2: An illustration of the simulation of the proton–proton collision. The incoming black lines show the parton content of the protons involved in the interaction. The large green circle represents the point where the hard scattering process occurs and the green lines indicate the products of the hard scattering process. The blue circle represents the underlying event. Red circles and lines show the parton shower simulation.

computes the possible interactions, but it does not take into account the probability of the occurrence of certain partons in a proton at a given energy scale. In order to have a precise estimate on this, the Parton Distribution Functions (PDFs), which are the probability densities for finding a parton as a function of momentum fraction x of the total proton momenta and the momentum transfer Q^2 are used. The perturbative QCD is not capable of fully predicting the PDFs due to non-perturbative behaviour of partons as they are not totally free particles. Therefore, experimental methods are employed to derive PDFs by various collaborations. The list of PDFs used in this analysis together with the generators are be listed in Section 5.3.

Underlying event

Apart from the hard scattering process, several other interactions can occur between the partons that are not involved in the hard scattering process which are called proton remnants. These additional interactions as a whole are called the underlying event. They occur with less energy, as the greater fraction of the energy of the protons is spent in the hard scattering process. The blue circle in Figure 5.2 indicates the underlying event process. It can take place between the partons originating from the protons involved in the hard scattering process as well as between partons originating from different hard scattering processes. In contrast to the hard scattering processes, the contributions from the underlying event processes are not directly calculated and simulated but they are derived by tuning the MC simulations to the observed data.

Simulation of parton showers

The particles that are involved in the hard scattering process can decay into other fundamental particles or may radiate additional particles. These additional particles/radiations are called Initial State Radiation (ISR) if they originate from the incoming particles and Final State Radiation (FSR) for the outgoing particles. The ISR and FSR contribute to the PS of the hard scattering and they should be simulated as well. In Figure 5.2 these are shown by red circles.

Simulation of hadronisation

After the hard scattering process, as the PS shower progresses, more and more particles are radiated, and in each step it becomes energetically more favourable for partons to form baryons and mesons. This process is called hadronisation. The partons then manifest themselves as jets in the detector. As in the case of the PDFs, the hadronisation process cannot be calculated, therefore it is modelled. The string fragmentation and the cluster fragmentation models are the two commonly used models, which are detailed in References [117, 118]. The hadronisation process is generally handled by the PS generators.

In every step of the event generation, energy, momentum and all quantum numbers of the interacting particles are passed on to the next step in order to ensure that the conservation laws are met.

5.2.2 Detector simulation

In the observed data, the particles that are produced after the proton–proton collisions traverse the ATLAS detector, therefore this has to be simulated in the MC as well. In order to achieve this, a very good understanding of the detector is required. This is a great challenge as the ATLAS detector is a highly complex machine. Every sub-component of it has to be understood well, and the response of each individual component after the interaction with a particle should be predicted with great accuracy. Furthermore, the tracks of the particles in the magnetic field has to be calculated. This is also a difficult task, especially due to the highly non-uniform magnetic field provided by the Toroid magnet, as described in Section 4.2.2. In order to achieve this, the GEANT4 software is used [119]. The entire detector in three dimensions is implemented into the software, where it can model the path of the particles in the magnetic field as well as their interactions with the material of the detector.

5.3 Simulation of SM backgrounds

This section details the SM model background processes considered in this analysis as well as the generators used to simulate them.

Several SM processes are expected to have a similar final-state topologies to the signal samples and are considered as background to the FCNC analysis. As described in the previous sections, events in which a light quark (u or c) interacts with a gluon to produce a single top quark are searched for. Only the SM decay modes of the top quark are considered, i.e. $t \to Wb$, where the W boson decays leptonically. Thus, the event signature consists of a high-p_{T} b-quark jet, a charged lepton and missing transverse momentum from the neutrino.

Events with a W boson produced in association with jets (W + jets background) are the dominant backgrounds because of their great similarity to the topology of the signal events. For instance, an event with a W boson and a c quark jet where the jet is misidentified as a b quark jet exactly matches to the topology of the signal event. Figure 5.3 shows the Feynman diagrams of two typical W+jets processes.

The W+jets background is split into two samples, namely the W+LF and the W+HF. LF stands for light flavour which indicates that the associated jet originates from a light quark (u, d and s) and HF stands for heavy flavour (c, b and t).

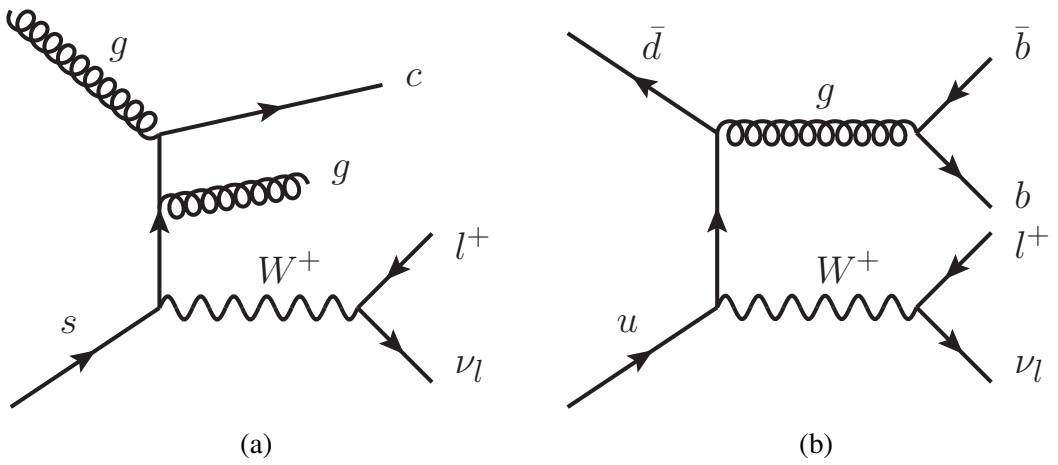

Figure 5.3: Two representative Feynman diagrams of W+jets background processes. Two quarks interact and create a W boson (which decays leptonically) and a gluon (which decays into a b and a $\bar{b}$ quark) (a) and a quark interacts with a gluon creates a W boson and a c quark (b). In the latter a gluon is also radiated.

The t-channel and Wt events (Figure 2.3) typically contain 2 or more jets, so a missing jet in these single top-quark events can mimic the signal as well. Similarly, $t\bar{t}$ events (Figure 2.2) also contain 2 or more jets and for the same reasoning, they can also leak into the final event selection. The Z + jets events, where the Z boson decays leptonically and one of the leptons is not identified can also mimic the signal events (Figure 5.4).

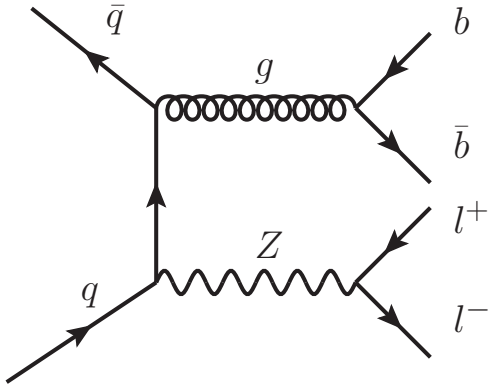

Figure 5.4: Feynman diagram of a Z+jets event. Two quarks interact where a gluon and a Z boson are produced. The gluon decays into a b and a $\bar{b}$ quark and the Z boson decays leptonically.

Diboson events (WW, ZZ, WZ), where one of the bosons decays hadronically and the other decays leptonically with missing jets and leptons can also create event topologies similar to that of signal (Figure 5.5).

To model the W boson and Z boson background, so called multileg generators are used. In order to get events of the same order in perturbation theory for different observed jet bins, processes with a different

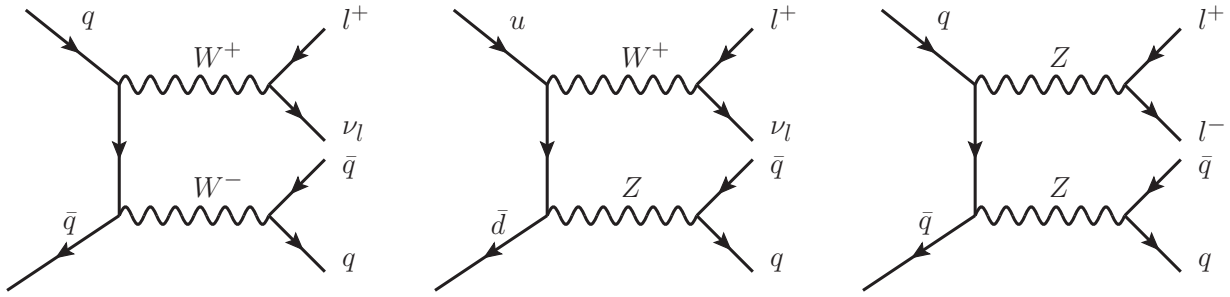

(a) (b) (c)

Figure 5.5: Feynman diagrams of three diboson events. Two quarks interact and a W boson pair is produced where one W boson decays leptonically and the other decays hadronically (a), two quarks interact where a W boson and a Z boson produced where the W boson decays leptonically and the Z boson decays hadronically (b), two quarks interact and a Z boson pair is produced where one Z boson decays leptonically and the other decays hadronically.

number of additional partons need to be merged together. Similar approaches are implemented in the Sherpa [120] and Alpgen [121] generators. Sherpa is a general purpose LO generator that is capable of simulating every step of the event generation. Alpgen is a LO matrix element generator which is not capable of the simulation of the parton shower and hadronisation. Therefore the samples that are produced with Alpgen are interfaced with Herwig which is another general purpose LO generator that is capable of simulation of parton shower and hadronisation.

For this analysis Sherpa (v.1.4.1) and the CT10 PDF [122] sets are used in order to simulate the W+jets background processes. Each background process is produced with a cross-section which is compatible with the centre-of-mass-energy of the proton-proton collisions. Corresponding cross-sections as well as the number of events generated per background process are reported in Table 5.1. The k-factors which are the corrections on the cross-sections are also listed. Sherpa uses the CKKW method [123] to remove overlaps between the n and $n+1$ parton samples. Double counting between the inclusive $W+n$ parton samples and samples with associated heavy quark pair production is avoided consistently by using massive c and b quarks in the shower. Sherpa is not only used to generate the hard process, but also for the complete event generation including the modelling of the underlying event.

For the generation of SM single top quarks in the t, Wt and s channels, as well as for $t\bar{t}$ events the Powheg [124] generator with the CT10 PDF set is used (Table 5.2). Powheg is a NLO matrix element generator and similar to Alpgen, it does not include the parton shower simulation. Therefore Powheg is interfaced to the Pythia [125] generator which is another LO generator similar to Sherpa. The parton shower and the underlying event were added using Pythia 6.4 and the Perugia2011C tune[2]. The $t\bar{t}$ cross-section is $\sigma_{tt} = 253$ pb. It has been calculated at next-to-next-to-leading order (NNLO) in QCD including resummation of next-to-next-to-leading logarithmic (NNLL) soft gluon terms with top++2.0 [28–30, 126–128]. The t-channel exchange of a virtual W boson has a predicted production cross-section of 87.8 pb [33]. The associated production of an on-shell W boson and a top quark (Wt-channel) has a predicted production cross-section of 22.3 pb [35] and the s-channel production has a predicted cross-section of 5.6 pb [34]. For these processes the theoretical uncertainties of 6 % for $t\bar{t}$ production and 5 % for single top-quark production are used [129].

Diboson events (WW, WZ and ZZ) are produced using Alpgen and Herwig [130] and the underlying event processes are produced with the Jimmy plugin [131]. The cross-sections and the k-factors for the diboson samples are given in Table 5.1. The uncertainty for these processes is 24 %. The 55% uncertainty

[2] In this context, the word tune means set of parameters

on W+HF given on Table 5.4 is due to assigning a conservative 50 % uncertainty on the heavy flavour plus 4% theory uncertainty and 24% per jet in the final selection (in this case only one jet); all three are added quadratically resulting a total of 55% uncertainty. The uncertainty on the W+LF is 24%.

	σ [pb]	k-factor	Generator	N_{MC}	Dataset ID
$W \to \ell\nu$	10 295	1.10	SHERPA	45 000 000	167742,167745,167748
$W \to \ell\nu$ b-filtered	140	1.10	SHERPA	45 000 000	167740,167741,167742
$W \to \ell\nu$ c-filtered	538	1.10	SHERPA	30 000 000	167741,167744,167747
$Z \to \ell\ell$	764	1.12	SHERPA	3 000 000	167751,167754,167757
$Z \to \ell\ell$ b-filtered	31	1.12	SHERPA	12 000 000	167749,167752,167755
$Z \to \ell\ell$ c-filtered	314	1.12	SHERPA	9 000 000	167750,167753,167756
WW	2.5	1.2	ALPGEN + HERWIG	255 000	107100
	1.2	1.2	ALPGEN + HERWIG	125 000	107101
	0.6	1.2	ALPGEN + HERWIG	60 000	107102
	2.5	1.2	ALPGEN + HERWIG	255 000	107103
	9.9	1.3	ALPGEN + HERWIG	995 000	110829
	5.0	1.3	ALPGEN + HERWIG	495 000	110830
	2.4	1.3	ALPGEN + HERWIG	235 000	110831
	1.3	1.3	ALPGEN + HERWIG	130 000	110832
WZ	0.8	1.3	ALPGEN + HERWIG	400 000	107104
	0.5	1.3	ALPGEN + HERWIG	260 000	107105
	0.3	1.3	ALPGEN + HERWIG	150 000	107106
	0.2	1.3	ALPGEN + HERWIG	95 000	107107
ZZ	0.6	1.4	ALPGEN + HERWIG	610 000	107108
	0.3	1.4	ALPGEN + HERWIG	290 000	107109
	0.1	1.4	ALPGEN + HERWIG	120 000	107110
	0.05	1.4	ALPGEN + HERWIG	60 000	107111

Table 5.1: Background MC samples used for the presented analysis. The "filtered" label indicates that in those samples, the events with $b(c)$ jets are kept. More than one cross-section value for diboson samples are due to the sub-processes that are involved. Each simulated process is assigned a dataset identification number (dataset ID) which are also given at the rightmost column.

The only background for which partially no simulated events are used, is the multi-jet background. This background consists of events with semileptonic b-quark decays, long-lived weakly decaying final states such as $\pi^{\pm}$ or K mesons, reconstruction of a π^0 shower as an electron, reconstruction of electrons from conversions or direct photons or other sources of misidentified electrons. The multi-jet events with one misidentified jet and one misidentified lepton can also pass the signal criteria. Although the double misidentification is unlikely, due to the large cross-section of multi-jet events they also appear as one of the major backgrounds in the analysis. Figure 5.6 shows the Feynman diagram of a typical mutli-jet process. The simulation of the multi-jet background is challenging for two reasons: first, this is the

	σ [pb]	Generator	N_{MC}	k-factor	Dataset ID
Wt all decays	22	POWHEG +PYTHIA	1 000 000	1.09	110 140
t-channel (lepton+jets) top	28	POWHEG +PYTHIA	5 000 000	1.05	110 090
t-channel (lepton+jets) anti-top	28	POWHEG +PYTHIA	5 000 000	1.06	110 091
s-channel (lepton+jets) top/anti-top	1.8	POWHEG +PYTHIA	5 000 000	1.06	110 119
$t\bar{t}$ all decays	114	POWHEG +PYTHIA	100 000 000	1.12	117 050

Table 5.2: Top quark event MC samples used for this analysis. The cross-section column includes k-factors and branching ratios.

dominant process at low energies and because of this, a large set of MC samples has to be produced in order to achieve enough statistically sufficient events in the signal region. This is almost impossible. The second reason is the complicated nature of the processes that are involved in this background. Furthermore, the estimation of amount of single, double and triple misidentification is difficult. Because of these reasons, different approaches than that of the other backgrounds presented here are employed to produce a sample for this background. In the analysis presented here, several multi-jet background estimation methods are tested and their performance is studied in detail. Therefore, a dedicated chapter is spared to explain the studies that are performed on this background. The details of the techniques used for the multi-jet background sample production are given Chapter 8.

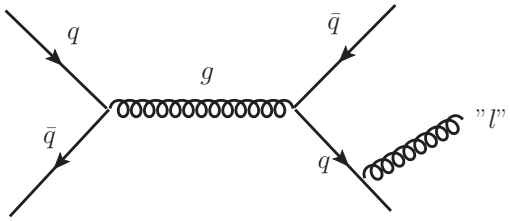

Figure 5.6: Feynman diagram of a multi-jet process. Two quarks interact where a gluon is produced. The gluon decays into another quark-antiquark pair where one of the quarks radiate a gluon which is later misidentified as a lepton.

5.3.1 Signal

There were various analyses published by the ATLAS collaboration for FCNC searches involving top quarks such as the one presented here. Up until the 8 TeV analyses, the signal MC was produced by a LO generator PROTOS [132] such as the similar study performed with data from 7 TeV collisions [83]. In this analysis, as well as the analysis that used 14 fb^{-1} data from 8 TeV collisions [133], which was published as a conference note, a relatively recent generator called METOP [47] is used for simulating strong FCNC processes at the NLO approximation. METOP introduces strong top-quark FCNC interactions through two different effective operators enabling it to generate several event topologies including the direct single top-quark production, top+gluon and top+light quark production as described earlier. This allows for the investigation of $2 \rightarrow 2$ processes in combination with the formerly used (LO) direct FCNC single top-quark production process. To generate Monte Carlo (MC) samples with METOP, one has to choose values for the coupling constants κ_{ugt} and κ_{cgt}. Compared to PROTOS, a more straightforward

parametrisation of the coupling constants is used in MEtop. The full strong FCNC Lagrangian as it is used in the package is

$$\mathcal{L}_S = co1\, O_{uG} + co2\, O_{cG}\,, \tag{5.1}$$

where

$$O_{uG} = i\frac{g_s}{\Lambda}\,\bar{u}\,\lambda^a\,\sigma^{\mu\nu}\,(f_u + h_u\gamma_5)\,t\,G^a_{\mu\nu} \text{ and } O_{cG} = i\frac{g_s}{\Lambda}\,\bar{c}\,\lambda^a\,\sigma^{\mu\nu}\,(f_c + h_c\gamma_5)\,t\,G^a_{\mu\nu}\,. \tag{5.2}$$

The parameters $co1$ and $co2$ hence directly represent the coupling constants $\kappa_{gut}/\kappa_{gct}$, f_q/h_q are real constants to be chosen to define different chiralities. For the generated samples, the most conservative assumption of a purely left-handed top-quark production like in the SM was chosen. Allowing for right-handed contributions would give rise to additional shape differences of the FCNC signal in comparison to the SM top-quark production. The polarisation of the produced top quarks is reflected in particular in the angular distributions of their decay products and hence any deviation from purely left-handed production would lead to higher separation power of the trained neural network. Two samples are generated, one for $ug \to t$ and the other for $cg \to t$. The parameters for the coupling constants κ_{ugt} and κ_{cgt} are set to 0.01, to represent values close to the currently existing limits. The corresponding cross-sections times the branching ratio ($\mathcal{B}$) of the leptonic decay obtained with these coupling values are listed in Table 5.3. It has been verified in [134] that the kinematic shapes of both samples are independent of the choice of the coupling constants by comparing the kinematic distributions of samples, generated using different choices for κ_{ugt} and κ_{cgt} with values 0.002 to 0.05. As motivated in the previous section the top quark is assumed to decay as in the SM. All the leptonic decay modes of the W boson are considered and no hadronic decay mode is taken into account. The CT10 [122] parton distribution function (PDF) sets are used with the MEtop generator. All signal events are hadronised with Pythia 6.421 [125] and the corresponding P2011C tune [135] to the ATLAS data is used. The masses of the top quark, W boson and Z boson are set to 172.5 GeV, 80.403 GeV and 91.187 6 GeV, respectively.

	t	$\bar{t}$	Total
$ug \to t$	3.41 pb	0.76 pb	4.17 pb
$cg \to t$	0.48 pb	0.45 pb	0.93 pb

Table 5.3: Generated cross-sections times branching ratio for the channels $u(c)g \to t$, determined using the MEtop generator. The given cross-sections times branching ratios consider the top quark decaying into a W and b and the leptonic decay of the W.

The data events typically contain more than one proton–proton collisions. This is because the bunches are very dense and when an event is triggered, there are already several other collisions taking place in the same time window. This phenomenon is called pile-up and this has to be taken into account as well during MC production. For the pile-up simulation, Pythia8 [136] minimum bias events (see Section 6.2.3) are used. The variable pile-up rate was based on a guess of the accelerator performance and is depicted in Figure 5.7 compared to the distribution (rescaled by 0.9) obtained from observed events in the final data sample from 2012 pp collisions. To account for the difference all MC samples are reweighted using these two histograms using the standalone `PileupReweighting` tool [137].

5.4 Summary on uncertainties on the background processes

Table 5.4 summarises the normalisation uncertainties for all considered background processes as described earlier and in Section 5.3. The derivation of the multi-jet background normalisation uncertainty (17 %) is

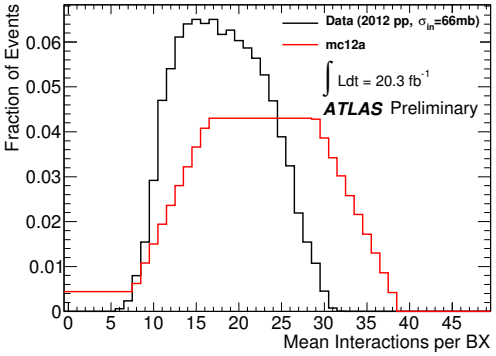

Figure 5.7: Average number of interactions per bunch crossing (μ) used in the MC production (red) and obtained in the observed events (black) [138].

explained in Section 10.3.

Process	Relative uncertainty
Single top	5 %
$t\bar{t}$	6 %
W+LF	24 %
W+HF	55 %
Z+jets/diboson	24 %
Multi-jets	17 %

Table 5.4: Summary of the uncertainties on the background estimations.

CHAPTER 6

Reconstruction of Physics Objects

As discussed in Section 4.2, the purpose of the ATLAS detector is to detect, distinguish and identify the vast amount of particles created in the proton-proton collisions provided by the LHC at the interaction points located in the center of the detector.

The first step in order to be able to identify the particles relies on the information gathered from the raw data provided by the different components of the detector.

This information is then processed in order to form the physics objects relevant to the analysis presented in this thesis. The typical physics objects, which are the outcome of the FCNC interactions described in Chapter 3, are electrons, muons, missing tranverse momentum due to a neutrino from the leptonic decay of the W boson and the jets originating from b-quarks. These physics objects have to be identified and reconstructed using the data provided by the ATLAS detector. They are constructed using higher-level information gathered in the detector, such as tracks of the charged particles left in the ID, tracks in the Muon Spectrometer, energy deposits in the ECAL and HCAL, and the vertices where the interaction of the incoming particles occur. This chapter provides an overview of these fundamental objects as well as the physics objects derived from them which are relevant to this analysis. Figure 6.1 demonstrates how different particles leave their signatures inside ATLAS and how each component of the detector work together to identify these particles.

6.1 Fundamental Objects

6.1.1 Tracks

Tracks are reconstructed trajectories of the charged particles passing through the in the ID and the Muon Spectrometer. They are crucial for the identification and the reconstruction of the electrons and muons and they also play an important role for identifying the jets originating from a b-quark.

In the ID, the charged particles pass through the Pixel Detector, SCT and the TRT sub-components and follow bent trajectories due to the strong magnetic field provided by the Solenoid Magnet, forming helix structures. At the Pixel and SCT, the trajectories are composed of *hits*, when a signal is registered in the pixels or strips, respectively. At the TRT, the hit equivalents are the *drift circles* created in the ionized gas by the charged particles passing through the straw tubes.

In the Pixel Detector, the charged particles usually create not only a single hit for a given layer but a group of hits in the neighbouring elements of that particular layer. Therefore, the raw hits are first combined into objects named clusters. Clusters are then used to form three-dimensional (3D) space points in order to reconstruct the trajectories of the passing particle.

In the SCT, the clusters of hits can only give precise information in the $r - \phi$ plane. To be able to have a precise information on the z-coordinate of the trajectory, the cluster pairs of hits from both sides of the double-sided SCT module are used.

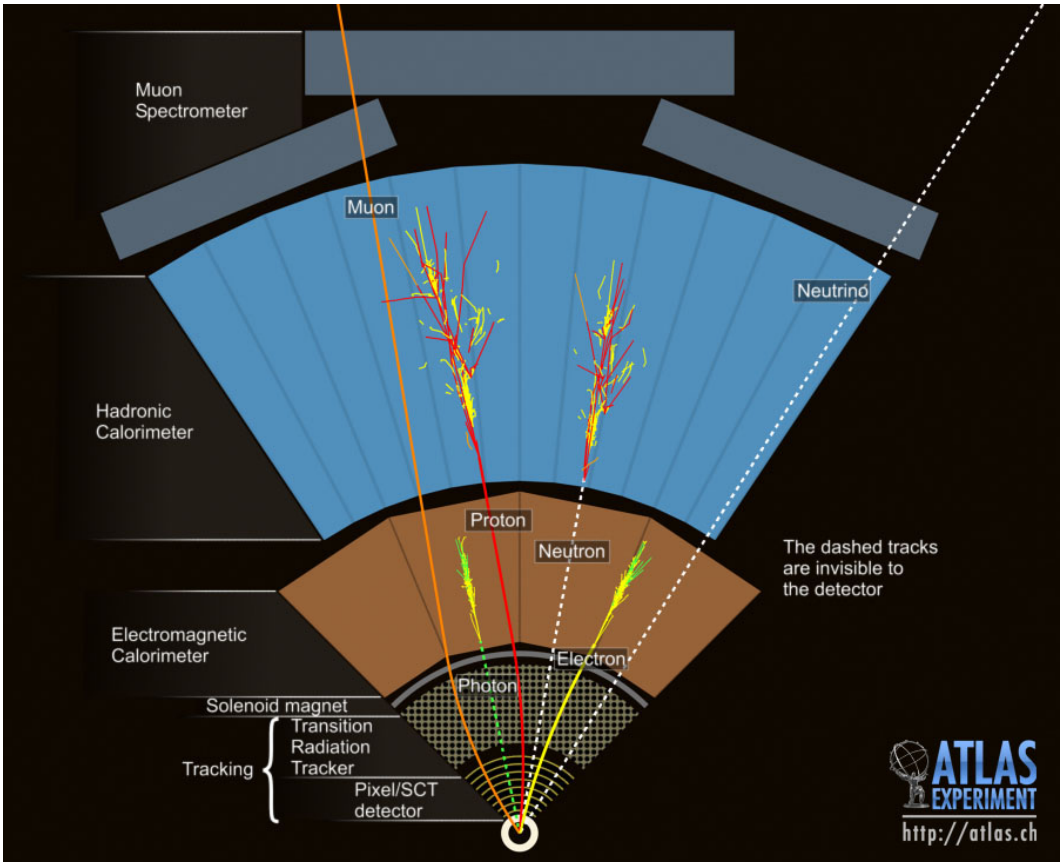

Figure 6.1: A schmatic of the cross-sectional view of the ATLAS detector [139]. The illustration of the different particles and their corresponding signatures in the sub-components of the ATLAS detector is shown.

The reconstruction of the particle trajectories is done by using the so-called iterative track reconstruction chain [140]. As a first step of the iteration, all the possible combinations of 3D space points are used to construct track seeds. Combination of the points is done using a Kalman Filter [141] which starts from the inner-most point, developing outwards in a progressive manner. The trajectories of the track candidates are extrapolated along the direction of the candidate track and new points are searched in the vicinity of the path of the extrapolated trajectory. As new points are found along the trajectory, they are added to the track candidate, therefore elongating it. The track candidates are later scored based on

several parameters such as the length of the track candidate and the number of points it contains. Sorting is necessary in order to separate the track candidates that overlap with each other and to remove the badly reconstructed track candidates e.g. too short tracks. The remaining tracks are then extrapolated to the TRT. These track candidates are then refitted, this time using all three components of the TRT. However, the hits in the TRT are used in the fit only if they improve the fit quality, nevertheless they are still associated to the track. This step then completes the inside-out sequence of reconstruction. Finally, an outside-in sequence fit is performed using the remaining hits in order to reconstruct tracks that originate from secondary vertices.

6.1.2 Calorimeter clusters

In the context of ATLAS calorimetry, a cluster is a group of calorimeter cells which has received energy depositions from a passing-through particle. Clusters are used to identify and reconstruct electrons, photons, jets and missing transverse momentum as well as measure their energy.

ATLAS uses two different algorithms for clustering of the calorimeter cells, namely the topological clusters and the sliding window techniques [142]. Initially, both of the algorithms form towers from the cells that receive energy depositions along the path of the particle. Towers are longitudinal windows perpendicular to the $\eta - \phi$ plane. If a cell is used by two different towers, its energy is shared between the towers depending on the area of the cell occupied by those towers.

In the sliding window algorithm, a fixed size rectangular window is moved from one tower of energy deposit to the other. In each step, the transverse energy within the window is measured. If the energy within the window is above a certain threshold $E_{\mathrm{T}}^{\mathrm{thresh}}$ and if a local maximum is measured among the towers neighbouring each other, then a cluster is formed.

The sliding window algorithm is fast and very precise for the identification of smooth energy deposits; therefore it is mostly used in the ECAL for the electron and photon identification. It is also used in τ-lepton identification as well as in jet finding algorithms by combining the information from the HCAL.

The topological cluster algorithm is used both in the ECAL and the HCAL. It starts with a set of seed cells in which the signal-to-noise ratio is typically greater than 4. It then scans the neighbouring cells and adds them to the original set of cells if the neighbouring cells have a signal-to-noise ratio greater than 2. The cluster is formed by merging the seed cells with the cells surrounding them if they satisfy the signal-to-noise ratio requirement. If the signal-to-noise ratio of the cells that lie between two separate clusters is at an intermediate level (i.e. between 2 and 4) then the two clusters can be merged. Increasing the signal-to-noise ratio requirement for the peripheral cells can significantly reduce the noise thus making the topological cluster algorithm suitable for the hadronic jet reconstruction with various energy deposit patterns as well as for reconstruction of the missing transverse momentum.

6.1.3 Vertices

The vertex in this context is the point where two or more tracks cross each other. Vertices are either the interaction points of the colliding protons (primary vertex) or the points where the long-lived particles decay (secondary vertex).

Accurate reconstruction of the tracks leads to a precise measurement of the location of the vertices. This is very important since the primary vertex plays a vital role in suppressing the pile-up events. The primary and the secondary vertices are also used the in determining the types of the particles. The distances between the primary and secondary vertex is directly related to the lifetimes of the hadrons. For instance the vertex information is imperative for identifying the flavour of quarks.

The information for the vertex reconstruction is provided solely by the Inner Detector. The algorithms that are utilized for the primary vertex reconstruction[143] work as follows: a collection of tracks is used to form the vertex seeds using the tracks with transverse momentum of $p_{\mathrm{T}} > 150$ MeV. These tracks are required to be reconstructed from at least six hits in the SCT and Pixel Detector and at least four of these six hits should be in the SCT. In order to remove the tracks originating from secondary vertices, the transverse impact parameter of the track is required to be $|d_0| < 4$ mm and its uncertainty $\sigma(d_0) < 5$ mm. The uncertainty on the longitudinal impact parameter is required to be $\sigma(z)_0 < 5$ mm. Later the *adaptive vertex fitting* algorithm[144], which is a χ^2-based algorithm, is used to determine the vertex position. The algorithm uses the vertex seed location and the tracks in the vicinity of the seed. The tracks are weighted depending on how compatible they are with a vertex candidate. If the mismatch between the track and the vertex seed is more that 7σ, the track is used to seed a new vertex. This procedure continues until no new vertices are found or no tracks are left.

6.2 Reconstruction of physics objects

The next step after reconstructing the tracks, calorimeter clusters and vertices, is to reconstruct the actual physics objects which form the basis of the physics variables relevant to the analysis presented here.

6.2.1 Electrons

In ATLAS, the reconstructed electrons are first counted as electron candidates. During their reconstruction, the efficiency is taken as the priority aspect in order to be able to cover all possible real electrons. They are reconstructed based on very loose identification criteria, therefore containing significant amount of fake electrons i.e. other physics objects mistakenly identified as electrons. The reconstructed electron candidates are then subjected to a set of identification criteria to be able to suppress the fake electron content. The electrons considered in the analysis presented here originate from a primary vertex, therefore other real electrons originating from different sources are considered as background as well. The sources of those electrons that are not originating from a primary vertex can be photon conversions and the semileptonic decays of charm or bottom hadrons. Reference [145] details the ATLAS software used in the reconstruction and identification of electrons.

The electron definition adopted in this analysis uses the recommendations given in Reference [146].

Trigger Signature and Reconstruction

The reconstruction of the electron candidates starts already during data taking. The ECAL is a crucial component of the ATLAS detector for the reconstruction and identification of the electrons. At L1, a *quick-and-dirty* selection of electron candidates is made by requiring an energy deposition of $E_{\mathrm{T}} > 30\,\mathrm{GeV}$ or $E_{\mathrm{T}} > 18\,\mathrm{GeV}$ and an additional isolation of the electron. Later, at L2 and EF, the tracks from the inner detector and the EM clusters are roughly matched. At this point the electron candidates should have at least 60 GeV transverse energy or at least 24 GeV transverse energy with the following condition: the ratio of total transverse momenta of the tracks in the vicinity of the electron candidate (within a cone of $\Delta R < 0.2$) and the transverse energy of the electron candidate should be $\sum P_{\mathrm{T}}^{\mathrm{tracks}}/E_{\mathrm{T}}^{\mathrm{el}} < 0.1$. So far, only events with a high probability of containing an electron are selected. The actual reconstruction and identification of electrons is detailed in the following. The reconstruction of the electron candidates is performed offline. During reconstruction, electron candidates only at the central region ($\eta < 2.47$) are considered. The sliding window algorithm described in Section 6.1.2 with a window dimension of 3×3 in the $\eta \times \phi$ plane is used to determine the electron cluster seeds. Each seed is required to have an energy

deposit of at least 2.5 GeV. The electron cluster seeds and the reconstructed tracks (detailed in Section 6.1.1) are matched by extrapolating the tracks to the ECAL and checking if they overlap with each other in an angular region of 0.005 in $\delta\eta$ and $\delta\phi$. The tracks lose energy due to bremsstrahlung while passing through the magnetic field and because of this, their paths are bent further. In order to account for this bending, the track and EM cluster seed matching criteria is relaxed to $\delta\phi < 0.1$ in the direction of the bending. If there is more than one track satisfying the matching criteria, the one with the best match is taken.

After the matching of tracks to the EM clusters, the energy of the EM cluster is re-calculated, this time with a broader window size (endcap: 5×5 cells and barrel: 3×7 cells) in order to account for the energies deposited outside the sliding window. After adding this energy to the cluster, the energy obtained is then used as the energy of the electron.

While the ECAL provides a very good measurement of the energy of the electron, the direction of the electron is mostly based on the information from the inner detector. Hence the transverse momentum of the electron candidates is measured using both detector subcomponents:

$$p_{\mathrm{T}} = \frac{E(\text{EM cluster})}{\cosh \eta(\text{track})}$$

where E(EM cluster) is the energy deposited to the EM cluster by the electron candidate and $\cosh \eta$(track) is the hyperbolic cosine of the η of the associated track.

Identification

In order to purify the electron sample, the reconstructed electron candidates are subjected to further selection criteria. The electrons have exceptionally high identification efficiency. However, in addition to the real electrons, many background electrons, as well as different objects (such as jets) are incorrectly identified as electrons as well. In order to suppress the fake electrons, a set of cuts in three steps are applied:

- **Loose:** This selection implies cuts on the shower shape variables of the middle layer of the ECAL as well as restrictions on the amount of energy deposit leakage to the HCAL in the longitudinal direction.
- **Medium:** At this step the ECAL is required to have energy deposition at the innermost layer. A better match is required between the track and the EM cluster and the associated track is required to have higher number of hits in the SCT and the Pixel.
- **Tight:** Agreement between the energy of the EM cluster and the momentum of the track is required. A portion of the hits in the TRT are required to be high threshold in order to suppress against pions and muons (see Section 4.2.3). Additional quality cuts which are detailed in Reference [145] are also applied.

The above sets of cuts are applied successively and inclusively i.e. the medium criteria is applied only if loose criteria are already applied. In this analysis electrons passing the tight criteria are used.

Isolation requirements

The electrons in this analysis are high p_{T} electrons and as discussed in Chapter 3, they are associated with a W boson. These electrons usually occur isolated from other objects in the event such as jets. However,

background objects such as electrons from a semileptonic decay of heavy flavour quarks, hadronic jets which are faking an electron, or electrons from pile-up events tend to appear together with other objects. Therefore, isolation criteria are applied both on the deposited transverse energy of the electron in the ECAL and on the transverse momentum of the associated track in order to suppress these backgrounds from the signal electrons[1]. The transverse energy deposited in the ECAL around the electron inside a cone of radius 0.2 in the $\eta - \phi$ plane is not allowed to exceed a certain value [146]. A similar requirement on the transverse momentum of the associated tracks is also applied within a cone of radius 0.3 around the electron track. The isolation requirement on the deposited transverse energy is adjusted in order to achive a uniform isolation efficiency of 90% across the η of the energy cluster. This is called the working point `EtCone20@90` (ECAL isolation within a cone of radius 0.2 with 90% efficiency). Similarly, the requirements on the transverse momentum of the track are tuned to achieve a uniform isolation efficiency of 90% in p_{T} which is called the `PtCone30@90` (track isolation within a cone of radius 0.3 at 90% efficiency). The working point `EtCone20@90` is later corrected for the energy leakage into the isolation cone and for pile-up effects.

Efficiency correction factors, energy calibration and resolution

The MC simulations have to be able to represent the inefficiencies that exist in data. The inefficiencies typically arise during electron trigger, reconstruction, identification and isolation of the electron. These inefficiencies are estimated in the form of correction factors and then applied to the MC. $Z \to e^+e^-$ and $J/\psi \to e^+e^-$ events in the full 20.3 fb^{-1} 8 TeV ATLAS data [147] are considered to obtain the correction factors using a tag-and-probe method [148]. The reconstruction and identification correction factors are measured in bins of transverse energy and pseudo-rapidity of electron. The combined reconstruction and identification efficiency is around 92% for the loose selection and around 68% for the tight selection. Figure 6.2 shows the combined reconstruction and identification efficiencies in bins of transverse energy and pseudo-rapidity of the electron for various selection criteria.

The efficiencies and correction factors for electron isolation and trigger are derived only from $Z \to e^+e^-$ events. They are calculated in bins of transverse momentum and pseudo-rapidity of the elecron (9 and 12 bins in η and E_{T} for the isolation; 9 and 15 bins in η and E_{T} for trigger). A set of trigger efficiencies are obtained for each different run period.

$Z \to e^+e^-$ events are used also to obtain correction factors on the scale of the energy of clusters in the ECAL (electron energy scale). The correction factors are obtained using two different methods, namely the template method and the likelihood fit, which are detailed in Reference [149] where both methods employ the invariant mass of the reconstructed Z-boson distribution from $Z \to e^+e^-$ events as the basis of the extraction technique. Figure 6.3(a) shows the invariant mass of the e^+e^- system from the Z-boson decays for data and MC before and after the obtained correction factors are applied. A near perfect agreement is observed between data and the MC after the corrections. In order to cross-check the validity of the used technique, $J/\psi- > e^+e^-$ events are employed. Figure 6.3(b) shows the reconstructed invariant mass of the e^+e^- system in J/ψ resonance. Similarly, a very good agreement is observed.

The energy resolution in the ECAL is measured by comparing the data and MC simulations again using the invariant mass of the $Z \to e^+e^-$ events. The resolution is parametrized as follows:

$$\left(\frac{\sigma_E}{E}\right)^{\mathrm{data}} = \left(\frac{\sigma_E}{E}\right)^{\mathrm{MC}} \oplus c \tag{6.1}$$

where the terms on the right hand side are the sampling term and constant term, respectively. The value of

[1] From now on, the term signal indicates "used in this analysis" if not specified otherwise.

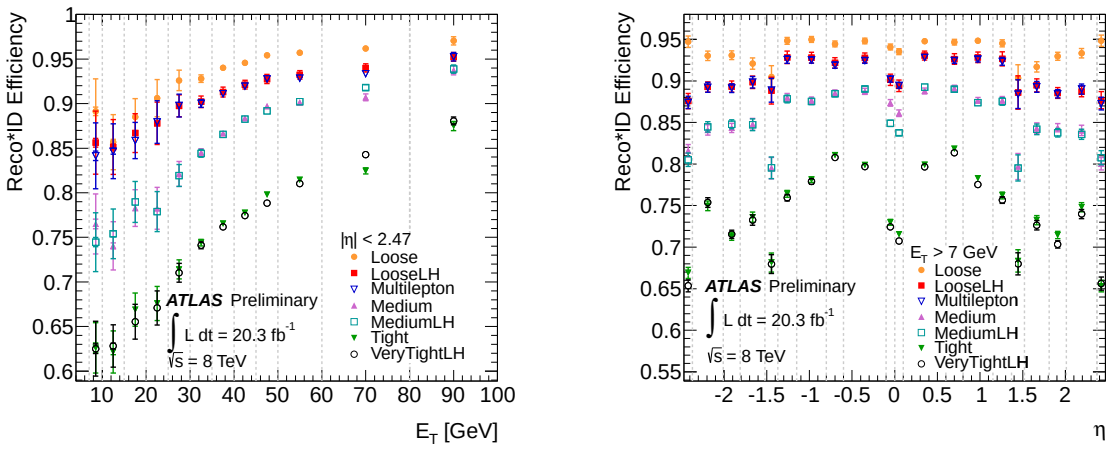

(a) (b)

Figure 6.2: The combined efficiencies of the electron reconstruction and identification in bins of (a) electron transverse momentum and (b) pseudo-rapidity for several different selection criteria [147]. The tight selection is used in this analysis. The efficiencies are derived before the isolation requirement is applied.

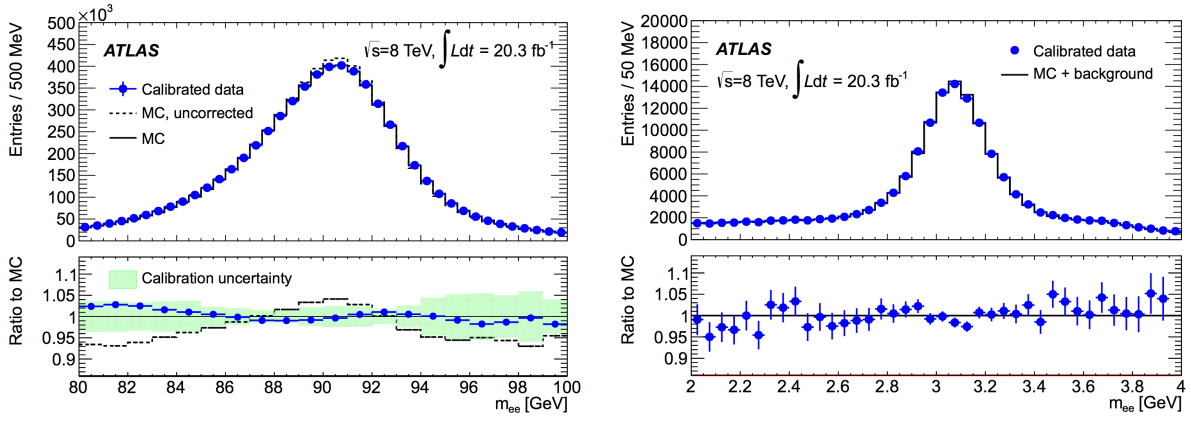

(a) (b)

Figure 6.3: The invariant mass of the e^+e^- system from (a) the Z-boson decay and (b) the J/ψ resonance decay for data and MC before and after the electron energy scale corrections applied [150].

the sampling term is obtained from the simulations with 10% uncertainty. The derivation of the value of the constant term c is very similar to that of the derivation of the electron energy scale, where again two methods are used, namely the template method with varied c values and a likelihood fit method [149].

6.2.2 Muons

The reconstruction and the identification methods of the muons are in some ways similar to those that were described for the electrons and in others are different. While the similar points will be mentioned briefly, the main focus in the following will be on the different techniques used in the muon reconstruction and identification.

Reconstruction, identification and isolation

Similar to the electrons, the muons are reconstructed as candidates before they pass a certain set of identification criteria. For the muons used in this analysis, the most relevant components of the ATLAS detector are the Muon Spectrometer and the Inner Detector, while there are other muon reconstruction algorithms which employ the ECAL information as well. Extensive information about the muon reconstruction algorithms can be found in the Reference [151] and [152], while here only the relevant parts will be discussed.

Possible muon events are triggered online by requiring a track in the muon spectrometer with $p_{\mathrm{T}} > 15$ GeV at L1 trigger stage. Later, at the L2 stage, a rough matching to an Inner Detector track is required. At the EF level, two different trigger techniques are employed. The first one requires an online reconstructed muon with rather high transverse momentum ($p_{\mathrm{T}} \geq 36$ GeV) and the second one requires an online reconstructed muon with $p_{\mathrm{T}} > 24$ GeV and an isolation around the muon within a cone of radius of 0.2. The sum of the transverse momenta of the tracks in the cone, except the muon itself, divided by the transverse momentum of the muon should be less than 0.12.

The offline reconstruction of the muon candidates begins by first checking hits in the Muon Spectrometer. Not only muons but sometimes other particles such as charged pions can reach the Muon Spectrometer and may leave hits in the inner layers. Therefore, the muon track reconstruction in the Muon Spectrometer starts from the outermost layer. The hits which are used as seeds for the tracks are found by a pattern recognition algorithm. Starting from the outermost chamber, a track segment is formed for each chamber. Later the track segments are combined with each other to construct the whole track in the Muon Spectrometer. The tracks in the Muon Spectrometer are extrapolated to the Inner Detector to check if there are matching tracks. If the two tracks, one from the Muon Spectrometer and one from the Inner Detector match, they are combined. If there are more tracks in the Inner Detector within the vicinity of the extrapolation, a χ^2 fit is performed to choose the best matching one. After the matching, a global fit using the hits along the path of the two tracks is performed to finally reconstruct the combined muon track candidate. This muon reconstruction is called the combined (CB) algorithm.

Loose, tight and medium identification criteria, similar to that of the electron, are employed to have a control over the background rejection and muon identification efficiency. The loose criteria combine all the muon candidates reconstructed from all the available reconstruction algorithms[2]. The medium criteria accept muons only from certain reconstruction algorithms including the CB algorithm. Finally, the tight criteria accept muons only if they are reconstructed with the CB algorithm. This analysis uses the tight definition for the muons.

A series of additional quality cuts are applied on the identified muons: there has to be at least one hit in the Pixel Detector belonging to the muon track and at least 5 hits in the SCT. For the TRT, if the track

[2] Here, the only reconstruction algorithm that is mentioned is the one that is taken as basis for this analysis.

is in the TRT coverage then at least six hits are required else the requirement on TRT is dropped. Lastly, a primary vertex that can be associated to the muon track ($z_0 < 2$ mm) must exist.

In order to distinguish the signal muons from muons coming from other sources such as heavy quark decays, an additional isolation requirement is performed in addition to the online isolation. The so-called mini-isolation [153] requirement is imposed to reduce the contribution of the background muons. The isolation defines a varying cone radius as a function of the lepton p_{T} in order to improve the pile-up robustness and performance in boosted signal event topologies. The mini-isolation variable is defined as the scalar sum of the transverse momenta with p_{T} above 1 GeV from all tracks (except the one matched to the muon) within a cone with radius

$$R_{\mathrm{iso}} = \frac{10\ \mathrm{GeV}}{p_{\mathrm{T}}(\mu)}. \tag{6.2}$$

Muons are accepted if the mini-isolation divided by the muon p_{T} is less than 0.05.

In addition, an overlap removal between jets and muons is applied, removing any muon whose momentum direction is within a $\Delta R < 0.4$ cone of a jet with $p_{\mathrm{T}} > 25$ GeV and jet vertex fraction (see Sec. 6.2.3) |JVF| > 0.5 (for jets with $p_{\mathrm{T}} < 50$ GeV).

Efficiency correction factors, momentum calibration and resolution

A tag-and-probe approach is used in $Z \to \mu\mu$, $J/\psi \to \mu\mu$ and $\Upsilon \to \mu\mu$ events in data in order to determine the efficiencies of reconstruction and isolation in a way similar to that of electrons [154]. The efficiency correction factors are obtained to account for the differences between data and MC. The reconstruction efficiencies are measured to be ~99 % with an uncertainty of 0.25% and the isolation efficiency is ~ 97% with an uncertainty of 2%. The Figure 6.4 shows the reconstruction efficiencies for different algorithms as a function of the muon pseudo-rapidity and the transverse momentum.

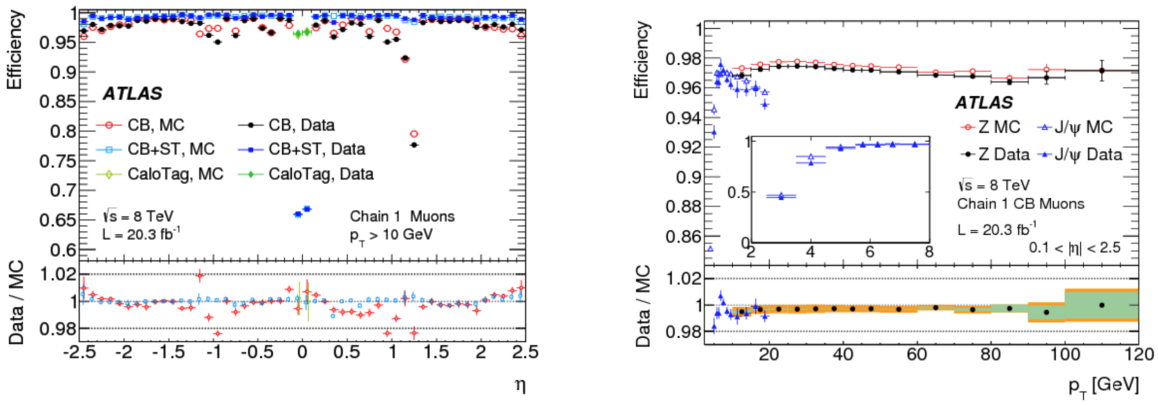

(a) (b)

Figure 6.4: Muon reconstruction efficiency as a function of η (a) measured in $Z \to \mu\mu$ events for muons with $p_{\mathrm{T}} >$ 10 GeV for different muon reconstruction types and as a function of p_{T} (b) [147]. In the latter one only the CB algorithm is shown.

The invariant mass distributions of the $\mu\mu$ system from the Z, J/ψ and the Υ are used to derive the muon momentum scale correction factors. As for the electrons, the correction factors are obtained using a similar template method. Several sets of MC simulations are produced with different Z masses and correction parameters and the one that describes the data best is chosen using a binned likelihood fit.

Figure 6.5 shows the invariant mass distributions before and after the muon momentum scale corrections are applied.

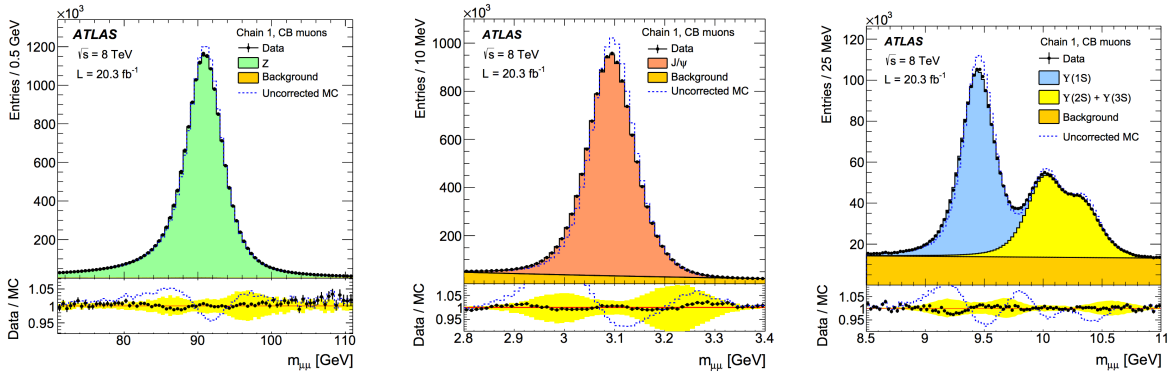

(a) (b) (c)

Figure 6.5: The invariant mass distribution of the $\mu\mu$ system from (a) the Z-boson decay and (b) the J/ψ resonance decay and from (c) the Υ decay for data and MC before and after the muon momentum scale corrections applied [154].

The muon momentum resolution is calculated with the formula:

$$\frac{\sigma(p_{\mathrm{T}})}{p_{\mathrm{T}}} = \frac{r_0}{p_{\mathrm{T}}} \oplus r_1 \oplus r_2 \cdot p_{\mathrm{T}} \tag{6.3}$$

where the first term on the right hand side (inversely proportional to p_{T}) corresponds to the loss of energy through the traversed material, the second term (constant in p_{T}) accounts for multiple scattering and impurities in the local magnetic field and the third term (proportional to p_{T}) corresponds to the residual misalignment and intrinsic detector resolution. The resolution is then measured in bins of p_{T} and pseudo-rapidity or as a function of p_{T} and pseudo-rapidity Its value is lowest at low p_{T} (<100 GeV) and low $|\eta|$ (<1) and is measured to be 1.2 % and highest at high p_{T} (>100 GeV), and at high $|\eta|$ (>1) where it is 3%.

6.2.3 Jets

Particles that carry a colour charge cannot propagate singly and cannot be detected directly due to the colour confinement phenomenon as discussed in Section 2.3.2. The colour carrying particles produced in the proton–proton collisions in LHC almost instantly form hadrons. These hadrons then penetrate into the ECAL and HCAL, and deposit their energies in the form of parton showers which then form the calorimeter clusters detailed in Section 6.1.2. If the deposit of the energy in the calorimeters can be associated with a parton shower, these objects are called jets[3]. In this section the reconstruction and identification algorithms of the jets and their energy resolution and calibration measurements will be discussed.

[3] Sometimes the showers in the calorimeter originating from a lepton can also be called a jet. In this thesis the term jet indicates that it has a hadronic origin.

Reconstruction and identification

Although many jet reconstruction algorithms exist, the anti-k_{T} algorithm [155] is by far the most commonly used algortihm in ATLAS analyses and it is also the adopted algorithm here.

Every component of ATLAS detector plays a role in jet reconstruction in one way or another, but the most crucial components are the ECAL and HCAL. The building blocks of the jets are the calorimeter clusters. A distance parameter $d_{i,j}$ is defined between two calorimeter clusters i and j as follows:

$$d_{i,j} = \min\Big(\frac{1}{p^2_{\mathrm{T},i}}, \frac{1}{p^2_{\mathrm{T},j}}\Big)\frac{\Delta R^2_{i,j}}{R^2} \tag{6.4}$$

where $p_{\mathrm{T},i,j}$ are the transverse momenta of the two clusters, R is the distance parameter which controls the width of the jets and their distance from each other and $\Delta R^2_{i,j} = (y_i - y_j)^2 + (\phi_i - \phi_j)^2$ where y is the rapidity. Here, the value of R is set to 0.4.

The anti-k_{T} algorithm then searches for the smallest distance ($d_{i,j}$) between two clusters and merges them until the smallest distance is greater than d_{iB} where d_{iB} is the distance to the beam for the object i and is defined as $d_{iB} = 1/p^2_{\mathrm{T},i}$. When $d_{i,j} = d_{iB}$ is reached, the cluster i (which is now usually composed of more than one cluster) is removed from the list of clusters to be used for jet finding and labeled as a jet candidate unless its $p_{\mathrm{T}} < 7$ GeV. The algorithm then runs again with the remaining clusters until no single cluster is left. When the algortihm ends, a list of jet candidates is created per event. The jet candidates are later subjected to a series of quality cuts in order to reject leptons faking jets, showers originating from cosmic rays and beam-pipe interactions.

One quality criterion that is commonly used with jets is the so-called jet vertex fraction (JVF). It is a measure of how likely it is for a jet to actually originate from a primary vertex. It is also an effective way of rejecting jets originating from pile-up events. It is defined as follows: within a cone of radius $\Delta R = 0.4$ around a given jet, JVF is the ratio of the momenta of the tracks associated to a primary vertex i divided by the momenta of all the tracks in the cone:

$$\mathrm{JVF} = \frac{\sum_i p_{\mathrm{T}}(\mathrm{track}_i)}{\sum_j p_{\mathrm{T}}(\mathrm{track}_j)}, \tag{6.5}$$

where the track_i are the tracks that are associated with the vertex i within the cone ΔR and track_j are all the tracks inside the cone ΔR.

The JVF requirement is only applied on jets with $p_{\mathrm{T}} < 50$ GeV, as jets with higher p_{T} are very unlikely to originate from pile-up events. In this analysis a cut on JVF > 0.5 is required.

Furthermore, jets are rejected if the distance ΔR between them and an electron is less than 0.2. However if there is more than one jet within $\Delta R < 0.2$ to an electron, then only the closest jet is rejected. This requirement is applied because it is very likely that the jet candidate and the electron are actually the same object.

The jets that are reconstructed successfully but originate from different sources than proton–proton collisions are called *bad jets*. There are various sources of them, such as cosmic rays and beam induced backgrounds which originate from the interaction of the beam and the gas atoms in the beam pipe. Bad jets are detected based on several criteria. They usually have a different direction than that of the jets that actually originate from proton–proton collisions. They are not associated with a track. Their timing information is not compatible with a given proton–proton collision.

Efficiency correction, energy calibration and resolution

The effect of the JVF requirement on the efficiencies in data and MC is observed to be different [156]. Therefore, correction factors are derived to account for the differences in data and MC using a tag-and-probe technique obtained from $Z + ee$ + jets and $Z + \mu\mu$ + jets events.

However, the efficiency of jet reconstruction is almost identical for data and MC except for the very low p_{T} jets [157]. These jets are excluded from this analysis (See Section 7.3), therefore no special correction factor for the efficiency differences between data and MC for the jet reconstruction is applied.

Besides the efficiency correction, a series of calibrations and additional corrections are applied on the jet and its energy scale (JES) [158]:

- **Jet direction:** The direction of the jet is recalculated after associating the jet to a primary vertex from a hard collision.
- **Pile-up correction:** The amount of transverse energy originating from a pile-up event but still associated to the jet needs to be subtracted. In order to estimate the average pile-up contribution, comparisons to a set of minimum bias collision data in which the bunch crossings are rather separated to minimize the effect from the pile-up is made.
- **Energy correction:** The information from the PYTHIA inclusive QCD truth jet samples is used to derive a calibration to correct the energy scale of the jets. The calibration accounts for the energy loss in dead material, the showers depositing energy outside the calorimeters, the energy deposits below the threshold energy of the calorimeter cells to suppress noise and energy measurement differences between the HCAL and ECAL. The calibration is done in a E_{T} and η dependent manner. Figure 6.6 shows the jet energy response as a function of detector η_{det} (η measured with respect to the center of the detector) for various energy scales.

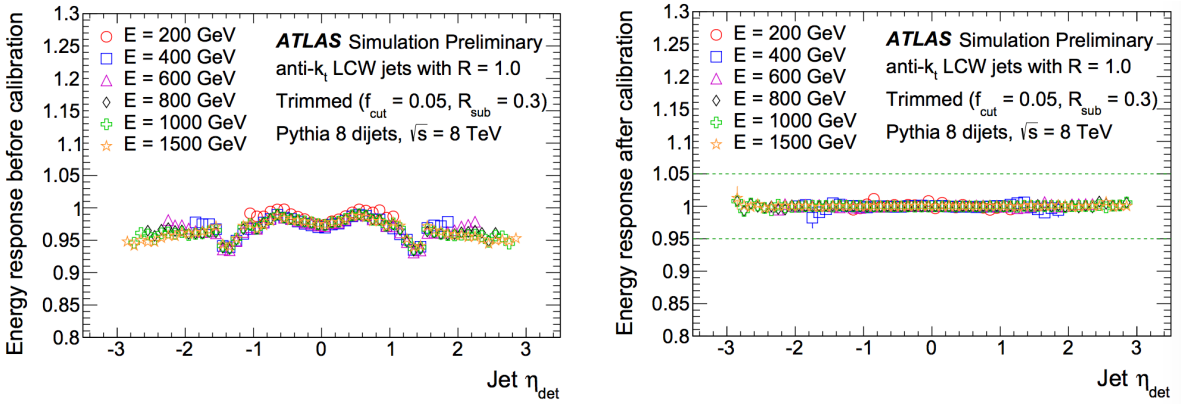

(a) (b)

Figure 6.6: The jet energy response as a function of η_{det} for various energy scales before (a) and after (b) the JES calibration [158]. The response is almost perfectly flat for the entire η_{det} range for all the energy scales after the corrections are applied.

The jet energy resolution (JER) is parametrized as follows [157]:

$$\frac{\sigma(p_{\mathrm{T}})}{p_{\mathrm{T}}} = \frac{N}{p_{\mathrm{T}}} \oplus \frac{S}{\sqrt{p_{\mathrm{T}}}} \oplus C, \tag{6.6}$$

where the first term on the right-hand side (inversely proportional to p_T) corresponds to the electronic and pile-up related noise, the second term (iversely proportional to $\sqrt{p_T}$) corresponds to the effects of statistical fluctuations at very high p_T and the constant term C is responsible for the effects due to energy loss through the dead material.

The JER is obtained by comparing data and MC simulations in dijet events. Several different methods [159] are employed for the resolution estimation and they all agree well with each other. Figure 6.7 shows the JER as a function of the jet p_T for data and MC with different methods. Overall the JER in data is well modelled by the MC.

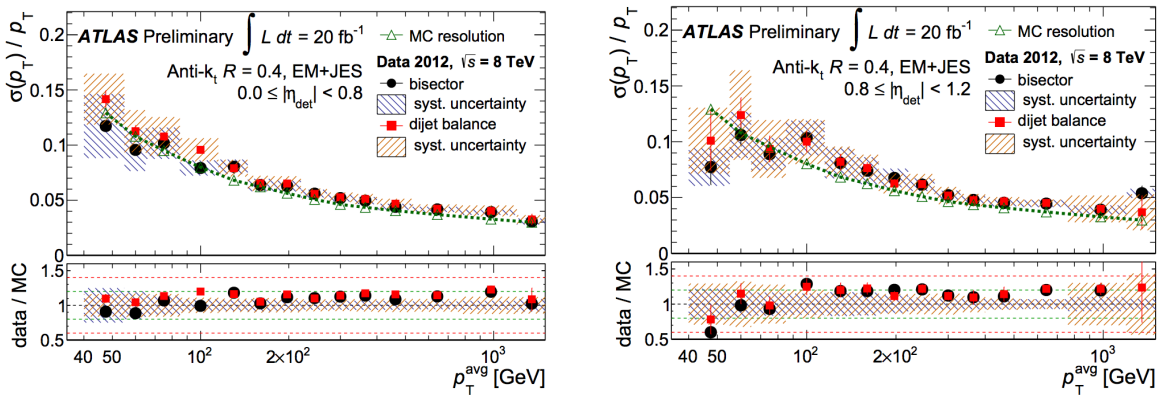

(a) (b)

Figure 6.7: The JER as a function of jet p_T for $0.0 \leq |\eta_{\text{det}}| < 0.8$ (a) and $0.8 \leq |\eta_{\text{det}}| < 1.2$. Both data and MC (two different methods, namely bisector and dijet balance) are shown. They all agree well within the systematic uncertainties [159].

b-quark identification methods

It is very important to have a mechanism that can tell whether the identified identified jets originate from a b-quark or not since an existence of a b-quark jet in the event is one of the strongest indicators of a top quark decay as discussed in Section 3.2.

The algorithms that are used to identify jets originating from b-quarks (*b-tagging*) exploit the distinguishing physical properties of b-quarks and/or b-hadrons. In general three main aspects of b-hadrons/quarks are used for the b-tagging:

- The most important distinguishing property of the b-hadrons is their lifetime which is of the order of a picosecond. This allows them to travel a measurable distance before they decay. The typical decay-length of b-hadrons is a few milimeters after which a reconstructable secondary vertex is created. The existence of a secondary vertex in an event with a distance to the primary vertex compatible to the decay-length of a b-hadron is a good indicator that the associated jet originates from a b-quark.

- Another important property of the b-hadrons is their relatively large masses compared to hadrons formed by lighter quarks. This makes the showers in the calorimeter from b-hadron cascades wider because a larger number of particles will be created in this process.

- Jets originating from a b-quark tend to carry higher momenta compared to the jets originating from lighter quarks, again due to the larger mass of the b-hadron.

Despite the existence of these distinguishing properties, the *b*-tagging is a very challenging task. *b*-tagging algorithms can work in different ways. They use parameters like the invariant mass of the tracks associated to the secondary vertex, the fraction of the tracks in a jet associated to the secondary vertex and the impact parameter of the tracks[4]. However they all rely on the properties mentioned above.

In the analysis presented here, the MV1 and MV1c *b*-tagging algorithms are used [160]. The MV1 tagger is a multivariate (where the MV in MV1 comes from) *b*-tagging algorithm which employs artificial neural networks. It takes the output of other *b*-tagging algorithms and uses them as an input to the neural network. The algorithms whose are outputs used by the MV1 tagger are the SV1, JetFitterCombNN, and IP3D [161][162].

The SV1 tagger relies heavily on the secondary vertices as a discriminating variable for *b*-jet identification as well as the invariant mass of the tracks associated to the secondary vertex.

The JetFitterCombNN tagger is an artificial neural network based tagger which takes sevaral secondary vertex related variables such as the distance between the primary and secondary vertex, invariant mass of the vertex and number of tracks associated with the vertex as input to the neural network.

The IP3D tagger makes use of the property that the tracks associated to a jet originating from a *b*-quark tend to have larger impact parameters.

The MV1 tagger combines the discrimination power of these three *b*-tagging algorithms to create one single output variable called the *b-tagging weight*. The *b*-tagging weight is a measure of the probability of a jet to originate from a *b*-quark and every identified jet is assigned a *b*-tagging weight. The larger the value of the *b*-tagging weight, the more likely the jet is originating from a *b*-quark. Another quantity, called the *b-tagging working point* or simply the *working point* is a cut applied on the *b*-tagging weight. A choice of a smaller working point means that the cut accepts more jets. However the chances of the obtained sample after the cut being more contaminated with jets that are not actually originating from a *b*-quark is higher. In the end it is a balance between efficiency versus quality. Usually every value of the working point refers to an efficiency which is derived using a pure $t\bar{t}$ sample in which both top quarks decay semileptonically. A working point with 90% efficiency means that from a sample of pure *b*-quark jets, approximately 90% of them will be identified as a correctly tagged *b*-quark jet. The lower the efficiency the higher the changes of the jet originating from a *b*-quark.

The MV1c tagger is essentially the same as the MV1 tagger, except that for MV1c, the neural network training uses an additional sample with c-quark jets rather than a pure light-flavour jet sample. This allows the MV1c tagger to have a better suppression against *c*-quark jets. A detailed information of the working points and the usage of the MV1 and MV1c taggers in this analysis is given in Section 7.1.4.

6.2.4 Reconstruction of the neutrino

The *W* boson from the top quark is assumed to decay leptonically in this analysis, producing a charged lepton and a neutrino. The neutrinos practically never interact with the ATLAS detector; therefore their direct measurement is impossible. Nevertheless, despite being challenging, the neutrinos can still be reconstructed. The key element to be able to identify the existence of a neutrino in an event is to exploit the momentum conservation in the transverse plane. Since the proton beams collide in the *z*-direction, all the reconstructed momenta in the transverse plane should add up to zero. Therefore a non-zero value of the total transverse momentum in a given event is a strong indicator of a neutrino escaping the detector in the opposite direction. The momentum which has the same magnitude but opposite direction of the total non-zero momentum in the event is called the missing transverse momentum, $E_{\mathrm{T}}^{\mathrm{miss}}$, and considered to represent the transverse momentum of the neutrino. A detailed description of the reconstruction of the

[4] The impact parameter of a track is the distance of closest approach to the primary vertex that it is associated with.

$E_{\mathrm{T}}^{\mathrm{miss}}$ in ATLAS can be found in Reference [163].

In this analysis, the $E_{\mathrm{T}}^{\mathrm{miss}}$ is defined as:

$$E_{x,y}^{\mathrm{miss}} = -\left(E_{x,y}^{\mathrm{RefEl}} + E_{x,y}^{\mathrm{RefMu}} + E_{x,y}^{\mathrm{RefJet}} + E_{x,y}^{\mathrm{RefSoftJet}} + E_{x,y}^{\mathrm{CellOut}}\right) \tag{6.7}$$

and from there, the magnitude is calculated as follows:

$$E_{\mathrm{T}}^{\mathrm{miss}} = \sqrt{(E_x^{\mathrm{miss}})^2 + (E_y^{\mathrm{miss}})^2} \tag{6.8}$$

The azimuthal angle of the $E_{\mathrm{T}}^{\mathrm{miss}}$ is defined as:

$$\phi^{\mathrm{miss}} = \arctan\left(\frac{E_y^{\mathrm{miss}}}{E_x^{\mathrm{miss}}}\right) \tag{6.9}$$

The meaning of the terms on the right hand side of Equation 6.7 is as follows:

- **RefEl:** This is the electron contribution to the $E_{\mathrm{T}}^{\mathrm{miss}}$ calculation. This term is reconstructed exactly as the electrons described in Sec. 6.2.1 except here the out-of-cluster corrections are not applied.
- **RefMu:** This refers to the muon contribution. All momenta from the muons defined in Sec.6.2.2 (combined muons) are included. In addition, the momenta of muons outside the inner detector angular range (η >2.5) but still within the muon spectrometer range (η <2.7) are also included. If there is a jet in the vicinity of the muon (within $\Delta R < 0.3$), the energy deposit is included in the **RefJet** term instead of **RefMu** term.
- **RefJet:** Calorimeter clusters associated to jets with $p_{\mathrm{T}} > 20$ GeV are included in this term. Their energy is calibrated to the hadronic scale.
- **RefSoftJet:** Clusters associated to jets with 10 GeV $< p_{\mathrm{T}} <$ 20 GeV are included in this term. Their energy is calibrated to the electromagnetic scale.
- **RefCellOut:** All the clusters in the calorimeters which are not assigned to a physics object are included in this term. They are calibrated to the electromagnetic scale.

The uncertainties in each term above is reflected as a systematic uncertainty on the $E_{\mathrm{T}}^{\mathrm{miss}}$. The largest uncertainty comes from the **RefSoftJet** term. The systematic uncertainties on the $E_{\mathrm{T}}^{\mathrm{miss}}$ are detailed in Section 8.4. In the special case of the neutrino originating from a W boson, it is possible to estimate not only the transverse component of the neutrino momentum but also the component in the z direction. This is done by exploiting the known value of the W boson mass.

In case of the leptonic decay of the W boson:

$$|p(W)| = m(W) = |p(\nu) + p(l)| \tag{6.10}$$

Where $m(W) = 80.399$ GeV. From there, the z component of the neutrino momentum can be solved. Since the equation is quadratic in $p_z(\nu)$, two real solutions arise for $m_W - M_{\mathrm{T}}^W > 0$ and imaginary solutions arise when $m_W - M_{\mathrm{T}}^W < 0$ where M_{T}^W is the transverse mass of the W boson. The one solution case where $m_W - M_{\mathrm{T}}^W = 0$ practically never occurs but still it is straightforward to solve and implemented in the analysis. For the two solution case, the one with smaller $p_z(\nu)$ is chosen, as comparisons to generator-level MC showed that this choice is more often correct than the other. The imaginary solution case is assumed to originate from the mismeasurement of the $\vec{p}_T(\nu)$, since the lepton component of the

three-momentum is measured much more precisely. Therefore $\vec{p}_T(\nu)$ is varied until one real solution is found. There are several other approaches for estimating the z-component of the neutrino momentum which are detailed in Reference [164].

CHAPTER 7

Event Selection

In Chapter 5, the data and the MC samples that are used in this analysis were presented and in Chapter 6 the physics objects and how they are reconstructed using the information gathered by the ATLAS detector were described. Therefore, now the events and the objects contained in them are accessible. The next task is to select events, both in the data and in the MC, that have the topology of the FCNC processes described in Chapter 3, namely a high-p_{T} jet originating from a b quark (b-jet), a lepton (electron or muon) and $E_{\mathrm{T}}^{\mathrm{miss}}$ due to the neutrino.

Before proceeding to the details of the event selection, a few facts have to be noted. In Section 5.3.1, it is mentioned that the signal MC generator METOP is capable of simulating the $2 \rightarrow 2$ process which allows one to investigate the final event topologies with more than one jet. However the previous analysis [133] showed that addition of a second jet does not improve the results of the analysis.

Another important fact to note is the simplicity of the final event topology. There are only three physics objects to consider. Although it may seem as an easy task, in fact this is one of the biggest challenges of the analysis presented here. When there are very few objects in the final state, the number of background processes which can mimic the signal process increases due to the simplicity of the event topology. This makes this analysis prone to huge amount of background processes such as the W+jets and the multi-jet. Both of these backgrounds have large uncertainties. Especially the multi-jet background process is very hard to simulate and usually it has worse data/MC agreement compared to the other background processes. Because of the reasons mentioned above, simply selecting events with the three physics objects is far from sufficient. One has to come up with sophisticated techniques that would suppress the background processes. In order to achieve this, a set of cuts are developed and signal separation techniques are employed. The list of cuts are given in this chapter and the signal separation technique that is adopted in this analysis is presented in Chapter 9.

It is also worthwhile to note that at this step, the several selection criteria on the physics objects that was discussed in Chapter 6 have already been applied.

7.1 Event selection

7.1.1 Event cleaning cuts

These are a set of cuts which are not directly related to the FCNC event topology. They are rather more general cuts which are not unique to this analysis and they have the purpose of producing a set of high quality events.

Only those events are which belong to the runs in the GRL (see Section 5.1) are selected.

An event is rejected in case at least one bad jet (see Section 6.2.3) with a transverse momentum of $p_{\mathrm{T}} > 20\,\mathrm{GeV}$ is found. Each event is required to have at least one primary vertex reconstructed from at least 5 tracks. The events with noise bursts from the electromagnetic calorimeter are also removed.

7.1.2 Overlap removal

Although it was partially mentioned in Chapter 6, the criteria that are used to remove the overlapping event objects are summarised in this section. Overlap removal for various event objects is performed as follows:

- For electrons: electrons are almost always reconstructed also as a jet. Hence the jet is removed if it is matched to an electron, i.e. $\Delta R < 0.2$.
- For muons: muons inside the jets are mostly from semi-leptonic heavy flavour decays and thus not the muons of interest. They are therefore removed from the event if they overlap with any jet with $p_{\mathrm{T}} > 20\,\mathrm{GeV}$ within $\Delta R < 0.4$.
- Electrons and muons: the event is rejected if the electron and muon share an ID track.

7.1.3 Selection of leptons and $E_{\mathrm{T}}^{\mathrm{miss}}$

It is not sufficient to simply select an event with let's say an electron but the electron contained in the event also has to fulfil certain criteria. For instance leptons with low transverse momenta have lower purity and efficiency.

Events containing exactly one electron or one muon are selected. The electrons are required to have $p_{\mathrm{T}} > 30\,\mathrm{GeV}$ and $|\eta_{\mathrm{clus}}|$ <2.47, where $|\eta_{\mathrm{clus}}|$ indicates the pseudo-rapidity of the calorimeter cluster. For electron clusters, the pseudo-rapidity region $1.37 < |\eta_{\mathrm{clus}}| < 1.52$ is also excluded as this region falls into the barrel-endcap transition region in the calorimeter. The muons are required to have $p_{\mathrm{T}} > 25\,\mathrm{GeV}$ and $|\eta| < 2.5$ The reason to choose electrons with higher p_{T} compared to muons is that at lower energies, the efficiency is lower for electrons and the quality of the MC description of the data is worse. This is due to the fact that the fake electrons (which occur more often in lower energies) are harder to simulate.

The events with exactly one lepton are also required to have isolated missing transverse energy with $E_{\mathrm{T}}^{\mathrm{miss}} > 30\,\mathrm{GeV}$.

7.1.4 Selection of jets

Events containing exactly one jet are selected. The jet is required to have a transverse momentum $p_{\mathrm{T}} > 30\,\mathrm{GeV}$ and to be in the pseudo-rapidity region $|\eta| < 2.5$.

In order to make sure that the jet in the selected event is originating from a b quark, the b-quark identification methods mentioned in Section 6.2.3 are employed. In this analysis, the MV1c tagger which has a better suppression against c-quark jets compared to the MV1 tagger is used. This is essential. For

instance, the background with a W boson in association with a c-quark jet (W+c background) can easily mimic the signal topology if the c-quark jet is misidentified as originating from a b-quark. The working point efficiency for the MV1c tagger is chosen to be 50%. This is a rather harsh requirement. However, this approach suppresses the W+jets background significantly; overall the amount of background is reduced by a factor of ten solely due to this requirement, compared to a softer requirement, 85% efficiency working point with the MV1 tagger.

The jet vertex fraction requirement for the jets, which was mentioned in Section 6.2.3, has already been applied at this stage.

7.1.5 The multi-jet veto

Fake electrons from multi-jet events tend to have low $E_{\mathrm{T}}^{\mathrm{miss}}$ and low transverse W boson mass relative to single top-quark events. Hence, in addition to the cut on $E_{\mathrm{T}}^{\mathrm{miss}}$, a cut using the transverse W boson mass is an effective way to reduce this background. The W boson mass is reconstructed using the transverse momentum of the lepton, the azimuthal angle between the lepton and the direction of the missing transverse momentum and the $E_{\mathrm{T}}^{\mathrm{miss}}$ itself. The cut applied is $m_{\mathrm{T}}(W) > 50\,\mathrm{GeV}$, where

$$m_{\mathrm{T}}(W) = \sqrt{2 p_{\mathrm{T}}(\ell) E_{\mathrm{T}}^{\mathrm{miss}} \left(1 - \cos\Delta\phi\left(\ell, E_{\mathrm{T}}^{\mathrm{miss}}\right)\right)} \tag{7.1}$$

7.1.6 Triangular cut

As mentioned previously, the leptons, especially the electrons, are poorly described by the MC at lower energies. Because of this, and in order to further suppress the multi-jet background, an additional cut has been developed which is applied on the transverse momenta of the leptons and the azimuthal angle between the lepton and the jet. The cut is given below:

$$p_{\mathrm{T}}(\ell) > 90\,\mathrm{GeV}\left(1 - \frac{\pi - |\Delta\phi(\ell, \mathrm{jet})|}{\pi - 2}\right) \tag{7.2}$$

In order to motivate the cut, Figure 7.1 shows the distribution of the lepton transverse momentum and the azimuthal angle between the lepton and the jet. The colours shows the data after all the background except for the multi-jet background is subtracted in order to enrich the data with this particular background. The black line shows where the triangular cut is applied. The events that fall into the lower-right of the part of the distribution are removed. As it can be seen in the figure, the multi-jet enriched data points accumulate at lower lepton transverse momenta and large azimuthal angle between the lepton and the jets region. This is due to the following reason: in the the multi-jet events with two jets, the jets are usually produced back-to-back, giving a large angle between the two. When one of the jets is misidentifed as a lepton, these events can leak into the signal event selection.

This cut is the most studied cut in this analysis. It is specifically designed for this analysis and many variations of it has been tested. The parameters and the numbers of the cut has been varied and the effect of them are observed. While doing that, its impact is tested not only on the multi-jet background but also on the other backgrounds, data and the signal MC.

There were several criteria that were considered while developing the cut, such as how much of the multi-jet background it suppresses, how many signal events it cuts away, what happens to the data/MC agreement and what is the impact of it on the results of the analysis. These points were all considered at the same time and the most optimum values are found. The position of the black line in the Figure 7.1 has been changed, and it's orientation has also been varied (such as varying the position of its edges at the angular and the transverse momentum axis). In the end, the form presented in the Eqn. 7.2 is obtained.

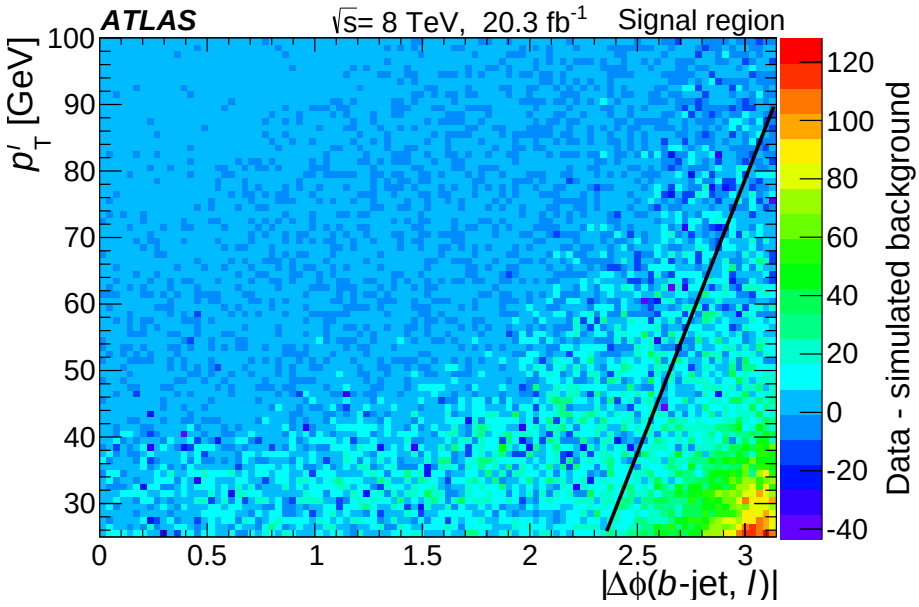

Figure 7.1: The lepton transverse momentum versus the azimuthal angle between the lepton and the jet [86]. The colours indicate the data after subtracting all backgrounds except for the multi-jet background.

The cut in its final form, removes more than 50% of the multi-jet background. It also removes a tiny fraction of the signal sample (which is unavoidable). However, overall, the signal-to-background ratio has been increased by 20% which has a direct positive impact on the results of the analysis presented in Chapter 11.

The distributions in the Appendix A demonstrate the effect of the triangular cut on data, multi-jet background and the signal sample separately.

7.2 Definition of signal and control regions

The selection described until here defines the signal sample or the signal region. This is the final selection of the FCNC candidate events involving top quarks used in this analysis. In addition to the signal region selection, another selection called the control region is also chosen. This is a selection which is enriched by the SM background processes. The necessity for such a selection is to ensure that, in a region which is dominated by the SM background processes, the data and the MC agree well.

The control region has exactly the same selection as the signal region except for the b-tagging requirement. Rather than applying the harsh 50% efficiency working point, that requirement is inverted. Therefore, all the events in the signal region are rejected and the sample is enriched with background. After inverting the b-tagging requirement, a much milder b-tagging is applied, namely 85% efficiency with the MV1 tagger. The reason for applying a mild b-tagging requirement is to have a control region which is not kinematically too different from the signal region. Therefore, a comparison between the two regions can still be made in a sensible way.

7.3 Background estimation

This section explains how the background rates are estimated for the different background contributions.

In order to obtain the event rate for the multi-jet background, a fit to data using the $E_{\mathrm{T}}^{\mathrm{miss}}$ distribution is performed. The details of the production of the multi-jet background sample and estimation of the event rates for this background are given in Chapter 8. During the fit, the other backgrounds are also allowed to vary within their cross-section uncertainties. Therefore, scale factors (see Table 8.3) for these backgrounds are obtained as well.

For the W+jets (W+LF and W+HF) background, the shape of distributions is modelled using MC samples and the normalisation taken from (N)NLO calculations. In order to check the modelling of kinematic distributions, the theoretical cross-sections are corrected by scale factors obtained in the fit to the $E_{\mathrm{T}}^{\mathrm{miss}}$ distribution. The flavour composition is taken from MC samples. The same procedure is applied to the top-quark processes, where the overall normalisation of all SM top quark processes from the fit to the $E_{\mathrm{T}}^{\mathrm{miss}}$ distribution is used, keeping the relative fraction according to the theory predictions. Simulated events and theory cross-sections are used for the remaining backgrounds.

7.3.1 Re-weighting of the W+jets background events

It is known that the W+jets background events do not describe the data well for certain variables [165]. This is assumed to be due to the badly modelled kinematic variables in the Sherpa generator. Example distributions in the signal region, of transverse momentum of the W boson that show the mismodelling are given in Figure 7.4(a) and Figure 7.3(b) for electron and muon channels, respectively. This is the variable where the mismodelling is the most prominent.

In order to resolve the mismodelling, an approach based on re-weighting these backgrounds to the data is chosen. The re-weighting is done in the control region in order to enrich the selection with W+jets events. The weights are obtained from the transverse momentum of the W boson variable (because the disagreement in this variable is the worst). The distribution used for the re-weighting is shown in Figure 7.2. The W+jets sample is split into its W+LF and W+HF components.

The re-weighting is done as follows: in the control region, where the W+LF and W+HF samples are the dominant backgrounds, all other backgrounds are subtracted from the data. The data (which now should now contain W+LF/HF background) is compared to these backgrounds in the transverse momentum of the W boson distribution. The distribution is finely binned over a range of 0-200 GeV, in steps of 5 GeV, which makes a total of 40 bins. For each bin, the data/background ratio is extracted and saved. The background events that fall in a given bin are re-weighted by the inverse of the data/background ratio that is extracted for that particular bin. While re-weighting, it was made sure that the normalisation is not affected, but only the shape of the distribution is changed.

In order to display the improvement obtained by the re-weighting method described above, the lepton transverse momentum distribution in the electron channel signal region is shown before and after re-weighting for comparison in Figure 7.4.

Estimation of the W+jets background

The kinematic shape of the W+jets backgrounds is taken from MC simulation samples. While the kinematic shape and acceptances of the W+jets background are taken from MC simulation samples, the overall normalisation is taken from (N)NLO calculations. The dominant W+jets process in the b-tagged sample is W+c+jets production. The k-factor is calculated by comparing the NLO and LO calculation

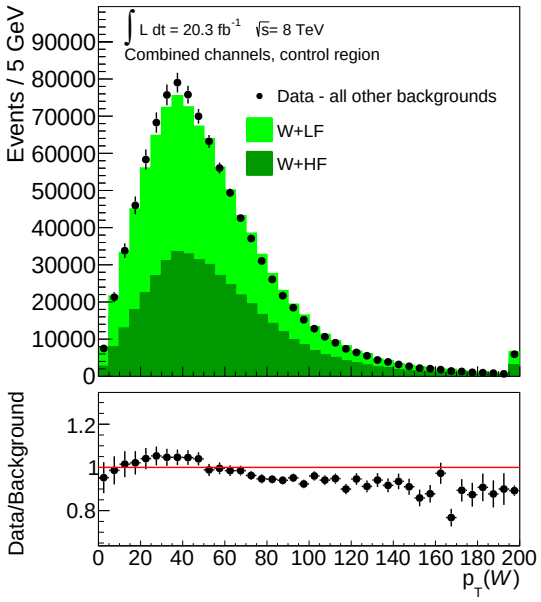

Figure 7.2: Transverse momentum of the W boson distribution in the control region for combined the electron and muon channels. All the backgrounds are subtracted from the data except for the W+LF and W+HF backgrounds.

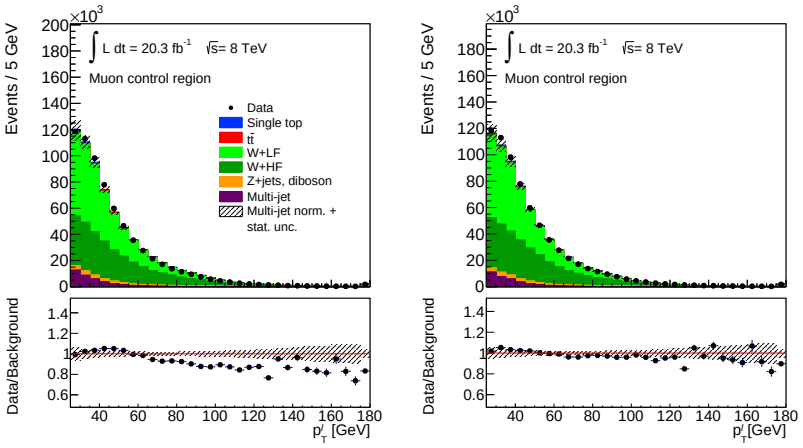

(a) (b)

Figure 7.3: The transverse momentum of the lepton in the muon control region before the W+jets background re-weighting (a), and after the re-weighting (b). The distributions are shown side by side in order to present the effect of the re-weighting. The hatched error bands denote the statistical uncertainty and the uncertainty on the multi-jet background normalisation.

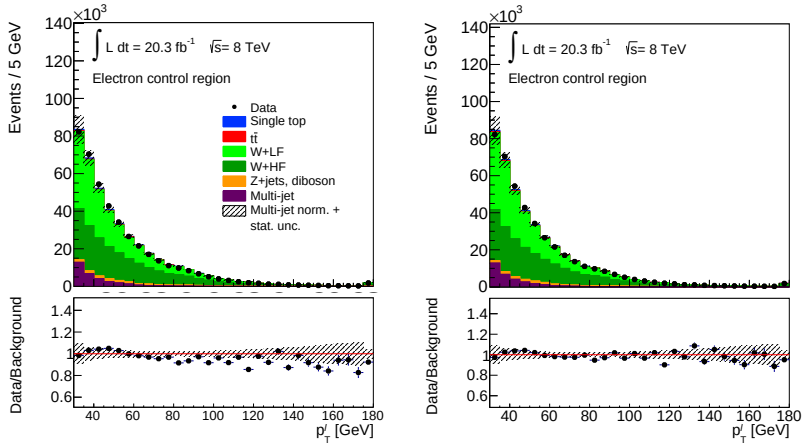

Figure 7.4: The transverse momentum of the lepton in the electron control region before the W+jets background re-weighting (a), and after the re-weighting (b). The distributions are shown side by side in order to present the effect of the re-weighting. The hatched error bands denote the statistical uncertainty and the uncertainty on the multi-jet background normalisation.

using MCFM [166]. The production cross-sections of all the other W/Z+jets processes are normalised to the corresponding NNLO cross-section prediction passed in [167].

7.3.2 Event yields and control distributions

Since the event selection is applied on the MC exactly the same way as the data, it is expected to have a similar number of events (event yields) for both, after the MC samples are scaled to their respective cross-sections. This is the first way of checking the data and the SM background MC agreement in the control region. In this analysis, a good agreement between the data and the MC in the signal region is also expected, since the upper limits on the cross-section of the FCNC involving top quarks are in the order of a few pb, which would hardly make any difference in the total event yields even if this process exists in nature.

The number of observed and expected background events for the signal region in the electron and muon channel are listed in Table 7.1. Table 7.2 summarises the event yields for the control region. The event yields are calculated using the acceptance from MC samples normalised to their respective theoretical cross-sections including the (N)NLO k factors. The number of events for multi-jet background reflects the yields obtained from maximum likelihood fit explained in Chapter 8. The main background contribution arises from W+HF production. The observed event yield in data agrees well with the background prediction for both signal and control regions.

The next step to check the agreement between the data and the MC is to inspect various kinematic distributions of the event variables. For the same reason mentioned above, a good agreement between the data and the MC in the distributions is expected not only in the control region but also in the signal region.

Kinematic distributions in the control region of the identified lepton, reconstructed jet, $E_{\mathrm{T}}^{\mathrm{miss}}$ and $m_{\mathrm{T}}(W)$ are shown in Figure 7.5 and Figure 7.6 for the electron and muon channels, respectively. These distributions are normalised using the scale factors obtained in the $E_{\mathrm{T}}^{\mathrm{miss}}$ fit, described in Chapter 8. The hatched uncertainty band in the distributions includes the statistical and systematical uncertainties considered in the analysis presented here. The details of the estimation of the uncertainty band are

Process	Electron channel Central	Electron channel Forward	Electron channel Total	Muon channel Total
Single top	4 600 ± 230	1 200 ± 58	5 800 ± 290	8 600 ± 430
$t\bar{t}$	4 100 ± 240	1 000 ± 62	5 100 ± 310	6 900 ± 410
W+LF	1 800 ± 420	860 ± 210	2 600 ± 630	4 100 ± 990
W+HF	18 000 ± 9 700	6 500 ± 3 600	24 000 ± 13 000	38 000 ± 21 000
Z+jets	1 000 ± 250	390 ± 93	1 400 ± 640	3 600 ± 860
Multi-jets	790 ± 290	1 700 ± 840	2 500 ± 1 100	5 000 ± 2 500
Total expected	30 000 ± 11 000	12 000 ± 3 700	42 000 ± 16 000	66 000 ± 26 000
Data	30 292	11 555	41 847	66 305

Table 7.1: Number of observed and expected events for both lepton channels in the signal sample. The uncertainties shown are derived using the statistical uncertainty and the uncertainty on the theoretical cross-section only or multi-jets normalisation. Additional scale factors, e.g. as obtained in the likelihood fits for the multi-jet estimation, are not applied.

Process	Electron channel Central	Electron channel Forward	Electron channel Total	Muon channel Total
Single top	4 300 ± 230	1 100 ± 58	5 400 ± 280	7 900 ± 400
$t\bar{t}$	3 700 ± 300	1 000 ± 61	4 700 ± 360	6 300 ± 380
W+LF	160 000 ± 40 000	79 000 ± 19 000	240 000 ± 60 000	410 000 ± 110 000
W+HF	180 000 ± 97 000	56 000 ± 31 000	230 000 ± 130 000	340 000 ± 190 000
Z+jets	20 000 ± 4 900	9 500 ± 2 300	30 000 ± 7 100	39 000 ± 9 300
Multi-jets	11 000 ± 5 700	23 000 ± 12 000	34 000 ± 17 000	32 000 ± 16 000
Total expected	380 000 ± 150 000	170 000 ± 65 000	550 000 ± 210 000	840 000 ± 25 000
Data	381 178	173 188	554 366	826 517

Table 7.2: Number of observed and expected events for both lepton channels in the control sample. The uncertainties shown are derived using the statistical uncertainty and the uncertainty on the theoretical cross-section only or multi-jets normalisation. Additional scale factors, e.g. as obtained in the likelihood fits for the multi-jet estimation, are not applied.

explained in Chapter 11.

The same distributions are also shown for the signal selection in Figure 7.7 and Figure 7.8. The cross-section of the FCNC signal process is scaled to 50 pb and overlayed on the SM backgrounds in the control distributions in the signal region. Overall a very good agreement between the observed and simulated distributions is seen.

Finally the same distributions in the combined electron and muon channels in the control region are shown in Figure 7.9.

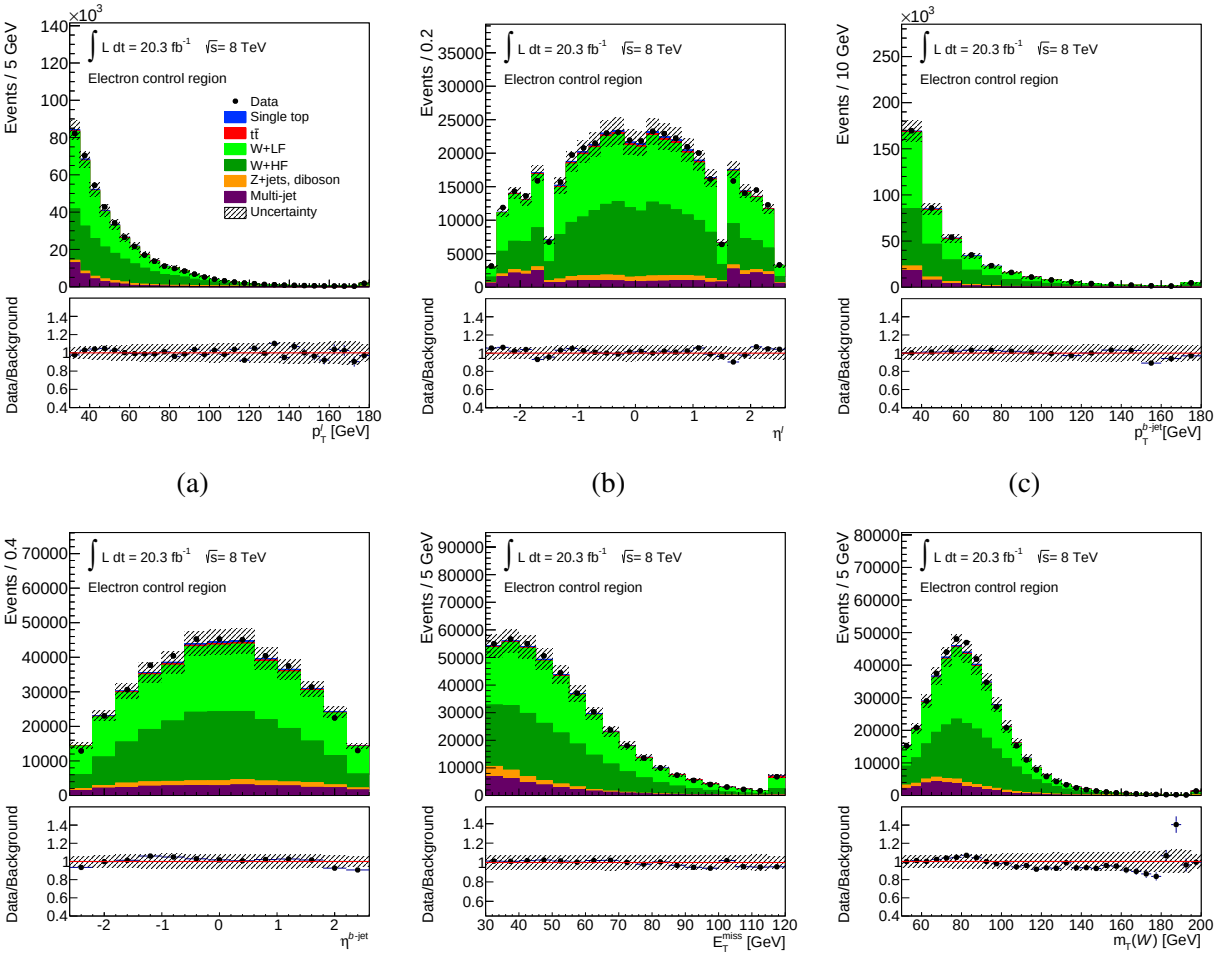

Figure 7.5: Basic kinematic distributions of the control region for the electron channel. All processes are normalised to the result of the binned maximum likelihood fit used to determine the fraction of multi-jet events. Shown are: (a) the transverse momentum and (b) pseudo-rapidity of the lepton, (c) the transverse momentum and (d) pseudo-rapidity of the jet, (e) the missing transverse energy and (f) transverse W-boson mass. The last histogram bin includes overflow events and the hatched band indicates the combined statistical and systematic uncertainties.

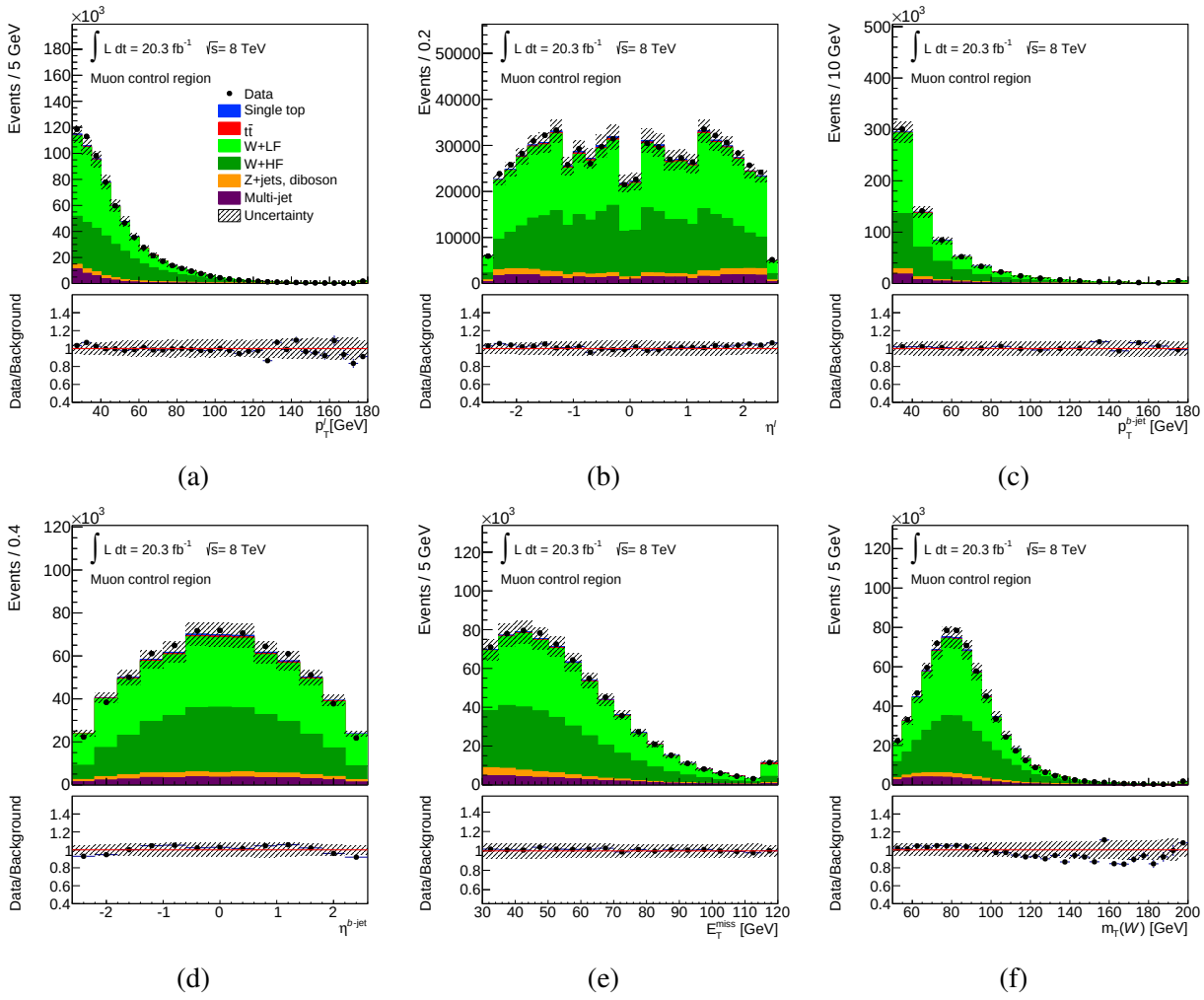

Figure 7.6: Basic kinematic distributions of the control region for the muon channel. All processes are normalised to the result of the binned maximum likelihood fit used to determine the fraction of multi-jet events. Shown are: (a) the transverse momentum and (b) pseudo-rapidity of the lepton, (c) the transverse momentum and (d) pseudo-rapidity of the jet, (e) the missing transverse energy and (f) transverse W-boson mass. The last histogram bin includes overflow events and the hatched band indicates the combined statistical and systematic uncertainties.

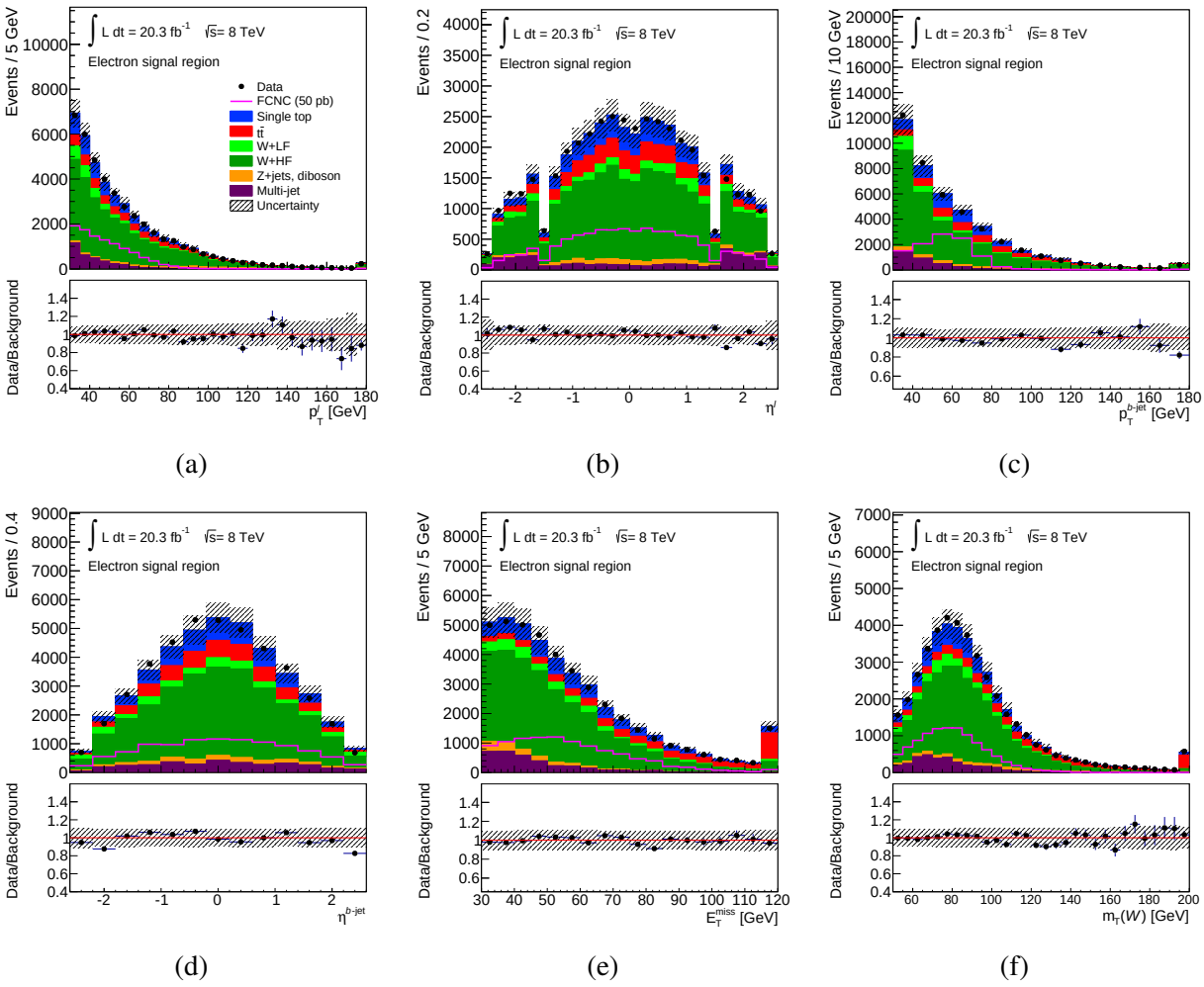

Figure 7.7: Basic kinematic distributions of the signal region for the electron channel. All processes are normalised to the result of the binned maximum likelihood fit used to determine the fraction of multi-jet events. Shown are: (a) the transverse momentum and (b) pseudo-rapidity of the lepton, (c) the transverse momentum and (d) pseudo-rapidity of the jet, (e) the missing transverse energy and (f) transverse W-boson mass. The last histogram bin includes overflow events and the hatched band indicates the combined statistical and systematic uncertainties.

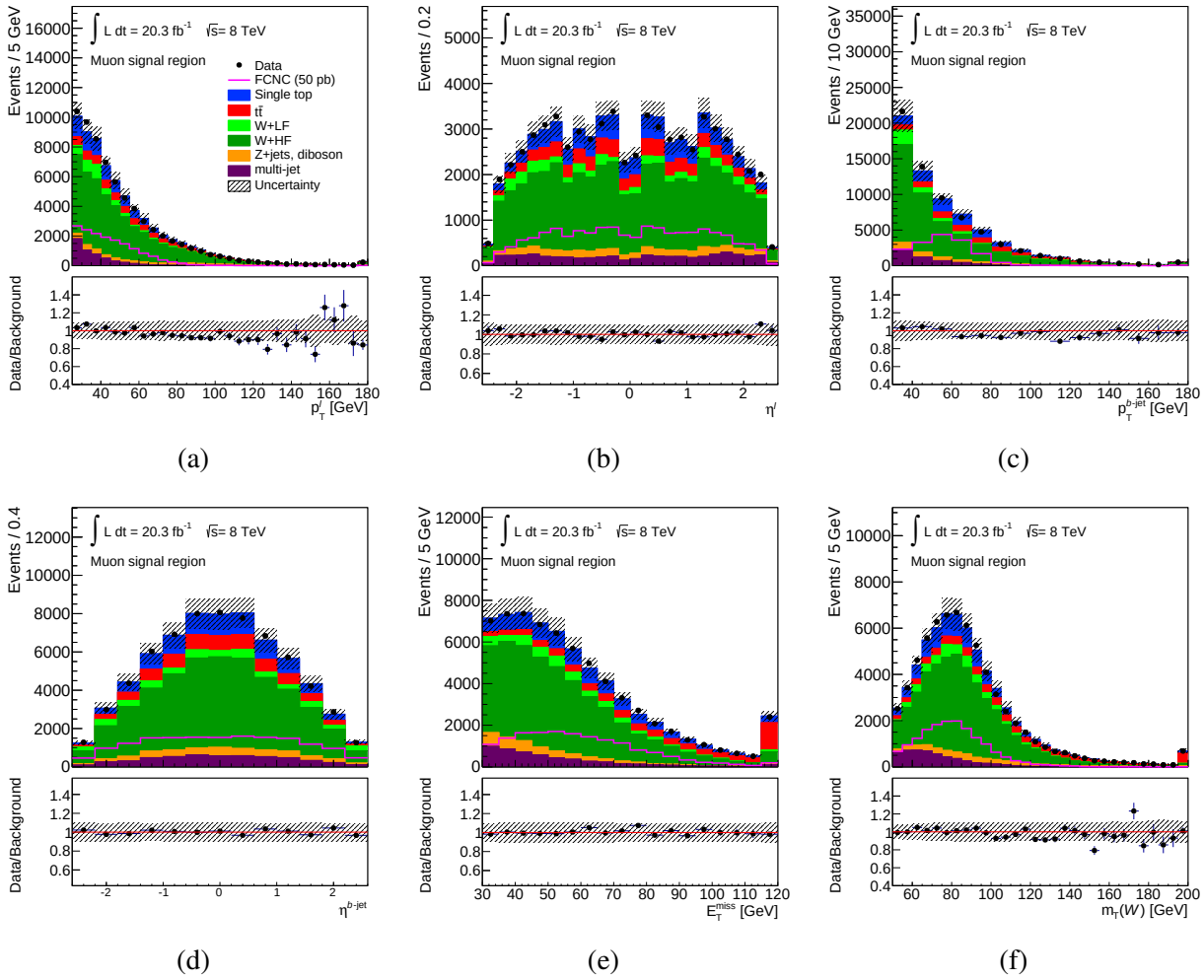

Figure 7.8: Basic kinematic distributions of the signal region for the muon channel. All processes are normalised to the result of the binned maximum likelihood fit used to determine the fraction of multi-jet events. Shown are: (a) the transverse momentum and (b) pseudo-rapidity of the lepton, (c) the transverse momentum and (d) pseudo-rapidity of the jet, (e) the missing transverse energy and (f) transverse W-boson mass. The last histogram bin includes overflow events and the hatched band indicates the combined statistical and systematic uncertainties.

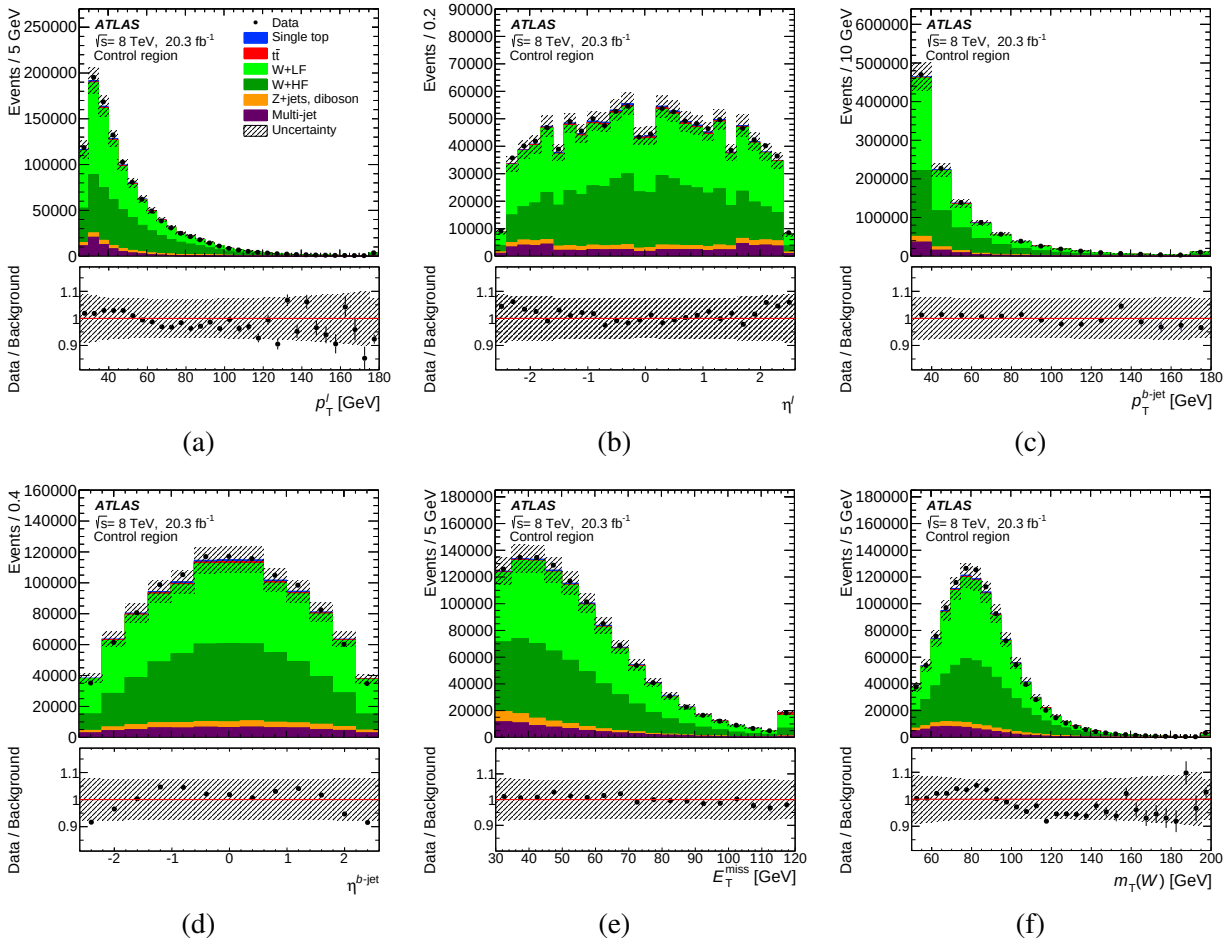

Figure 7.9: Basic kinematic distributions in the control region for combined channels[86]. All processes are normalised to the result of the binned maximum likelihood fit used to determine the fraction of multi-jet events. Shown are: (a) the transverse momentum and (b) pseudo-rapidity of the lepton, (c) the transverse momentum and (d) pseudo-rapidity of the jet, (e) the missing transverse energy and (f) transverse W-boson mass. The last histogram bin includes overflow events and the hatched band indicates the combined statistical and systematic uncertainties.

7.3.3 Event reconstruction

Several categories of variables are considered as potential discriminators between the signal and background processes. Apart from basic event kinematics such as the $m_{\mathrm{T}}(W)$ or H_{T} (sum of the transverse momenta) and those of the final state objects, various object combinations were considered as well. This includes the basic kinematic properties of reconstructed objects like the W boson or the top quark, as well as angular distances in η and ϕ between the reconstructed and final state objects in the laboratory frame, as well as in the rest frames of the W boson and top quark. Further, integer variables like the charge of the lepton are considered for signal separation and background studies.

To reconstruct the four-vectors of these objects the neutrino four-momentum has to be derived from the measured $E_{\mathrm{T}}^{\mathrm{miss}}$, since it cannot be measured directly. The neutrino longitudinal momentum ($p_{z,\nu}$) can be calculated by imposing a W-boson mass constraint:

$$(p_W)^2 = (p_\ell + p_\nu)^2 = m_W^2 = (80.4\,\mathrm{GeV})^2, \tag{7.3}$$

where p_W,p_ℓ and p_ν are the four vectors of the W boson, lepton or neutrino, respectively. If the equation has solutions where $p_{z,\nu}$ is real, the one with the smaller $|p_{z,\nu}|$ is taken. In about 30 % of the events the equation has imaginary solutions. In this case, the $E_{\mathrm{T}}^{\mathrm{miss}}$ is rescaled by a factor such that the imaginary part vanishes. By calculating the full neutrino four-vector, the W boson can be reconstructed as the sum of the neutrino four-vector and the lepton four-vector. The top-quark four-vector is then given by the sum of the W-boson four-vector and the four vector of the b-quark jet. A distinctive variable in the top-quark decay is the helicity of the W boson. This can be accessed via the angle $\cos\theta^*$ between the momentum of the charged lepton in the W-boson rest-frame and the momentum of the W boson as seen in the top-quark rest-frame.

CHAPTER 8

Estimation of Multi-jet Background

The multi-jet background is the second largest background in this analysis. Furthermore, as previously mentioned, it is also one of the hardest to simulate. During the analysis presented here, several approaches have been tested in order to estimate this background. A significant amount of work has been spent on the multi-jet background studies, therefore, it is worthwhile to spare a dedicated chapter in order to present these studies.

The following sections detail the methods that are tried to estimate this background, present the performance comparisons of these methods as well as the results of them.

8.1 Multi-jet background estimation methods

Some of the methods are developed for individual lepton channels only, therefore these methods are tested for each lepton channel separately.

For the electron channel the methods tested are:

- jet-electron method,
- matrix method,

and for the muon channel:

- anti-muon method,
- matrix method.

As can be seen above, only the matrix method is applicable for both lepton channels.

8.1.1 Jet-electron method

This is the only method where MC simulations are used partially. The jet-electron method establishes a shape for the multi-jet background by choosing events with almost the same kinematics as the signal selection but with a jet used in place of the electron, therefore the name "jet-electron". The misreconstruction of the jet as an electron is done on purpose in order to simulate the fake electrons which are prominent in the multi-jet background events.

The model uses a MC dijet sample generated by PYTHIA to which the following selection is applied to all jets present in the event. The jet that resembles an electron has to have $E_{\mathrm{T}} > 25\,\mathrm{GeV}$ and the same coverage in η as the signal electrons. The fraction of the electromagnetic energy of the jet, f_{EM}, has to be between 0.8 and 0.95. By demanding that at least four tracks have been found in the jet, the number of converted photons is reduced. To avoid a contamination of the jet-electron sample by W+jets events, events are vetoed if they contain one or more leptons that are identified according to high-efficiency but low-purity identification criteria (loose selection, see Section 6.2.1). The event is accepted if exactly one "jet-electron" is found. In Table 8.1 the applied cuts are summarised.

The selection that is applied on the dijet MC simulation in order to generate a jet-electron sample provides only the shape of the kinematic distribution. The number of multi-jet events is obtained by applying a fit to the observed data using the $E_{\mathrm{T}}^{\mathrm{miss}}$ distribution, where the details are be discussed later. Since the selected jet-electron events are only used as a background model to obtain a template for the $E_{\mathrm{T}}^{\mathrm{miss}}$ distribution, no special trigger requirement is applied.

Variable	Cut
Transverse energy of jet	$E_{\mathrm{T}} > 25\,\mathrm{GeV}$
η of jet	$\lvert\eta\rvert < 2.47$, no *crack* region
EM fraction	$0.8 < f_{\mathrm{EM}} < 0.95$
Number of tracks within the jet	$n_{\mathrm{tracks}} > 3$

Table 8.1: Applied cuts to define a "jet-electron" sample.

8.1.2 Anti-muon method

The anti-muon method builds a multi-jet model derived from collision data for the muon channel. Some of the muon identification cuts are inverted or changed, in order to obtain a sample highly enriched with muons from multi-jet events. The resulting sample contains only a small number of signal muons from Z and W boson decays. Similar to the jet-electron method, this approach provides only the shape for the multi-jet background. However, in the anti-muon method, the shape is obtained solely from the collision data. In order to enrich the data with multi-jet background in the muon channel, the following selection criteria are applied apart from the nominal selection: the longitudinal impact parameter z_0 requirement (see Section 6.1.3) for the associated vertex is removed. The mini-isolation requirement R_{iso} (see Section 6.2.2) is also removed, instead a milder requirement is applied (R_{iso}<0.1). Another isolation criterion which is applied is the ratio of the energy deposits in the calorimeter within a cone $\Delta R = 0.2$ around the muon, `EtCone20`, to the transverse momentum of the muon $p_{\mathrm{T}}^{\mathrm{muon}}$. This ratio is required to be `EtCone20`/p_{T}^{muon} >30%. A flag provided by the calorimeter called `energyLossType` or "NotIsolated" is required be *true*, which indicates that the fake muons which are inside the jet cone are selected. The events with fake jets originating from real muons are omitted by requiring an energy loss, `energyLoss`<6 GeV.

Table 8.2 summarises the cuts that are different from the standard identification cuts.

Variable	Cut
Longitudinal impact parameter z_0	no cut
Isolation	`eTcone20`$/p_{\mathrm{T}}^{\mathrm{muon}} > 0.3$, $R_{\mathrm{iso}} < 0.1$
Energy loss type	`energyLossType` == 1, (Not Isolated)
Energy loss	`energyLoss` < 6 GeV

Table 8.2: Cuts that are different from the nominal cuts in the anti-muon sample.

The data used in the analysis are identical to the data that are used to obtain the multi-jet background in the muon channel. The aforementioned cuts generate a sample which provide a shape for the multi-jet events in the muon channel and similar to the jet-electron method, the normalisation of the sample is obtained by a fit to the data in the $E_{\mathrm{T}}^{\mathrm{miss}}$ distribution.

A multi-jet sample for the electron channel using a similar approach as described above can also be obtained (anti-electron method), however this approach has not been tested in this analysis.

8.1.3 Matrix method

This is another multi-jet estimate method that relies on the collision data. This method is tested for both lepton channels. The estimation employs the loose and tight identification criteria for leptons (see Section 6.2.1, and 6.2.2). The tight criterion is used for the nominal selection of leptons in this analysis which is a subset of the loose leptons. The loose lepton events sample is significantly larger than that of tight leptons. The method estimates the number of fake leptons originating from multi-jet events in the tight selection. It is achieved by defining the following:

$$N_{\mathrm{L}} = N_{\mathrm{L}}^{\mathrm{R}} + N_{\mathrm{L}}^{\mathrm{F}}$$

and

$$N_{\mathrm{T}} = N_{\mathrm{T}}^{\mathrm{R}} + N_{\mathrm{T}}^{\mathrm{F}}$$

where N_{L} and N_{T} are the number of leptons passing the loose and tight criteria, respectively. R stands for real and F stands for fake leptons. If one defines the real and fake efficiencies ϵ_{R} and ϵ_{F} as:

$$\epsilon_{\mathrm{R}} = \frac{N_{\mathrm{T}}^{\mathrm{R}}}{N_{\mathrm{L}}^{\mathrm{R}}} \text{ and } \epsilon_{\mathrm{F}} = \frac{N_{\mathrm{T}}^{\mathrm{F}}}{N_{\mathrm{L}}^{\mathrm{F}}},$$

then for the $N_{\mathrm{T}}^{\mathrm{F}}$ one can obtain:

$$N_{\mathrm{T}}^{\mathrm{F}} = \frac{\epsilon_{\mathrm{R}} N_{\mathrm{R}} - N_{\mathrm{T}}}{\epsilon_{\mathrm{R}} - \epsilon_{\mathrm{F}}} \epsilon_{\mathrm{F}}. \tag{8.1}$$

The important step is to be able to determine the efficiencies ϵ_{R} and ϵ_{F}. These are quantities that are measured using the collision data [168]. The efficiencies are measured by preparing two sets of collision data, one is enriched with fake leptons and the other with real leptons. The data used for the derivation of the efficiencies is identical to the data that is used in this analysis. The selection of the events for these regions is similar to the event selection described in Chapter 7 but differs in certain aspects explained in the following. It uses a different b-tagging requirement for the jet (MV1 with 70% efficiency). For electrons the region which is enriched with fakes is selected by requiring $E_{\mathrm{T}}^{\mathrm{miss}} + m_{\mathrm{T}}(W) < 60$ GeV or $E_{\mathrm{T}}^{\mathrm{miss}}$ <20 GeV. This region can still contain real electrons, therefore by using comparisons to MC

simulations, the events with real electrons are removed. The real electron enriched region is achieved by requiring $E_{\mathrm{T}}^{\mathrm{miss}}$ >120 GeV. The efficiencies are measured as functions of kinematic variables, namely the η and the p_{T} of the electron, azimuthal angle between the $E_{\mathrm{T}}^{\mathrm{miss}}$ and the electron, sum of all transverse energy and the ΔR between the jet and the electron. This parametrisation is done in order to avoid bias from dependencies on the event topologies.

The fake-enriched region in the muon channel is prepared by requiring a transverse impact parameter significance of $|d_0|/(\Delta d_0)$ >5. This requirement ensures that the track associated with the muon candidate is less likely to have a primary vertex. The region with real muons is obtained by selecting events with $m_{\mathrm{T}(W)} > 100$ GeV.

Using these efficiencies, each event in the data is assigned a weight:

$$w_{\mathrm{L}} = \frac{\epsilon_{\mathrm{F}}}{\epsilon_{\mathrm{R}} - \epsilon_{\mathrm{F}}}(\epsilon_{\mathrm{F}} - 1) \text{ and } w_{\mathrm{T}} = \frac{\epsilon_{\mathrm{F}}}{\epsilon_{\mathrm{R}} - \epsilon_{\mathrm{F}}}\epsilon_{\mathrm{R}} \tag{8.2}$$

in order to obtain a sample enriched with multi-jet events.

Matrix method provides both shape of the kinematic variables and the normalisation for the multi-jet events. Therefore, unlike the other methods mentioned above, a fit to data is not required in this method.

8.2 Maximum likelihood fits for jet-electron and anti-muon methods

To determine the normalisation of the multi-jet background template in both the electron and the muon channel derived by the jet-electron and anti-muon methods, respectively, a binned maximum likelihood fit is performed in the $E_{\mathrm{T}}^{\mathrm{miss}}$ distribution after applying all selection criteria described in Chapter 7, except for the $E_{\mathrm{T}}^{\mathrm{miss}}$ >30 GeV requirement. This cut is released in order to enrich the sample in multi-jet events. The fits are done in the control region and the signal region separately. Since the η^l distribution of the jet-lepton model does not describe the data well, the electron channel is divided into central ($|\eta^l| < 1.5$) and forward ($|\eta|^l > 1.5$) electrons and the fit is performed in these regions separately. In the muon channel no specific η region is chosen.

The multi-jet template is fitted together with templates derived from MC simulation for all other background processes (single top, $t\bar{t}$, W+HF/LF, Z+jets, dibosons) whose normalisation uncertainties (see Table 5.4) are accounted for in the fitting process in the form of additional, constrained nuisance parameters. For the purpose of fits, the contributions from W+HF and W+LF backgrounds are joined in one template. Similarly the ones from Z+jets and the dibosons were also joined; $t\bar{t}$ and single top-quark production are treated independently.

To account for the similar shape of the Z+jets contributions with respect to the W+HF/LF backgrounds in the $E_{\mathrm{T}}^{\mathrm{miss}}$ distribution, the rate for Z+jets is fixed in the fitting process. In the muon channel, the anti-muon method and in the electron channel the jet-electron method are used to obtain the shape of the multi-jet background. A fit to the $E_{\mathrm{T}}^{\mathrm{miss}}$ distribution is performed, in which the multi-jet rate is unconstrained and scale factors for the the multi-jets and remaining background processes are obtained.

The scale factors obtained for the combined contributions of W+HF and W+LF and of $t\bar{t}$ and single top-quark production are shown in Table 8.3 for both lepton channels. These values are not used in the later analysis and are only applied to scale the respective backgrounds in the control plots in order to check the modelling of the kinematic distributions. For the neural network training (see Chapter 9) as well as for the final statistical analysis (see Chapter 11), the normalisation for all but the multi-jets background is taken solely from MC simulations scaled to their respective cross-section predictions as described in Section 7.3.2.

The resulting estimates of the rates and fractions of the multi-jet background in the selected region

	Control region		Signal region	
Channel	Electrons	Muons	Electrons	Muons
W+HF / W+LF	1.02 ± 0.00	1.1 ± 0.00	1.03 ± 0.02	1.01 ± 0.02
$t\bar{t}$	1.01 ± 0.04	0.95 ± 0.04	0.95 ± 0.03	0.95 ± 0.03
Single top	1.00 ± 0.04	0.99 ± 0.04	0.99 ± 0.04	1.03 ± 0.03
Z+jets / dibosons	Fixed	Fixed	Fixed	Fixed

Table 8.3: Scale factors for the combined contributions from W+HF/W+LF, from $t\bar{t}$ and single top-quark production in the signal and control region as obtained from the simultaneous binned maximum likelihood fit to the $E_{\mathrm{T}}^{\mathrm{miss}}$ distribution. The quoted uncertainties represent the statistical uncertainty of the fit.

$E_{\mathrm{T}}^{\mathrm{miss}} > 30\,\mathrm{GeV}$ in both lepton channels and for both, the tagged and control datasets, are given in Table 8.4. The corresponding $E_{\mathrm{T}}^{\mathrm{miss}}$ distributions leading to these results are shown in Figure 8.1 for the electron channel and in Figure 8.2 for the muon channel.

	Control region		Signal region	
Channel	Events	Fraction	Events	Fraction
Electrons central	$11\,000 \pm 1\,900$	2.9 %	790 ± 130	2.5 %
Electrons forward	$23\,000 \pm 3\,900$	13.2 %	$1\,700 \pm 280$	14.4 %
Electrons combined	$34\,000 \pm 5\,700$	6.1 %	$2\,500 \pm 420$	2.9 %
Muon	$32\,000 \pm 5\,500$	3.9 %	$5\,000 \pm 840$	7.4 %

Table 8.4: Estimate of the multi-jet background in the for the signal and control region using the binned maximum likelihood fit to the $E_{\mathrm{T}}^{\mathrm{miss}}$ distribution. The quoted numbers are the expected number of events in each region, the uncertainties given reflect the uncertainty in the multi-jet normalisation of 17 % (see Section 10.3).

8.3 Matrix method results and the comparison to the other methods

The matrix method results in the signal region are given in Figure 8.3. Overall, the matrix method performed poorly for both lepton channels compared to the jet-electron and the anti-muon method. The data/MC agreement is worse in both electron and muon channels compared to the other methods. For more kinematic distributions generated by the matrix method, see Appendix B. In the analysis presented here, the jet-electron method in the electron channel and the anti-muon method in the muon channel is chosen to generate the multi-jet background sample. The multi-jet background in all the distributions that were presented in Chapter 7 and in the distributions in the following chapters are provided by these two methods.

Although the matrix method is not used as a template for the multi-jet background in this analysis, it is used to derive an uncertainty on the normalisation (17 %) and the shape of the multi-jet background events. The estimation method for these uncertainties are described in Section 10.3. During the earlier analyses performed on this channel for both 7 and 8 TeV centre-of mass collisions, a flat normalisation uncertainty of 50% was assigned on the multi-jet background rates and no shape uncertainty for this background was evaluated. This number was a conservative guess and no detailed study was performed to evaluate this uncertainty due to the lack of additional multi-jet background estimation methods to compare to.

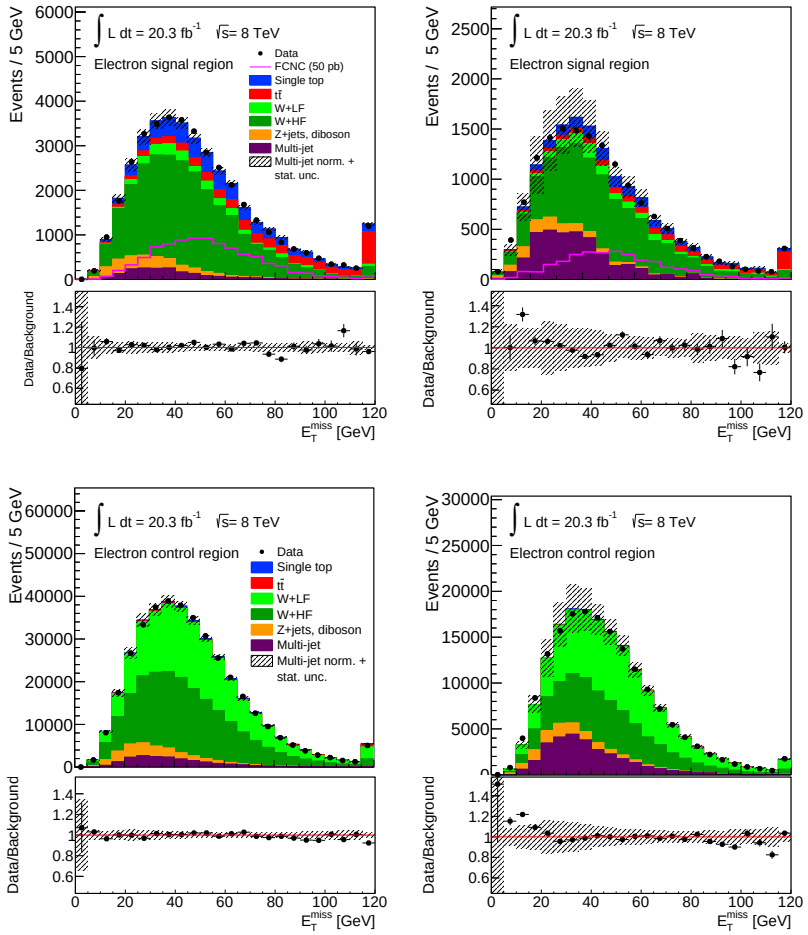

Figure 8.1: Fitted $E_{\mathrm{T}}^{\mathrm{miss}}$ distributions for the signal (top row) and control sample (bottom row) for electrons in the central (left) and forward (right) regions, respectively. The error bands denote the combined MC statistical and the assigned multi-jet rate uncertainty of 17 % (see Section 10.3).

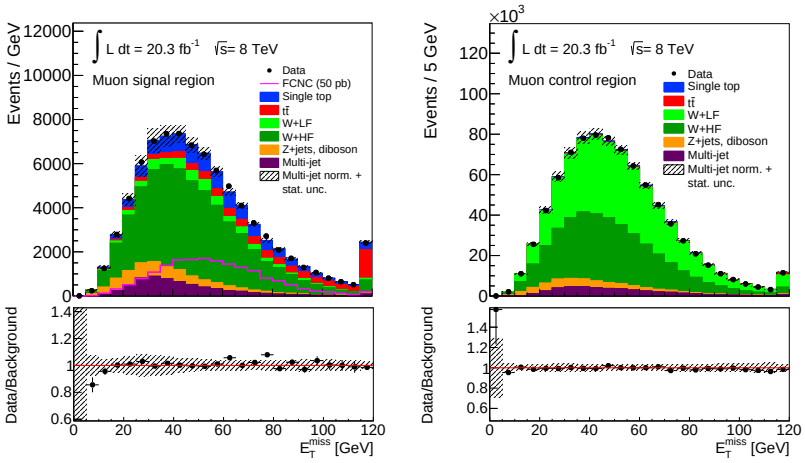

Figure 8.2: Fitted $E_{\mathrm{T}}^{\mathrm{miss}}$ distributions in the muon channel for the signal (left) and control samples (right). The error bands denote the combined MC statistical and the assigned multi-jet rate uncertainty of 17 % (see Section 10.3).

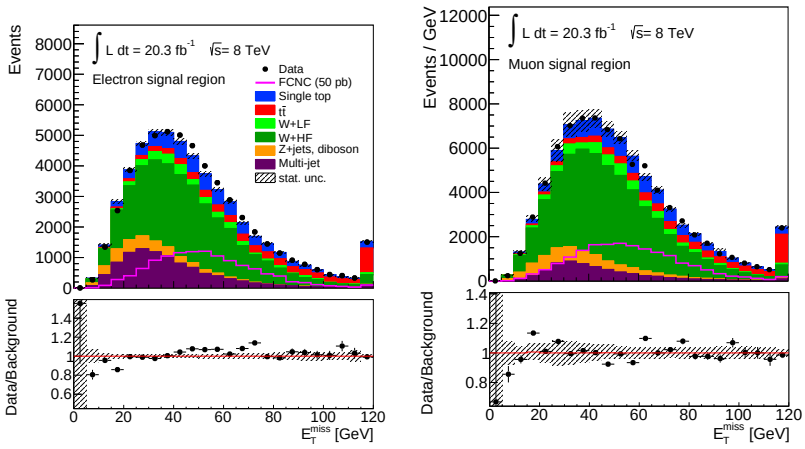

Figure 8.3: $E_{\mathrm{T}}^{\mathrm{miss}}$ distributions in the signal region for electron channel (left and) muon channel (right) where the mutli-jet contributions are generated by the matrix method. The error bands denote the combined MC statistical and the assigned multi-jet rate uncertainty of 17 % (see Section 10.3).

CHAPTER 9

Signal Separation

Up to this point, everything that has been explained specific to the analysis presented here was about the preparation of the data and the MC simulations. The ATLAS data have been processed in order to reconstruct the physics objects. Signal and background MC samples have been prepared and an event selection has been applied to select events with the same topology of the FCNC at top-quark production processes. The next step is to be able to discriminate the signal events from the SM background. For this purpose, simply applying the event selection described in Chapter 7 is far from being sufficient due to the following reasons. First of all, the signal event topology is either identical or very similar to many of the background topologies. This makes it almost impossible to distinguish any shape differences by simply looking at kinematic variables. Secondly, the previously observed upper limits on the cross-sections of the FCNC various processes is of the order of a few picobarns, which means that a difference in the rates of the data and the SM background is very difficult to observe. Furthermore, large statistical and systematic uncertainties can also diminish any visible signal if it exists. Because of these reasons, multivariate analysis methods, which take advantage of not only event rates of single variable, but a number of kinematic variables therefore enhancing the signature of a possible signal significantly, are incorporated into statistical analyses in high energy physics.

The multivariate technique used in the analysis presented here is an artificial neural network (ANN) based on machine learning. The software that is used in the analysis presented here is NeuroBayes® [169].

9.1 Artificial Neural Networks with NeuroBayes®

There are several ways of constructing ANN algorithms. In this thesis, the implementation in NeuroBayes® is discussed. The animal brain is composed of specialised cells, which are called neurons and each neuron is connected to many other neurons. Neurons receive signal and are stimulated either by signals

from the sense organs or by other neurons. When the amount of stimuli reaches a certain threshold, the neuron itself sends out a signal. Similarly, the ANNs are constructed by nodes, sometimes called as "neurons", which are connected to each other. When the nodes are "stimulated" by other nodes, they send out a signal. The importance of the connection between each node is called the weight. The ANNs are usually formed in several layers. The NeuroBayes® ANN is composed of three layers, namely the input layer, the hidden layer and the output layer. The signal flow is always from one layer to the other and not the other way around (i.e. from input layer to the output layer). Because of this, the ANN type that is adopted in Neurobayes® is called three-layer feed-forward ANN. The number of nodes in the input layer is equal to the number of input variables (plus a bias node, see below) that is needed to be processed as each variable is assigned to a single input node. The number of hidden layers is adjustable by the user. It should be large enough to provide sufficient degree of freedom to software to the process the information. However too many hidden layer nodes can make the ANN prone to the statistical fluctuations. The number of output nodes is related to the operation that is demanded from the ANN; for a classification process (a yes-or-no output, as in the case for this analysis) there is one node in the output layer. The structure of the layers and nodes in NeuroBayes® is illustrated in Figure 9.1.

The working principle of the ANNs implemented in NeuroBayes® is as follows: a classifier function C is defined as a superposition of nonlinear functions k_j:

$$C(\vec{x}) = w_0 + \sum_{j=1}^{N} w_j k_j(\vec{x}), \tag{9.1}$$

where coefficients w_j are the weights mentioned above and the vector $\vec{x}$ holds all the input variables. N is the dimension of the superposition and can be chosen freely. The nonlinear functions k_j can be replaced by only one nonlinear function k, which turns Equation 9.1 into form:

$$C(\vec{x}) = w_0 + \sum_{j=1}^{N} [w''_j k(w'_{0j}) + \sum_{l=1}^{D} w'_{jl} x_l]. \tag{9.2}$$

The w'_{jl} terms are the weights in Equation 9.1 and the w''_j represent the scales of the nonlinear function k. Apart from the nodes that hold the kinematic variables, an additional node in the input layer is added, which is called the bias node. The w'_{0j} terms are the weights between bias node and the other nodes in the hidden layer. The idea behind the addition of the bias node is to find the correct working points for the activation functions, which are used for the non-linear function k. The weights w'_{ij} scale the linear combination of the input variables. In analogy to the animal brain, they represent the threshold of a neuron to fire. For the nonlinear function k, a symmetric sigmoid function of the form:

$$k(x) = S(x) = \frac{2}{1 + e^{-x}} - 1 \tag{9.3}$$

is used, which maps the range of x to an interval of [-1,1].

Finally, another sigmoid function is employed for the output of the ANN without an overall scale w. The ANN output can then be written as:

$$C(\vec{x}) = S\Big(\sum_{j=1}^{N} w''_j S(w'_{0j} + \sum_{l=1}^{D} w'_{jl} x_l) \Big). \tag{9.4}$$

The weights between the nodes, the sigmoid functions k_l and the classifiers are also shown in Figure 9.1.

The classification functionality of NeuroBayes® is used to determine the background- and signal-like events in the data by employing the kinematic variables as input for each node in the input layer. The target value for signal events is 1 whereas the target value for background events is -1. However, the actual ANN output is a continuous distribution between -1 and 1. Therefore the signal-and background-like events can be separated with a certain efficiency.

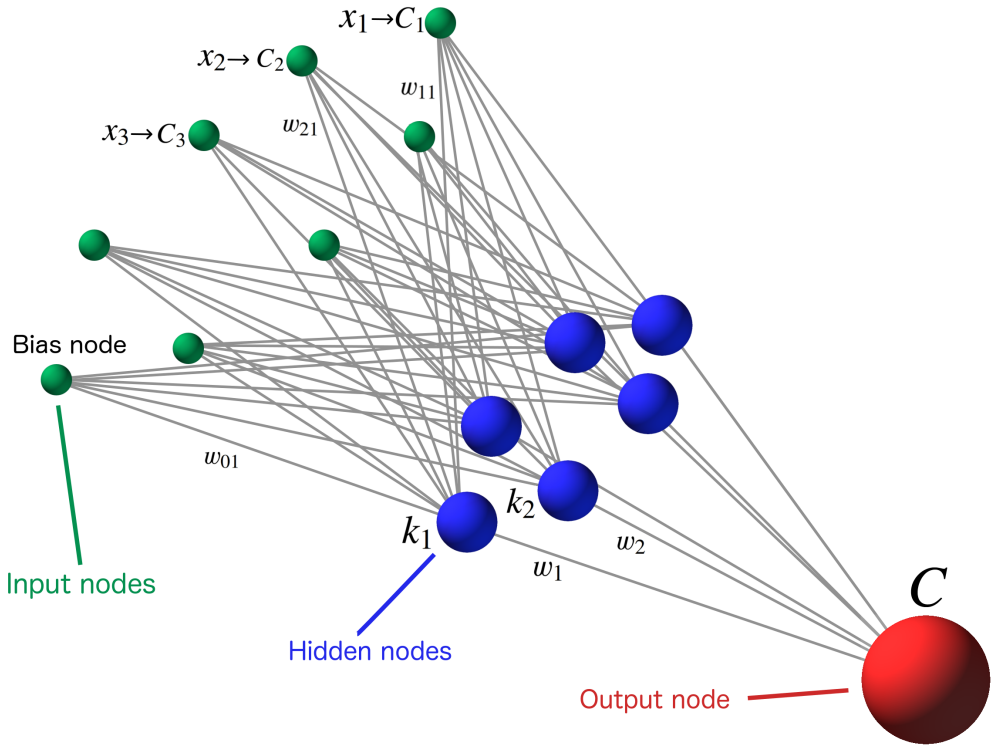

Figure 9.1: Illustration of ANNs implemented in NeuroBayes®. Green, blue and red spheres represents the nodes in the input layer, hidden layer and the output layer respectively. The weights are also shown for a few layers.

9.1.1 Neural network training

In order to train the ANN, the MC simulations are employed as input. The signal MC sample is trained against the sum of all SM background samples[1]. Many kinematic variables are constructed using the physics objects after the event selection, i.e. a b-tagged jet, $E_{\mathrm{T}}^{\mathrm{miss}}$ and a lepton for the ANN input. The number of possible kinematic variables, which can be reconstructed out of these three objects is significantly high.

The *entropy loss function* used for the training is of the form:

$$E = \sum_{i}^{\text{events}} \log\left(\frac{1 + C_i^{\text{target}} \cdot C_i}{2} + \epsilon\right). \tag{9.5}$$

For event i, C_i^{target} is the target output, namely -1 and 1 for background and signal events respectively.

[1] For the background processes involved in the ANN training, only the ones that are simulated (not data-driven) are used, i.e. the multi-jet background is excluded from the training.

For a given event and a set of weights, the entropy loss function is used to calculate the rate of the misclassification. The function is minimised by an algorithm called *back propagation* [170]. The weights are updated after 200 events in the ANN, depending on how large E changes when the weight between two nodes is varied. When convergence is reached the training is stopped.

The sensitivity to the statistical fluctuations mentioned briefly in the previous section is called overtraining and it should be avoided. Usually every multivariate analysis technique is prone to overtraining one way or another. In the case of NeuroBayes®, Bayesian regularisation techniques are used in order to prevent overtraining [171]. In this method, during the training process, the weights are gradually reduced in addition to the variation of the weights in the entropy loss function, therefore the statistical fluctuations are decreased. The training is then only sensitive to recurring patterns. Nevertheless, the occurrence of overtraining is tested and details are explained in Section 9.2.

9.1.2 Preprocessing of the input variables

In NeuroBayes®, before the ANN training, a preprocessing procedure of the input variables is performed. The preprocessing consists of three steps: transformation of the variables, sorting of the variables depending on their signal separation power and decorrelation of the variables.

As a first step, a nonlinear transformation is applied on the input variables which converts the variables into flat distributions. The outcome distribution has a variable bin width where each bin contains roughly the same number of background and signal events. A purity distribution is obtained from the flat distribution using the following definition:

$$P_i = \frac{N_i^{\text{signal}}}{N_i^{\text{signal}} + N_i^{\text{background}}} \tag{9.6}$$

where i is the particular bin in the flat distribution and N_i^{signal} and $N_i^{\text{background}}$ are the number of entries in that bin for signal and background, respectively. In order to suppress the influences from possible statistical fluctuations, a spline fit is performed on the purity distribution resulting in a smooth function that reflects the purity for each bin. The resulting function is then applied on the original variable and a transformation into a Gaussian distribution is applied where the mean is positioned at 0 and its variance is scaled to 1. This procedure of transforming the input variables provides the optimum working conditions to the ANN training [172]. The transformation also avoids the influences that can be caused by extreme outliers.

The second step is the decorrelation of the input variables in order to maximize the performance of the ANN training. Figure C.2 shows the correlation matrix of the input variables after decorrelation.

Finally, the third step is the ranking procedure. First, the *total correlation to target* (exactly -1 and 1 for signal to background) is calculated for all variables in percentages. Then a total significance of the correlation is calculated in terms of standard deviations. The ranking of the input variables is performed in an iterative manner. All candidate[2] input variables are introduced to the ranking procedure. The total significance is calculated and then the variable with the least contribution to the total significance is removed and the total significance is recalculated. The contribution of an individual variable is derived by removing each variable one at a time to calculate the decrease in significance by excluding only this variable. The variable that causes the smallest significance decrease is assumed to be the least contributing and removed. The significance loss caused by removing that particular variable is called

[2] Not all the variables that are introduced to the preprocessing are used in the ANN training. Among all the variables, only a list of most significant variables, i.e. the variables with the best separation power, is chosen.

additional significance. The last remaining variable is ranked the best in terms of its separation power.

In addition to the total and additional significance, three quantities are also calculated during preprocessing:

- **Single significance**
  The single significance of a variable is the total significance calculated only from that variable. Naturally, the variable that is ranked the best has equal single and additional significance.

- **Significance loss**
  It is the loss of significance when only a particular variable is removed from the set of input variables. This is the significance loss mentioned above.

- **Global correlation**
  This is the correlation of a variable to all the other input variables.

After the ranking procedure, the variables are fed to the ANN training. However, the number of input variables that will go into the training can be adjusted by the user. Furthermore, a variable can be excluded although it is ranked as a good variable. There are several reasons for this. For instance, a variable can have a bad data/MC agreement which could cause a bias. Or a variable can have a high additional significance only when used together with other variables. However these variables can be ranked low and therefore excluded. This causes the variable with high additional significance to lose its separation power. In the following section, the choice of input variables and the training results are presented.

9.2 ANN training results

A measure of the separation power of the network is given by the Gini index which is determined as follows: after the training, the so-called Lorentz curve is derived, which is the dependence of the signal efficiency (ratio of selected signal events by the training over all signal events) on the total efficiency (ratio of selected events over all events), see Figure 9.2 (blue curve). The Gini index is then given by the area between the Lorentz curve and the unity line, divided by the area below the unity line. If the Lorentz curve lies on the unity line itself (Gini index = 0), no separation is achieved at all since signal and background events are equally classified by the network. The maximum possible value of the Gini index is limited to 0.5 (or 50 %) since the ratio of signal/background events in the training is chosen to be 50:50.

After preprocessing, it is possible to cut on the significance of the variables, in order to incorporate only those which include relevant information that is not already incorporated by other variables. Removing variables with a significance below 3σ has no measurable effect on the Gini index. However, removing variables with higher significance tends to result in a lower Gini index, signalling a worse separation power. In the end, the number of variables is chosen such that with a minimal set of variables a reasonable separation between the signal and background processes is achieved. If an additional variable does not add a significant improvement, it is not taken into account.

This leads to 13 variables remaining for the network as listed in Table 9.1. The modelling of the input variables is checked in the control region as described in the previous section.

The $qg \to t \to b\ell\nu$ process is characterised by three main differences from SM processes that pass the event selection requirements. Firstly, in single top-quark production via FCNC, the top quark is produced almost without any transverse momentum, since the main contribution is the $2 \to 1$ process.

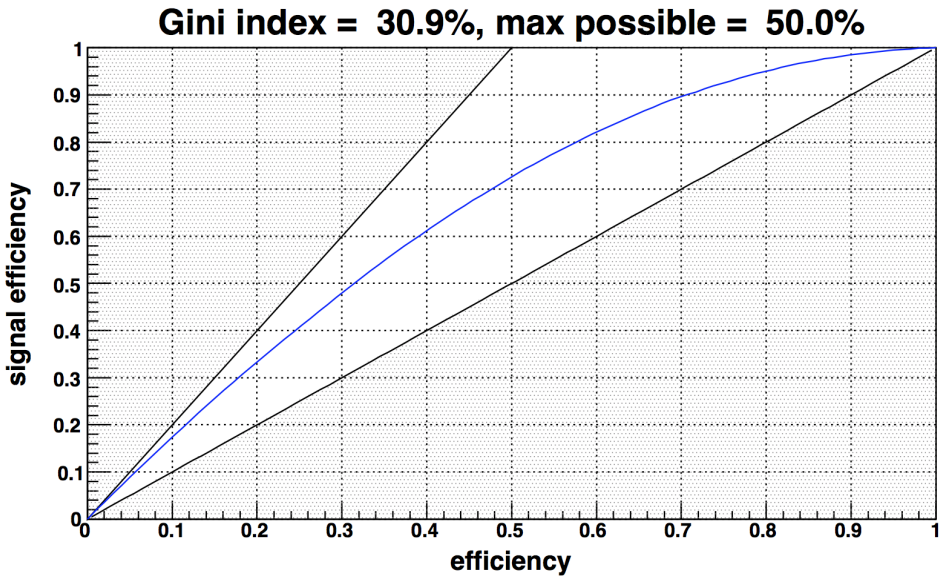

Figure 9.2: Lorentz curve (blue) for the network used.

Variable	Definition	Significance (σ)
$m_{\mathrm{T}}(\mathrm{top})$	Transverse mass of the reconstructed top quark	75
p_{T}^{ℓ}	Transverse momentum of the charged lepton	39
$\Delta R(\mathrm{top}, \ell)$	Distance in the η–ϕ plane between the reconstructed top quark and the charged lepton	33
$p_{\mathrm{T}}^{b\text{-jet}}$	Transverse momentum of the b-tagged jet	25
$\Delta\phi(\mathrm{top}, b\text{-jet})$	Difference in azimuth between the reconstructed top quark and the b-tagged jet	22
$\cos\theta(\ell, b\text{-jet})$	Opening angle of the three-vectors between the charged lepton and the b-tagged jet	21
q^{ℓ}	Charge of the lepton	20
$m_{\mathrm{T}}(W)$	W-boson transverse mass	15
η^{ℓ}	Pseudorapidity of the charged lepton	14
$\Delta\phi(\mathrm{top}, W)$	Difference in azimuth between the reconstructed top quark and the W boson	12
$\Delta R(\mathrm{top}, b\text{-jet})$	Distance in the η–ϕ plane between the reconstructed top quark and the b-tagged jet	11
η^{top}	Pseudorapidity of the reconstructed top quark	7.0
p_{T}^{W}	Transverse momentum of the W boson	3.6

Table 9.1: Variables used in the training of the neural network ordered by their descending importance.

Hence, in the considered FCNC processes, top quarks are produced with a much softer p_{T} distribution than in SM top quark production, which is why variables correlated to the top quark kinematic properties form the most significant input to the network. Secondly, the strong FCNC top production is highly charge asymmetric which provides additional separation power from the considered SM background processes. This includes also the charge asymmetric SM single top-quark production, which has a smaller asymmetry. The FCNC processes are predicted to produce 3.2 times more single top quarks than antitop quarks, whereas in SM single top-quark production, and all other SM backgrounds this ratio is at most two. Further, unlike in the W/Z+jet and diboson backgrounds, the W boson from the top decay has a harder p_{T} spectrum leading to higher boosts and smaller relative angles of its decay products in the laboratory frame.

The shape distributions of the three most important variables are shown in Figure 9.3 for the combined electron and muon channels.

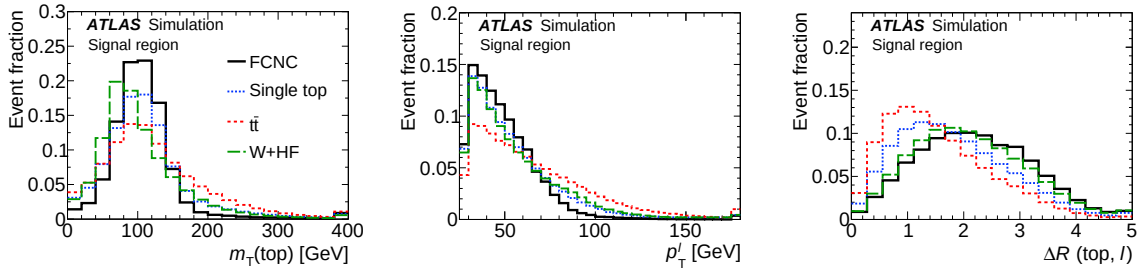

(a) (b) (c)

Figure 9.3: Shape distributions of the three most important discriminating variables: (a) transverse mass of the reconstructed top quark; (b) the transverse momentum of the charged lepton; and (c) the distance in the $\eta - \phi$ plane between the charged lepton and the reconstructed top quark [86]. Only the dominant backgrounds are shown. The signal and each background are area normalised to unity. The last histogram bin includes overflows.

As mentioned before, the ratio of signal to background events in the training was 50:50, where different background processes are weighted according to their number of expected events. 20 nodes are used in the hidden layer as it gives the best results in terms of separation power of the final network. Only processes from simulated events are considered in the training, i.e. no multi-jet events are used. In order to ensure not to overtrain the neural network, 20 % of the available events are used as test sample. The remaining 80 % are used for the actual training and the training is applied on the whole sample. A study on overtraining check is summarised in Appendix C.1.

Figure 9.4 shows the result of ANN training. The signal is represented with red and the background is represented with blue line. The distributions are area normalised to unity. The signal events are accumulated mostly towards +1 and background events are accumulated towards -1 as explained in Section 9.1.1. A very clear separation between the signal and the background samples is visible. This distribution emphasises on the power of multivariate analysis techniques in analyses such as the one presented here where the expected signal and background topologies are very similar. The shape distributions of the best three variables in terms of separation power (Figure 9.3) show only a mild difference between the signal and the background. Despite the fact that these are the most discriminating variables, the separation power of the ANN is far more superior compared to what one can obtain from single variables.

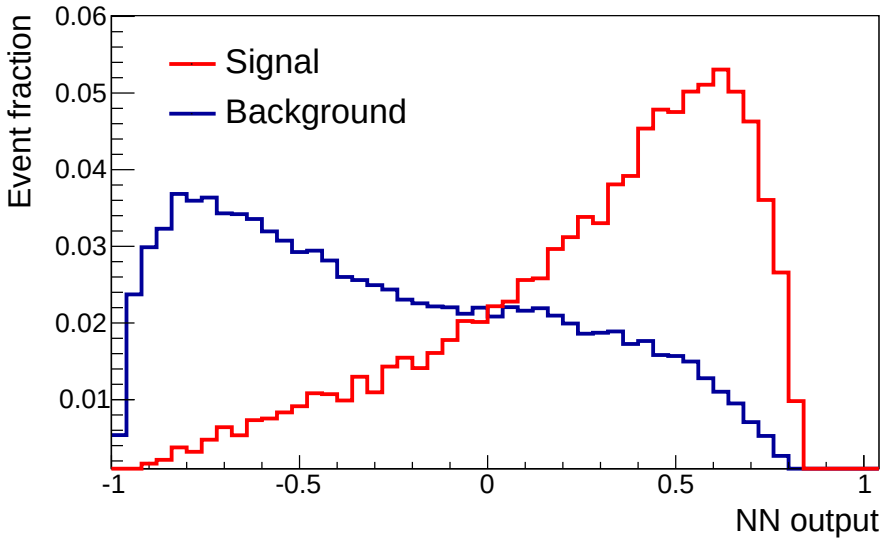

Figure 9.4: The distribution of the ANN output. The number of signal and background events are each normalised to unity.

9.3 Control distributions of input variables and applying the ANN on data

The input variables that are picked up by the ANN have to be validated. The stacked distributions of the three most important discriminating variables (except for the transverse momentum of the charged lepton, as it is already shown in Chapter 7) are presented in Figure 9.5. The rest of the variables, in the electron and muon channels separately, can be found in Appendix D. Overall, a very good agreement between the data and the MC events is observed in both control and signal regions for every variable that is used in the training.

It should be noted that some of the reconstructed variables have been excluded from the training on purpose. For these variables, the MC simulation provides a poor description of the data in the signal region. This would introduce a bias and can mimic a fake signal. Since the expected cross-section of the FCNC involving top quark events is very small, it is considered that an actual signal cannot cause a significant data/MC disagreement. Therefore the bad description of the data by the MC events in these variables is attributed to bad modelling in the MC. The excluded variables are presented in Figure 9.8.

Since the training of the ANN is done with simulated events, it is necessary to validate the output distribution with observed events. Therefore, the training is applied on the data and the MC and the stack plots of the neural network output are produced. Figure 9.6 shows the neural network output distributions in the control and signal regions for the combined electron and muon channels. The same distributions for the electron and the muon channels separately can be found in Appendix D. In these figures all processes are normalised to the result of the binned maximum likelihood fit used to determine the fraction of multi-jet events. The hatched bands represent the combination of statistical uncertainty and the systematic uncertainties. The signal contribution arising from the combination of both the $ug \to t$ and $cg \to t$ processes are shown with an assumed cross-section of 50 pb.

Overall, the MC agrees well with the data within the uncertainties. In Figure 9.6(a), although no data point is outside the uncertainty band, a trend is visible. This is thought to be due to the following: the training is performed in the signal region, which is dominated by the W+HF background events.

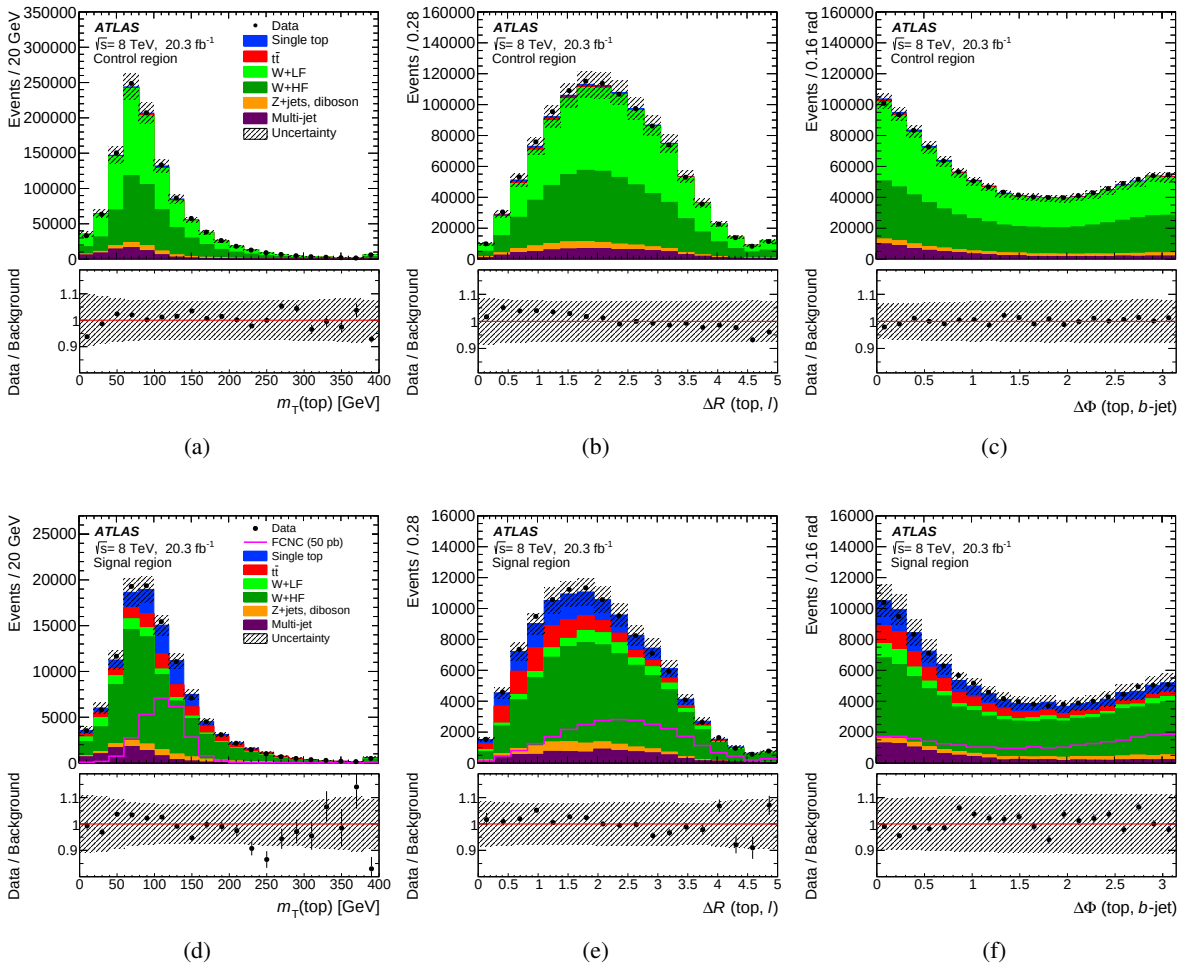

Figure 9.5: Distributions of three important discriminating variables (except for the transverse momentum of the lepton): (a) and (d) the top-quark transverse mass in the control and signal regions; (b) and (e) the ΔR between the lepton and the reconstructed top quark in the control and signal regions; (c) and (f) the $\Delta\phi$ between the jet and the reconstructed top quark [86]. All processes are normalised using the scale factors obtained in the binned maximum-likelihood fit to the $E_{\mathrm{T}}^{\mathrm{miss}}$ distribution. The FCNC signal cross-section is scaled to 50 pb and overlayed on the distributions in the signal region. The last histogram bin includes overflow events and the hatched band indicates the combined statistical and systematic uncertainties, evaluated after the fit discussed in Section 11.1.4.

However it is applied on the selection of the control region which, which is dominated by the W+LF background events. This could introduce a kinematic difference between the signal and the background region. The response of different kinematic regions can be different to the ANN. Again, it is considered that the trend that is visible ANN distribution cannot be the sign of a possible FCNC signal in the control region, where the signal-like events are highly suppressed by inverting the b-tagging requirement. On the contrary, in the signal region (Figure 9.6(b)) where a sign of a possible signal could occur, the data and the SM background agrees almost perfectly.

Figure 9.7 shows the shape distribution of neural network output where the signal and the background processes are normalised to unity.

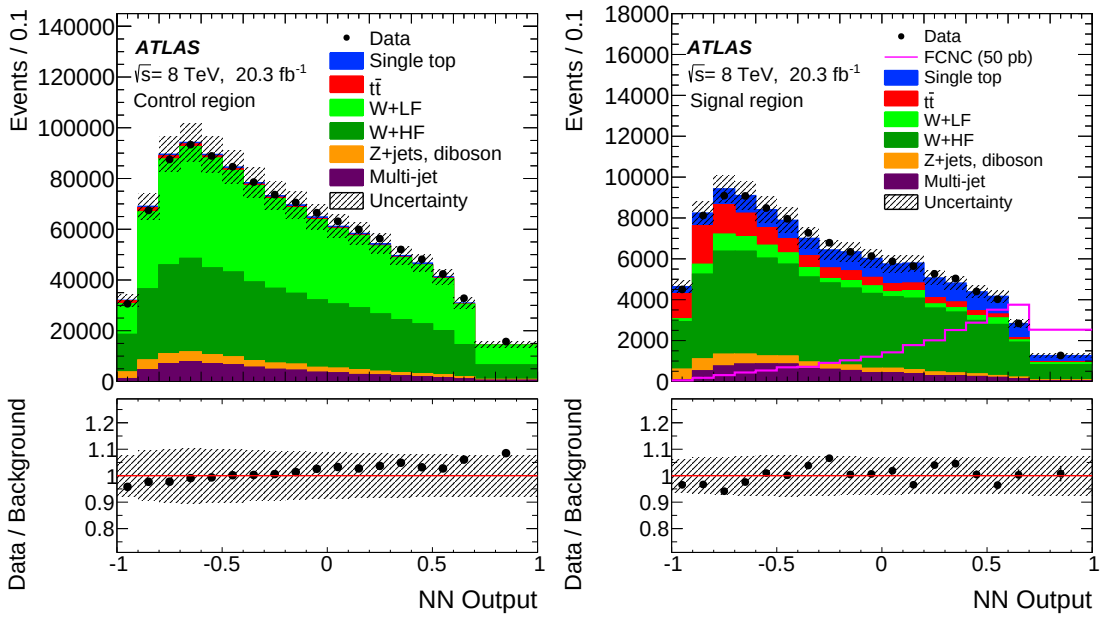

(a) (b)

Figure 9.6: Neural-network output distribution (a) in the control region and (b) in the signal region [86]. The shape of the signal scaled to 50 pb is shown in (b). All background processes are shown normalised to the result of the binned maximum-likelihood fit used to determine the fraction of multi-jet events. The hatched band indicates the combined statistical and systematic uncertainties, evaluated after the fit discussed in Section 11.1.4.

After applying the ANN training on the observed data, no sign of a signal is visible by eye in the output distribution. A detailed statistical analysis is required in order to be able to tell if the most discriminating variable, the neural network output distribution can provide a hint of a signal. Before proceeding to the final statistical analysis, all systematic uncertainties have to be taken into account and their effects have to be evaluated. Chapter 10 details the systematic uncertainties that are considered in the analysis presented here. Chapter 11 explains the statistical analysis and the results.

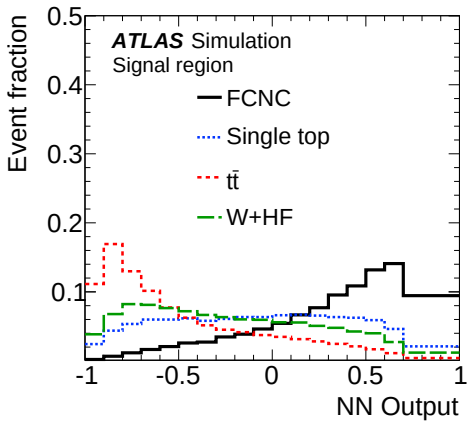

Figure 9.7: Probability density of the neural-network output distribution for the signal and the most important background processes [86].

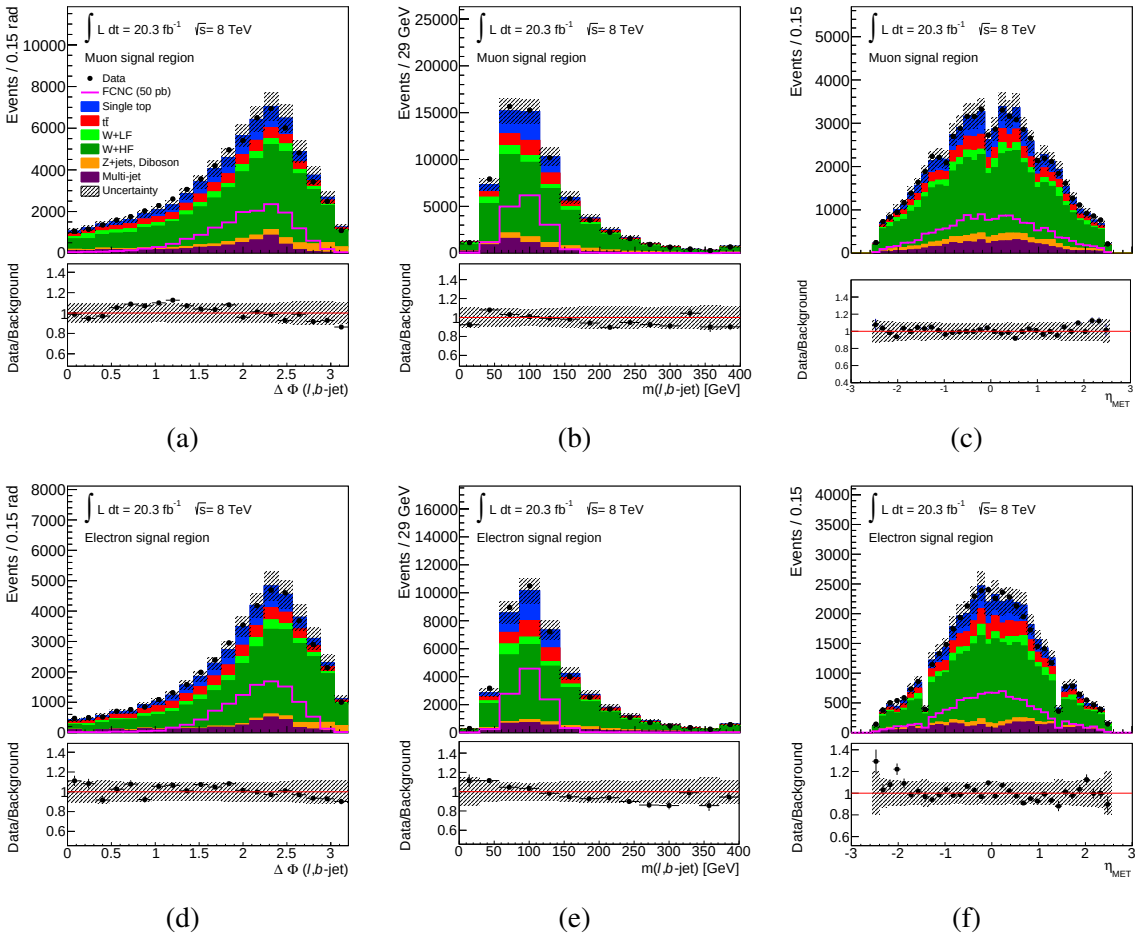

Figure 9.8: The variables which are not used in the neural network training. (a,d) $\Delta\Phi(l, b\text{-jet})$, (b,e) invariant mass of lepton and jet and (c,f) the pseudo-rapidity of the missing transverse energy.

CHAPTER 10

Systematic Uncertainties

This chapter details the systematic uncertainties that are considered in the analysis presented in this thesis. The systematic uncertainties have various sources and most of them originate from the measurements performed by ATLAS detector itself since it is a very complex instrument. For instance the uncertainty on the finite precision of every measurement due to limited detector resolution introduces a systematic uncertainty. One of the greatest source of uncertainties appear during object identification, reconstruction and modelling. Furthermore, each assumption in the MC simulation introduces an uncertainty as well. Limited size of the data and the MC samples also introduce an uncertainty. The MC samples are scaled to their theoretical cross-sections which also have an uncertainty. In addition to these, there are uncertainties introduced during the analysis, for example the re-weighting of the W+LF/HF samples (see Section 7.3.1).

Apart from the uncertainties that are unique to the analysis presented here, the methods recommended for the estimation of the systematic uncertainties are developed by the ATLAS Collaboration. Over the years, these methods are improved and refined as the understanding of each uncertainty increased by each analysis. The ATLAS Collaboration regularly updates the analysers about list of systematic uncertainties and the methods to estimate them.

As mentioned in the previous chapter, the ANN output is the main input used to search for an FCNC signal as it is the single most discriminating variable obtained in the analysis. The systematic uncertainties have two different sorts of effect on the ANN output distribution, namely the rate and shape uncertainties. Systematic uncertainties affect the normalisation of the individual backgrounds and the signal acceptance (rate uncertainties) as well as the shape of the neural network output distribution (shape uncertainties).

A description of each systematic uncertainty is introduced in the following.

10.1 Object modelling

These are the uncertainties arising from the residual differences between data and the MC simulations of the jets, electron and muon reconstruction and the errors on the corrective scale factors. The effects of these uncertainties are propagated to the event yields. Most of the uncertainties presented here arise from the reconstruction of physics objects explained in Chapter 6. The main source of uncertainty comes from the jet energy scale, including pile-up effects, and the modelling of b-jet identification.

10.1.1 Lepton reconstruction

The mis-modelling of muon (electron) trigger, reconstruction and selection efficiencies in simulations are corrected for by the scale factors derived from measurements of the efficiency in data. $Z \to \mu\mu$ ($Z \to ee$ and $W \to e\nu$) decays are used to obtain scale factors as functions of the lepton kinematics (see Sections 6.2.1, 6.2.2). The uncertainties are evaluated by varying the lepton and signal selections and from the uncertainty in the evaluation of the backgrounds. The scale factor uncertainties are around 5 %.

10.1.2 Lepton momentum/energy scale and resolution

Muon momentum scale and resolution

The invariant mass distributions of the $\mu\mu$ system from the Z boson, J/ψ and the Υ are used to derive the muon momentum scale correction factors using a template method (see Section 6.2.2). The uncertainties due to the scale factors are derived by varying them. To evaluate the effect of momentum scale uncertainties, the event selection is repeated with the lepton momentum varied up and down within the uncertainty that is derived while generating the scale factors. The uncertainty on the muon momentum scale is around 1-2% for $\eta < 2.5$.

The uncertainty due to the muon momentum resolution is obtained by varying the invariant mass window of the Z boson. The uncertainty is applied by smearing the muon momentum resolution up and down.

Electron energy scale and resolution

Similar to the muon momentum scale, the electron energy scale uncertainty is derived by varying the electron energy scale factors. The variations are obtained by comparing the likelihood fit with the template methods (see Section 6.2.1) and the uncertainties arising from individual methods. The uncertainties vary between 1-2% for $\eta < 2.47$. Additional uncertainties originate from the modelling of the detector material, hardware modelling and pile-up. The event selection applied on the MC simulations is repeated after varying the energy of the electron by $\pm 1\sigma$.

The systematic uncertainty that is associated with the electron energy resolution is derived by applying a smearing to the cluster energy. The smearing is performed via up and down variations by employing random numbers provided by modified Gaussian distributions.

10.1.3 Jet energy scale

In order to obtain the uncertainty on the JES, the LHC collision data, test-beam data and MC simulations are employed. There are many sources contributing to this uncertainty which are briefly explained here. The uncertainties arise from the quark/gluon composition (flavour composition) of the MC samples,

pile-up, the mis-measurements from close-by jets and the statistical limitations of the samples are some of the contributors to the JES uncertainty.

Overall, the JES uncertainty varies between 2.5 % and 8 % (3.5 % and 14 %) in the central (forward) region, depending on jet p_{T} and η [173]. This includes uncertainties in the flavour composition of the samples and mis-measurements from close-by jets. Additional uncertainties due to pile-up can be as large as 5 % (7 %) in the central (forward) region. An additional jet energy scale uncertainty of up 2.5 %, depending on the p_{T} of the jet, is applied for b-quark induced jets due to differences between light-quark and gluon jets compared to jets containing b-hadrons. The `MultijetJESUncertaintyProvider` tool is used to scale the energy of each jet up or down by 1σ. This change, as well as the changes due to the other components of JES, is propagated to the missing transverse energy calculation and the object and event selection re-applied to measure the effect on the cross-section measurement. The pile-up uncertainty and b-tagged JES uncertainty are added in quadrature to the uncertainty provided by this tool.

10.1.4 Jet energy resolution

The jet energy resolution (JER) is obtained by comparing data and MC simulations in dijet events by employing several different methods (see Section 6.2.3).

In order to account for the impact of the JER uncertainty, the energy of the jets (in this case only one) is smeared by a conservative estimate in a p_{T} and η dependent manner. Similar to the JES, the JER uncertainty is also reflected to the missing transverse energy calculation.

10.1.5 Missing transverse energy:

The uncertainties from the scale and resolution corrections on leptons and jets are propagated to the calculation of the missing transverse energy. Additional inherent uncertainties arise from contributions of calorimeter cells which are not associated to any jets and soft jets ($7\,\mathrm{GeV} < p_{\mathrm{T}} < 20\,\mathrm{GeV}$), originating from e.g. pile-up, `TopoCluster` energy scale and threshold uncertainties and uncertainties within the MC simulation such as the shower modelling, final state/soft radiation and limited knowledge of the dead material. The $Z \rightarrow ll$ events are employed in data to derive the $E_{\mathrm{T}}^{\mathrm{miss}}$ scale and resolution uncertainties. A detailed description of the systematic uncertainties about the $E_{\mathrm{T}}^{\mathrm{miss}}$ can be found in References [174] and [175].

10.1.6 b-tagging efficiency:

The uncertainties arising from the methods used for b-jet identification are evaluated by varying the efficiency corrections in the MC simulations. These uncertainties originate from the methods used to extract the b-tagging efficiency scale factors and have several components. The largest contributions to the b-tagging efficiency uncertainties are due to the production and decay modelling of the jets originating from a heavy flavour quark and the limited knowledge og the JES and JER. The uncertainties are evaluated depending on the p_{T} of the jet, varying from 5-20%. More information on the estimation of the uncertainties on the b-tagging efficiencies can be found in References [161], [176] and [177].

The uncertainties on the c-tagging efficiencies and mistag rate are also estimated. Depending on the p_{T} of the jet, the uncertainty on the c-tagging efficiency varies between 10-25%. The uncertainties on the mistag rate vary between 18-50%. References [178] and [177] provide a detailed description on the estimation of the uncertainties on the c-tagging efficiencies and mistag rate, respectively.

10.1.7 Lepton charge misidentification

The uncertainties that arise from the lepton charge misidentification have been studied and their effects are found to be negligible. Therefore this uncertainty is not included in the final statistical analysis presented here.

10.1.8 Jet vertex fraction

The performance of JVF is measured in data using a tag&probe method in Z+jets events [179]. Two different sources of uncertainties are used to evaluate the systematic uncertainty associated to the data-to-simulation scale factors of the hard scatter jet selection efficiency and the mistag rate for a hard scatter jet. A fit uncertainty is applied to account for the systematic uncertainty from the quality of the scale factors fits. Secondly, a selection uncertainty is evaluated by varying the criteria used to define the hard-scatter. After applying the variations the resulting scale factors are fitted again. The absolute value of the difference between the up (down) variation and the nominal fit is taken as the up (down) selection uncertainty for the hard scatter jet selection efficiency mistag rate scale factors. The fit and selection uncertainties are added in quadrature to obtain the final systematic uncertainty for a given JVF scale factor.

10.2 Theory modelling and MC generators

The systematic uncertainties arising from theory modelling implemented in the MC generators are estimated by varying the parameters for the event generation or by comparing the base samples with alternative samples derived by different generators. For each systematic uncertainty that is taken into account, a rate and a shape uncertainty is derived.

10.2.1 Initial and final state radiation

In order to evaluate the systematic uncertainties arising during the simulation of ISR/FSR, for all the single top-quark backgrounds, the Powheg scale variation samples [180] are used. These are samples which differ from the base sample only with varied generator variables. Factorisation and renormalisation scales are varied independently by factors of 0.5 and 2.0, while the scale of the parton shower is varied consistently with the renormalisation scale using specialised Perugia 2012 tunes. For each background sample, the largest possible variations are considered. For the $t\bar{t}$ background, Alpgen + Pythia samples with the ISR/FSR variations are used. For the signal, the MEtop + Pythia samples with varied parameters are used and the same technique as for single top-quark samples is applied for the evaluation of this systematic uncertainty.

10.2.2 NLO subtraction method

In order to evaluate the systematic uncertainties due to the specific methods in which the parton-level NLO calculation is matched to the parton shower for the s-channel, Wt channel and $t\bar{t}$ backgrounds, the Powheg + Herwig samples are compared to MC@NLO + Herwig samples. For the t-channel background the Powheg + Herwig sample is compared to aMC@NLO + Herwig sample.

10.2.3 Parton showering

The effects of parton shower modelling for the top quark processes are tested by comparing two POWHEG samples interfaced to HERWIG and PYTHIA, respectively. The two sets of samples are compared to each other and the difference between the two (both rate and shape) is taken as the uncertainty.

10.2.4 Top-quark mass

In order to evaluate the uncertainties arising from the top mass assumptions made in MC generation, the signal and background samples generated with varied top-quark masses are compared. The difference is found to be negligible therefore this systematic uncertainty is excluded.

10.2.5 The re-weighting of the W+LF/HF events

The re-weighting of the W+LF/HF events using the transverse momentum of the W boson distribution due to the SHERPA mismodelling is explained in Section 7.3.1. In order to estimate the systematic uncertainties arising from this method, the re-weighted and non-re-weighted W+LF/HF neural network output distributions are compared. The difference in both rate and shape of the distributions is taken as an uncertainty. The final statistical analysis is repeated with and without this uncertainty included and it is found out that this uncertainty has no effect in the final results, therefore it is excluded.

10.2.6 Parton distribution functions

The systematic uncertainties arising from PDFs for the signal and each background event (except for multi-jet background) are estimated. The MC simulation production process is computationally very demanding and usually each sample takes several months to produce. Therefore, it is not feasible to generate the same signal and background samples with different PDFs in order to estimate the PDF uncertainties. Because of this, the events are re-weighted according to each of the PDF uncertainty eigenvectors. The uncertainties are calculated using the formula given in Equation 43 of Reference [181].

An uncertainty envelope from the the CT10 PDF set, the MSTW2008nlo [182] PDF set, and the NNPDF2.3 [183] set is constructed based on the PDF4LHC recommendation [184].

10.2.7 MC statistics

The uncertainties arise from the finite size of the statistics of the MC simulations are taken into account. The size of the MC samples is sufficiently large (see Table 5.1 and 5.2), leaving very few room for statistical limitations. Nevertheless, the statistical uncertainty is estimated and its effect is reflected to the final analysis.

10.2.8 Theoretical cross-section normalisation

The MC simulations for the signal and each background process are normalised using their respective theoretical cross-sections for 8 TeV proton–proton collisions and 20.3 fb^{-1} integrated luminosity as explained in Section 5.3 and 5.4. The theory uncertainties on the cross-sections are taken as systematic uncertainty (except for the multi-jet background). These are purely rate uncertainties. The evaluation of multi-jet background normalisation uncertainty is detailed in the following section.

10.3 Multi-jet background

The uncertainties on the multi-jet background processes, which are partially data-driven, are evaluated differently from the uncertainties on the signal and other background processes which are determined by varying the MC simulations.

In order to estimate the uncertainties on this background, the samples generated with the jet-electron method in the electron channel (see Section 8.1.1) and the anti-muon method in the muon channel (see Section 8.1.2) are compared to the samples that are generated with the matrix method (see Section 8.1.3). After the signal region event selection is applied on all the multi-jet background samples, the event yield differences are taken as the rate uncertainty which is around 17%. In order to estimate a shape uncertainty, the ANN output distributions of the base multi-jet samples are compared to the distribution obtained by the matrix method.

10.4 Luminosity

The measurement uncertainty on the integrated luminosity is estimated using Van-der-Meer scans, where the details of techniques used for the estimation are given in Reference [185]. The uncertainty on the luminosity is 2.8% which is applied on the NN output distribution of the signal and all background samples. This is purely a rate uncertainty.

As mentioned before, all the shape uncertainties are estimated and applied upon the NN output distribution, on which the final statistical analysis is applied. Figure 10.1 shows an example of the impact of a shape uncertainty (JES) on the NN output distribution of the signal, W+HF events and single top-quark events. The rest of the shape distributions for all the uncertainties and backgrounds are provided in Appendix E.

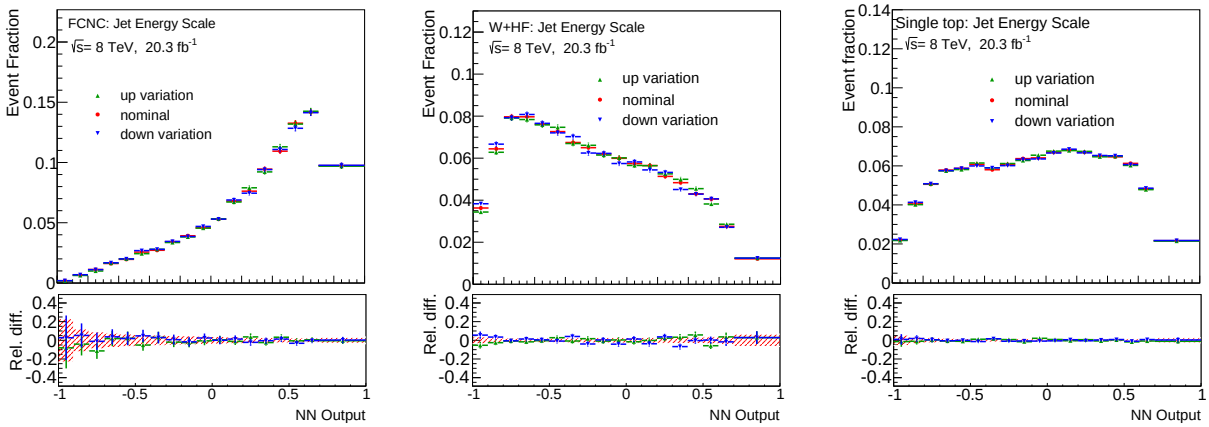

(a) (b) (c)

Figure 10.1: Shape distribution for the JES uncertainty for (a) the signal events, (b) W+HF events and (c) single top-quark events.

CHAPTER 11

Statistical analysis and results

After performing an event selection in order to make the possible FCNC during single-top quark production events more prominent in the data and the MC samples, a discriminator variable is reconstructed (NN output) using machine learning techniques. The NN output distribution is at the heart of the last step of the analysis presented here since the final statistical analysis to search for signal events is based on it. The impact of the uncertainties that arise during the analysis are applied on the NN output distribution.

The next step is to use statistical methods and perform an analysis on the NN output distribution to investigate whether a signal can be observed or not. This chapter details the final statistical analysis and the results.

11.1 Statistical analysis

The software that is used for the statistical analysis is the BILL tool which stands for **BI**nned **L**og **L**ikelihood [186]. BILL is a software that can perform binned maximum likelihood fits based on the frequentist approach. In short, the frequentist statistical approach relates the probability of an event occurring with the frequency of the outcome of a repeatable experiment [5]. The main uses of BILL in high energy physics statistical analyses are measurements of cross-sections of physics processes, computing the significance of an observed signal using hypothesis testing and setting upper limits on the cross-sections. BILL has been developed at the Physics Institute of the University of Wuppertal.

BILL uses histograms as inputs and in this case the NN output distribution is provided to BILL for the statistical analysis.

The NN output distributions of data, signal and each background after the signal region event selection are each prepared as a separate ROOT[1] file. In addition to the NN output distribution, the ROOT file

[1] ROOT is a C++ framework for statistical data analysis and visualisation [187].

also contains the information of number of events for data and each MC sample. Each file is called a template and the set of files mentioned above are called the nominal templates, which do not contain any systematic uncertainties.

For each MC simulation sample, the number of events in the templates are scaled to their theoretical cross-sections for 8 TeV centre-of-mass collision energy with 20.3 fb^{-1} data. The FCNC signal process cross-section is scaled to 1 pb. This number is rather arbitrary, but still compatible with the current upper limits which are of the order of a few picobarns.

The systematic uncertainties are introduced to BILL as follows: a pair of NN output distributions is prepared for each variation of a given systematic uncertainty for each given background and signal. The variations are usually called up and down variations, since the estimation of systematic uncertainties are done in that fashion where the up variation usually have higher event rates and down variation usually have lower event rates compared to the nominal templates. Each distribution is then saved as a ROOT file. These files are then called systematic templates. They differ from the nominal NN output distribution not only in event rates but also in shape (of course if a shape shape uncertainty exists, for instance some of the systematic uncertainties are purely rate uncertainties, i.e. uncertainty in the luminosity measurement). In the end, the number of input files to BILL is in the order of a few hundred.

In order to estimate the signal content in the data (or in the pseudo-data, see Section 11.1.3) a maximum likelihood fit to the NN output distributions is performed. A detailed description of the definition and the usage of likelihood fits is given in Reference [188]. Including all bins of the NN output distributions in the fit has the advantage of making maximal use of all signal events remaining after the event selection, and, in addition, allows the background rates to be constrained by the data. Furthermore, it allows one to scan the whole parameter space. The sensitivity to the background rates is given by the background-dominated region of the NN output distribution, that is the region close to -1.

11.1.1 Likelihood function

The likelihood function used in the fit is given by the product of the Poisson likelihoods of the individual bins of the NN output distribution. The rates of the W+heavy flavour and top quark processes are constrained by Gaussian priors, while the other small backgrounds are fixed in the fit. The rate of the multijet background is also fixed, since the normalisation was already determined in data, while the others are fixed due to their small statistics. The uncertainties of the rates of the latter processes are accounted for in the pseudo-experiments. The usage of pseudo-experiments is explained in Section 11.1.3.

$$L(\beta_j^{\text{s}};\beta_j^{\text{b}}) = \prod_{k=1}^{M} \frac{e^{-\mu_k}\cdot\mu_k^{n_k}}{n_k!} \cdot \prod_j G(\beta_j^{\text{b}};1,\Delta_j) \quad \text{with} \tag{11.1}$$

$$\mu_k = \sum_{j=1}^{S}\mu_{jk}^{\text{s}} + \sum_{j=1}^{B}\mu_{jk}^{\text{b}}\,, \quad \mu_{jk}^{\text{s}} = \beta_j^{\text{s}}\cdot\tilde{\nu}_j^{\text{s}}\cdot\alpha_{jk}^{\text{s}}\,, \quad \text{and} \quad \mu_{jk}^{\text{b}} = \beta_j^{\text{b}}\cdot\tilde{\nu}_j^{\text{b}}\cdot\alpha_{jk}^{\text{b}}\,. \tag{11.2}$$

Here $\tilde{\nu}_j^{\text{s}}$ and $\tilde{\nu}_j^{\text{b}}$ are the predicted numbers of FCNC single top-quark signal or background events of the different components in the selected MC distributions, respectively. M is the number of bins in the templates used in the fit to the data or pseudo-data in the NN output distribution. The index j runs over all signal and background processes that are considered. The number of considered background processes is $B = 5$. The number of observed events in bin k is denoted by n_k. The number of expected events in bin k is μ_k and is given by the sum over the expected number of events in bin k for each process μ_{jk}^{b} or μ_{jk}^{s}, respectively. The number of expected events of a certain process in each bin is given by the product of

the predicted events in the selected MC distributions, $\tilde{\nu}_j^{\mathrm{s}}$ for signal and $\tilde{\nu}_j^{\mathrm{b}}$ for backgrounds, scale factors β_j^{s} and β_j^{b}, and the relative fraction of signal events given by α_{jk}^{s} and background events given by α_{jk}^{b}, respectively. The set of α_{jk} constitutes the normalised template histogram for process j obeying the normalisation condition

$$\sum_{k=1}^{M} \alpha_{jk} = 1\,. \tag{11.3}$$

The scale factors β_j^{s} for signal and β_j^{b} for the backgrounds are the parameters of the likelihood function that are obtained by a fit to the observed data. The background scale factors are constrained by Gaussian penalty terms to account for the *a priori* knowledge on the backgrounds. The Gaussian functions of the background priors have a mean of one and a width of Δ_j which is the relative uncertainty with which the background cross-sections are predicted. We use the cross-section uncertainties as quoted in Section 5.3. The values of β^{FCNC} and for the signal and β^{b} for the background processes after the fit to the data are given in Table 11.1. The values for the background processes are close to one except for the $t\bar{t}$ events. This is considered to be due to the fact that the $t\bar{t}$ events have relatively different event topologies containing in general at least two jets. and for the signal the value is compatible with zero. The significance of this is discussed in the following sections. Before the fit to the data, pseudo-experiments (see Section 11.1.3) are employed in order to validate the method used to extract the scale factors from the fit to the data. The background and the signal processes are fitted to the pseudo-data and the scale factors obtained after the fit are all one for the background processes and compatible with zero for the signal process.

Process	Beta factor
W+HF	1.03 ± 0.02
Single top	1.04 ± 0.05
$t\bar{t}$	0.80 ± 0.04
Signal	-0.43 ± 0.55

Table 11.1: The beta-factors for each process after the fit to the data.

11.1.2 The Q-value test statistic

The compatibility of the observed data with the signal hypothesis, which depends on the coupling constants and the background hypothesis, is evaluated by performing frequentist hypothesis tests based on pseudo-experiments where the pseudo-experiments also contain the effects of the systematic uncertainties. Two hypotheses are compared, the null hypothesis H_0 and the signal+background hypothesis H_1, which includes FCNC single top-quark production. The signal strength used for the null hypothesis is zero and the signal strength used for the signal+background hypothesis is one. For both scenarios, ensemble tests, i.e. large sets of pseudo-experiments, are performed. To distinguish between the two hypotheses the so-called Q value is used as a test statistic. It is defined in (11.4) and basically consists of the logarithm of the ratio of the likelihood function L, evaluated for the different hypotheses.

$$Q = -2\ln\left(\frac{L\left(\beta^{\mathrm{FCNC}}=1\right)}{L\left(\beta^{\mathrm{FCNC}}=0\right)}\right). \tag{11.4}$$

The βs are the pre-fit signal strengths, which are used to define the corresponding likelihoods in the equation above. $L\left(\beta^{\mathrm{FCNC}}=1\right)$ corresponds the signal+background hypothesis and $L\left(\beta^{\mathrm{FCNC}}=0\right)$ corresponds to the null hypothesis. The Q-value distributions, $q_0(Q)$ for the null hypothesis and $q_1(Q)$ for the signal hypothesis, are generated by running a large set of pseudo-experiments. By normalising these distributions the probability densities $\hat{q}_0(Q)$ and $\hat{q}_1(Q)$ are obtained.

To test the compatibility of the observed data with the two hypotheses, H_0 and H_1, the observed Q-value Q^{obs} is computed by fitting the signal and background discriminant distributions to data and comparing Q^{obs} with the two probability densities $\hat{q}_0(Q)$ and $\hat{q}_1(Q)$.

In the analysis that is presented here, 100000 pseudo-experiments are used for the Q-value test statistics. The probability density distributions for null and signal hypotheses are shown in Figure 11.1. The observed Q-value is also shown.

In order to search for a hint of the existence of FCNC during top-quark production processes, there are several criteria considered, which are listed below. Overall, no sign of signal is observed in ATLAS data with 20.3 fb^{-1} at 8 TeV centre-of mass energy, due to following reasons. First of all, no significant rate differences is observed between the data and the SM backgrounds in the neural network output distribution, especially in the sensitive region, i.e. the region around 1. Secondly, the beta-factor for the signal processes during the fit to the data is negative (see Table 11.1) and it is compatible with zero within the error. The negativity indicates that the fit tries to suppress the signal process for a better match to the data. Lastly, the observed Q-value is 5 which is compatible with the mean value of the Q-value distribution of the background only hypothesis (see Figure 11.1).

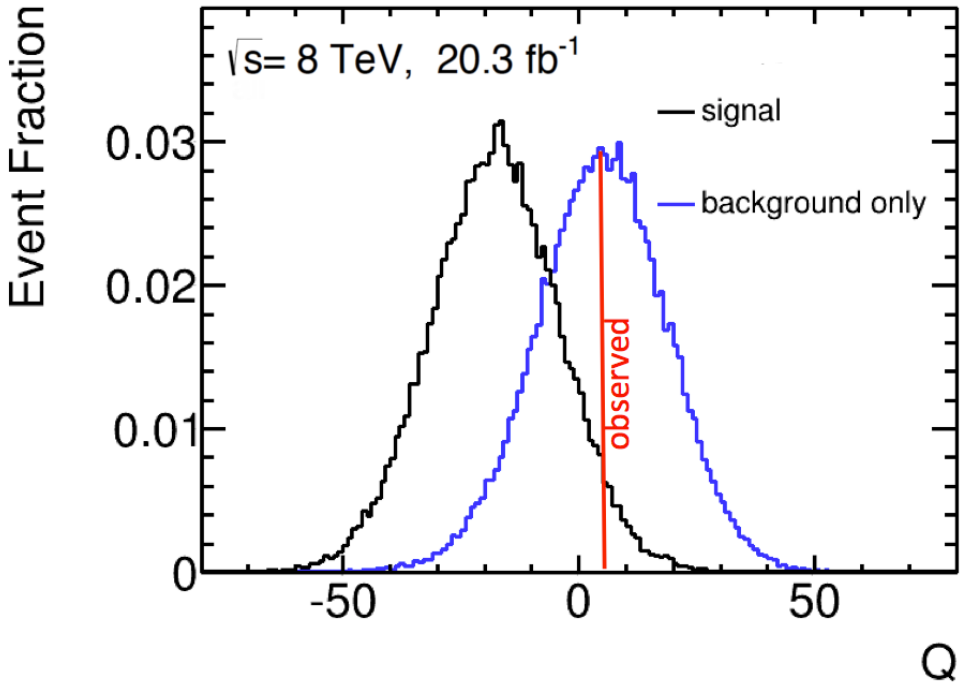

Figure 11.1: Q-value distributions for null (background only) and signal hypotheses. The position of the observed Q-value is also shown with the red line.

11.1.3 Exclusion limits

As no sign of FCNC during top-quark production processes is observed, expected and observed upper limits on the cross-section of the signal process are set using the Q-value distributions which are obtained by hypothesis testing. The null hypothesis H_0 and the signal hypothesis H_1 are compared using the Q-value test statistics as explained in the previous section. The CL_s method [189] is used to derive confidence levels (CL) for a certain value of Q^{obs}. Based on the Q-value probability densities $\hat{q}_0(Q)$ and $\hat{q}_1(Q)$ the following p-values are computed:

$$p\left(Q^{\text{obs}}\right) = \int_{-\infty}^{Q^{\text{obs}}} \hat{q}_0\left(Q'\right) dQ' \tag{11.5}$$

$$p_{\text{s+b}}\left(Q^{\text{obs}}\right) = \int_{Q^{\text{obs}}}^{\infty} \hat{q}_1\left(Q'\right) dQ' \,. \tag{11.6}$$

The definition of CL_s is given by:

$$CL_s = \frac{p_{\text{s+b}}}{1 - p_{\text{b}}} \,. \tag{11.7}$$

Due to the denominator, the CL_s method includes the sensitivity to distinguish between the considered hypotheses and thus avoids spurious exclusions. A particular signal hypothesis H_1, determined by given coupling constants κ_{ugt} and κ_{cgt} is excluded at the 95 % CL if a $CL_s < 0.05$ is found. The details of the procedure are explained in the following: for simplicity, the usage of pseudo-experiments for the statistical analysis for limit setting is explained for the NN output distribution for one background, one signal and one observed data sample and for one systematic uncertainty. For the expected limit, one pseudo-experiment is a variation of the NN output distribution of the background using Poisson sampling. Each bin content of the background NN output distribution is varied using the Poisson distribution as follows:

$$P(x) = \frac{e^{-\lambda}\lambda^x}{x!} \tag{11.8}$$

Here, e is Euler's number, λ is the bin content of the given bin, and x takes positive integer values, therefore $P(x)$ is a discrete distribution. A random number generator uses the $P(x)$ distribution as a seed and throws an integer therefore, the probability of the number being chosen is by the random number generator is maximum near $x = \lambda$. This procedure is repeated for each bin content of the NN output distribution. Furthermore, the effect of the systematic uncertainty is included by sampling from a standard normal distribution (a Gaussian distribution with mean at zero and one standard deviation at unity). For a given bin, the difference between the bin content of the up variation of the systematic uncertainty and the bin content of the pseudo-experiment generated using the Poisson distribution is taken (let's call it up content). The same is done for the down variation as well (down content). Then the random number generator uses the standard normal distribution as a seed and generates a number. The up content is then multiplied by the number provided by the number generator in order to estimate the impact of the systematic uncertainty. This number is then added to the bin content of the pseudo-experiment for a given bin. It is easier to demonstrate it with an example. Let's assume that the bin content of the pseudo-experiment in the first bin is 1000 and the bin content of the up variation for a given systematic uncertainty is 1200. Therefore the up content is 200. Let's consider that the random number generator generates the number 0.15. Therefore the effect of the systematic uncertainty becomes 30. This is then added to the bin content of the pseudo-experiment which then becomes 1030. The above steps are then

repeated for the down variation of the systematic uncertainty. This procedure can then be generalised for more than one background and more than one systematic uncertainty. The effect of systematic uncertainty (30 in the given example) is additive. For each background and for each systematic uncertainty the above steps are repeated and the resulting bin contents of the each background is summed. This then finalises the first pseudo-experiment. Using this technique, 1000000 pseudo-experiments are generated.

For the observed limits, exactly the same procedure is done, except that this time the NN output distribution of the data is used instead of the NN output distribution of the backgrounds.

For each of 1000000 pseudo-experiments, the Q-values are calculated. Subsequently, two distributions, $\hat{q}_0(Q')$ and $\hat{q}_1(Q')$ are obtained for the null and the signal+background hypotheses, respectively. From these distributions the p-values p_{s+b} and p_b are evaluated using the Equation 11.5 and 11.6. From these numbers, a single CL_s value is obtained using the Equation 11.7. BILL uses the 1 pb FCNC signal cross-section as an input and calculates a CL_s value. Then in the second attempt, it increases the input signal cross-section slightly and generates another set of 1000000 pseudo-experiments and obtains another CL_s value. Depending on whether the new value of CL_s has increased or decreased in comparison to the previous one, it varies the input cross-section again. This procedure is repeated many times until the value of CL_s reaches below 0.05. The signal cross-section value where CL_s reaches below 0.05 is then the 95 % CL upper limit. It can be interpreted as follows: out of many repeated experiments, 95 % of the times the measured cross-section will not be higher than the derived upper limit. In other words, there's only 5 % chance that the signal cross-section is higher than the derived upper limit.

11.1.4 The effect of systematic uncertainties on the error bands of the distributions

The explanation of the method used to estimate the impact of the systematic uncertainties on the error bands in the control distribution had to wait until this point since only now all the necessary information is provided. Before proceeding to the final results of the analysis, this section details the method used in the error band estimation of the control distribution.

During the pseudo-experiment generation while setting expected limits, there are two sets of scale factors that are produced. The NN output distribution of each background is varied using Poisson sampling as explained to generate a pseudo-experiment. For a given pseudo-experiment, the scale factor that quantifies how much the produced pseudo-experiment deviates from the original NN output distribution of a given background is called the generated scale factor and denoted as β^{gen}. Therefore, the number of β^{gen}s for a given background is the same as the number of produced pseudo-experiment.

The second set of scale factors are produced as follows: for a given pseudo-experiment (where this time the impact of systematic uncertainties using the standard distribution, as explained in the previous section, are included), the background NN output distributions are fitted to the produced pseudo-data. The scale factors obtained from the fit for a given background are called the fitted scale factors and denoted as β^{fitted}. One should note that the β^{fitted}s contain the impact of the systematic uncertainties.

Both sets of scale factors form a distribution. In order to estimate the impact of the systematic uncertainties for a given background, the subtracted distribution, β^{fitted}-β^{gen}, is produced for each background. A Gaussian fit is applied to the distribution and the root-mean-square (RMS) is extracted. The RMS is treated as the indicator of the size of systematic uncertainties for each background.

Later, for a given control distribution of a variable, each bin content for a given background is multiplied by the RMS value, which is described above, for that background . This number is added quadratically to the statistical uncertainty of that bin. The resulting number is then used as the uncertainty of that bin for the given background distribution of a variable. The Figure 11.2 shows the β^{fitted}-β^{gen} distributions for W+HF, single top-quark and $t\bar{t}$ backgrounds.

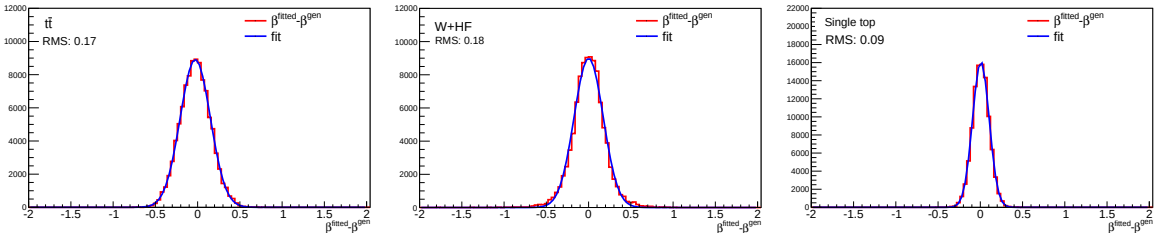

(a) (b) (c)

Figure 11.2: The β^{fitted}-β^{gen} distributions for the $t\bar{t}$, W+HF and single top-quark backgrounds. The RMS values of the fits are also presented.

11.2 Expected and observed limits

This section presents the results of the calculation of the expected and observed 95 % CL upper limits on the anomalous FCNC single top-quark production cross-section. The results are derived by taking all the systematic uncertainties described in Chapter 10. The expected 95 % CL upper limit on the anomalous FCNC single top-quark production cross-section multiplied by the $t \to Wb$ branching fraction, including all uncertainties, is 2.9 pb. The individual effect of each systematic uncertainty is also evaluated as follows. The expected limit is set taking the statistical uncertainty due to the limited size of samples and the cross-section normalisation uncertainties of the MC backgrounds. This forms the base upper limit which is 1.5 pb. Later each systematic uncertainty is included to the normalisation and statistical uncertainties, one at a time, and upper limits are set for each systematic uncertainty. The list of the effect of each systematic uncertainty in terms of upper limits and in terms of percentage changes in the base limit is given in Table 11.2. The uncertainties that have the highest impact are the jet energy resolution, $E_{\text{T}}^{\text{miss}}$ modelling, and the multi-jet normalisation and modelling uncertainties. The uncertainties related to $E_{\text{T}}^{\text{miss}}$ and multi-jet background are large due to the difficulties in modelling. The jet energy resolution uncertainty is large because of the following reason. The one jet selection in this analysis has the highest number of events compared to selections with higher multiplicity of jets. When the jet energy resolution is varied, the single jet in the event may not be compatible with the jet definition anymore. Therefore these event are rejected, which notably change the event yields. The opposite is also possible; the events with jets that do not match the jet definition can enter the event selection after varying the jet energy resolution. This causes a significant change in the event yields.

The observed 95 % CL upper limits on the anomalous FCNC single top-quark production cross-section including only the statistical uncertainties and the uncertainties on the normalisation is 1.5 pb and including all uncertainties 3.34 pb. In order to check the compatibility of the observed and the expected limits, the ± 1 standard deviation variations of the expected upper limits are calculated. The $\pm 1\sigma$ variation limits are derived by using the Neyman construction method [190]. The +1 σ deviation expected upper limit is 4.8 pb and the -1 σ deviation expected upper limit is 1.7 pb. The observed limit lies well within the ± 1 σ deviation expected upper limits. A summary of the expected and observed 95 % CL upper limits is given in Table 11.3.

In order to visually demonstrate the observed upper limit, the FCNC signal process cross-section is normalised to 3.4 pb and stacked on top of the background processes in the NN output distribution and the results are shown in Figure 11.3. The SM background processes are compatible with the data. The FCNC signal contribution at 3.4 pb is small, therefore the addition of the FCNC signal on top of the background processes does not make a notable change in the ratio distribution.

Using Equation 3.9 the upper limit on the cross-section can be converted into a limit on the coupling

Source	Expected 95 % CL upper limit [pb]	Change in the upper limit [%]
Normalisation & MC statistics	1.5	-
Multi-jets normalisation and modelling	1.8	25
Luminosity	1.5	5
Lepton identification	1.5	3
Electron energy scale	1.6	8
Electron energy resolution	1.5	4
Muon momentum scale	1.5	1
Muon momentum resolution	1.5	5
Jet energy scale	1.6	8
Jet energy resolution	1.9	32
Jet reconstruction efficiency	1.5	4
Jet vertex fraction scale	1.5	3
b-tagging efficiency	1.5	3
c-tagging efficiency	1.5	4
Mistag acceptance	1.5	2
$E_{\mathrm{T}}^{\mathrm{miss}}$ modelling	1.9	34
PDF	1.5	5
Scale variations	1.5	2
MC generator (NLO subtraction method)	1.6	8
Parton shower modelling	1.5	5
All systematic uncertainties	2.9	-

Table 11.2: The effect of a single systematic uncertainty in addition to the cross-section normalisation and MC statistical uncertainties alone (top row) on the expected 95 % CL upper limits on the anomalous FCNC single top-quark production $qg \to t \to b\ell\nu$. The relative change quoted in the third column is with respect to the expected limit with normalisation and MC statistical uncertainties only.

	Expected	Observed
Normalisation & MC statistics	1.5 pb	1.5 pb
All systematic uncertainties	2.9 pb	3.4 pb
Including all systematics +1 σ	4.8 pb	
Including all systematics -1 σ	1.7 pb	

Table 11.3: Expected and observed 95% CL upper limits on the anomalous FCNC single top-quark production $qg \to t$.

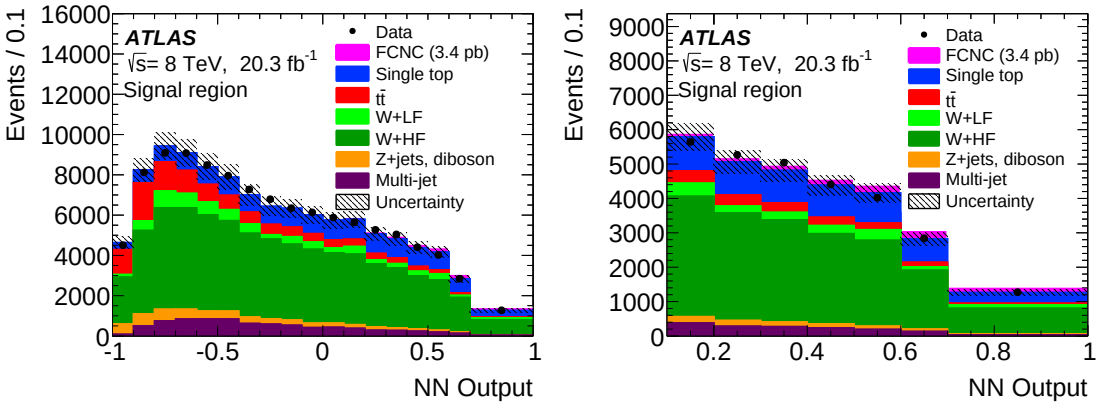

(a) (b)

Figure 11.3: (a) Neural-network output distribution in the signal region and (b) in the signal region with neural network output above 0.1. In both figures the signal contribution scaled to the observed upper limit is shown. The hatched band indicates the total posterior uncertainty as obtained from the limit calculation.

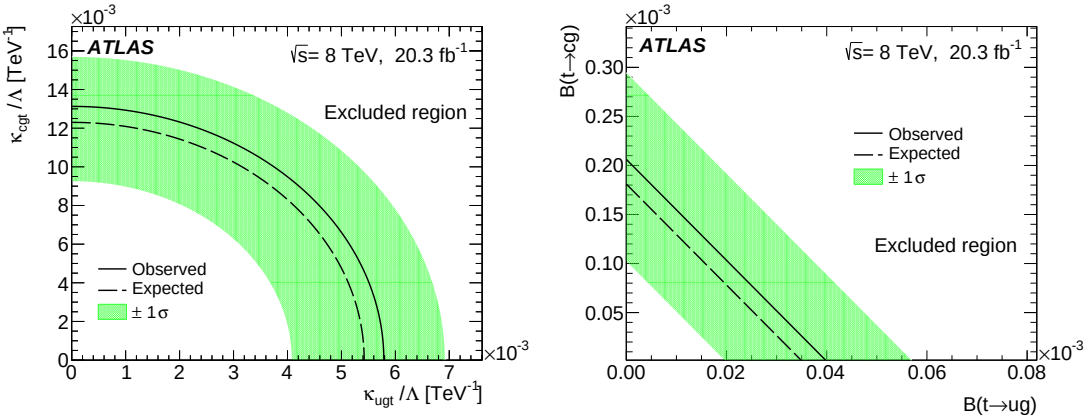

(a) (b)

Figure 11.4: (a) Upper limit on the coupling constants κ_{ugt} and κ_{cgt} and (b) on the branching fractions $\mathcal{B}(t \to ug)$ and $\mathcal{B}(t \to cg)$. The shaded band shows the one standard deviation variation of the expected limit.

constants κ_{ugt}/Λ and κ_{cgt}/Λ. Assuming $\kappa_{cgt}/\Lambda = 0 \Rightarrow \kappa_{ugt}/\Lambda < 6.0 \cdot 10^{-3}\,\text{TeV}^{-1}$ and $\kappa_{ugt}/\Lambda = 0 \Rightarrow \kappa_{cgt}/\Lambda < 13 \cdot 10^{-3}\,\text{TeV}^{-1}$. Distributions of the upper limits on the coupling constants for combinations of *cgt* and *ugt* channels are shown in Fig. 11.4(a).

Using Equation 3.5 the upper limit on the branching fraction is derived as $\mathcal{B}(t \to ug) < 4.0 \cdot 10^{-5}$ assuming $\mathcal{B}(t \to cg) = 0$ and $\mathcal{B}(t \to cg) < 20 \cdot 10^{-5}$ assuming $\mathcal{B}(t \to ug) = 0$. Possible combinations of the latter are shown in Figure 11.4(b).

The expected and the observed upper limits presented in this thesis are the most stringent limits set in this channel. A detailed discussion of the impact of the results presented here on the predictions of the BSM theories and the expectations from the future experiments is given in the following chapter.

CHAPTER 12

Impact of the Results on the Theory Predictions, Future Experimental Expectations and Summary

In this chapter, the impact of the analysis that is presented here on the theory predictions is presented. Furthermore, the expectations from the possible future analyses of the search for anomalous FCNC single top-quark production at higher centre-of-mass energies with larger integrated luminosity at the LHC is described. The chapter finishes with a brief summary of this thesis.

12.1 Impact of the analysis on the theory predictions

Many BSM theories predict a wide range of cross-sections and branching fractions for the FCNC involving top-quark processes. These predictions have been described in Chapter 3. Some models predict branching fractions as high as 10^{-4} (2HDM in the *cgt* channel, SUSY in the *ugt* channel, see Table 3.1). The 95% CL observed upper limits on the branching fractions of the FCNC involving top-quark processes presented in this thesis are of the order of 10^{-5} for both the *ugt* and *cgt* channels. This is two orders of magnitude smaller than the predictions of BSM theories that are mentioned above. Inevitably, this conclusion raises the question whether these BSM theories are excluded by the experimental results presented here or not.

The answer to this question is both yes and no. As mentioned, BSM theories predict a range of branching fractions, usually covering a range that spans many orders of magnitude. Sometimes these predictions can go as low as the SM predictions. Therefore, the exclusion of the entire parameter space predicted by the BSM theories is not possible by the current experimental analyses done in this channel. However, the experimental results (such as the one presented here) penetrate deep into the predicted

parameter space of the BSM theories, at least excluding them partially.

Another important question arises from the experimental results presented here is whether it is possible to experimentally scan the entire parameter space of the predictions of the BSM theories. To be able to scan very small branching fractions and cross-sections, two limiting factors, which are the statistically limited data samples and large systematic uncertainties have to be addressed. A theory article predicting a range of branching fractions for the FCNC processes involving top quarks in the context of 2HDM [51] notes *"The current experimental bound is far above the theory prediction. Therefore, it would be hard to constrain the top quark FCNC parameter space with anomalous single top-quark production measurement at the LHC."* To be able to address these kind of claims and to have an understanding of what could be expected from future analyses performed on the LHC data, a study is performed which is described in the following section.

At this point, it is worthwhile to emphasise the interdependency and cooperation between theory and experiment. Theories are regularly updated based on the experimental results and experiments are performed to test the predictions of the theories. This cooperation and the iterative, progressive and persistent aspect of science leads to the development of our current understanding of the nature. In other words, the *truth* is being cornered by excluding everything that is not true by our current understanding of nature.

12.2 Future experimental expectations

In order to estimate the expectations from a possible and very likely analysis similar to the one presented here, but performed with larger statistics and at higher centre-of-mass energies, a study has been performed using the results of this thesis and expected future LHC runs.

The study aims at offering a rough prediction on how the results of the analysis presented here would improve with higher statistics and at higher centre-of-mass energies. For this purpose, two possible future ATLAS-LHC datasets are considered. The first dataset is from the proton–proton collisions at 13 TeV centre-of-mass energy with an integrated luminosity of 300 fb^{-1} and the second data set is from the collisions at 14 TeV centre-of-mass energy with an integrated luminosity of 3000 fb^{-1}.

The study performs an extrapolation on the results of the analysis presented here to the datasets mentioned above. The extrapolation strategy is as follows: two new sets of NN output templates are created, similar the ones described in Section 11.1. However, instead of their cross-sections and event yields at 8 TeV centre-of-mass energy with 20.3 fb^{-1} data, each template for a given sample is scaled to their expected theoretical cross-section and event yield at the centre-of-mass energies and integrated luminosities of the future datasets given above.

The study has the following assumptions: in the future datasets, the shape of the NN output distribution would remain the same for all samples. The object definition, trigger requirements, event selection, systematic uncertainties and the analysis strategy (such as the number and the type of variables used in the NN training) also remain the same.

All systematic uncertainties described in Chapter 10 are taken into account. Naturally, the templates for the systematic uncertainties for each sample are also scaled to their respective values for the two new datasets.

Due to these assumptions, which are likely to change, this extrapolation study is obviously far from perfect. However, it should give a rough idea on how these results presented here can be enhanced with improved statistics.

The next step is to set expected limits on the cross-section of the FCNC single top-quark production. The same limit setting procedure as in Section 11.1.3 is performed using the new templates.

At 13 TeV centre-of-mass energy with 300 fb^{-1} data, the expected 95% CL upper limit on the FCNC single top-quark production cross-section including all systematic uncertainties is 0.26 pb. At 14 TeV centre-of-mass energy with 3000 fb^{-1} data, the expected upper limit on the cross-section is 0.17 pb.

Following the steps described in Section 11.2, the upper limits on the cross-sections are converted to the upper limits on coupling constants. At 13 TeV centre-of-mass energy with 300 fb^{-1} data, the expected upper limits on the coupling constants are:

- $\kappa_{ugt}/\Lambda < 1.6 \cdot 10^{-3}$ TeV^{-1} assuming $\kappa_{cgt}/\Lambda = 0$ and
- $\kappa_{cgt}/\Lambda < 4 \cdot 10^{-3}$ TeV^{-1} assuming $\kappa_{ugt}/\Lambda = 0$.

At 14 TeV centre-of-mass energy with 3000 fb^{-1} data, the expected upper limits on the coupling constants are:

- $\kappa_{ugt}/\Lambda < 1.3 \cdot 10^{-3}$ TeV^{-1} assuming $\kappa_{cgt}/\Lambda = 0$ and
- $\kappa_{cgt}/\Lambda < 3.4 \cdot 10^{-3}$ TeV^{-1} assuming $\kappa_{ugt}/\Lambda = 0$.

Possible combinations of the upper limits on the coupling constants in *ugt* and *cgt* channels from the two datasets, together with the current upper limits are shown in Figure 12.1(a). Similarly, the limits on the coupling constants are converted to limits on the branching fractions. At 13 TeV centre-of-mass energy with 300 fb^{-1} data, expected upper limits on the branching fractions:

- $\mathcal{B}(t \to ug) < 3.1 \cdot 10^{-6}$ assuming $\mathcal{B}(t \to cg) = 0$ and
- $\mathcal{B}(t \to cg) < 2.1 \cdot 10^{-5}$ assuming $\mathcal{B}(t \to ug) = 0$.

At 14 TeV centre-of-mass energy with 3000 fb^{-1} data, the expected upper limits on the branching fractions:

- $\mathcal{B}(t \to ug) < 2.1 \cdot 10^{-6}$ assuming $\mathcal{B}(t \to cg) = 0$ and
- $\mathcal{B}(t \to cg) < 1.4 \cdot 10^{-5}$ assuming $\mathcal{B}(t \to ug) = 0$.

Possible combinations of the limits on the branching fractions are shown in Figure 12.1(b).

With the 300 fb^{-1} integrated luminosity dataset, the expected upper limits on the branching fractions are improved by an order of magnitude compared to the current results. However, the same improvement is not observed with the 3000 fb^{-1} integrated luminosity dataset compared to the 300 fb^{-1} dataset. The reason for this is, as the accumulated statistics increase, the results begin to approach the limitations that arise from the systematic uncertainties.

The lowest upper limit obtained from this extrapolation study is of the order of 10^{-6}. Although this penetrates further into the parameter space of the predictions provided by the BSM theories, no specific model is excluded. Therefore, it is unlikely that a future LHC run will entirely exclude a BSM theory. However, this result should not be taken as a discouragement. This extrapolation study merely shows roughly how far a possible future analyses can scan the parameter space of the theory predictions. Finding a signal of FCNC involving top-quark processes in the territories which have not been probed by current experiments is still possible. Furthermore, the statistical data analyses techniques have been improving since the first particle collision experiments took place. For instance, the introduction of the multivariate techniques such as neural networks, in the field of experimental particle physics have provided the scientists a great signal distinguishing power, which otherwise would be very difficult. Looking at the current trend, it is very likely that the analysis techniques used in experimental particle physics would continue to improve. Therefore, the future analyses on this channel have the potential of achieving better result than what is predicted in this extrapolation study as this study cannot take into account the improvements in the analyses techniques.

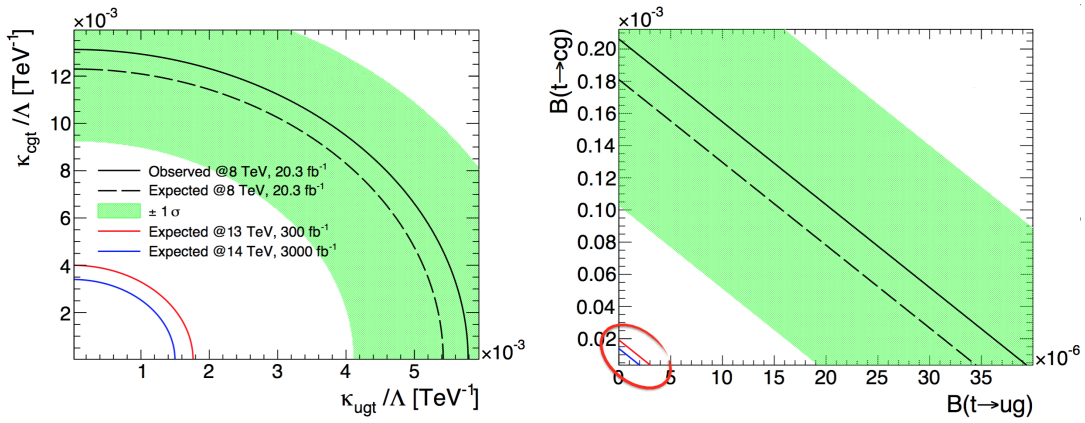

(a) (b)

Figure 12.1: (a) The current and possible future upper limits on the coupling constants κ_{ugt} and κ_{cgt} and (b) on the branching fractions $\mathcal{B}(t \to ug)$ and $\mathcal{B}(t \to cg)$. The shaded band shows the one standard deviation variation of the current expected limit. The expected upper limits for the possible future analyeses are encircled with red marker on the right plot.

12.3 Summary and conclusions

An analysis of the search for anomalous FCNC single top-quark production using the ATLAS data collected from proton–proton collisions at the LHC with an integrated luminosity of 20.3 fb^{-1} at 8 TeV centre-of-mass energy is presented.

FCNC are highly suppressed in SM, however predicted by several extensions of the SM at much higher cross-section and branching fractions. Therefore, a sign of a FCNC signal can directly indicate new physics, making this channel an excellent tool to probe BSM phenomena.

The signal FCNC events are expected to contain a jet originating from a b-quark, an isolated lepton or muon and missing transverse energy. Therefore the appropriate event selection described in Chapter 7 is applied on the observed data and the MC samples for the background and the signal processes. Additional selection criteria are also employed in order to enrich the samples with the possible FCNC signal.

To be able to separate the signal from the SM background, multivariate analyses techniques, in this case neural networks, are employed. A significant separation between the signal and the background MC events is achieved.

The ATLAS detector is a highly complex tool and understating its entirety is challenging. The measurements performed by the detector introduce many systematic uncertainties that have to be evaluated. A wide range of systematic uncertainties are studied and their impacts are reflected on the results.

The NN output distribution, which combines the separation power of several variables into one, is used as the distinguishing parameter for the statistical analysis performed to search for the signal.

As no sign of a signal of the FCNC single top-quark production processes is observed, expected and observed upper limits on the cross-section are set using the CL_s method.

The expected 95 % CL upper limit on the anomalous FCNC single top-quark production cross-section multiplied by the $t \to Wb$ branching fraction, including all uncertainties, is 2.9 pb and the observed limit is 3.4 pb.

The observed upper limit on the cross-section can be converted into a limit on the coupling constants κ_{ugt}/Λ and κ_{cgt}/Λ. Assuming $\kappa_{cgt}/\Lambda = 0 \Rightarrow \kappa_{ugt}/\Lambda < 6.0 \cdot 10^{-3}$ TeV^{-1} and $\kappa_{ugt}/\Lambda = 0 \Rightarrow \kappa_{cgt}/\Lambda <$

$13 \cdot 10^{-3}\,\mathrm{TeV}^{-1}$.

The upper limit on the branching fraction is derived as $\mathcal{B}(t \to ug) < 4.0 \cdot 10^{-5}$ assuming $\mathcal{B}(t \to cg) = 0$ and $\mathcal{B}(t \to cg) < 20 \cdot 10^{-5}$ assuming $\mathcal{B}(t \to ug) = 0$.

The impact of the results on the BSM theories are investigated. Although no certain extension of the SM is entirely excluded by these results, their predicted ranges of branching fractions are narrowed.

In order to estimate the outcome of a future analysis performed on the LHC data with higher statistics, an extrapolation study is performed. The study predicts roughly an order of magnitude improvement on the current results.

The results presented in this thesis constitute the most stringent upper limits on this channel.

Bibliography

[1] K. Schmidt,
Göbekli Tepe, Southeastern Turkey. A Preliminary Report on the 1995-1999 Excavations.,
Paléorient **26**.1 (2000) 45, ISSN: 0153-9345,
URL: http://www.persee.fr/doc/paleo_0153-9345_2000_num_26_1_4697
(cit. on p. 1).

[2] G. Magli, *Sirius and the project of the megalithic enclosures at Gobekli Tepe*,
ArXiv e-prints (July 2013), arXiv: 1307.8397 (cit. on p. 1).

[3] A. S. Goldhaber and M. M. Nieto, *Photon and Graviton Mass Limits*,
Rev. Mod. Phys. **82** (2010) 939, arXiv: 0809.1003 [hep-ph] (cit. on p. 6).

[4] F. Ynduráin, *Limits on the mass of the gluon*, Physics Letters B **345**.4 (1995) 524,
ISSN: 0370-2693,
URL: http://www.sciencedirect.com/science/article/pii/0370269394016775
(cit. on p. 6).

[5] K.A. Olive et al. (Particle Data Group), *Review of Particle Physics*,
Chinese Physics (2014) 090001, URL: http://pdg.lbl.gov (cit. on pp. 7, 11, 13, 115).

[6] F. Olness and R. Scalise, *Regularization, Renormalization, and Dimensional Analysis: Dimensional Regularization meets Freshman E&M*, Am. J. Phys. **79** (2011) 306,
arXiv: 0812.3578 [hep-ph] (cit. on p. 7).

[7] Yvette Kosmann-Schwarzbach, *The Noether Theorems*, 2011 (cit. on p. 8).

[8] F. Halzen and A. D. Martin, *Quarks and Leptons*, Wiley and Sons, 1984 6 (cit. on p. 9).

[9] S. Weinberg, *A Model of Leptons*, Phys. Rev. Lett. **19** (21 Nov. 1967) 1264,
URL: http://link.aps.org/doi/10.1103/PhysRevLett.19.1264 (cit. on p. 9).

[10] A. Salam, *Weak and Electromagnetic Interactions*, Conf. Proc. **C680519** (1968) 367
(cit. on p. 9).

[11] S. Glashow, *Partial-symmetries of weak interactions*, Nuclear Physics **22**.4 (1961) 579,
ISSN: 0029-5582 (cit. on p. 9).

[12] *The Nobel Prize in Physics 1979*,
URL: http://www.nobelprize.org/nobel_prizes/physics/laureates/1979
(cit. on p. 9).

[13] UA1 Collaboration, *Experimental observation of isolated large transverse energy electrons with associated missing energy at* $\sqrt{s}$ = 8=*540 GeV*, Physics Letters B **122**.1 (1983) 103,
ISSN: 0370-2693 (cit. on p. 9).

[14] The UA2 Collaboration, *Observation of single isolated electrons of high transverse momentum in events with missing transverse energy at the {CERN} pp collider*,
Physics Letters B **122**.5–6 (1983) 476, ISSN: 0370-2693 (cit. on p. 9).

[15] G. Arnison et al., *Experimental Observation of Lepton Pairs of Invariant Mass Around 95-GeV/c^2 at the CERN SPS Collider*, Phys. Lett. **B126** (1983) 398 (cit. on p. 9).

[16] P. Bagnaia et al., *Evidence for Z0 —> e+ e- at the CERN anti-p p Collider*,
Phys. Lett. **B129** (1983) 130 (cit. on p. 9).

[17] Y. Fukuda et al., *Evidence for oscillation of atmospheric neutrinos*,
Phys. Rev. Lett. **81** (1998) 1562, arXiv: hep-ex/9807003 [hep-ex] (cit. on p. 10).

[18] *The Nobel Prize in Physics 2004*,
URL: http://www.nobelprize.org/nobel_prizes/physics/laureates/2004
(cit. on p. 12).

[19] M. Gell-Mann and F. E. Low, *Quantum Electrodynamics at Small Distances*,
Phys. Rev. **95** (5 Sept. 1954) 1300,
URL: http://link.aps.org/doi/10.1103/PhysRev.95.1300 (cit. on p. 12).

[20] F. Englert and R. Brout, *Broken Symmetry and the Mass of Gauge Vector Mesons*,
Phys. Rev. Lett. **13** (9 Aug. 1964) 321,
URL: http://link.aps.org/doi/10.1103/PhysRevLett.13.321 (cit. on p. 13).

[21] P. W. Higgs, *Broken Symmetries and the Masses of Gauge Bosons*,
Phys. Rev. Lett. **13** (16 Oct. 1964) 508,
URL: http://link.aps.org/doi/10.1103/PhysRevLett.13.508 (cit. on p. 13).

[22] S. Chatrchyan et al.,
Observation of a new boson at a mass of 125 GeV with the CMS experiment at the LHC,
Phys. Lett. **B716** (2012) 30, arXiv: 1207.7235 [hep-ex] (cit. on p. 13).

[23] ATLAS Collaboration, *Observation of a new particle in the search for the Standard Model Higgs boson with the ATLAS detector at the LHC*, Phys. Lett. **B716** (2012) 1,
arXiv: 1207.7214 [hep-ex] (cit. on p. 13).

[24] *The Nobel Prize in Physics 2013*,
URL: http://www.nobelprize.org/nobel_prizes/physics/laureates/2013/
(cit. on p. 13).

[25] M. Kobayashi and T. Maskawa, *CP Violation in the Renormalizable Theory of Weak Interaction*,
Prog. Theor. Phys. **49** (1973) 652 (cit. on p. 14).

[26] S. Abachi et al., *Observation of the top quark*, Phys. Rev. Lett. **74** (1995) 2632,
arXiv: hep-ex/9503003 [hep-ex] (cit. on p. 14).

[27] F. Abe et al., *Observation of top quark production in $\bar{p}p$ collisions*,
Phys. Rev. Lett. **74** (1995) 2626, arXiv: hep-ex/9503002 [hep-ex] (cit. on p. 14).

[28] M. Czakon, P. Fiedler and A. Mitov,
The total top quark pair production cross-section at hadron colliders through $O(\alpha_S^4)$ (2013), arXiv: 1303.6254 [hep-ph] (cit. on pp. 14, 53).

[29] M. Czakon and A. Mitov,
NNLO corrections to top pair production at hadron colliders: the quark-gluon reaction, JHEP **1301** (2013) 080, arXiv: 1210.6832 [hep-ph] (cit. on pp. 14, 53).

[30] M. Czakon and A. Mitov, *NNLO corrections to top-pair production at hadron colliders: the all-fermionic scattering channels*, JHEP **1212** (2012) 054, arXiv: 1207.0236 [hep-ph] (cit. on pp. 14, 53).

[31] R. P. Feynman, *Space-Time Approach to Quantum Electrodynamics*, Phys. Rev. **76** (6 Sept. 1949) 769, URL: http://link.aps.org/doi/10.1103/PhysRev.76.769 (cit. on p. 14).

[32] S. Mandelstam, *Determination of the Pion-Nucleon Scattering Amplitude from Dispersion Relations and Unitarity. General Theory*, Phys. Rev. **112** (4 Nov. 1958) 1344, URL: http://link.aps.org/doi/10.1103/PhysRev.112.1344 (cit. on p. 14).

[33] N. Kidonakis, *Next-to-next-to-leading-order collinear and soft gluon corrections for t-channel single top quark production*, Phys. Rev. **D83** (2011) 091503, arXiv: 1103.2792 [hep-ph] (cit. on pp. 14, 53).

[34] N. Kidonakis, *NNLL resummation for s-channel single top quark production*, Phys. Rev. **D81** (2010) 054028, arXiv: 1001.5034 [hep-ph] (cit. on pp. 14, 53).

[35] N. Kidonakis, *Two-loop soft anomalous dimensions for single top quark associated production with a W- or H-boson*, Phys. Rev. **D82** (2010) 054018, arXiv: 1005.4451 [hep-ph] (cit. on pp. 15, 53).

[36] T. Aaltonen et al., *First Observation of Electroweak Single Top Quark Production*, Phys. Rev. Lett. **103** (2009) 092002, arXiv: 0903.0885 [hep-ex] (cit. on p. 15).

[37] V. M. Abazov et al., *Observation of Single Top Quark Production*, Phys. Rev. Lett. **103** (2009) 092001, arXiv: 0903.0850 [hep-ex] (cit. on p. 15).

[38] V. M. Abazov et al., *Model-independent measurement of t-channel single top quark production in $p\bar{p}$ collisions at $\sqrt{s} = 1.96$ TeV*, Phys. Lett. **B705** (2011) 313, arXiv: 1105.2788 [hep-ex] (cit. on p. 15).

[39] T. A. Aaltonen et al., *Observation of s-channel production of single top quarks at the Tevatron*, Phys. Rev. Lett. **112** (2014) 231803, arXiv: 1402.5126 [hep-ex] (cit. on p. 15).

[40] ATLAS Collaboration,
Evidence for single top-quark production in the s-channel in proton-proton collisions at $\sqrt{s}$ =8 TeV with the ATLAS detector using the Matrix Element Method, Phys. Lett. **B756** (2016) 228, arXiv: 1511.05980 [hep-ex] (cit. on p. 15).

[41] CMS Collaboration, *Single Top associated tW production at 8 TeV in the two lepton final state*, CMS-PAS-TOP-12-040, CERN, Geneva (2013) (cit. on p. 15).

[42] S. L. Glashow, J. Iliopoulos and L. Maiani, *Weak Interactions with Lepton-Hadron Symmetry*, Phys. Rev. D **2** (7 Oct. 1970) 1285, URL: http://link.aps.org/doi/10.1103/PhysRevD.2.1285 (cit. on p. 17).

[43] G. Eilam, J. L. Hewett and A. Soni,
Rare decays of the top quark in the standard and two-Higgs-doublet models,
Phys. Rev. D **44** (1991) 1473, [Erratum-ibid. D **59** (1999) 039901] (cit. on p. 17).

[44] Y. R. Peters, "Top anti-top Asymmetries at the Tevatron and the LHC",
Proceedings, 32nd International Symposium on Physics in Collision (PIC 2012): Strbske Pleso, Slovakia, September 12-15, 2012, 2012 27, arXiv: 1211.6028 [hep-ex],
URL: https://inspirehep.net/record/1203849/files/arXiv:1211.6028.pdf
(cit. on p. 20).

[45] W. Buchmüller and D. Wyler,
Effective lagrangian analysis of new interactions and flavour conservation,
Nuclear Physics B **268**.3 (1986) 621, ISSN: 0550-3213,
URL: http://www.sciencedirect.com/science/article/pii/0550321386902622
(cit. on p. 22).

[46] P. Ferreira and R. Santos,
Strong flavor changing effective operator contributions to single top quark production,
Phys.Rev. **D73** (2006) 054025, arXiv: hep-ph/0601078 [hep-ph] (cit. on p. 23).

[47] R. Coimbra et al., *MEtop - a generator for single top production via FCNC interactions*,
Eur. Phys. J. C **72** (2012) 2222, arXiv: 1207.7026 [hep-ph] (cit. on pp. 23, 25, 55).

[48] C. S. Li, R. J. Oakes and T. C. Yuan, *QCD corrections to $t \to W^+ + b$*,
Phys. Rev. D **43** (11 June 1991) 3759,
URL: http://link.aps.org/doi/10.1103/PhysRevD.43.3759 (cit. on p. 24).

[49] J. J. Zhang et al., *Next-to-leading order QCD corrections to the top quark decay via the Flavor-Changing Neutral-Current operators with mixing effects*, Phys. Rev. **D82** (2010) 073005,
arXiv: 1004.0898 [hep-ph] (cit. on p. 24).

[50] J. Gao et al., *Search for anomalous top quark production at the early LHC*,
Phys. Rev. Lett. **107** (2011) 092002, arXiv: 1104.4945 [hep-ph] (cit. on p. 25).

[51] C. S. Kim, Y. W. Yoon and X.-B. Yuan,
Exploring top quark FCNC within 2HDM type III in association with flavor physics,
JHEP **12** (2015) 038, arXiv: 1509.00491 [hep-ph] (cit. on pp. 27, 126).

[52] T. P. Cheng and M. Sher,
Mass-matrix ansatz and flavor nonconservation in models with multiple Higgs doublets,
Phys. Rev. D **35** (11 June 1987) 3484,
URL: http://link.aps.org/doi/10.1103/PhysRevD.35.3484 (cit. on p. 27).

[53] C. Gross et al.,
Light axigluon explanation of the Tevatron $t\bar{t}$ asymmetry and multijet signals at the LHC,
Phys. Rev. D **87** (1 Jan. 2013) 014004,
URL: http://link.aps.org/doi/10.1103/PhysRevD.87.014004 (cit. on p. 27).

[54] C.-X. Yue, S.-Y. Cao and Q.-G. Zeng, *Light axigluon and single top production at the LHC*,
JHEP **04** (2014) 170, arXiv: 1401.5159 [hep-ph] (cit. on p. 27).

[55] CDF Collaboration, *Search for new particles decaying to dijets at CDF*,
Phys. Rev. D **55** (9 May 1997) R5263,
URL: http://link.aps.org/doi/10.1103/PhysRevD.55.R5263 (cit. on p. 28).

[56] J. J. Liu et al., *Single top quark production via SUSY-QCD FCNC couplings at the CERN LHC in the unconstrained MSSM*, Nucl. Phys. **B705** (2005) 3, arXiv: hep-ph/0404099 [hep-ph] (cit. on p. 28).

[57] ATLAS Collaboration, *Summary of the searches for squarks and gluinos using $\sqrt{s} = 8$ TeV pp collisions with the ATLAS experiment at the LHC*, JHEP **10** (2015) 054, arXiv: 1507.05525 [hep-ex] (cit. on p. 29).

[58] T. P. Cheng and M. Sher, *Mass Matrix Ansatz and Flavor Nonconservation in Models with Multiple Higgs Doublets*, Phys. Rev. D **35** (1987) 3484 (cit. on p. 29).

[59] B. Grzadkowski, J. F. Gunion and P. Krawczyk, *Neutral current flavor changing decays for the Z boson and the top quark in two Higgs doublet models*, Phys. Lett. B **268** (1991) 106 (cit. on p. 29).

[60] M. E. Luke and M. J. Savage, *Flavor changing neutral currents in the Higgs sector and rare top decays*, Phys. Lett. B **307** (1993) 387, arXiv: hep-ph/9303249 (cit. on p. 29).

[61] D. Atwood, L. Reina and A. Soni, *Probing flavor changing top-charm-scalar interactions in e^+e^- collisions*, Phys. Rev. D **53** (1996) 1199, arXiv: hep-ph/9506243 (cit. on p. 29).

[62] D. Atwood, L. Reina and A. Soni, *Phenomenology of two Higgs doublet models with flavor changing neutral currents*, Phys. Rev. D **55** (1997) 3156, arXiv: hep-ph/9609279 (cit. on p. 29).

[63] S. Bejar, J. Guasch and J. Sola, *Loop induced flavor changing neutral decays of the top quark in a general two-Higgs-doublet model*, Nucl. Phys. B **600** (2001) 21, arXiv: hep-ph/0011091 (cit. on p. 29).

[64] C. S. Li, R. J. Oakes and J. M. Yang, *Rare decay of the top quark in the minimal supersymmetric model*, Phys. Rev. D **49** (1994) 293, [Erratum-ibid. D **56** (1997) 3156] (cit. on p. 29).

[65] G. M. de Divitiis, R. Petronzio and L. Silvestrini, *Flavour changing top decays in supersymmetric extensions of the standard model*, Nucl. Phys. B **504** (1997) 45, arXiv: hep-ph/9704244 (cit. on p. 29).

[66] J. L. Lopez, D. V. Nanopoulos and R. Rangarajan, *New supersymmetric contributions to $t \to cV$*, Phys. Rev. D **56** (1997) 3100, arXiv: hep-ph/9702350 (cit. on p. 29).

[67] J. Guasch and J. Sola, *FCNC top quark decays: A door to SUSY physics in high luminosity colliders?*, Nucl. Phys. B **562** (1999) 3, arXiv: hep-ph/9906268 (cit. on p. 29).

[68] D. Delepine and S. Khalil, *Top flavour violating decays in general supersymmetric models*, Phys. Lett. B **599** (2004) 62, arXiv: hep-ph/0406264 (cit. on p. 29).

[69] J. J. Liu et al., *$t \to cV$ via SUSY FCNC couplings in the unconstrained MSSM*, Phys. Lett. B **599** (2004) 92, arXiv: hep-ph/0406155 (cit. on p. 29).

[70] J. J. Cao et al., *SUSY-induced FCNC top-quark processes at the Large Hadron Collider*, Phys. Rev. D **75** (2007) 075021, arXiv: hep-ph/0702264 (cit. on p. 29).

[71] J. M. Yang, B.-L. Young and X. Zhang,
Flavor-changing top quark decays in R-parity violating SUSY, Phys. Rev. D **58** (1998) 055001, arXiv: hep-ph/9705341 (cit. on p. 29).

[72] G. Eilam et al., *Top quark rare decay $t \to ch$ in R-parity-violating SUSY*,
Phys. Lett. B **510** (2001) 227, arXiv: hep-ph/0102037 (cit. on p. 29).

[73] G. Lu et al., *The rare top quark decays $t \to cV$ in the topcolor-assisted technicolor model*,
Phys. Rev. D **68** (2003) 015002, arXiv: hep-ph/0303122 (cit. on p. 29).

[74] J. Diaz-Cruz et al., *Flavor-changing radiative decay of the t quark*, Phys. Rev. D **41** (1990) 891 (cit. on p. 29).

[75] A. Arhrib and W.-S. Hou,
Flavor changing neutral currents involving heavy quarks with four generations,
JHEP **0607** (2006) 009, arXiv: hep-ph/0602035 (cit. on p. 29).

[76] G. Branco and M. Rebelo,
New Physics in the Flavour Sector in the presence of Flavour Changing Neutral Currents,
PoS(Corfu2012) (2013) 024, arXiv: 1308.4639 [hep-ph] (cit. on p. 29).

[77] J. A. Aguilar-Saavedra and B. M. Nobre, *Rare top decays $t \to c\gamma, t \to cg$ and CKM unitarity*,
Phys. Lett. B **553** (2003) 251, arXiv: hep-ph/0210360 (cit. on p. 29).

[78] F. del Aguila, J. A. Aguilar-Saavedra and R. Miquel,
Constraints on top couplings in models with exotic quarks, Phys. Rev. Lett. **82** (1999) 1628,
arXiv: hep-ph/9808400 (cit. on p. 29).

[79] J. A. Aguilar-Saavedra, *Effects of mixing with quark singlets*,
Phys. Rev. D **67** (2003) 035003, Erratum-ibid. D **69** (2004) 099901, arXiv: hep-ph/0210112
(cit. on p. 29).

[80] J. Aguilar-Saavedra,
Top flavor-changing neutral interactions: Theoretical expectations and experimental detection,
Acta Phys. Polon. B **35** (2004) 2695, arXiv: hep-ph/0409342 (cit. on pp. 29, 30).

[81] F. Larios, R. Martinez and M. Perez,
New physics effects in the flavor-changing neutral couplings of the top quark,
Int. J. Mod. Phys. A **21** (2006) 3473, arXiv: hep-ph/0605003 (cit. on pp. 29, 30).

[82] ZEUS Collaboration, H. Abramowicz et al.,
Search for single-top production in ep collisions at HERA, Phys. Lett. B **708** (2012) 27,
arXiv: 1111.3901 [hep-ex] (cit. on p. 29).

[83] ATLAS Collaboration,
Search for FCNC single top-quark production at $\sqrt{s} = 7$ TeV with the ATLAS detector,
Phys. Lett. B **712** (2012) 351, arXiv: 1203.0529 [hep-ex] (cit. on pp. 29, 30, 55).

[84] CMS Collaboration, *Search for flavor-changing neutral currents in top-quark decays $t \to Zq$ in pp collisions at $\sqrt{s} = 8$ TeV*, Phys. Rev. Lett. **112** (2014) 171802, arXiv: 1312.4194 [hep-ex]
(cit. on p. 29).

[85] ATLAS Collaboration,
Search for top quark decays $t \to qH$ with $H \to \gamma\gamma$ using the ATLAS detector,
JHEP **1406** (2014) 008, arXiv: 1403.6293 [hep-ex] (cit. on pp. 29, 31).

[86] ATLAS Collaboration, *Search for single top-quark production via flavour-changing neutral currents at 8 TeV with the ATLAS detector*, Eur. Phys. J. **C76**.2 (2016) 55, arXiv: 1509.00294 [hep-ex] (cit. on pp. 30, 78, 87, 103, 105–107).

[87] M. Beneke et al., *Top quark physics, in: Proceedings of the "1999 CERN Workshop on SM physics (and more) at the LHC* (2000), arXiv: hep-ph/0003033 (cit. on p. 30).

[88] A. A. Ashimova and S. R. Slabospitsky, *The Constraint on FCNC Coupling of the Top Quark with a Gluon from ep Collisions*, Phys. Lett. **B668** (2008) 282, arXiv: hep-ph/0604119 (cit. on p. 30).

[89] A. Aktas et al., *Search for single top quark production in ep collisions at HERA*, Eur. Phys. J. **C33** (2004) 9, eprint: hep-ex/0310032 (cit. on p. 30).

[90] S. Chekanov et al., *Search for single-top production in e p collisions at HERA*, Phys. Lett. **B559** (2003) 153, eprint: hep-ex/0302010 (cit. on pp. 30, 31).

[91] V. M. Abazov et al., *Search for flavor changing neutral currents via quark- gluon couplings in single top quark production using 2.3 fb^{-1} of $p\bar{p}$ collisions*, Phys. Lett. **B693** (2010) 81, arXiv: 1006.3575 [hep-ex] (cit. on p. 30).

[92] T. Aaltonen et al., *Search for top-quark production via flavor-changing neutral currents in W+1 jet events at CDF*, Phys. Rev. Lett. **102** (2009) 151801, arXiv: 0812.3400 [hep-ex] (cit. on p. 30).

[93] A. Heister et al., *Search for single top production in e+ e- collisions at s**(1/2) up to 209-GeV*, Phys. Lett. **B543** (2002) 173, eprint: hep-ex/0206070 (cit. on p. 31).

[94] J. Abdallah et al., *Search for single top production via FCNC at LEP at s**(1/2) = 189-GeV - 208-GeV*, Phys. Lett. **B590** (2004) 21, eprint: hep-ex/0404014 (cit. on p. 31).

[95] G. Abbiendi et al., *Search for single top quark production at LEP2*, Phys. Lett. **B521** (2001) 181, eprint: hep-ex/0110009 (cit. on p. 31).

[96] P. Achard et al., *Search for single top production at LEP*, Phys. Lett. **B549** (2002) 290, eprint: hep-ex/0210041 (cit. on p. 31).

[97] The LEP Exotica WG, *Search for single top production via flavour changing neutral currents: preliminary combined results of the LEP experiments* (), eprint: LEPExoticaWG2001-01 (cit. on p. 31).

[98] F. D. Aaron et al., *Search for Single Top Quark Production at HERA*, Phys. Lett. **B678** (2009) 450, arXiv: 0904.3876 [hep-ex] (cit. on p. 31).

[99] F. Abe et al., *Search for flavor-changing neutral current decays of the top quark in $p\bar{p}$ collisions at $\sqrt{s}$ = 1.8 TeV*, Phys. Rev. Lett. **80** (1998) 2525 (cit. on p. 31).

[100] V. M. Abazov et al., *Search for flavor changing neutral currents in decays of top quarks*, Phys. Lett. B **701**.3 (2011) 313, ISSN: 0370-2693 (cit. on p. 31).

[101] CMS Collaboration, *Search for flavor changing neutral currents in top quark decays in pp collisions at 8 TeV*, CMS-PAS-TOP-12-037 (2013) (cit. on p. 31).

[102] D. Acosta et al., *First evidence for $B_s^0 \to \phi\phi$ decay and measurements of branching ratio and A_{CP} for $B^+ \to \phi K^+$*, Phys. Rev. Lett. **95** (2005) 031801, arXiv: hep-ex/0502044 [hep-ex] (cit. on p. 30).

[103] O. S. Brüning et al., eds., *LHC Design Report. 1. The LHC Main Ring*, CERN-2004-003-V-1, CERN-2004-003, Geneva, 2004, URL: https://cdsweb.cern.ch/record/782076 (cit. on p. 33).

[104] *Proceedings of the 2012 Evian Workshop on LHC Beam Operation*, CERN, Geneva: CERN, 2013, URL: https://cds.cern.ch/record/1562028 (cit. on p. 34).

[105] *Proceedings of the 2011 Evian Workshop on LHC Beam Operation*, CERN, Geneva: CERN, 2011, URL: https://cds.cern.ch/record/1451243 (cit. on p. 34).

[106] ATLAS Collaboration, *The ATLAS Experiment at the CERN Large Hadron Collider*, JINST **3** (2008) S08003 (cit. on p. 34).

[107] CMS Collaboration, *The CMS experiment at the CERN LHC*, JINST **3** (2008) S08004 (cit. on p. 34).

[108] K. Aamodt et al., *The ALICE experiment at the CERN LHC*, JINST **3** (2008) S08002 (cit. on p. 35).

[109] A. A. Alves Jr. et al., *The LHCb Detector at the LHC*, JINST **3** (2008) S08005 (cit. on p. 35).

[110] J. Pequenao, "Computer generated image of the whole ATLAS detector", Mar. 2008, URL: http://cds.cern.ch/record/1095924 (cit. on p. 36).

[111] ATLAS Collaboration, *The ATLAS Experiment at the CERN Large Hadron Collider*, Journal of Instrumentation **3**.08 (2008) S08003, URL: http://stacks.iop.org/1748-0221/3/i=08/a=S08003 (cit. on p. 37).

[112] ATLAS Collaboration, URL: http://atlasexperiment.org/photos/inner-detector-combined.html (cit. on p. 39).

[113] ATLAS Collaboration, *ATLAS pixel detector electronics and sensors*, Journal of Instrumentation **3**.07 (2008) P07007, URL: http://stacks.iop.org/1748-0221/3/i=07/a=P07007 (cit. on p. 38).

[114] ATLAS Collaboration, *Operation and performance of the ATLAS semiconductor tracker*, JINST **9** (2014) P08009, arXiv: 1404.7473 [hep-ex] (cit. on p. 38).

[115] G. Aad et al., Journal of Instrumentation **3**.02 (2008) P02013, URL: http://stacks.iop.org/1748-0221/3/i=02/a=P02013 (cit. on p. 38).

[116] ATLAS Collaboration, URL: http://atlasexperiment.org/photos/calorimeters-combined-barrel.html (cit. on pp. 41, 42).

[117] B. Andersson et al., *Parton Fragmentation and String Dynamics*, Phys. Rept. **97** (1983) 31 (cit. on p. 51).

[118] B. R. Webber, *A QCD Model for Jet Fragmentation Including Soft Gluon Interference*, Nucl. Phys. **B238** (1984) 492 (cit. on p. 51).

[119] S. Agostinelli, et al., *Geant4—a simulation toolkit*, Nuclear Instruments and Methods in Physics Research Section A: Accelerators, Spectrometers, Detectors and Associated Equipment **506**.3 (2003) 250, ISSN: 0168-9002, URL: http://www.sciencedirect.com/science/article/pii/S0168900203013688 (cit. on p. 51).

[120] T. Gleisberg et al., *Event generation with SHERPA 1.1*, JHEP **0902** (2009) 007, arXiv: 0811.4622 [hep-ph] (cit. on p. 53).

[121] M. L. Mangano et al., *ALPGEN, a Generator for Hard Multiparton Processes in Hadronic Collisions*, JHEP **07** (2003) 001, arXiv: hep-ph/0206293 (cit. on p. 53).

[122] H.-L. Lai et al., *New parton distributions for collider physics*, Phys. Rev. **D82** (2010) 074024, arXiv: 1007.2241 [hep-ph] (cit. on pp. 53, 56).

[123] S. Hoeche et al., *QCD matrix elements and truncated showers*, JHEP **0905** (2009) 053, arXiv: 0903.1219 [hep-ph] (cit. on p. 53).

[124] S. Frixione, P. Nason and C. Oleari, *Matching NLO QCD computations with Parton Shower simulations: the POWHEG method*, JHEP **0711** (2007) 070, eprint: arXiv:0709.2092 (cit. on p. 53).

[125] T. Sjostrand, S. Mrenna and P. Z. Skands, *PYTHIA 6.4 Physics and Manual*, JHEP **05** (2006) 026, arXiv: hep-ph/0603175 [hep-ph] (cit. on pp. 53, 56).

[126] M. Cacciari et al., *Top-pair production at hadron colliders with next-to-next-to-leading logarithmic soft-gluon resummation*, Phys. Lett. B **710** (2012) 612, arXiv: 1111.5869 (cit. on p. 53).

[127] P. Baernreuther, M. Czakon and A. Mitov, *Percent Level Precision Physics at the Tevatron: First Genuine NNLO QCD Corrections to $q\bar{q} \to t\bar{t} + X$*, Phys.Rev.Lett. **109** (2012) 132001, arXiv: 1204.5201 [hep-ph] (cit. on p. 53).

[128] M. Czakon and A. Mitov, *Top++: A Program for the Calculation of the Top-Pair Cross-Section at Hadron Colliders* (2011), arXiv: 1112.5675 [hep-ph] (cit. on p. 53).

[129] *https://twiki.cern.ch/twiki/bin/view/AtlasProtected/TopSystematicUncertainties*, URL: https://twiki.cern.ch/twiki/bin/view/AtlasProtected/AtlasProductionGroup (cit. on p. 53).

[130] G. Corcella et al., *HERWIG 6.5: an Event Generator for Hadron Emission Reactions With Interfering Gluons (Including Supersymmetric Processes)*, JHEP **01** (2001) 010, arXiv: hep-ph/0011363 (cit. on p. 53).

[131] J. M. Butterworth, J. R. Forshaw and M. H. Seymour, *Multiparton interactions in photoproduction at HERA*, Z. Phys. **C72** (1996) 637, arXiv: hep-ph/9601371 [hep-ph] (cit. on p. 53).

[132] J. A. Aguilar-Saavedra, *Identifying top partners at LHC*, JHEP **11** (2009) 030, arXiv: 0907.3155 [hep-ph] (cit. on p. 55).

[133] ATLAS Collaboration, *Search for single top-quark production via FCNC in strong interactions in $\sqrt{s} = 8$ TeV ATLAS data*, ATLAS-CONF-2013-063, 2013, URL: http://cdsweb.cern.ch/record/1562777 (cit. on pp. 55, 75).

[134] M. Alhroob et al., *Search for single top quark production via strong FCNCs in $\sqrt{s} = 8$ TeV ATLAS data*, Geneva, Apr. 2013, URL: https://cds.cern.ch/record/1543449 (cit. on p. 56).

[135] ATLAS Collaboration,
Charged particle multiplicities in pp interactions at $\sqrt{s}$ = 0.9 and 7 TeV in a diffractive limited phase-space measured with the ATLAS detector at the LHC and new Pythia6 *tune*,
ATLAS-CONF-2010-031, 2010, URL: http://cdsweb.cern.ch/record/1277665
(cit. on p. 56).

[136] T. Sjostrand, S. Mrenna and P. Z. Skands, *A Brief Introduction to PYTHIA 8.1*,
Comput. Phys. Commun. **178** (2008) 852, arXiv: 0710.3820 (cit. on p. 56).

[137] *TWiki page: PileupReweighting*, URL:
https://twiki.cern.ch/twiki/bin/view/AtlasProtected/PileupReweighting
(cit. on p. 56).

[138] ATLAS luminosity task force, *Twiki page: General Production and Performance Public Results of the ATLAS Data Preparation Group, 2013*, URL: https://twiki.cern.ch/twiki/bin/view/AtlasPublic/DataPrepGenPublicResults
(cit. on p. 57).

[139] J. Pequenao and P. Schaffner,
"An computer generated image representing how ATLAS detects particles", Jan. 2013,
URL: https://cds.cern.ch/record/1505342 (cit. on p. 60).

[140] T. Cornelissen, M. Elsing, S. Fleischmann, et al.,
Concepts, Design and Implementation of the ATLAS New Tracking (NEWT).,
ATL-SOFT-PUB-2007-007, Geneva, Mar. 2007 (cit. on p. 60).

[141] R. E. Kalman, *A new approach to linear filtering and prediction problems*,
Journal of Fluids Engineering **82** (1960) 24 (cit. on p. 60).

[142] W. Lampl, S. Laplace, D. Lelas, et al.,
Calorimeter Clustering Algorithms: Description and Performance., ATL-LARG-PUB-2008-002,
Geneva, Apr. 2008 (cit. on p. 61).

[143] ATLAS Collaboration, *Performance of the ATLAS Inner Detector Track and Vertex Reconstruction in the High Pile-Up LHC Environment*, ATLAS-CONF-2012-042,
Geneva, Mar. 2012 (cit. on p. 62).

[144] ATLAS Collaboration, *Performance of primary vertex reconstruction in proton-proton collisions at $\sqrt{s}$ = 7 TeV in the ATLAS experiment*, ATLAS-CONF-2010-069, Geneva, July 2010
(cit. on p. 62).

[145] ATLAS Collaboration, *Expected electron performance in the ATLAS experiment*,
ATL-PHYS-PUB-2011-006, Geneva, Apr. 2011 (cit. on pp. 62, 63).

[146] ATLAS Collaboration, *Object selection and calibration, background estimations and MC samples for the Winter 2013 Top Quark analyses with 2012 data*,
ATL-COM-PHYS-2013-1016, Draft version 0.10, 31 July 2013, Geneva,
URL: https://cds.cern.ch/record/1509562 (cit. on pp. 62, 64).

[147] "Electron efficiency measurements with the ATLAS detector using the 2012 LHC proton-proton collision data", tech. rep. ATLAS-CONF-2014-032, CERN, June 2014,
URL: http://cds.cern.ch/record/1706245 (cit. on pp. 64, 65, 67).

[148] ATLAS Collaboration, *Electron performance measurements with the ATLAS detector using the 2010 LHC proton-proton collision data*, Eur. Phys. J. **72** (2012) 1909, arXiv: 1110.3174
(cit. on p. 64).

[149] ATLAS Collaboration,
Electron and photon energy calibration with the ATLAS detector using LHC Run 1 data,
Eur. Phys. J. **74** (2014) 3071, arXiv: 1407.5063 (cit. on pp. 64, 66).

[150] ATLAS Collaboration,
Electron and photon energy calibration with the ATLAS detector using LHC Run 1 data,
Eur. Phys. J. **C74**.10 (2014) 3071, arXiv: 1407.5063 [hep-ex] (cit. on p. 65).

[151] ATLAS Collaboration,
Expected Performance of the ATLAS Experiment - Detector, Trigger and Physics (),
arXiv: 0901.0512 (cit. on p. 66).

[152] ATLAS Collaboration, *Measurement of the muon reconstruction performance of the ATLAS detector using 2011 and 2012 LHC proton-proton collision data*, Eur. Phys. J. **74** (2014) 3110,
arXiv: 1407.5063 (cit. on p. 66).

[153] Keith Rehermann, Tweedie Brock,
Efficient Identification of Boosted Semileptonic Top Quarks at the LHC, JHEP **03** (2011) 059,
arXiv: 1007.2221 [hep-ph] (cit. on p. 67).

[154] ATLAS Collaboration, *Measurement of the muon reconstruction performance of the ATLAS detector using 2011 and 2012 LHC proton–proton collision data*,
Eur. Phys. J. **C74**.11 (2014) 3130, arXiv: 1407.3935 [hep-ex] (cit. on pp. 67, 68).

[155] M. Cacciari, G. P. Salam and G. Soyez, *The Anti-k(t) jet clustering algorithm*,
JHEP **04** (2008) 063, arXiv: 0802.1189 [hep-ph] (cit. on p. 69).

[156] ATLAS Collaboration, *Pile-up subtraction and suppression for jets in ATLAS*,
ATLAS-CONF-2013-083, Geneva, Aug. 2013 (cit. on p. 70).

[157] ATLAS Collaboration, *Jet energy resolution in proton-proton collisions at* $\sqrt{s} = 7$ *TeV recorded in 2010 with the ATLAS detector*, Eur. Phys. J. **C73**.3 (2013) 2306,
arXiv: 1210.6210 [hep-ex] (cit. on p. 70).

[158] ATLAS Collaboration, *Monte Carlo Calibration and Combination of In-situ Measurements of Jet Energy Scale, Jet Energy Resolution and Jet Mass in ATLAS*, ATLAS-CONF-2015-037,
Geneva, Aug. 2015 (cit. on p. 70).

[159] ATLAS Collaboration, *Data-driven determination of the energy scale and resolution of jets reconstructed in the ATLAS calorimeters using dijet and multijet events at* $\sqrt{s} = 7$ *TeV*,
ATLAS-CONF-2015-017, Geneva, Aug. 2015 (cit. on p. 71).

[160] ATLAS Collaboration,
Calibration of the performance of b-tagging for c and light-flavour jets in the 2012 ATLAS data,
ATLAS-CONF-2014-046, Geneva, July 2014 (cit. on p. 72).

[161] ATLAS Collaboration, *Measurement of the b-tag Efficiency in a Sample of Jets Containing Muons with 5* fb^{-1} *of Data from the ATLAS Detector*, ATLAS-CONF-2012-043,
Geneva, Mar. 2012 (cit. on pp. 72, 111).

[162] ATLAS Collaboration,
Commissioning of the ATLAS high-performance b-tagging algorithms in the 7 TeV collision data,
ATLAS-CONF-2011-102, Geneva, July 2011 (cit. on p. 72).

[163] ATLAS Collaboration, *Performance of Missing Transverse Momentum Reconstruction in Proton-Proton Collisions at 7 TeV with ATLAS*, Eur. Phys. J. **C72** (2012) 1844,
arXiv: 1108.5602 [hep-ex] (cit. on p. 73).

[164] T. Loddenkötter, "Implementation of a kinematic fit of single top-quark production in association with a W boson and its application in a neural-network-based analysis in ATLAS", BONN-IR-2012-06, PhD Thesis: University of Bonn, 2012, URL: http://hss.ulb.uni-bonn.de/diss_online (cit. on p. 74).

[165] K. Becker et al., "Estimation of non-prompt and fake lepton backgrounds in final states with top quarks produced in proton-proton collisions at $\sqrt{s} = 8$ TeV with the ATLAS detector", tech. rep. ATLAS-COM-CONF-2014-072, CERN, Sept. 2014, URL: https://cds.cern.ch/record/1755451 (cit. on p. 79).

[166] J. Campbell and R. Ellis, *Update on vector boson pair production at hadron colliders*, Phys. Rev. **D60** (1999) 113006, arXiv: hep-ph/9905386v2 (cit. on p. 81).

[167] ATLAS Collaboration, *Single Boson and Diboson Production Cross Sections in pp Collisions at $\sqrt{s} = 7$ TeV*, ATL-COM-PHYS-2010-695, 2010, URL: https://cds.cern.ch/record/1287902 (cit. on p. 81).

[168] ATLAS Collaboration, "Estimation of non-prompt and fake lepton backgrounds in final states with top quarks produced in proton-proton collisions at $\sqrt{s} = 8$ TeV with the ATLAS detector", tech. rep. ATLAS-CONF-2014-058, CERN, Oct. 2014, URL: http://cds.cern.ch/record/1951336 (cit. on p. 91).

[169] M. Feindt, U. Kerzel, *The NeuroBayes neural network package*, Nucl. Instrum. Meth. **A559** (2006) 190 (cit. on p. 97).

[170] D. Williams and G. Hinton, *Learning representations by back-propagating errors*, Nature **323**.6088 (1986) 533 (cit. on p. 100).

[171] David J. C. MacKay, *A Practical Bayesian Framework for Backpropagation Networks*, Neural Computation **4**.3 (1992) 448, URL: http://dx.doi.org/10.1162/neco.1992.4.3.448 (cit. on p. 100).

[172] Y. A. LeCun et al., "Efficient BackProp", *Neural Networks: Tricks of the Trade: Second Edition*, ed. by G. Montavon, G. B. Orr and K.-R. Müller, Berlin, Heidelberg: Springer Berlin Heidelberg, 2012 9, ISBN: 978-3-642-35289-8, URL: http://dx.doi.org/10.1007/978-3-642-35289-8_3 (cit. on p. 100).

[173] ATLAS Collaboration, *Jet energy scale and its systematic uncertainty in proton–proton collisions at $\sqrt{s} = 7$ TeV with ATLAS 2010 data*, ATLAS-CONF-2011-032, 2011, URL: http://cdsweb.cern.ch/record/1337782 (cit. on p. 111).

[174] ATLAS Collaboration, "Performance of Missing Transverse Momentum Reconstruction in ATLAS studied in Proton-Proton Collisions recorded in 2012 at 8 TeV", tech. rep. ATLAS-CONF-2013-082, CERN, Aug. 2013, URL: https://cds.cern.ch/record/1570993 (cit. on p. 111).

[175] "Performance of Missing Transverse Momentum Reconstruction in ATLAS with 2011 Proton-Proton Collisions at $\sqrt{s} = 7$ TeV", tech. rep. ATLAS-CONF-2012-101, CERN, July 2012, URL: http://cds.cern.ch/record/1463915 (cit. on p. 111).

[176] ATLAS Collaboration, *Measuring the b-tag efficiency in a $t\bar{t}$ sample with 4.7 fb^{-1} of data from the ATLAS detector*, ATLAS-CONF-2012-097, 2012, URL: http://cdsweb.cern.ch/record/1460443 (cit. on p. 111).

[177] "Measurement of the Mistag Rate with 5 fb^{-1} of Data Collected by the ATLAS Detector", tech. rep. ATLAS-CONF-2012-040, CERN, Mar. 2012, URL: http://cds.cern.ch/record/1435194 (cit. on p. 111).

[178] "b-jet tagging calibration on c-jets containing D^{*+} mesons", tech. rep. ATLAS-CONF-2012-039, CERN, Mar. 2012, URL: http://cds.cern.ch/record/1435193 (cit. on p. 111).

[179] B. Acharya et al., *Object selection and calibration, background estimations and MC samples for the Winter 2013 Top Quark analyses with 2012 data*, ATL-COM-PHYS-2013-088 (Jan. 2013) (cit. on p. 112).

[180] *TWiki page: POWHEG scale variation samples*, URL: https://twiki.cern.ch/twiki/bin/view/AtlasProtected/TopMC12SingleTopSamples#Singletop_Scale_Variation_Sample (cit. on p. 112).

[181] J. M. Campbell, J. Huston and W. Stirling, *Hard interactions of quarks and gluons: A primer for LHC physics*, Rept. Prog. Phys. **70** (2007) 89, arXiv: hep-ph/0611148 (cit. on p. 113).

[182] A. Martin et al., *Parton distributions for the LHC*, Eur. Phys. J. **C63** (2009) 189, arXiv: 0901.0002 (cit. on p. 113).

[183] R. D. Ball et al., *Impact of heavy-quark masses on parton distributions and LHC phenomenology*, Nucl. Phys. **B849** (2011) 296, arXiv: 1101.1300 (cit. on p. 113).

[184] Botje, Michiel and others, *The PDF4LHC Working Group Interim Recommendations* (2011), arXiv: 1101.0538 [hep-ph] (cit. on p. 113).

[185] ATLAS Collaboration, *Improved luminosity determination in pp collisions at sqrt(s) = 7 TeV using the ATLAS detector at the LHC*, Eur. Phys. J. **C73**.8 (2013) 2518, arXiv: 1302.4393 [hep-ex] (cit. on p. 114).

[186] ATLAS Top Group, *Bill tool*, URL: https://twiki.cern.ch/twiki/bin/view/AtlasProtected/BillTool (cit. on p. 115).

[187] I. Antcheva et al., *{ROOT} — A C++ framework for petabyte data storage, statistical analysis and visualization*, Computer Physics Communications **180**.12 (2009) 2499, 40 {YEARS} {OF} CPC: A celebratory issue focused on quality software for high performance, grid and novel computing architectures, ISSN: 0010-4655, URL: http://www.sciencedirect.com/science/article/pii/S0010465509002550 (cit. on p. 115).

[188] R. Barlow and C. Beeston, *Fitting using finite Monte Carlo samples*, Computer Physics Communications **77**.2 (1993) 219, ISSN: 0010-4655, URL: //www.sciencedirect.com/science/article/pii/001046559390005W (cit. on p. 116).

[189] A. L. Read, *Presentation of search results: The CL(s) technique*, J. Phys. **G28** (2002) 2693 (cit. on p. 119).

[190] A. P. Dempster, *A Selection of Early Statistical Papers of J. Neyman. University of California Press, Berkeley*, Science **160**.3828 (1968) 661 (cit. on p. 121).

Appendix

APPENDIX A

Triangular Cut

This section demonstrates the effect of the triangular cut that is applied on the lepton transverse momentum and the azimuthal angle between the jet and the lepton.

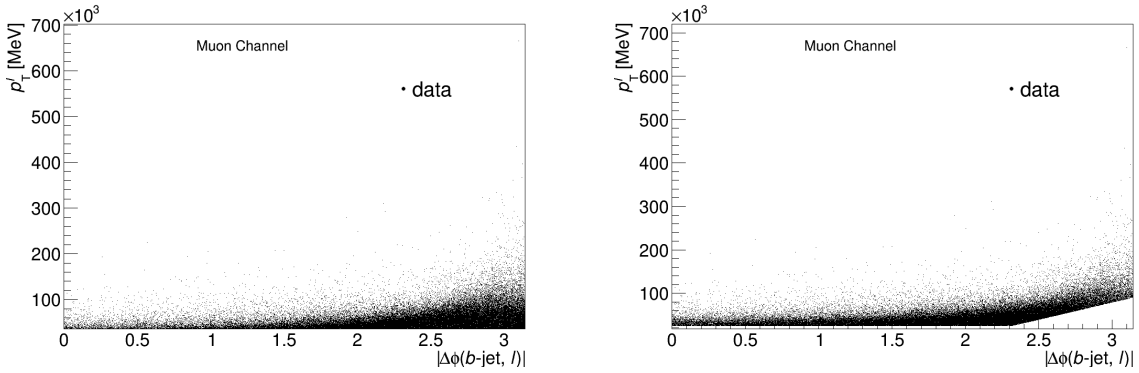

Figure A.1: The lepton transverse momentum and the azimuthal angle between the jet and the lepton distribution (a) before (b) after the triangular cut applied on the data in the muon channel.

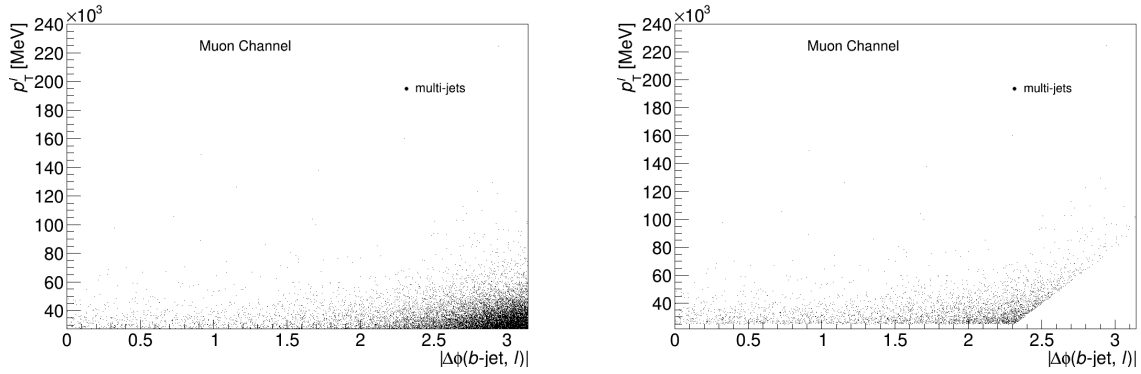

(a) (b)

Figure A.2: The lepton transverse momentum and the azimuthal angle between the jet and the lepton distribution (a) before (b) after the triangular cut applied on the multi-jet background in the muon channel.

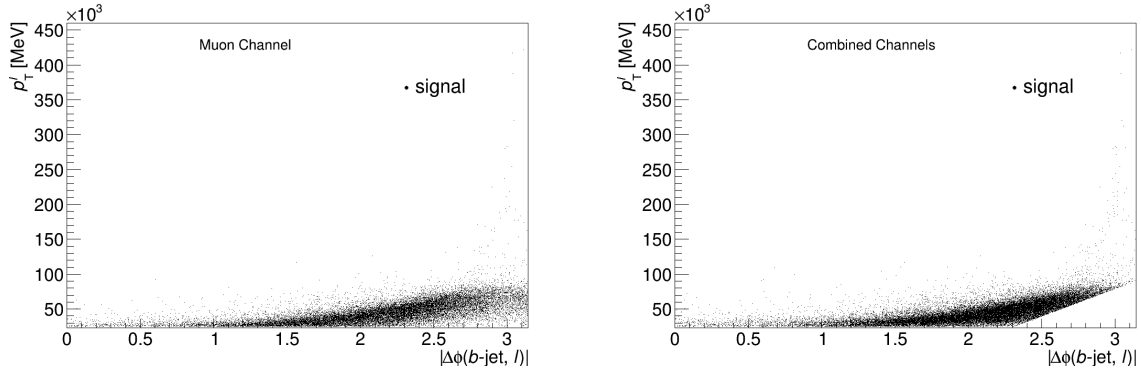

(a) (b)

Figure A.3: The lepton transverse momentum and the azimuthal angle between the jet and the lepton distribution (a) before (b) after the triangular cut applied on the signal in the muon channel.

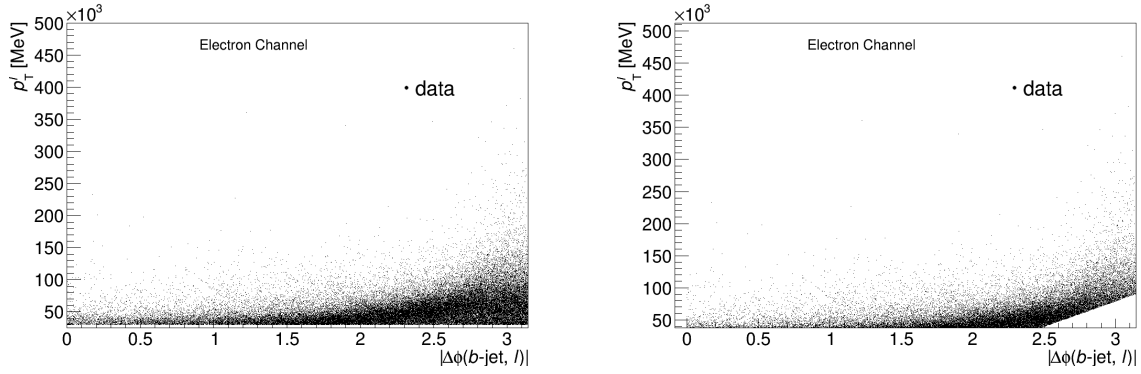

(a) (b)

Figure A.4: The lepton transverse momentum and the azimuthal angle between the jet and the lepton distribution (a) before (b) after the triangular cut applied on the data in the electron channel.

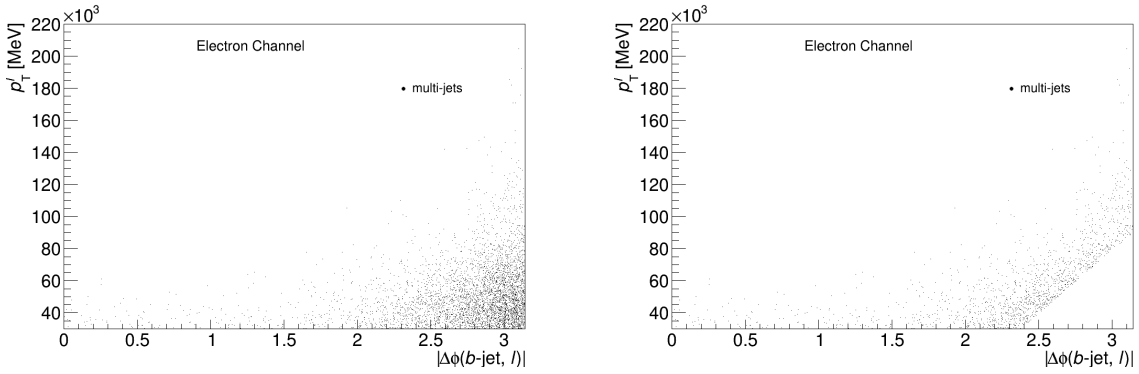

(a) (b)

Figure A.5: The lepton transverse momentum and the azimuthal angle between the jet and the lepton distribution (a) before (b) after the triangular cut applied on the multi-jet background in the electron channel.

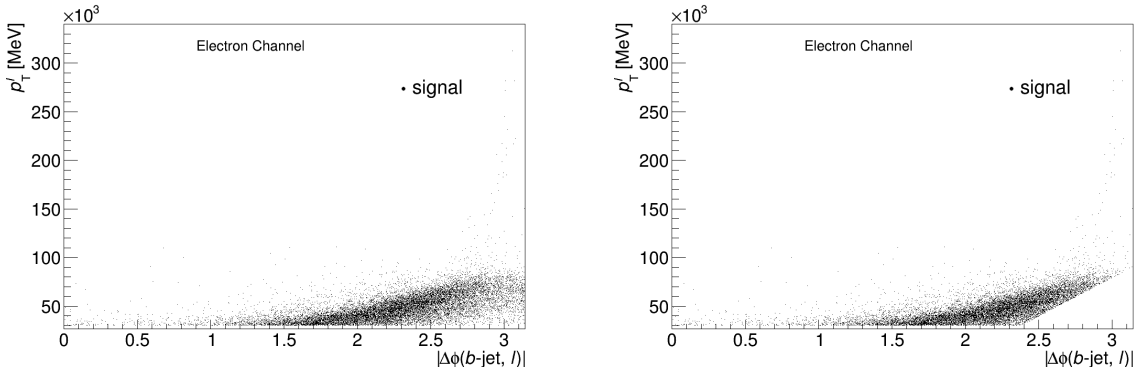

(a) (b)

Figure A.6: Thelepton transverse momentum and the azimuthal angle between the jet and the lepton distribution (a) before (b) after the triangular cut applied on the signal in the electron channel.

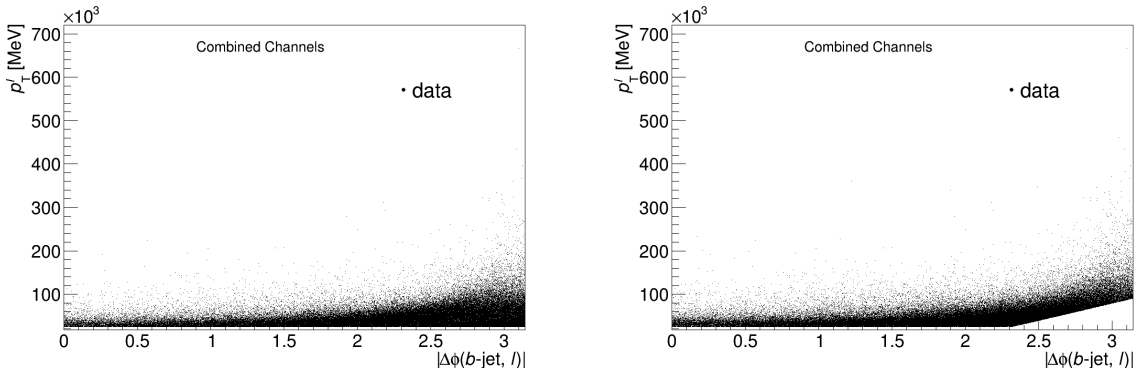

(a) (b)

Figure A.7: The lepton transverse momentum and the azimuthal angle between the jet and the lepton distribution (a) before (b) after the triangular cut applied on the data in the combined channels.

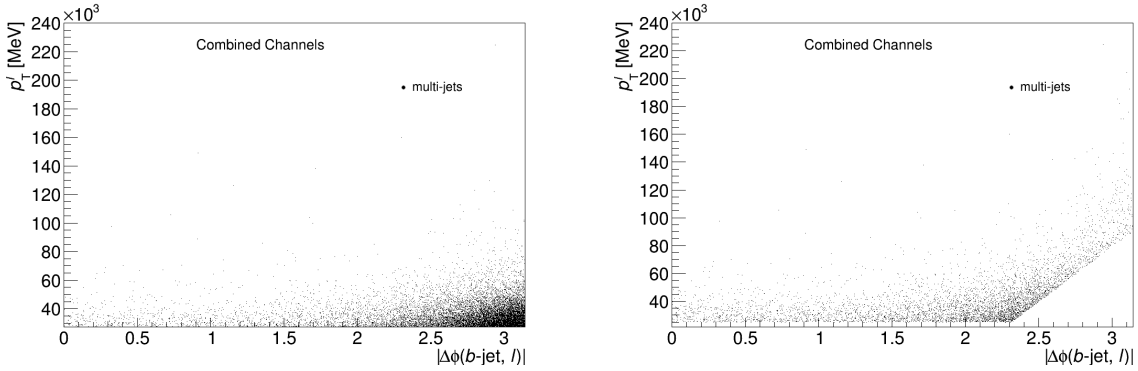

(a) (b)

Figure A.8: The lepton transverse momentum and the azimuthal angle between the jet and the lepton distribution (a) before (b) after the triangular cut applied on the multi-jet background in the combined channels.

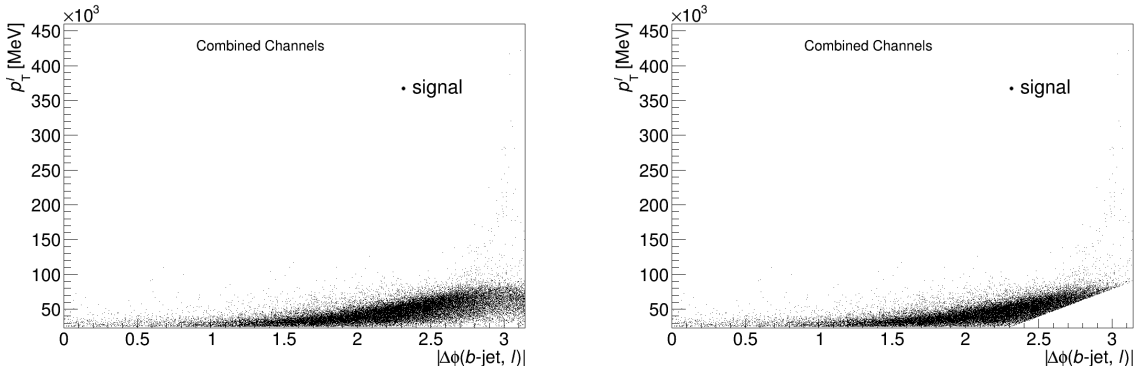

(a) (b)

Figure A.9: The lepton transverse momentum and the azimuthal angle between the jet and the lepton distribution (a) before (b) after the triangular cut applied on the signal in the combined channels.

APPENDIX B

Matrix method kinematic distributions

This section provides more control distributions generated by the matrix method.

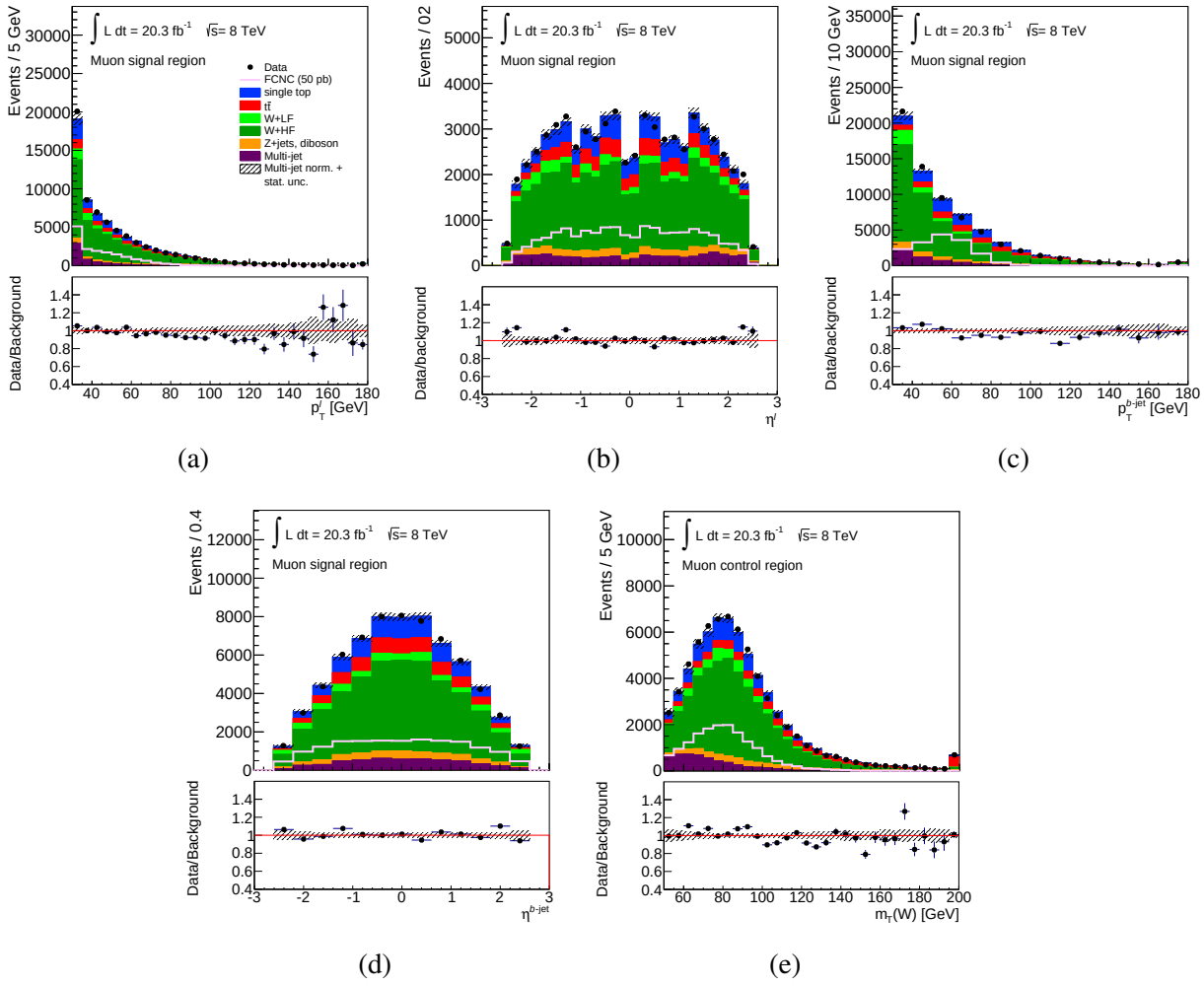

Figure B.1: Basic kinematic distributions of the signal region for the muon channel. The multi-jet background sample is produced using the matrix method. The hatched band indicates the combined statistical uncertainty and 17% multi-jet normalisation uncertainty. Shown are: (a) the transverse momentum and (b) pseudorapidity of the lepton, (c) the transverse momentum and (d) pseudorapidity of the jet, (e) transverse W-boson mass.

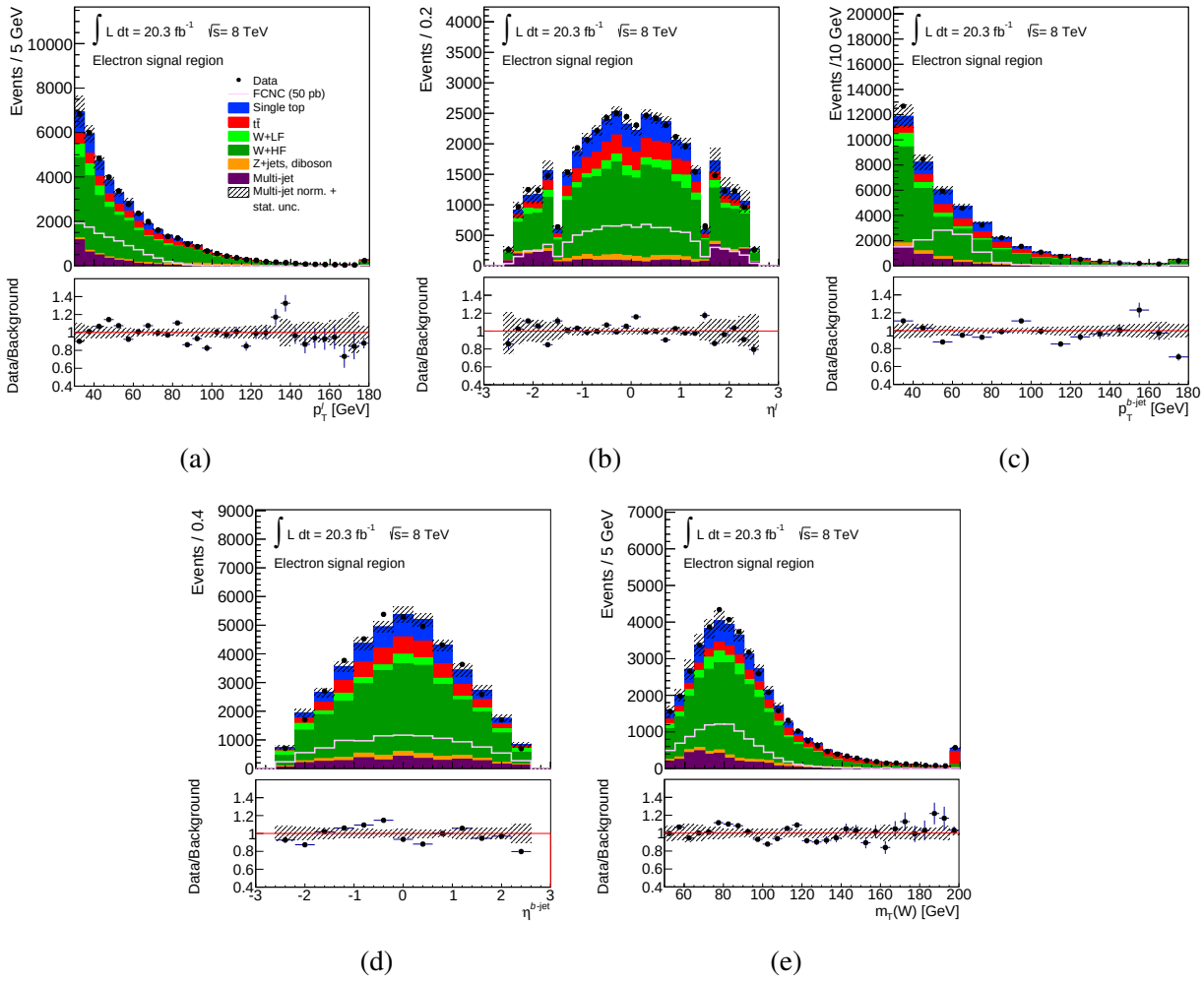

Figure B.2: Basic kinematic distributions of the signal region for the electron channel. The multi-jet background sample is produced using the matrix method. The hatched band indicates the combined statistical uncertainty and 17% multi-jet normalisation uncertainty. Shown are: (a) the transverse momentum and (b) pseudorapidity of the lepton, (c) the transverse momentum and (d) pseudorapidity of the jet, (e) transverse W-boson mass.

APPENDIX C

Additional checks for the neural network

C.1 Neural network overtraining test

MVA methods usually are subject to overtraining and thus to learn the kinematic configuration by heart which leads to worse performance and to a bias when applying the network on collision data. The overtraining in NeuroBayes is constantly checked during the training process using parts of the training samples as a test sample, the cross entropy error function of which is minimised after each training iteration. 80% of the MC events are used to train the neural network, the remaining 20% of are used as a test sample. The values of the error function for training and test samples are shown in Figure C.1. An increase of the value of the error on the test sample, would indicate an overtraining at a particular training iteration and leads to the training process being stopped, discarding the last iteration in which the overtraining occurred. Following this procedure the training is finished after 6 iterations for the network.

C.2 Variable decorrelation

During the neural network training, NeuroBayes decorrelates the input variables. The decorrelation is done based on the signal process. The Figure C.2 shows the correlation matrix of the input variables after the decorrelation is performed.

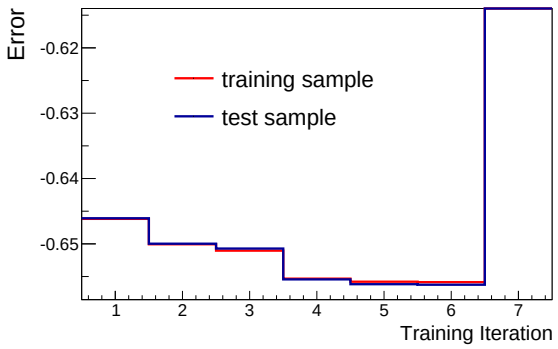

Figure C.1: Entropy error function during the training of the neural networks. The training sample is shown in red, the test sample shown in blue.

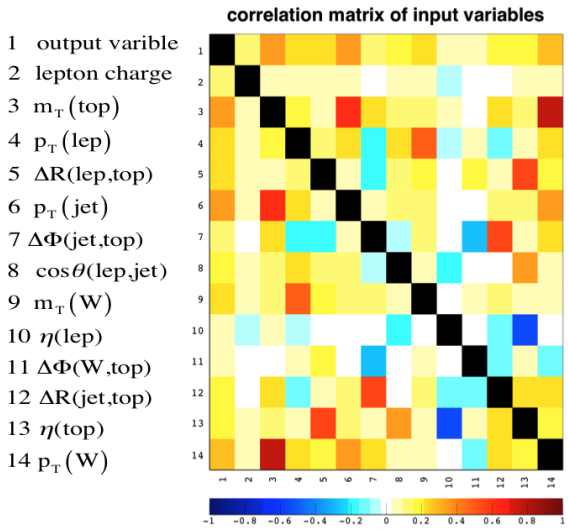

Figure C.2: The correlation matrix of the input variables after the neural network performs the decorrelation.

APPENDIX D

Control distributions of the ANN variables

This section provides the remaining control distributions of the input variables picked up by ANN.

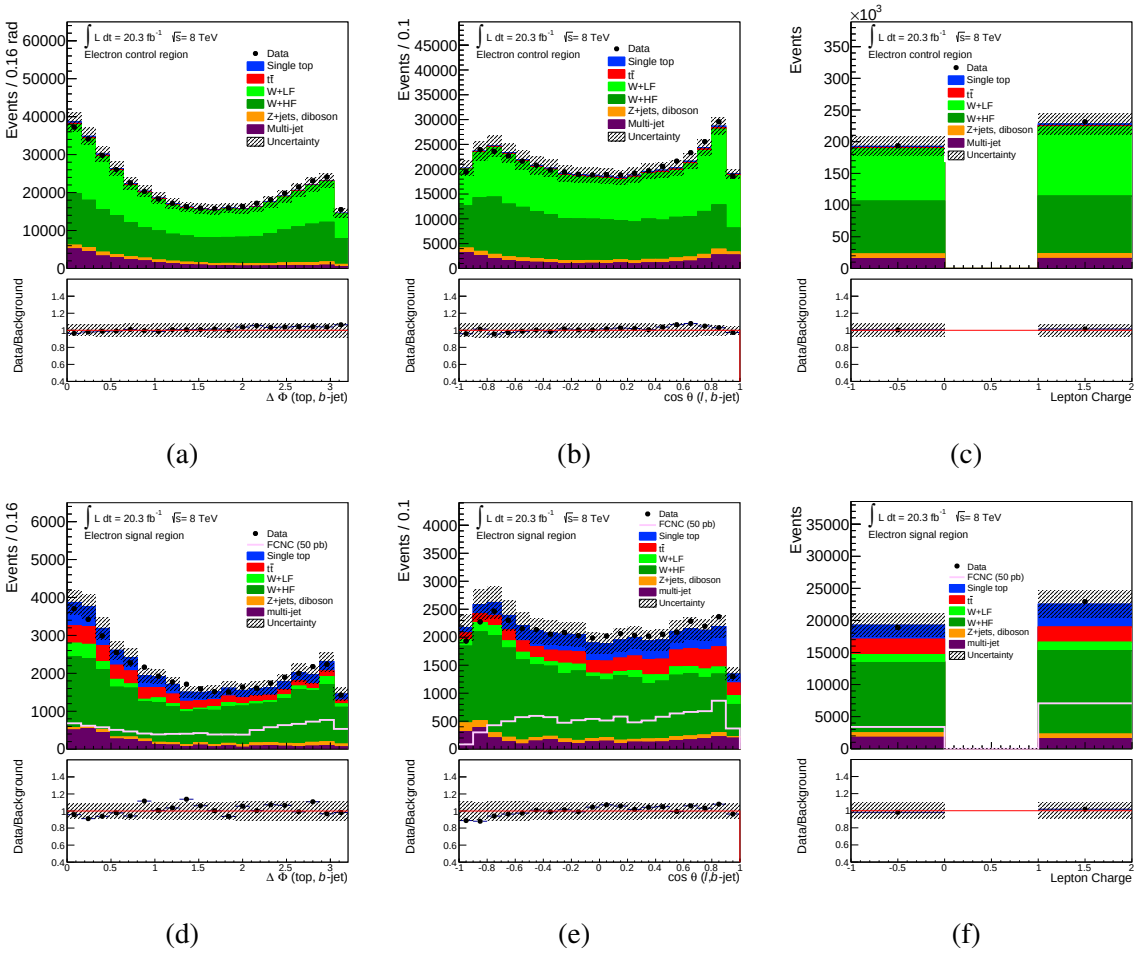

Figure D.1: Kinematic distributions of the input variables to the neural network in the electron channel control region (top row) and the signal region (bottom row) All processes are normalised to the result of the binned maximum likelihood fit used to determine the fraction of multi-jet events. The hatched bands represent the combination of the statistical uncertainty and the systematic uncertainties. Shown are the difference in azimuth between the reconstructed top quark and the *b*-tagged jet (a, d), opening angle of the three-vectors between the charged lepton and the *b*-tagged jet (b, e) and the charge of the lepton (c, f).

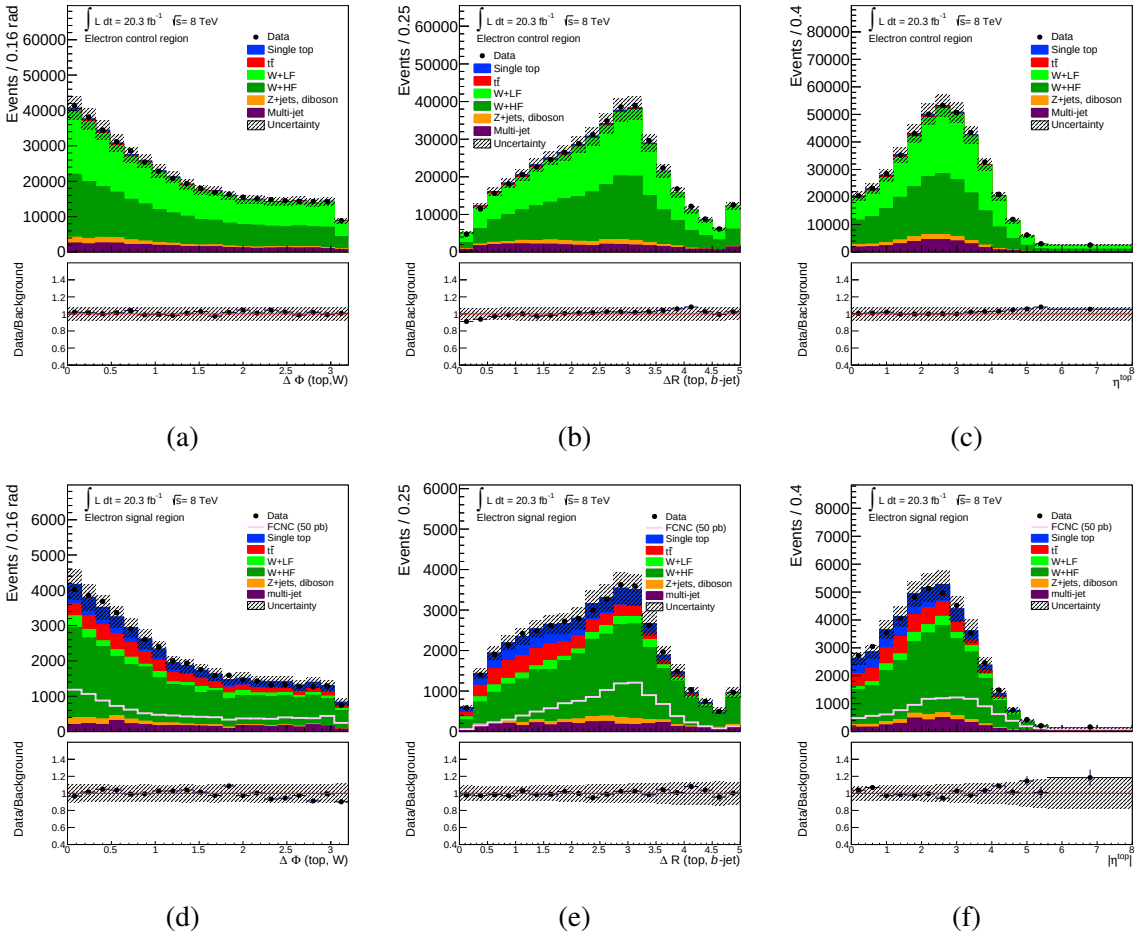

Figure D.2: Kinematic distributions of the input variables to the neural network in the electron channel control region (top row) and the signal region (bottom row) All processes are normalised to the result of the binned maximum likelihood fit used to determine the fraction of multi-jet events. The hatched bands represent the combination of the statistical uncertainty and the systematic uncertainties. Shown are the difference in azimuth between the reconstructed top quark and the reconstructed W-boson (a, d), distance in $\eta - \phi$ pane between the reconstructed top quark and the b-tagged jet (b, e) and the pseudorapidity of the reconstructed top quark (c, f).

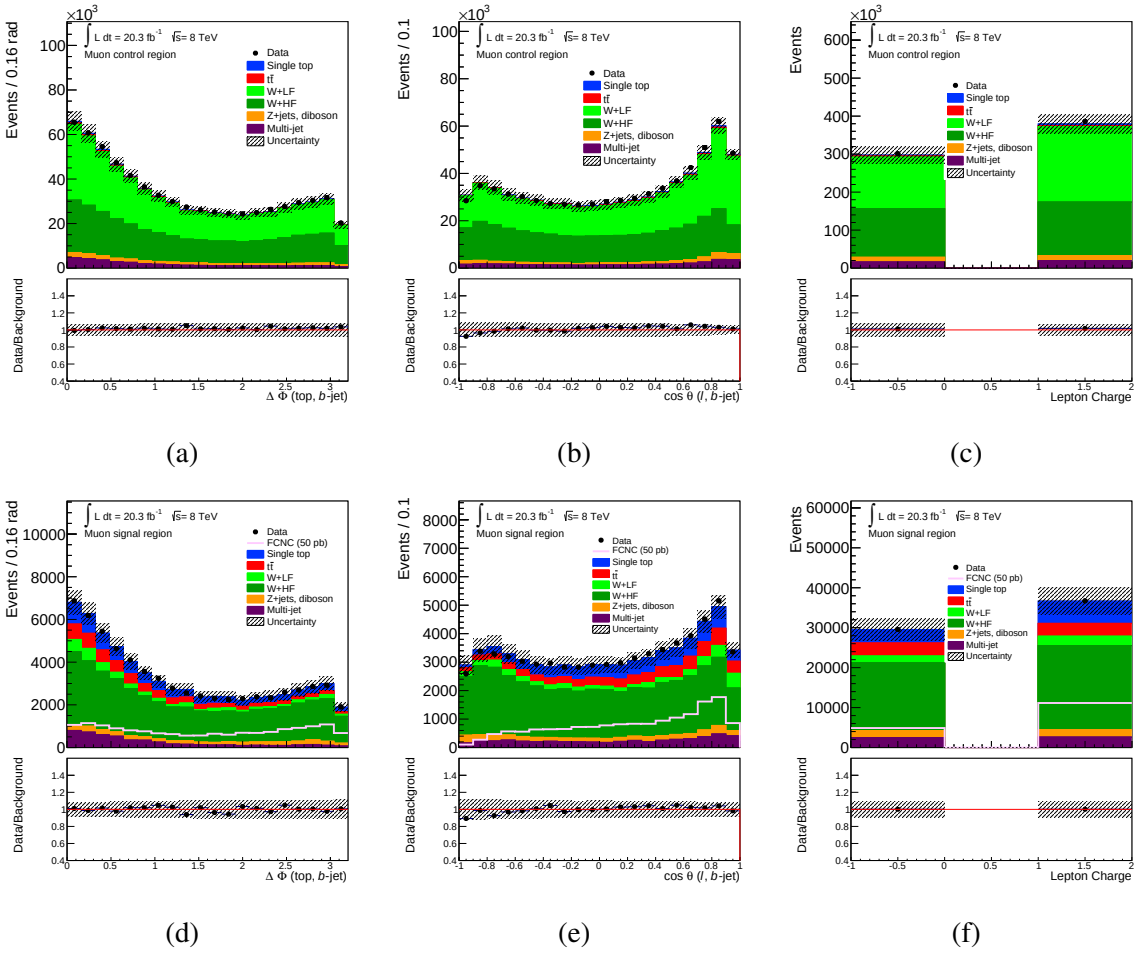

Figure D.3: Kinematic distributions of the input variables to the neural network in the muon channel control region (top row) and the signal region (bottom row) All processes are normalised to the result of the binned maximum likelihood fit used to determine the fraction of multi-jet events. The hatched bands represent the combination of the statistical uncertainty and the systematic uncertainties. Shown are the difference in azimuth between the reconstructed top quark and the *b*-tagged jet (a, d), opening angle of the three-vectors between the charged lepton and the *b*-tagged jet (b, e) and the charge of the lepton (c, f).

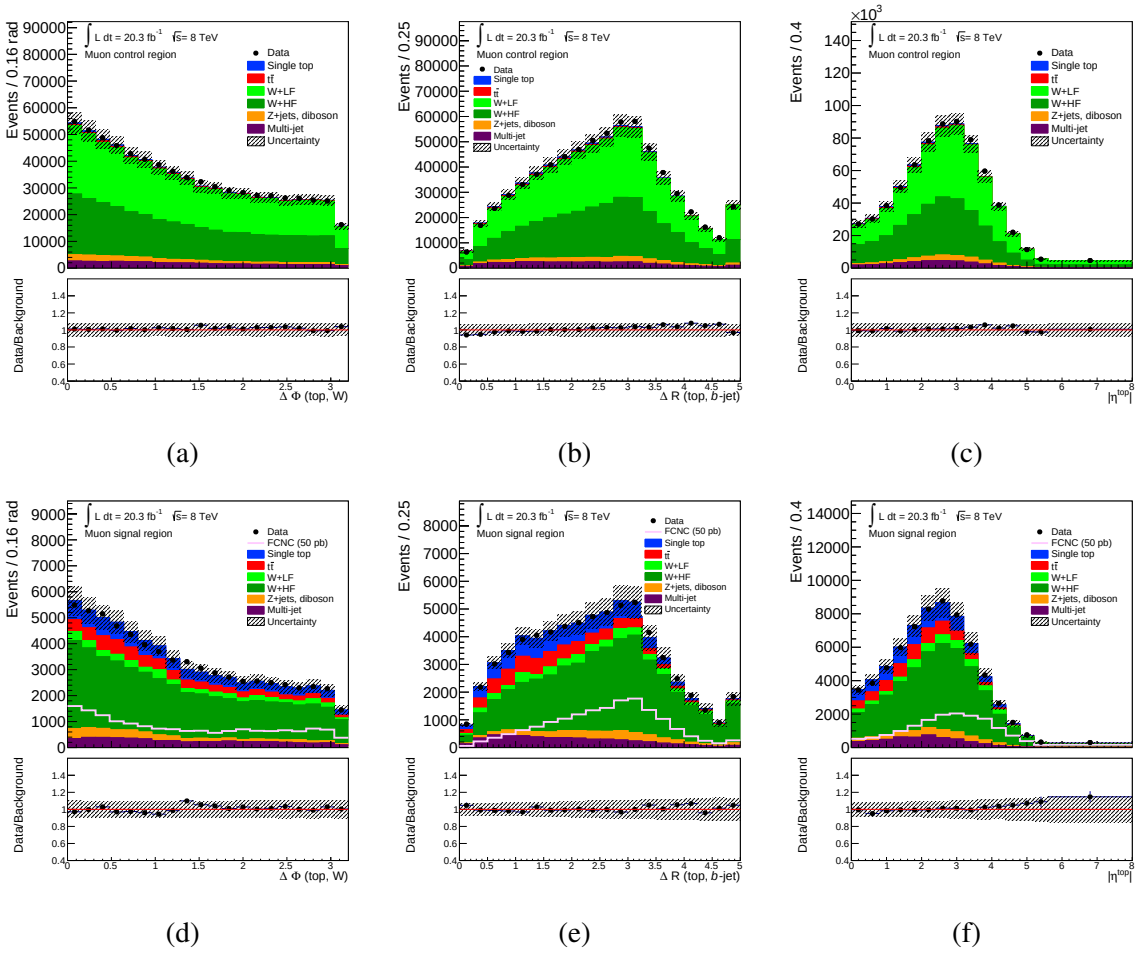

Figure D.4: Kinematic distributions of the input variables to the neural network in the muon channel control region (top row) and the signal region (bottom row) All processes are normalised to the result of the binned maximum likelihood fit used to determine the fraction of multi-jet events. The hatched bands represent the combination of the statistical uncertainty and the systematic uncertainties. Shown are the difference in azimuth between the reconstructed top quark and the reconstructed W-boson (a, d), distance in $\eta - \phi$ pane between the reconstructed top quark and the b-tagged jet (b, e) and the pseudorapidity of the reconstructed top quark (c, f).

APPENDIX E

Systematic uncertainties

E.1 Deviations in the neural network output distributions caused by the systematic uncertainties

This section shows all shape uncertainties which are considered in the final analysis.

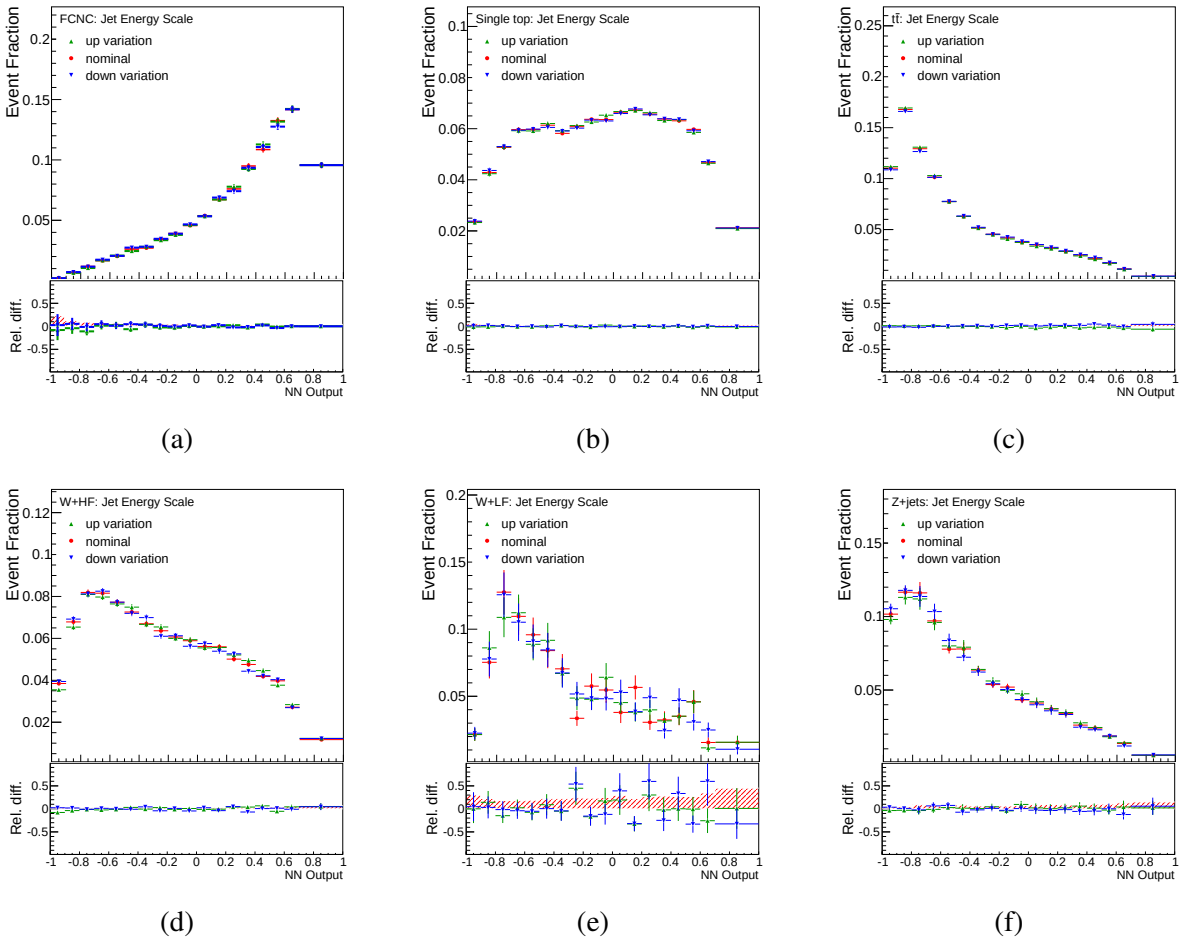

Figure E.1: Deviations in the network output distribution caused by the **jet energy scale uncertainty**.Shown are FCNC (a), single top (b), $t\bar{t}$ (c), W+HF (d), W+LF (e) and Z+jets (f).

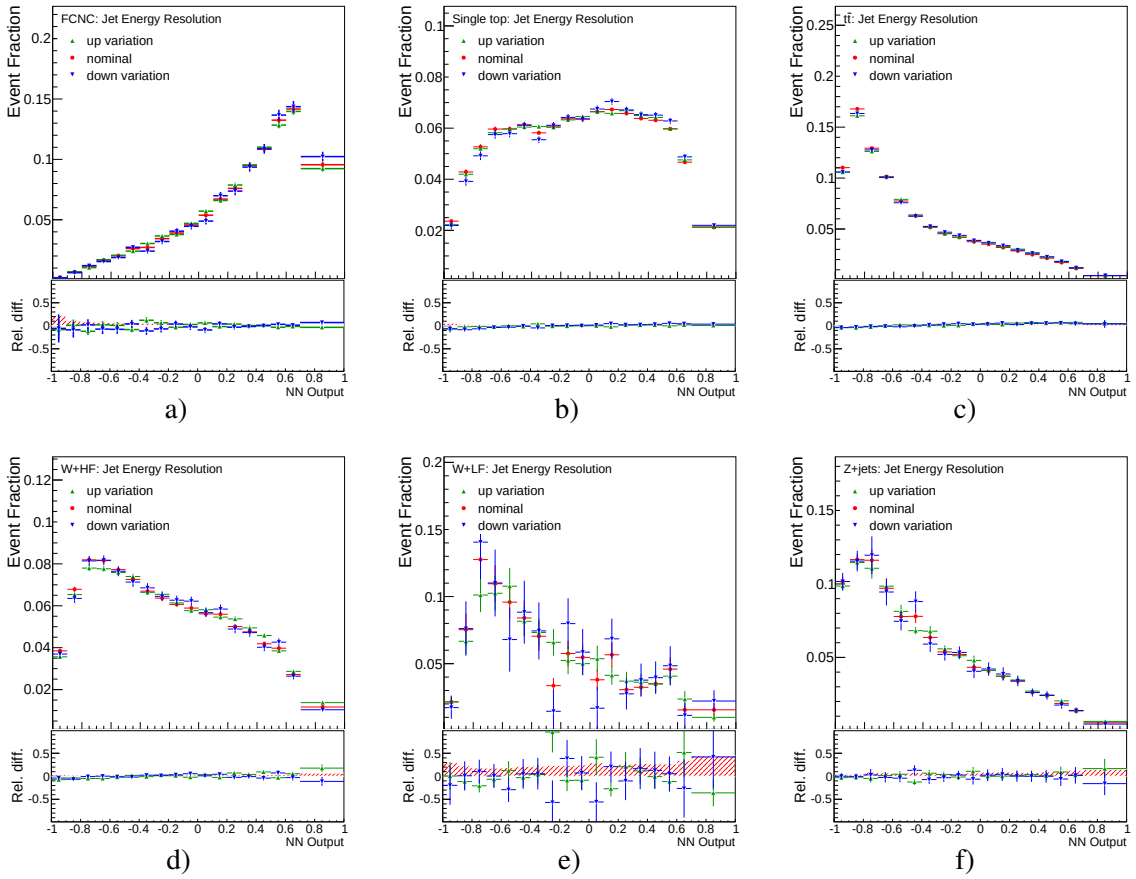

Figure E.2: Deviations in the network output distribution caused by the **jet energy resolution uncertainty**. Shown are FCNC (a), single top (b), $t\bar{t}$ (c), W+HF (d), W+LF (e) and Z+jets (f).

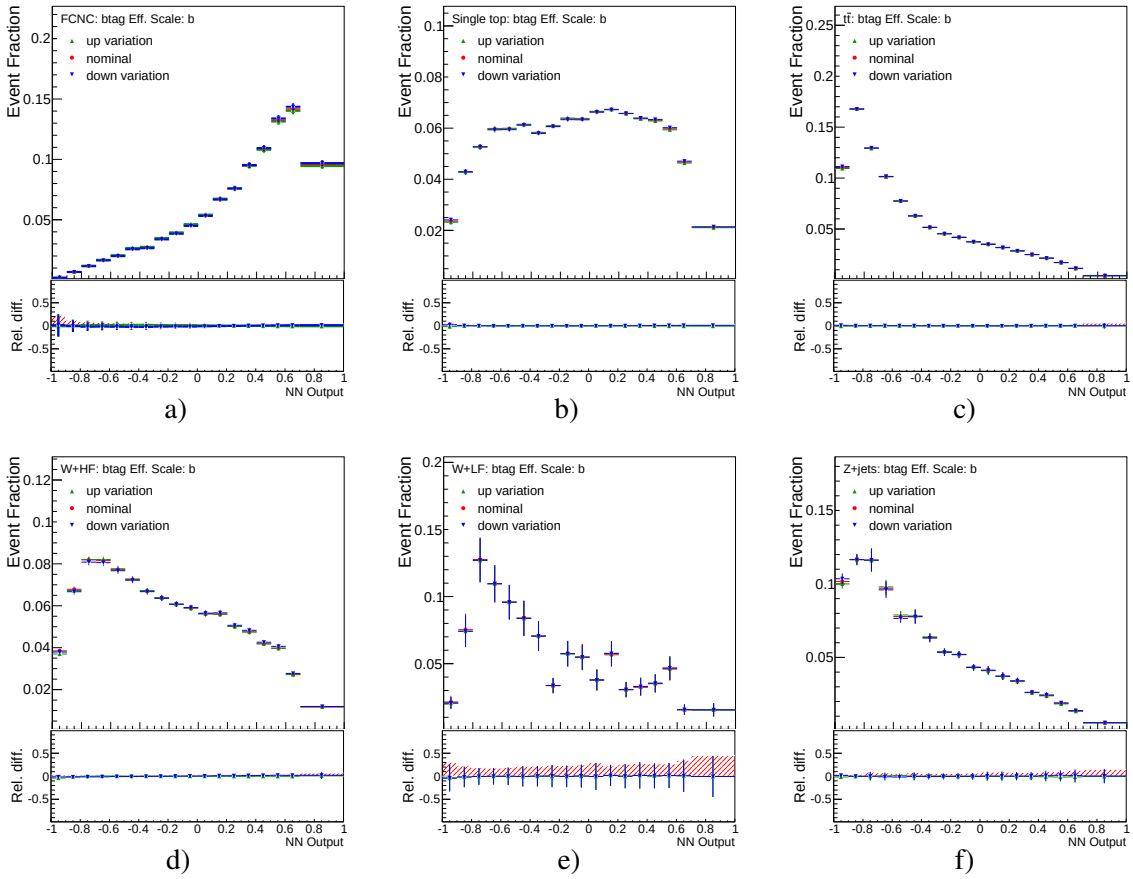

Figure E.3: Deviations in the network output distribution caused by the ***b*-tagging uncertainty**. Shown are FCNC (a), single top (b), $t\bar{t}$ (c), W+HF (d), W+LF (e) and Z+jets (f).

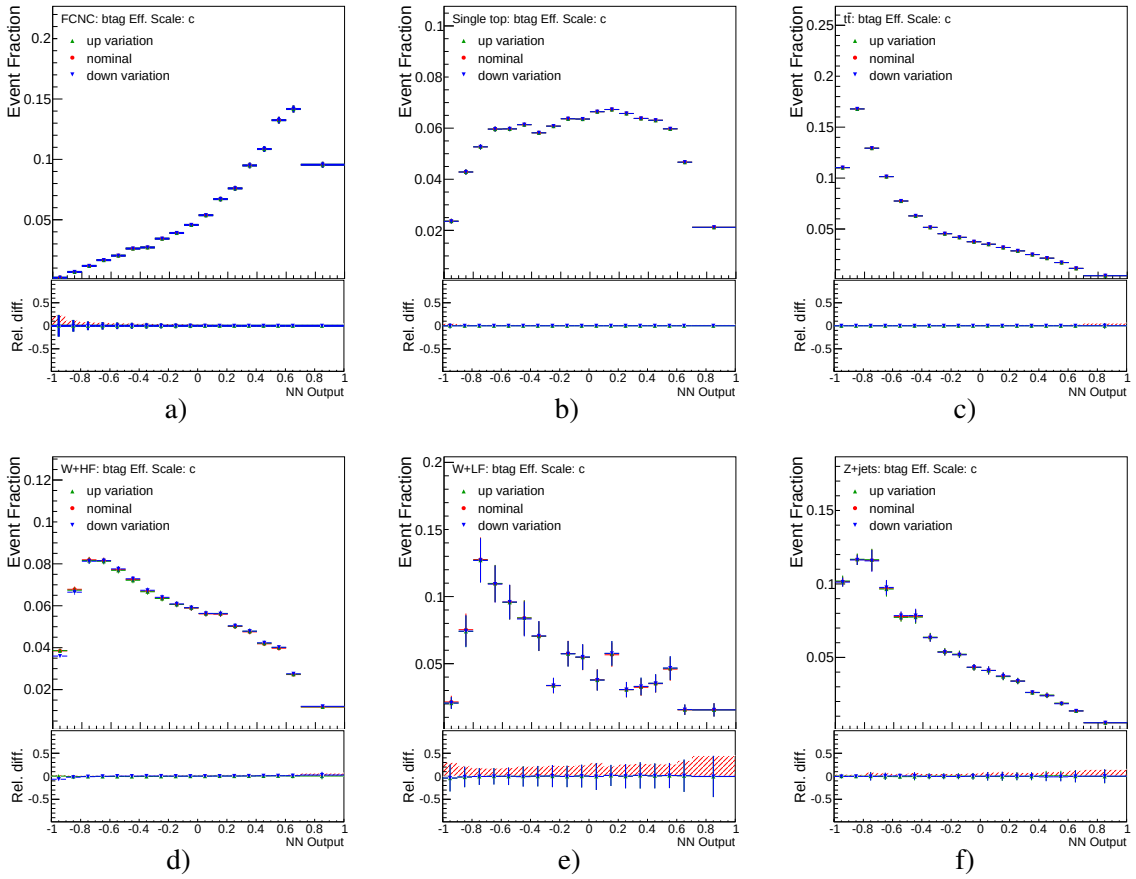

Figure E.4: Deviations in the network output distribution caused by the ***c*-tagging uncertainty**. Shown are FCNC (a), single top (b), $t\bar{t}$ (c), W+HF (d), W+LF (e) and Z+jets (f).

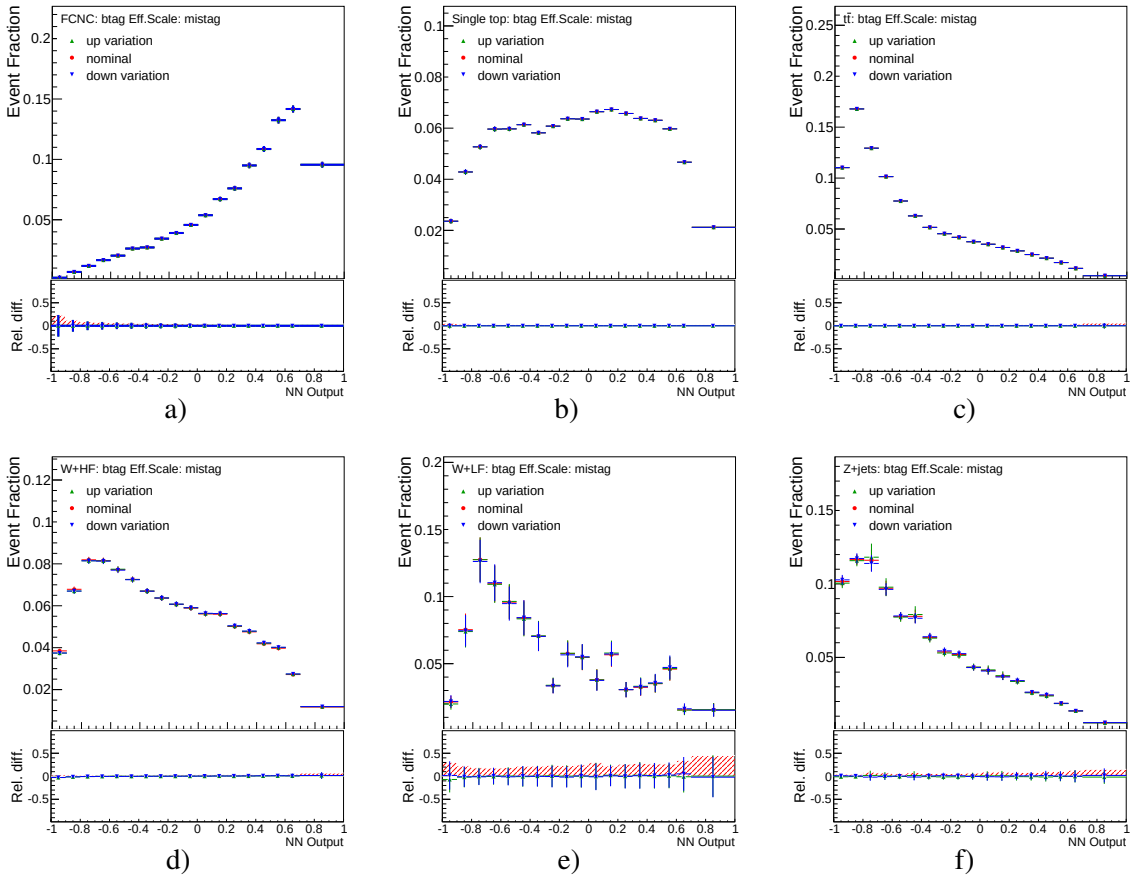

Figure E.5: Deviations in the network output distribution caused by the **mis-tagging uncertainty**. Shown are FCNC (a), single top (b), $t\bar{t}$ (c), W+HF (d), W+LF (e) and Z+jets (f).

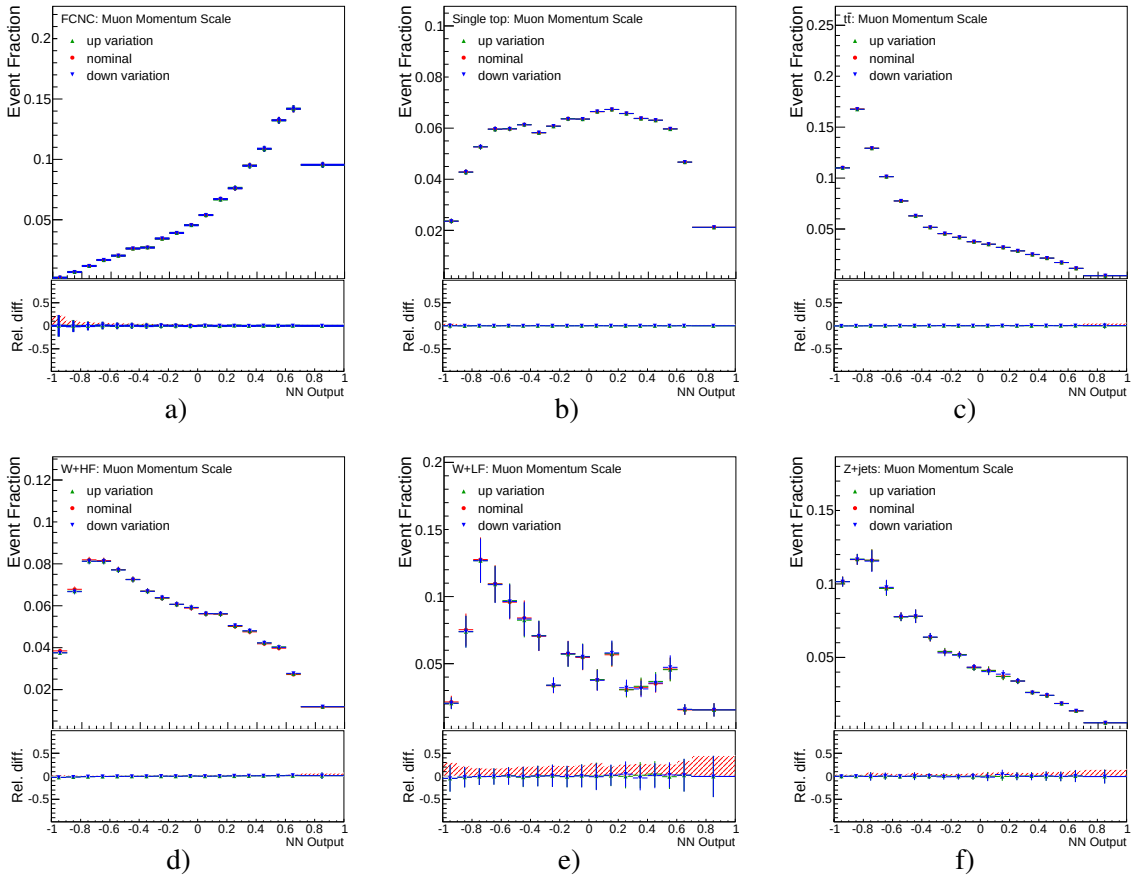

Figure E.6: Deviations in the network output distribution caused by the **muon momentum scale uncertainty**. Shown are FCNC (a), single top (b), $t\bar{t}$ (c), W+HF (d), W+LF (e) and Z+jets (f).

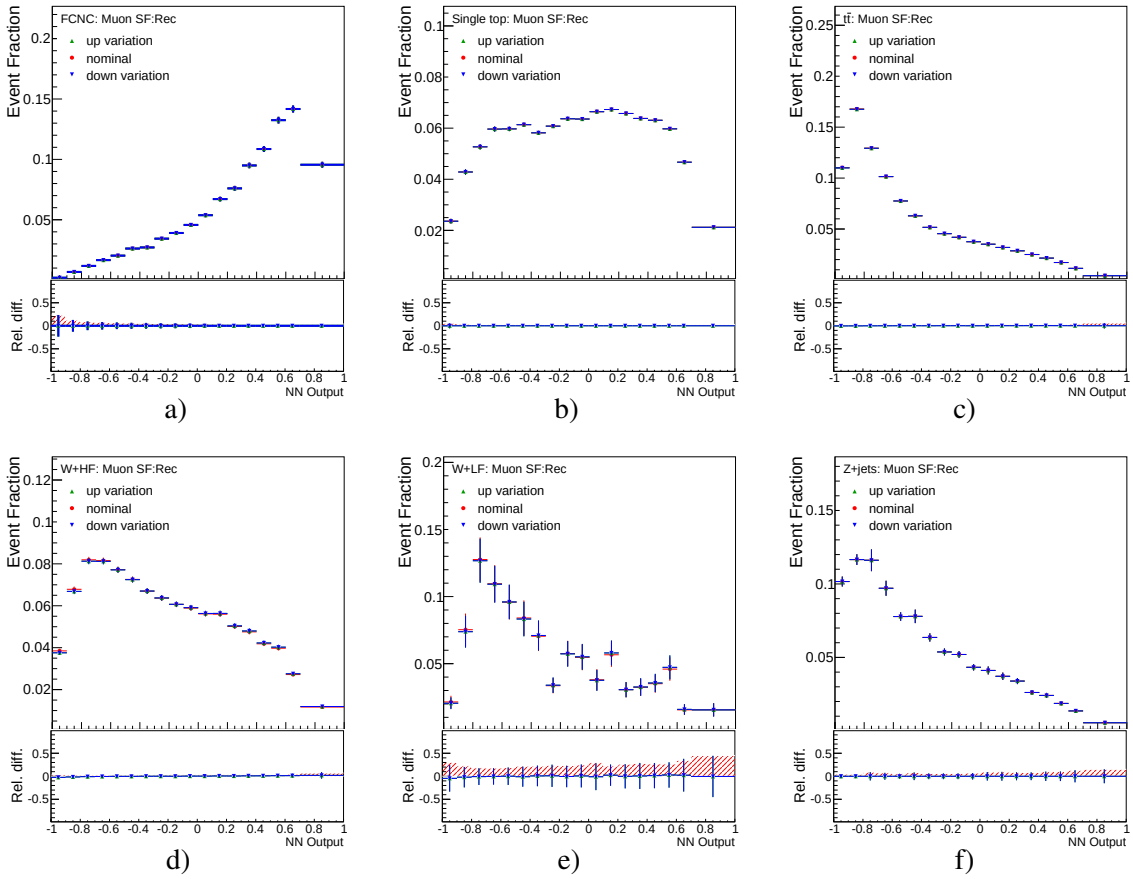

Figure E.7: Deviations in the network output distribution caused by the **muon reconstruction scale factor**. Shown are FCNC (a), single top (b), $t\bar{t}$ (c), W+HF (d), W+LF (e) and Z+jets (f).

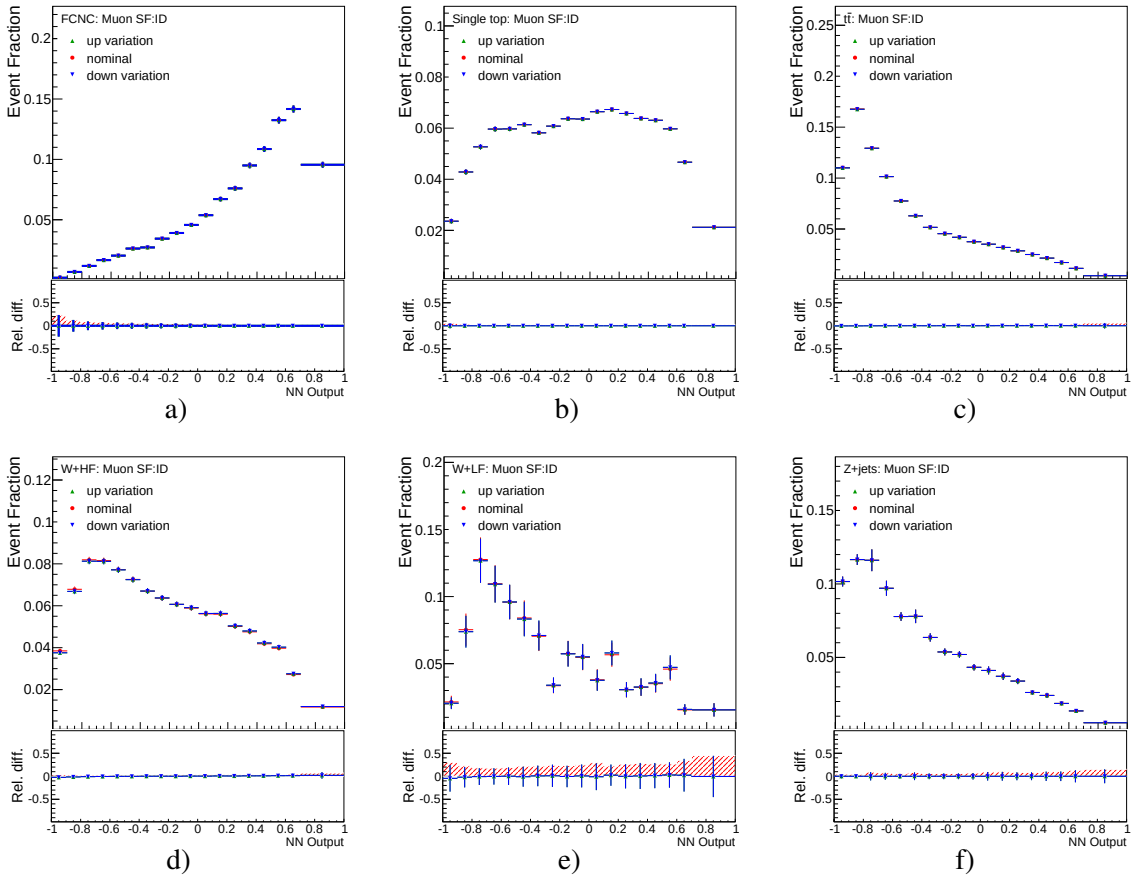

Figure E.8: Deviations in the network output distribution caused by the **muon identification scale factor uncertainty**. Shown are FCNC (a), single top (b), $t\bar{t}$ (c), W+HF (d), W+LF (e) and Z+jets (f).

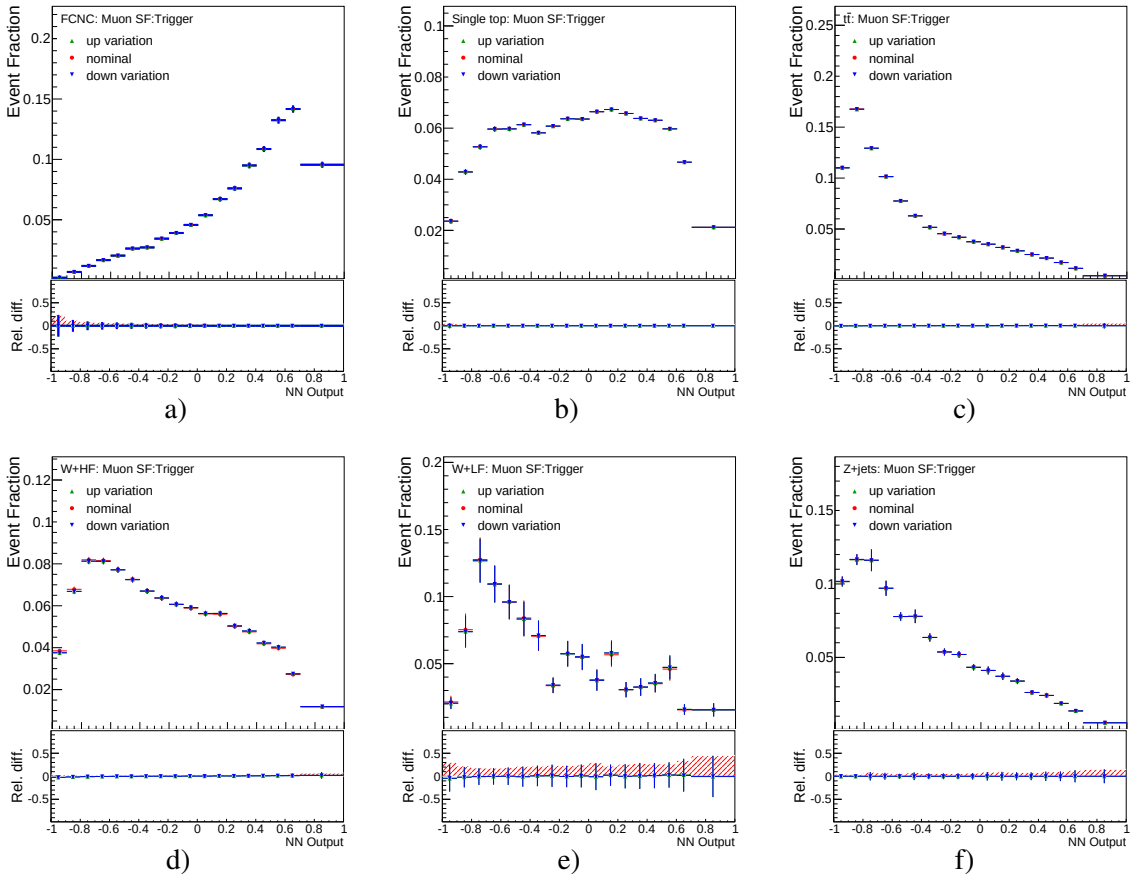

Figure E.9: Deviations in the network output distribution caused by the **muon trigger scale factor uncertainty**. Shown are FCNC (a), single top (b), $t\bar{t}$ (c), W+HF (d), W+LF (e) and Z+jets (f).

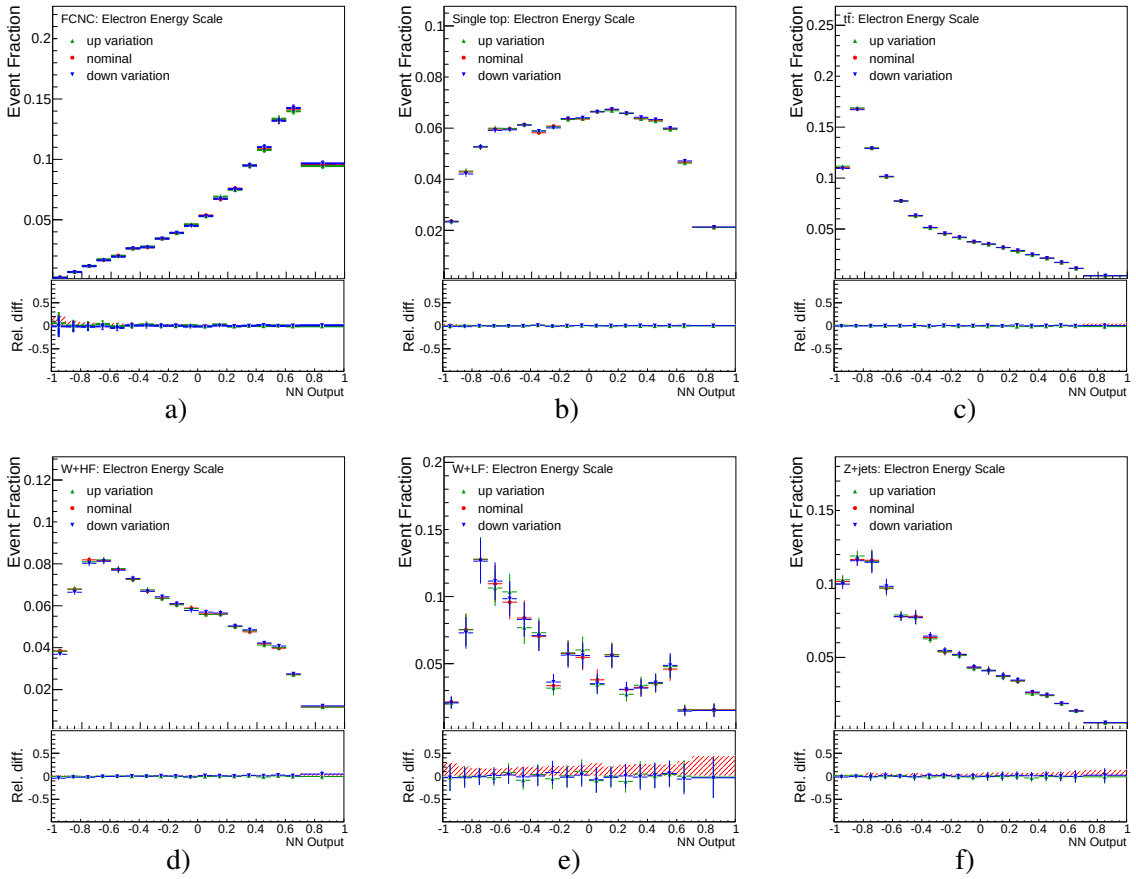

Figure E.10: Deviations in the network output distribution caused by the **electron energy scale**. Shown are FCNC (a), single top (b), $t\bar{t}$ (c), W+HF (d), W+LF (e) and Z+jets (f).

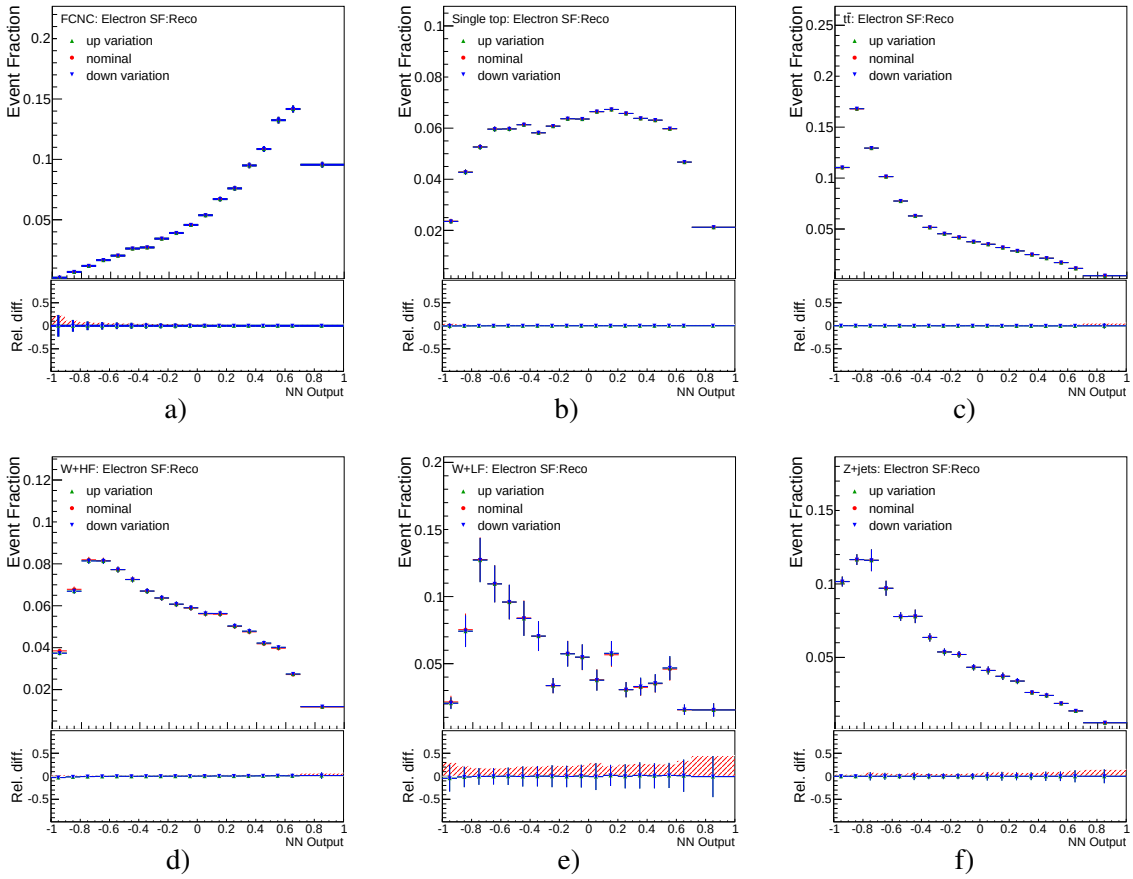

Figure E.11: Deviations in the network output distribution caused by the **electron reconstruction scale factor uncertainty**. Shown are FCNC (a), single top (b), $t\bar{t}$ (c), W+HF (d), W+LF (e) and Z+jets (f).

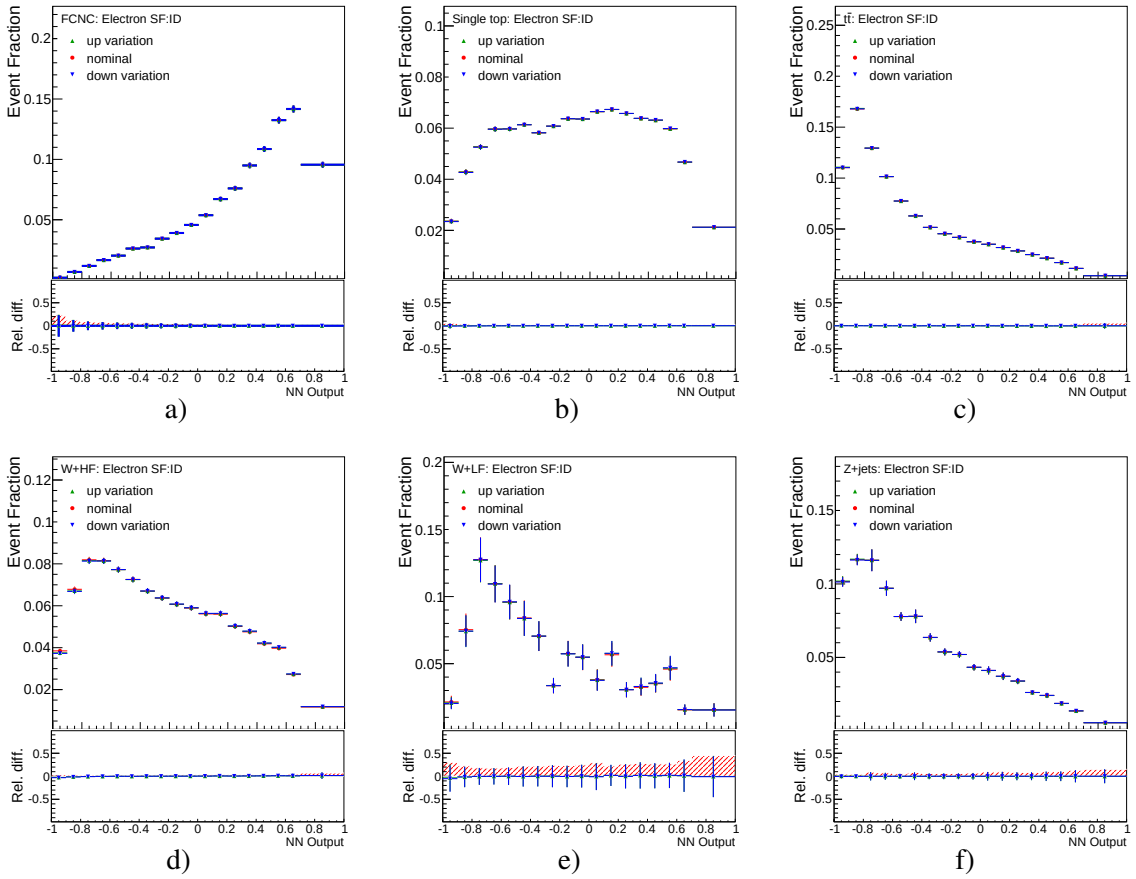

Figure E.12: Deviations in the network output distribution caused by the **electron identification scale factor uncertainty**. Shown are FCNC (a), single top (b), $t\bar{t}$ (c), W+HF (d), W+LF (e) and Z+jets (f).

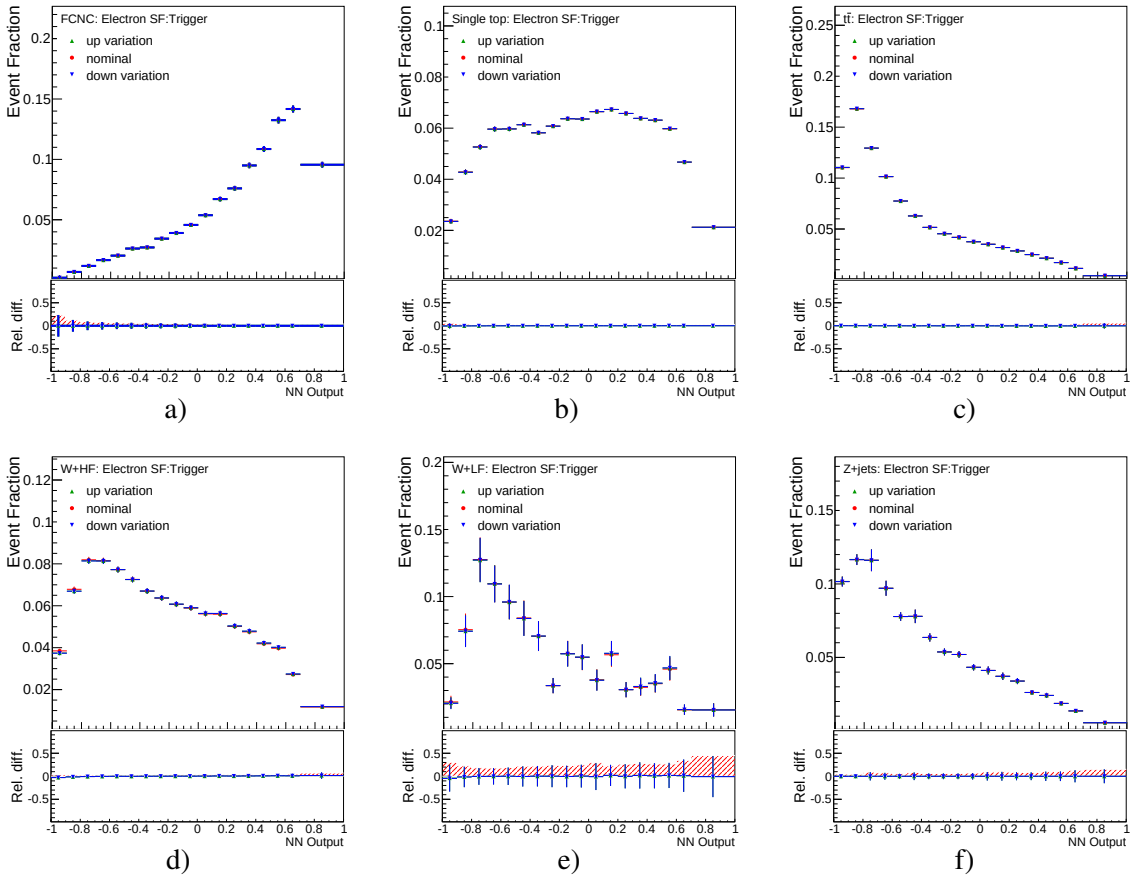

Figure E.13: Deviations in the network output distribution caused by the **electron trigger scale factor uncertainty**. Shown are FCNC (a), single top (b), $t\bar{t}$ (c), W+HF (d), W+LF (e) and Z+jets (f).

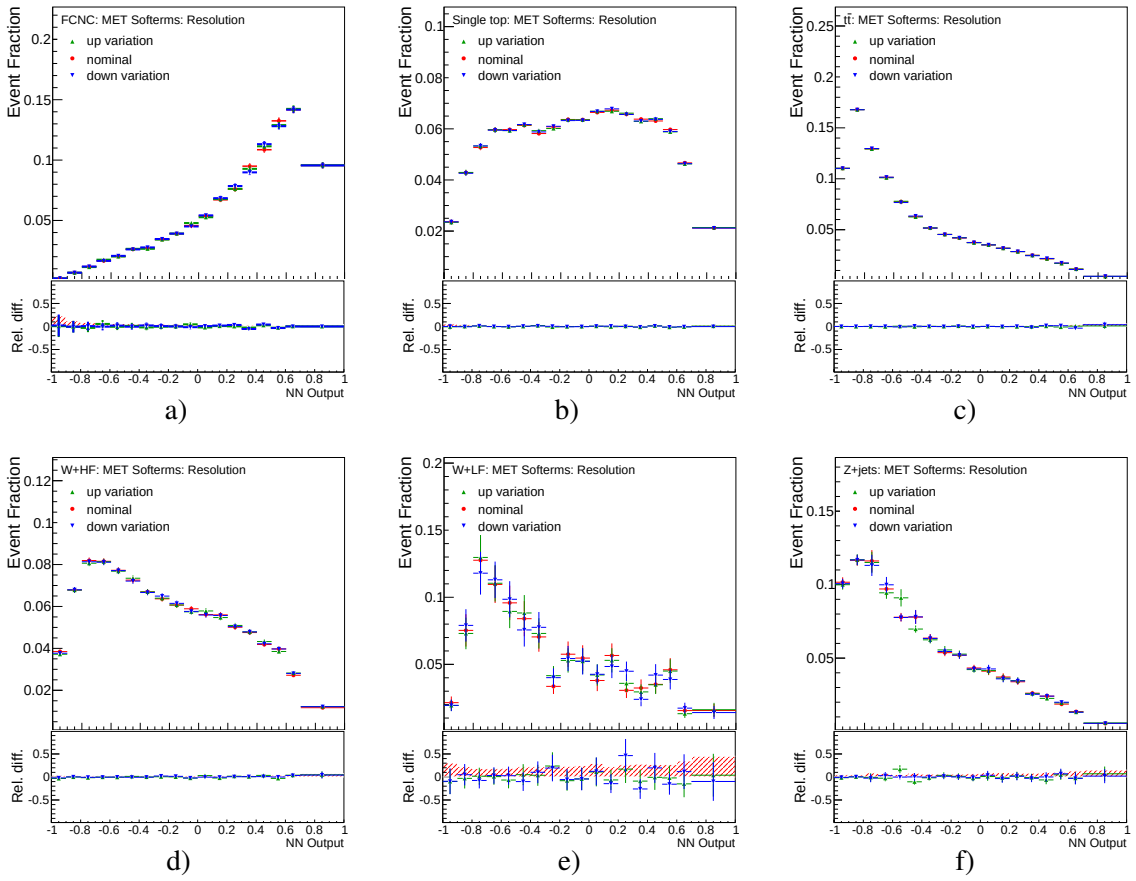

Figure E.14: Deviations in the network output distribution caused by the $\boldsymbol{E_{\mathrm{T}}^{\mathrm{miss}}}$ **cellout/softjets resolution uncertainty**. Shown are FCNC (a), single top (b), $\mathrm{t\bar{t}}$ (c), W+HF (d), W+LF (e) and Z+jets (f).

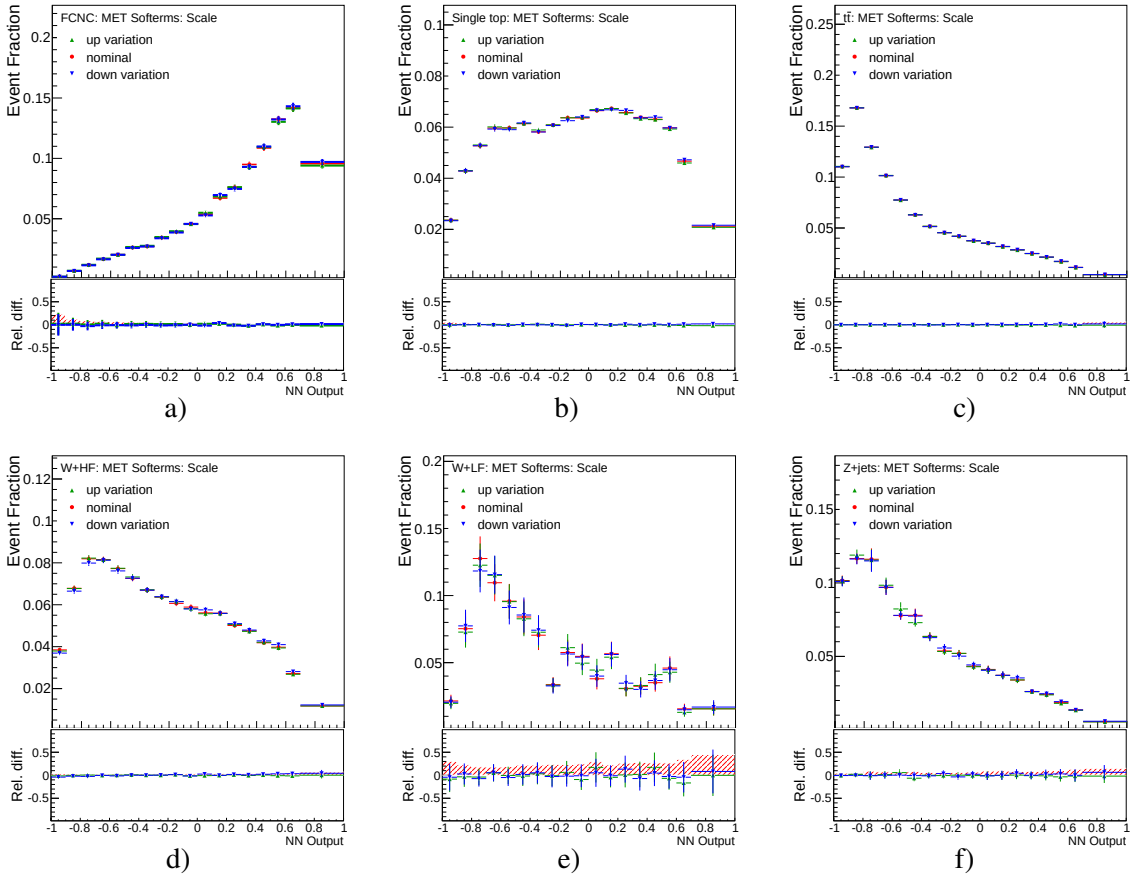

Figure E.15: Deviations in the network output distribution caused by the $\boldsymbol{E}_{\mathbf{T}}^{\mathbf{miss}}$ **cellout/softjets scale uncertainty**. Shown are FCNC (a), single top (b), $t\bar{t}$ (c), W+HF (d), W+LF (e) and Z+jets (f).

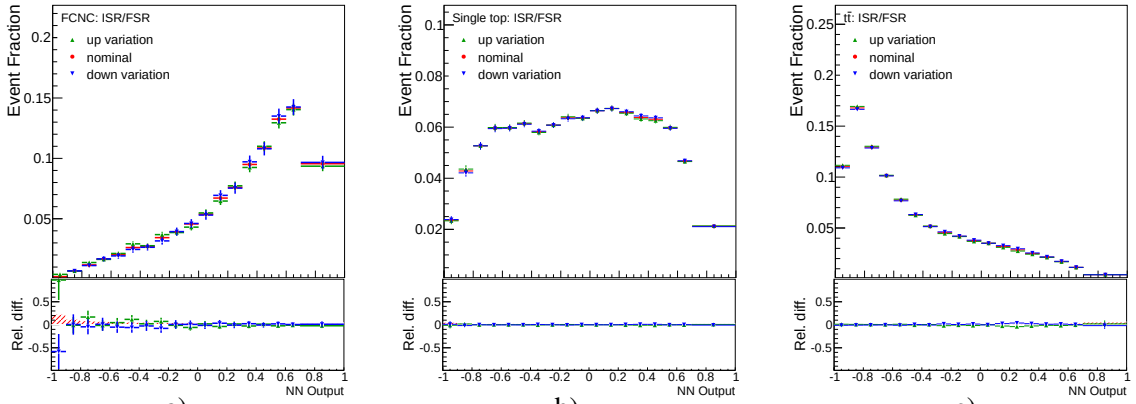

Figure E.16: Deviations in the network output distribution caused by the **ISR/FSR uncertainty**. Shown are FCNC (a), single top (b), $t\bar{t}$ (c).

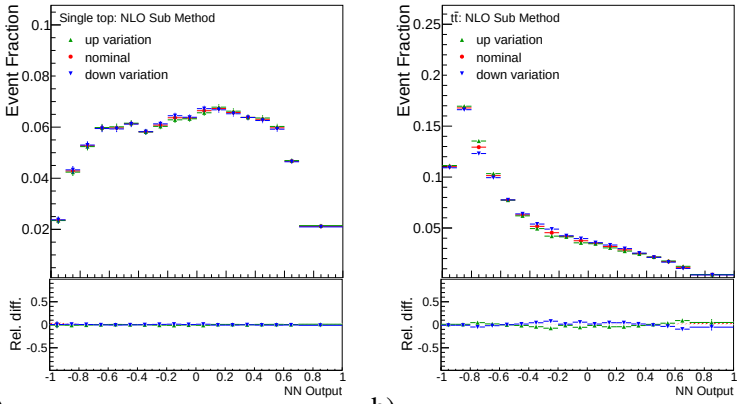

Figure E.17: Deviations in the network output distribution caused by the **NLO subtraction method uncertainty**. Shown are single top (a), $t\bar{t}$ (b).

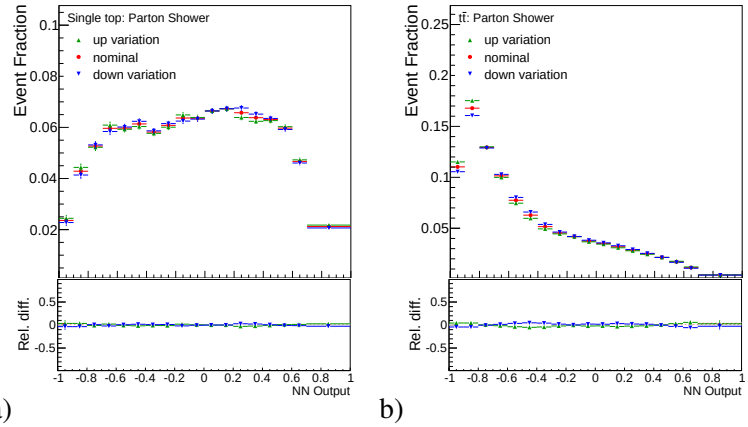

Figure E.18: Deviations in the network output distribution caused by the **parton shower uncertainty**. Shown are single top (a), $t\bar{t}$ (b).

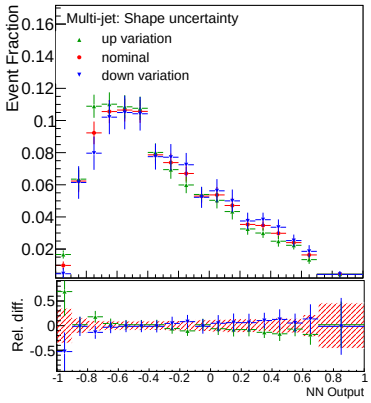

Figure E.19: Deviations in the network output distribution caused by the **multi-jet background shape uncertainty**.

E.2 The NN output distribution of W+LF and W+HF backgrounds in the signal region before and after the re-weighting

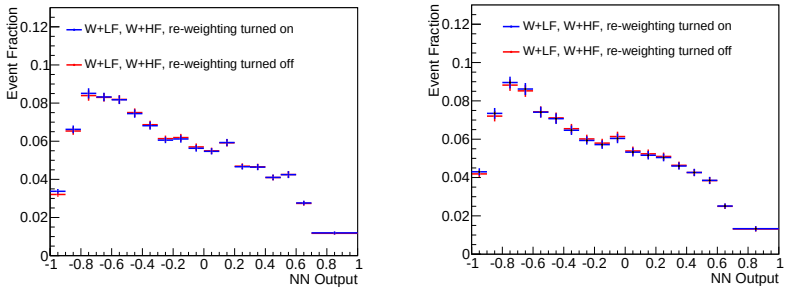

(a) (b)

Figure E.20: The shape comparison of NN output distribution for the W+LF and W+HF backgrounds before and after the re-weighting is applied the electron (a) and the muon (b) channels. The effect is small and it occurs mostly in the background region of the distribution.

List of Figures

List of Tables

Acknowledgements

First and foremost, I would like to thank my advisor, Professor Ian C. Brock. I am immensely thankful that he gave me the opportunity to join his working group therefore to work in a friendly and productive environment. His positive attitude, great knowledge in particle physics, supporting and thoughtful nature helped me finish this work. Without him, it would have been dreadfully difficult. It is impossible for me to repay him for all the time he invested in me and for making this work come true. I also would like to thank to Professor Jochen Dingfelder, Professor Bernard Metsch and Professor Irmgard Förster for taking their time and reading my thesis and for the constructive discussion during the examination.

I would like to thank the ATLAS Collaboration and CERN for allowing me to be a part of one of the biggest and most successful scientific communities in the world. It is indeed an honour for me to be involved in the experiments at CERN.

I would like to thank my colleagues at the University of Wuppertal, especially to Dominic Hirschbühl. His supervision and practical ideas helped this work proceed and overcome the direst situations.

I want to acknowledge the friendly guidance and support of my former colleagues Jan Stillings, Thomas Velz and Sebastian Mergelmeyer, especially for teaching me dozens of programming tricks. After Thomas started supervising me, the analysis accelerated and thanks to him, I was able to obtain my first results.

I thank Irina Cioară, for being a friend who is always there for me. I will cherish every nice moment we spent together both during and outside work. She is a true friend and a person that one can rely on. I thank her also for proof-reading my thesis and therefore contributing to accomplish this work.

I am grateful to Regina Moles Valls for her assistance and supervision as our Postdoc of the Brock group. She has a great personality and immense energy that kept the mood up and motivated the group. I wish her a successful academic career for the coming years ahead of her.

I am happy to have a friend like Anjishnu Bandyopadhyay; I will remember all the interesting, philosophical and hilarious discussions we had. I thank him for his help during writing my thesis. He gave me great suggestions especially for the theory and the statistical analysis parts of this thesis. He is a smart person with a bright future ahead of him.

I thank Rui Zhang, for being such an awesome friend. I will always remember the funny moments I experienced with him during every conference we attended together.

I am grateful to Peter Kövesárki, for our good times both at CERN and in Bonn. I am thankful for the

help that I received from him during my PhD and for his friendship afterwards.

I am pleased to have the opportunity to work with great colleagues and students, in particular with Elena Zarkh, Elena Nickel, Professor Ewald Paul, Muhammad Alhroob and Peter Falke.

Special thanks go to my dear Kris, for being beside me in the last stressful days before my examination. Her motivation and encouragement kept me focused. I am grateful to her for taking care of me in difficult moments and also for organising the after-party.

Lastly, I thank my parents for believing in me and for supporting me by any means. Without their support, it would only be a dream for me to achieve this work.